



## 저작자표시-비영리-변경금지 2.0 대한민국

이용자는 아래의 조건을 따르는 경우에 한하여 자유롭게

- 이 저작물을 복제, 배포, 전송, 전시, 공연 및 방송할 수 있습니다.

다음과 같은 조건을 따라야 합니다:



저작자표시. 귀하는 원저작자를 표시하여야 합니다.



비영리. 귀하는 이 저작물을 영리 목적으로 이용할 수 없습니다.



변경금지. 귀하는 이 저작물을 개작, 변형 또는 가공할 수 없습니다.

- 귀하는, 이 저작물의 재이용이나 배포의 경우, 이 저작물에 적용된 이용허락조건을 명확하게 나타내어야 합니다.
- 저작권자로부터 별도의 허가를 받으면 이러한 조건들은 적용되지 않습니다.

저작권법에 따른 이용자의 권리는 위의 내용에 의하여 영향을 받지 않습니다.

이것은 [이용허락규약\(Legal Code\)](#)을 이해하기 쉽게 요약한 것입니다.

[Disclaimer](#)

공학박사학위논문

**Computational Science Approach  
for Design and Optimization of  
Sustainable Process and Its  
Industrial Applications**

계산 과학적 접근을 통한 지속가능한 공정의  
최적 설계 및 산업에의 응용

2018 년 2 월

서울대학교 대학원

화학생명공학부

나 종 결

## **Abstract**

# **Computational Science Approach for Design and Optimization of Sustainable Process and Its Industrial Applications**

Jonggeol Na

School of Chemical & Biological Engineering

The Graduate School of Seoul National University

Recently, in the field of chemical engineering, many types of research based on high-performance computing have been combined with computer-aided process systems engineering. Therefore, various techniques of computational science such as computational fluid dynamics, optimization methodology, and machine learning have been applied to the problems of chemical reactor modeling and process optimization. Notably, in this advance computational science approach, the scope of research extends to non-traditional fields such as reactive research according to the 3D shape of the reactor that has not been

easily solved in the past and surrogate model based optimization using machine learning. In this thesis, various methods are proposed to obtain the maximum profit with minimum cost by making a breakthrough design.

In parallel, there is a growing demand for sustainable chemical processes in chemical engineering. Conventional chemical processes are highly dependent on oil prices, and unless a diverse portfolio is designed, the sustainability of their chemical industries can be violated because of the oil controlling from the Middle East or US. In addition, these crude oil based chemical processes and power plants generate a great deal of CO<sub>2</sub>. Therefore, it is not necessary to capture these CO<sub>2</sub> and make only meaningless storage but to reproduce it as a product that can be used and make it economical carbon capture, utilization, and storage (CCUS) technology. To solve this series of processes, the Gas-to-Liquid (GTL) process and CCUS are being researched and developed in various ways.

In this thesis, I will discuss the process modeling, optimizing, and designing the reactor and process using CFD, mathematical programming, machine learning, deep learning, and derivative-free optimization techniques in computational science. First of all, the Fischer-Tropsch microchannel reactor and 3-phase carbonation reactor, which are the key reactor of two most important processes of the sustainable process, the gas-to-liquid process (GTL) and the carbon capture, utilization, and storage (CCUS), are modeled by CFD.



Also, we propose an integration platform of CFD model and process simulator and conduct research from the point of view of combining with existing process engineering.

With these advanced reactor model, we propose a multi-objective optimization methodology using a stochastic optimization algorithm, a genetic algorithm (GA) with e-constraint method for simultaneously maximizing C<sub>5+</sub> productivity and minimizing the temperature rise of a Fischer-Tropsch microchannel reactor. The main mixed integer nonlinear programming (MINLP) optimization problem is decomposed into an external CFD reactor model function and internal optimization constraints. The methodology is applied to the catalyst packing zone division, which is divided and packed with a different dilution ratio to distribute the heat of reaction evenly. The best solutions of the proposed optimizer are reproducible with different crossover fractions and are more efficient than other traditional non-convex constraint local solvers. Based on the Pareto optimal solution of the final optimizer with 4 zones, discrete dilution increases C<sub>5+</sub> productivity to 22% and decreases  $\Delta T_{\max}$  to 63.2% compared to the single zone catalyst packing case. Finally, several Pareto optimal solutions and sub-optimal solutions are compared and the results are documented in terms of C<sub>5+</sub> productivity and maximum temperature increase.

In process scale optimization platform, a modified DIRECT algorithm with a sub-dividing step for considering hidden constraints is proposed. The

effectiveness of the algorithm is exemplified by its application to a cryogenic mixed refrigerant process using a single mixed refrigerant for natural gas liquefaction and its comparison with a well-known stochastic algorithm (GA, PSO, SA), and model based search algorithm (SNOBFIT), local solver (GPS, GSS, MADS, active-set, interior-point, SQP), and other hidden constraint handling methods, including the barrier approach and the neighborhood assignment strategy. Optimal solution calculated by the proposed algorithms decreases the specific power required for natural gas liquefaction to 18.9% compared to the base case. In the same chapter, heat exchanger network synthesis (HENS) has progressed by using mathematical programming-based simultaneous methodology. Although various considerations such as non-isothermal mixing and bypass streams are applied to consider real world alternatives in modeling phase, many challenges are faced because of its properties within non-convex mixed-integer nonlinear programming (MINLP). We propose a modified superstructure, which contains a utility substage for use in considering multiple utilities in a simultaneous MINLP model. To improve model size and convergence, fixed utility locations according to temperature and series connections between utilities are suggested. The numbers of constraints, discrete, and continuous variables show that overall model size decreases compared with previous research. Thus, it is possible to expand the feasible search area for reaching the nearest global solution. The model's effectiveness and applications are exemplified by several literature problems,

where it is used to deduce a network superior to that of any other reported methodology.

In the case of plant-wide scale systems, a non-linear surrogate model based on deep learning is proposed using a variational autoencoder with deep convolutional layers and a deep neural network with batch normalization (VAEDC-DNN) for real-time analysis of the probability of death ( $P_{\text{death}}$ ). VAEDC can extract representation features of the  $P_{\text{death}}$  contour with complicated urban geometry in the latent space, and DNN maps the variable space into the latent space for the  $P_{\text{death}}$  image data. The chlorine gas leak accident in the Mipo complex (city of Ulsan, Republic of Korea) is used for verification of the model. The proposed model predicts the  $P_{\text{death}}$  image within a mean squared error of 0.00246, and compared with other models, it exhibits superior performance. Furthermore, through the smoothness of image transition in the variable space, it is confirmed that image generation is not overfitting by data memorization.

Finally, a pilot scale (1.0 BPD) compact GTL process comprising of reforming section,  $\text{CO}_2$  separating section and Fischer -Tropsch (FT) synthesis section is presented. Systematic design procedure adopted for the design of a modular 0.5 BPD microchannel FT reactor block design consisting of 528 process channels is described. On average 98.27%  $\text{CH}_4$  conversion to syngas in reforming section comprising of a pre-reformer unit and a tri-reformer unit,

CO<sub>2</sub> separation rate of 36.75 % along with CO/H<sub>2</sub> reduction from 2.67 to 2.08 in CO<sub>2</sub> membrane separation section comprising of three membrane separators, for the entire plant operation duration of 450 hr demonstrated successful and stable operation of pre-processing sections of the present pilot-scale compact GTL process. Parallel operation of FT microchannel reactor and multitubular fixed bed type FT reactor proved failure for latter due to reaction runaway, while the former showed stable operation with high CO conversion of 83% and successful temperature control (at 220 °C, 230 °C and at 240 °C during the 139 hr operation), which demonstrated the appreciable performance of KOGAS-SNU novel microchannel FT reactor. Furthermore, a tank agitator carbonation reactor in which the reaction between calcium oxide and carbon dioxide takes place is studied to understanding that how 6 design variables (the number of impeller, impeller type, D/T, clearance, speed, baffle) affect to the solid dispersion using CFD simulation.

**Keywords:** Computational science; Computational fluid dynamics (CFD); Optimization; Design; Gas-to-Liquid (GTL); Fischer-Tropsch (FT); Microchannel reactor; Carbon capture, utilization, and storage (CCUS); Machine learning; Deep learning

**Student Number:** 2013-20968

# Contents

Abstract .....	i
Contents.....	vii
List of Figures .....	x
List of Tables .....	xv
CHAPTER 1. Introduction.....	17
1.1. Research motivation.....	17
1.1.1. Chronological stages of development of process design.....	19
1.1.2. Current status of process systems engineering with computational science approach.....	21
1.1.3. Introduction to the sustainable process .....	23
1.2. Research objectives .....	25
1.3. Outline of the thesis.....	26
1.4. Associated publications .....	29
CHAPTER 2. Study of the Novel Reactor Models using Computational Science .....	30
2.1. Introduction .....	30
2.2. Gas-to-Liquid (GTL) Fischer-Tropsch (FT) reactor model.....	32
2.2.1. 2D axisymmetric computational fluid dynamics (CFD) based Fischer-Tropsch microchannel reactor single-channel model.....	37
2.2.2. 3D CFD based Fischer-Tropsch microchannel reactor multi- channel model .....	52
2.3. Carbon Capture, Utilization, and Storage (CCUS) multiphase carbonation reactor model.....	75

2.3.1. Rigorous reaction kinetics for carbonation based CCUS reactor .....	77
2.3.2. Eulerian multiphase model for carbonation reactor .....	92
2.4. CFD-Process integrated platform for simultaneous process and reactor design .....	105
2.4.1. Introduction .....	105
2.4.2. Model formulation.....	106
2.4.3. Result and discussion .....	112
2.4.4. Conclusion.....	116
CHAPTER 3. Optimization for the Unit, Process, and Plant-wide Systems	117
3.1. Introduction .....	117
3.2. Reactor systems scale optimization.....	119
3.2.1. Multi-objective optimization of microchannel reactor for Fischer-Tropsch synthesis using computational fluid dynamics and genetic algorithm.....	119
3.3. Process systems scale optimization.....	152
3.3.1. A modified DIRECT algorithm for hidden constraints optimization problem .....	152
3.3.2. Simultaneous synthesis of a heat exchanger network with multiple utilities using utility substages .....	200
3.4. Plant-wide systems scale modeling and optimization .....	233
3.4.1. Toxic gas release modeling for real-time analysis using variational autoencoder with convolution neural networks.....	233
CHAPTER 4. Industrial Applications .....	276
4.1. Optimal Design and Operation of Fischer-Tropsch Microchannel Reactor for Pilot Scale Compact Gas-to-Liquid Process .....	276

4.1.1. Pilot scale compact GTL process .....	277
4.1.2. Microchannel FT reactor design.....	286
4.1.3. Pilot plant experiment .....	287
4.1.4. Result and discussion .....	291
4.1.5. Conclusion.....	304
4.2. Industrial scale (40 tonCO <sub>2</sub> /day) CCUS carbonation reactor geometry design optimization .....	306
4.2.1. Design procedure and simulation set-up .....	310
4.2.2. Result and Discussion .....	313
4.2.3. Conclusion.....	332
CHAPTER 5. Concluding Remarks .....	334
5.1. Summary of Contributions .....	334
5.2. Future Work.....	337
Nomenclature .....	340
Reference.....	346
Abstract in Korean (국문초록).....	360

## List of Figures

Figure 2-1. Validation CFD model geometry and boundary conditions. ...	45
Figure 2-2. Graph of model validation with a)comparing CO conversion and CH <sub>4</sub> selectivity between the experimental data and FTS microchannel reactor models and b)comparing temperature profile of reaction channel between Velocys model data [15] and proposed CFD reactor model with nonconstant coolant wall temperature.....	50
Figure 2-3. (a) Temperature profile, (b) species molar concentration, (c) reaction rate, (d) CO conversion and CH <sub>4</sub> selectivity at the center of the reaction channel of the base case simulation.....	51
Figure 2-4. Sequential methodology for understanding and suggesting the optimal design of FT microchannel reactor.....	55
Figure 2-5. General geometry of microchannel reactor with variables identification. ....	61
Figure 2-6. The heat of reaction curve with a linear fit approximation.....	65
Figure 2-7. Overall coolant wall heat flux trends with a) $C_W$ , b) $C_H$ , c) $CP_D$ , d) $CC_D$ . ....	68
Figure 2-8. Maximum temperature trend with a) $C_W$ , b) $C_H$ , c) $CP_D$ , d) $CC_D$ . ....	71
Figure 2-9. Overview of reaction mechanism for carbonation reaction in CCUS reactor. ....	80
Figure 2-10. CO <sub>2</sub> removal rate over different experiment set. ....	87
Figure 2-11. The result of parameter estimation. ....	90
Figure 2-12. Sensitivity analysis for CO <sub>2</sub> outlet volume fraction with a) temperature fluctuation and b) NaOH weight fluctuation. ....	91
Figure 2-13. Reactor geometry with design variables.....	98
Figure 2-14. Velocity vector field of each case. ....	102
Figure 2-15. Solid phase volume fraction for different impeller speed....	103



Figure 2-16. Solid particle volume fraction plot through reactor height..	104
Figure 2-17. Diagram of CFD-Process systems integration platform. ....	108
Figure 2-18. Geometry of FT multitubular fixed bed reactor.....	110
Figure 2-19. CFD-Process systems integration algorithm. ....	111
Figure 2-20. Coolant velocity profile and temperature profile of the multitubular reactor; side and front view. ....	114
Figure 2-21. Wall function heat transfer coefficient for each reaction tube at final converged state.....	115
Figure 3-1. Superstructure of 500 mm FTS single microchannel reactor for dividing catalyst packing zone optimization. ....	127
Figure 3-2. Block diagram of GA-CFD optimizer algorithm. ....	129
Figure 3-3. Pareto optimal curve between $\Delta T_{\max}$ and $1/C_{5+}$ productivity of total search and GA-CFD optimizer through $n=1, 2$ , and $3$ . ....	134
Figure 3-4. Comparing Pareto optimal curve with different $n$ and between 1 <sup>st</sup> stage and 2 <sup>nd</sup> stages. ....	138
Figure 3-5. Profile of $\Delta T$ , CO conversion, and $CH_4$ selectivity of the best found Pareto optimal curve calculated by the 4 zone 2 <sup>nd</sup> stage GA-CFD. ....	139
Figure 3-6. Comparison diagram of different zones and temperature constraint optimized by traditional non-convex constraint algorithm and proposed algorithm (GA-CFD) form of a) Pareto curve and b) group data chart. ....	141
Figure 3-7. Summarized result graph of $\Delta T_{\max}$ and $C_{5+}$ productivity through single zone packing, GA-CFD, and various local solver. ...	146
Figure 3-8. Polar contour graph of $\Delta T$ profile under similar $C_{5+}$ productivity of a) single zone catalyst full packing, b) two zone GA-CFD result, c) three zone GA-CFD result, d) four zone 2 <sup>nd</sup> stage GA-CFD result. ....	149
Figure 3-9. a) CO conversion and $CH_4$ selectivity and b) $C_{5+}$ reaction (ID=6) rate under the similar $\Delta T_{\max}$ point of single zone catalyst	

packing, two zone GA-CFD result, three zone GA-CFD result, and four zone 2-stage GA-CFD result. ....	151
Figure 3-10. Geometric interpretation of potentially optimal point and infeasible point using DIRECT with sub-dividing step algorithm on two dimension hidden constraints problem at a) the first iteration, b) the second iteration, c) the third iteration with the first sub-dividing step, d) the fourth iteration. ....	170
Figure 3-11. DIRECT with barrier, NAS, and sub-dividing step iteration for Goldstein-Price test function. ....	172
Figure 3-12. The points where Goldstein-Price test function is evaluated with barrier, NAS, and sub-dividing step at 2000 function evaluation. ....	173
Figure 3-13. Process flow diagram of single mixed refrigerant (SMR) natural gas liquefaction process. ....	179
Figure 3-14. Block flow diagram of optimization platform for DIRECT algorithm with sub-dividing step method for hidden constraint handling method and interconnection between optimization algorithm and Aspen HYSYS SMR process model. ....	182
Figure 3-15. Objective function value versus function evaluation of GA, DIRECT algorithm with barrier approach, NAS, and sub-dividing step. ....	190
Figure 3-16. Hot and cold composite curve of a) base case and b) optimal solution of DIRECT algorithm with sub-dividing step. ....	196
Figure 3-17. $\Delta T$ profile in the cold box of base case optimal and DIRECT algorithm with sub-dividing step. ....	197
Figure 3-18. Utility substage superstructure. ....	207
Figure 3-19. Optimized HEN with heat load, heat exchanger area, and annualized cost data for example 1. ....	220
Figure 3-20. Optimized HEN with heat load, heat exchanger area, and annualized cost data for example 3. ....	224
Figure 3-21. Optimized HEN with heat load, heat exchanger area, and annualized cost data for example 4 calculated by a) SYNHEAT, b)	

restricting series connection of utility, and c) utility substage superstructure. ....	229
Figure 3-22. Composite curve for example 4 calculated by a) SYNHEAT, b) restricting series connection of utility, and c) utility substage superstructure. ....	230
Figure 3-23. (a) The geometry of Mipo complex in Ulsan, (b) top view of CAD image, and (c) 3D view of CAD image in FLACS. ....	241
Figure 3-24. Data sampling and preprocessing flow chart. ....	249
Figure 3-25. VAEDC architecture. ....	255
Figure 3-26. DNN architecture for combining with VAEDC. ....	256
Figure 3-27. Comparison of epoch vs. loss function graphs for NN, DNN, AE-NN, DAE-NN, DAE-DNN, DCAE-NN, DCAE-DNN, VAE-NN, and VAEDC-DNN models. ....	263
Figure 3-28. Mean squared error of test set data. ....	265
Figure 3-29. Comparison of generated $P_{\text{death}}$ image ( $x_{\text{gen}}^{\text{test}}$ ) using $v^{\text{test}}$ with FLACS (CFD), which is ground truth, DNN, AE-NN, DAE-DNN, DCAE-DNN, and VAEDC-DNN. ....	268
Figure 3-30. “Walking in the variable space” of a VAEDC-DNN. ....	270
Figure 4-1. Overview of KOGAS compact GTL pilot plant (1 barrel per day) involved a) reformer section, b) CO <sub>2</sub> membrane separation section, and c) FT reactor section. ....	279
Figure 4-2. Process flow diagram of the compact GTL process which involves unit processes of reformer, CO <sub>2</sub> separation, and FT reaction process. ....	280
Figure 4-3. Location and index of the thermocouples (TC-(1-7)) in the front view of the reactor. ....	290
Figure 4-4. Temperature and composition profile after starting the operation of reformer and CO <sub>2</sub> membrane separation sections. ....	293
Figure 4-5. Reactor temperature of the microchannel FT reactor and multitubular fixed bed FT reactor as given by thermocouples installed inside the reactors. ....	296

Figure 4-6. CO conversion and CH <sub>4</sub> selectivity of compact GTL pilot plant with microchannel FT reactor in the FT reaction section.....	298
Figure 4-7. Visualization of cloud height of solid-liquid multiphase reactor .....	309
Figure 4-8. Particle volume fraction and velocity vector field of different impeller speed. ....	317
Figure 4-9. Particle volume fraction and velocity vector field of different D/T factor. ....	319
Figure 4-10. Particle volume fraction and velocity vector field of different Impeller type. ....	321
Figure 4-11. Particle volume fraction and velocity vector field of different baffle.....	323
Figure 4-12. Particle volume fraction and velocity vector field of different clearance and dual impeller I.....	326
Figure 4-13. Particle volume fraction and velocity vector field of different clearance and dual impeller II. ....	327
Figure 4-14. Particle volume fraction and velocity vector field of 2 <sup>nd</sup> design result. ....	331

## List of Tables

Table 2-1. Physical properties and reaction kinetics of FT synthesis catalyst.....	39
Table 2-2. Compositions of natural gas feed and refrigerant. ....	58
Table 2-3. Module and governing equations for CFD modeling.....	62
Table 2-4. Case specifications. ....	63
Table 2-5. Reaction kinetics and related parameters with references.....	81
Table 2-6. Experiment set using an orthogonal array for the design of the experiment.....	85
Table 2-7. Governing equations of the reactor model. ....	99
Table 3-1. Multiple execution results of the GA-CFD with various crossover fraction. ....	135
Table 3-2. Result of several optimal points given by GA-CFD optimizer.....	143
Table 3-3. Classification of derivative-free optimization.....	154
Table 3-4. Base operating condition of SMR process and NG feed composition. ....	177
Table 3-5. The lower and upper bounds of design variables.....	178
Table 3-6. Base operating condition of SMR process and NG feed composition. ....	180
Table 3-7. List of Algorithms for comparing the performance. ....	187
Table 3-8. Optimization result of SMR process. ....	189
Table 3-9. Stream information and cost function for example 1.....	219
Table 3-10. Stream information and cost function for example 2.....	223
Table 3-11. Stream information and cost function for example 3. ....	227

Table 3-12. Solution comparison for examples 1-3 regarding total annualized cost and model size. ....	228
Table 3-13. Scenario conditions .....	243
Table 3-14. Summary of various models for comparison (architecture, loss function, number of parameters); detailed descriptions are shown in the supplementary file. ....	260
Table 3-15. CPU computational time, storage space for saving the model, and use in real-time alarm systems. ....	273
Table 4-1. Variables specification. ....	312
Table 4-2. 1 <sup>st</sup> Design result of each case. ....	314
Table 4-3. 2 <sup>nd</sup> Design result of each case. ....	329

## CHAPTER 1. Introduction

### 1.1. Research motivation

Recently, in the field of chemical engineering, many types of research based on high-performance computing have been combined with computer-aided process systems engineering. Therefore, various techniques of computational science such as computational fluid dynamics, optimization methodology, and machine learning have been applied to the problems of chemical reactor modeling and process optimization. Notably, in this advance computational science approach, the scope of research extends to non-traditional fields such as reactive research according to the 3D shape of the reactor that has not been easily solved in the past and surrogate model based optimization using machine learning. In this paper, various methods are proposed to obtain the maximum profit with minimum cost by making a breakthrough design without performing lab scale experiment and finding a stochastic optimal design of experiment set.

In parallel, there is a growing demand for sustainable chemical processes in chemical engineering. Conventional chemical processes are highly dependent on oil prices, and unless a diverse portfolio is designed, the sustainability of their chemical industries can be violated because of the oil controlling from the Middle East or US. In addition, these crude oil based chemical processes and power plants generate a great deal of CO<sub>2</sub>. Therefore, it is not necessary to capture these CO<sub>2</sub> and make only meaningless storage but to reproduce it as a

product that can be used and make it economical carbon capture, utilization, and storage (CCUS) technology. To solve this series of processes, the Gas-to-Liquid (GTL) process and CCUS are being researched and developed in various ways.

Therefore, it is critical to establish various methodologies to design and optimize chemical process and reactor through the computational science approach. Furthermore, an industrial application that designs sustainable processes and its reactors using the proposed methodology and manages optimization is significant.



### **1.1.1. Chronological stages of development of process design**

Chronological stages of development of process design based on the description by [1] are very important to understand the research trend and the essential topic in process systems engineering. Until the 19th century, chemical engineering has been studied very usefully in various fields such as purifying metals, producing oil and extracting various materials from nature. However, the research method up to this point was an apprenticeship-based incremental evolutionary design, or it was applied to one side and then moved it to other places. Thus, many researchers treated the chemical engineering as the art. In the 20th century, a great change took place in the field of process design as the approach of scientific thinking and methodology became more popular and various problems were solved through its essence. First, unit operations concepts such as distillation, absorption, and crystallization, and unit processes such as hydrogenation, sulfonation, and carbonylation were developed and established, leading to a new field of conceptual design. These were possible through modeling using algebraic equations and development of various first principle equations. In addition, as theoretical support for thermodynamics, reaction kinetics, and physicochemical properties became available, a variety of reactors capable of large-scale processing reactor and process scale-up were developed. Since the 1930s, various mathematical models based on differential equations have been developed, and process simulators such as ASPEN Plus

and HYSYS have been developed, and computer-aided process systems engineering has begun. The advancement of these technologies has led to the development and construction of chemical processes faster and more accurately and has resulted in a numerical interpretation of many optimization problems that were previously difficult to solve. Due to these demands, scale-up through various verification and theoretical back-up through computer simulation and enterprise-wide optimization methodology beyond reactor and process scale are being studied.

### **1.1.2. Current status of process systems engineering with computational science approach**

As the high-performance computing and high fidelity measurements developed in the 2000s, fundamental phenomena on fluid and molecular dynamics began to be understood. In the field of reactor modeling and simulation, kinetics studies in molecular systems and turbulence effects inside the reactor are being studied at small eddy level. It is also possible to calculate the effective time in an effective solver in a complicated flow field, and effective analysis of the particle body with an inhomogeneous distribution such as bubble and solid by the introduction of techniques such as population balance model. The leading field in this computational science approach is computational fluid dynamics (CFD). In addition to the existing aerospace applications, various applications have begun to be applied in the field of chemical engineering including multiphase and chemical reaction.

Also, in the process systems part, it is judged that the trend shift is taking place in the sequential modular approach, which is a traditional process simulation technique, to the equation oriented approach, which includes gPROMS or PSE. The problems of existing initialization and problems caused by computation load are constrained to commercialization, but commercialization has become possible through several studies which have dramatically solved them. Through this method, it is possible to analyze the process with many loops easily and it is possible to apply general optimization

algorithms quickly and accurately to process design. However, this too cannot be regarded as meaningful because it is difficult to incorporate an external function model and is within the scope of conventional interpretation. Most recently, research has been actively conducted on data-driven modeling and analysis using computational science techniques. Also, optimization problems, such as optimization that considers uncertainty, have been proposed to obtain robust results in various scenarios beyond the use of existing deterministic variables. A variety of methodologies for global optimization without stopping at local optimum have been proposed. In particular, derivative-free optimization algorithms have been developed that can be interpreted in conjunction with existing chemical engineering software.

### **1.1.3. Introduction to the sustainable process**

In this study, a series of processes, which can be called sustainable process, are selected and used in the thesis. It is important to discuss sustainability in the traditional fossil fuel based chemical engineering industry. Currently, the chemical industry fluctuates greatly depending on the volatility of the oil price, and the united nations framework convention, which can be represented by the Paris Agreement, is regulating CO<sub>2</sub> emissions. Among these changes, the need for the development of various chemical processes and their reactors has emerged, and this thesis addresses two of the essential processes for sustainable processes.

First, the existing crude oil based chemical process is susceptible to oil prices and has many impurities, which is shown many things that are not sustainable in many ways. Recently, gas-based power plants and various processes have begun to be developed, starting with US shale gas, which shows stronger ability at high oil prices. Especially, Gas-to-Liquid (GTL) process has the greatest added value among natural gas process. It can synthesize high-value product like high-quality diesel by synthesizing natural gas with synthetic crude oil. Production of these products based on natural gas is a sustainable process because it can reduce various byproducts and toxic chemicals generated from refining crude oil. Especially, it is expected that it will be very efficient if we use GTL-FPSO vessels for developing stranded gas field or mid-scale gas

field, which exist in offshore. In this study, we tried to derive the miniaturization of the Fischer-Tropsch reactor, which is the most crucial development for GTL-FPSO ship development, through the concept of the microchannel reactor.

The synthetic crude oil thus produced is purified and processed through various chemical processes. In this process, a lot of CO<sub>2</sub> is generated. Thus, appropriate technology should be developed to capture this CO<sub>2</sub> adequately and store it properly. In keeping with these expectations, carbon capture and storage (CCS) technologies have evolved over the past few decades, but they are not readily available due to economic problems. Recently, researchers are being carried out to convert CO<sub>2</sub> into a product that can utilize CO<sub>2</sub> itself and to utilize it for production of economical products, rather than merely storing CO<sub>2</sub> by capturing meaningless storage. CO<sub>2</sub> is used to make formic acid, or carbonation reaction is used to make cement or concrete to be used as construction material. In this study, we will look at the carbon capture, utilization, and storage (CCUS) technologies in general and specifically focus on the multiphase carbonation reactor design.

## 1.2. Research objectives

In this thesis, we will discuss the process modeling, optimizing, and designing the reactor and process using CFD, mathematical programming, machine learning, deep learning, and derivative-free optimization techniques in computational science. Especially, for the reactors, the GTL FT microchannel reactor and the CCUS carbonation reactor are simulated through reactor modeling using CFD to be used in reactor design. A computational science approach that can be applied to optimization and analysis is to develop a methodology suitable for the situation from reactor scale to plant-wide scale systems. In the optimization methodology at the reactor level, multi-objective optimization methodology using GA and  $\epsilon$ -constraint is used in combination with CFD. At the process level, we developed global derivative-free optimization algorithms that consider hidden constraints efficiently and developed a simultaneous HENS method that considers multiple utilities and developed a systematic approach to the MINLP problem. In the plant-wide scale systems, we will discuss the toxic gas release real-time alarm system with the deep variational autoencoder with convolutional layers and deep neural network with batch normalization technique for finding latent space and non-linear mapping. Finally, we will show how the computational science approach in the sustainable process can be applied to industrial applications through the case of 1 BPD compact GTL pilot plant and 40 tonCO<sub>2</sub>/day CCUS process.

### 1.3. Outline of the thesis

From a modeling and technical perspective, the contribution of the thesis is to solve a variety of problems in process systems engineering, which have not been solved or efficiently interpreted by conventional methodologies, using computational science techniques. In particular, in CHAPTER 2, advanced reactor modeling and design using computational fluid dynamics (CFD) is performed to expand the chemical reactors that are limited to the 0-d model. Especially, by developing a CFD-process simulation platform, we propose a methodology that can perform both reactor design and process design simultaneously. We also propose an optimization framework that can be applied to the whole system from the reactor to plant-wide system by developing optimization and analysis method by integrating derivative-free optimization algorithm and machine learning technique.

From the application perspective, we introduce the actual pilot plant project case and the result which applied various reactor model and the optimization and analysis method developed in this study to CHAPTER 4, and confirm that this thesis can be applied to the real industry without stopping in theoretical study. In detail, the thesis is structured as follows:

- CHAPTER 2 constitutes an introduction of the two key reactors for the sustainable process, Gas-to-Liquid (GTL) Fischer-Tropsch (FT) microchannel reactor and carbon capture, utilization, and storage (CCUS)



carbonation reactor. 2D axisymmetric CFD model of FT microchannel reactor with porous media zone with lumped FT kinetics and the 3D CFD based FT microchannel reactor block model with external heat source calculated by Aspen Plus is introduced. In the same chapter, rigorous carbonation kinetics study with dynamics of the bubble and solid particle regarding DAE is performed. Eulerian-granular multiphase carbonation reactor is also modeled by CFD. Finally, extended CFD reactor model to CFD-process simulator integrated platform for designing process and reactor simultaneously is introduced.

- In CHAPTER 3, optimization, knowledge mining, and analysis methodology through the unit to the plant-wide scale systems is developed. CFD reactor model function is perfectly connected to GA based multi-objective algorithm with the  $\epsilon$ -constraint method. Pareto optimal curve of  $C_{5+}$  productivity and  $\Delta T_{\max}$  is successfully solved. Lipschitz continuous function based derivative-free optimization algorithm was introduced for considering hidden constraint which is very important for optimizing process systems scale simulation. In the same chapter, simultaneous synthesis of a heat exchanger network with multiple utilities using utility substages was explained. For plant-wide systems, a surrogate model for real-time analysis of toxic gas release in overall plant system using deep learning technology for reducing the data is proposed.

- CHAPTER 4 has two examples of industrial applications. 1 BPD scale compact GTL pilot plant constructed by KOGAS is tested with our FT microchannel reactor. Moreover, industrial application of computer-aided engineering reactor optimization procedure for 40 tonCO<sub>2</sub>/day CCUS carbonation reactor that will be constructed by Daewoo E&C.
- CHAPTER 5 summarizes the key contributions of the thesis and discusses ideas for future work.

## 1.4. Associated publications

The work presented in Chapter 2.2.1 and Chapter 3.2 are based on [2]. The work presented in Chapter 2.2.2 is introduced in [3]. The work presented in Chapter 2.3.2 is based on [4] co-authored by myself and main discussion with modified methodology is not presented in this thesis. The work presented in Chapter 3.3.1 is introduced in [5]. The work presented in Chapter 3.3.2 is based on [6]. The work presented in Chapter 3.4 has been submitted to *Chemical Engineering Journal* with K. Jeon (joint first author). The work presented in Chapter 4.1 has also been submitted to *Chemical Engineering and Processing: Process Intensification* with KS. Kshetrimayum (joint first author). More extended information of design procedure of Fischer-Tropsch microchannel reactor is not discussed in this thesis because KS. Kshetrimayum used it. Finally, the work presented in Chapter 4.2 is introduced in [4].

## **CHAPTER 2. Study of the Novel Reactor Models using Computational Science**

### **2.1. Introduction**

So far, in the field of process systems engineering, various methods have been used to model the reactor. Complex reaction kinetics and thermodynamics for each chemical species were selected, and the actual reactor was simulated through validation and parameter estimation through experiments. This well-modeled reactor was used to analyze the overall economics of the plant in conjunction with a process simulator and was used to derive the correct operating conditions. In particular, a reactor is a very important device that needs to be accurately interpreted and optimized, as a principal device that represents the characteristics of a particular chemical process than any other device.

These various reactors can be largely divided into continuous stirred tank reactor (CSTR), plug flow reactor (PFR), trickled bed reactor, moving bed reactors, slurry loop reactors, fluidized bed reactors, jet reactors, air-lift reactors, bubble column reactors, and bubble-slurry column reactors. Until the 20th century, many types of research have been conducted to make a proper calculation based on the characteristics of these reactors and to make a quick calculation and an appropriate calculation through the 0-d model. However,

recently, the influence of the geometry of the reactor and the flow analysis are simultaneously required.

In keeping with the demands of this age, computational fluid dynamics (CFD) technology has emerged as a key technology in reactor design for chemical engineering. In addition to the flow analysis according to the structure of the reactor, it is possible to analyze the phase separation and mixing effect through the multiphase analysis and to analyze the complicated physical phenomenon such as the reaction on the particle surface at one time. However, CFD is usually based on the complicated partial differential equation, Navier-Stokes equation, and it is necessary to model specific reactor for each research. Thus, exact and precise CFD modeling of the specific reactor with validating using experiment data set is very important. Also, since it is a simulation method that takes much computational loads, interworking with a general process simulator is still difficult.

In this study, the Fischer-Tropsch microchannel reactor and 3-phase carbonation reactor, which are the key reactor of two most important processes of the sustainable process, the gas-to-liquid process (GTL) and the carbon capture, utilization, and storage (CCUS), are modeled by CFD. In addition, we propose an integration platform of CFD model and process simulator and research the point of view of combining with existing process engineering.

## **2.2. Gas-to-Liquid (GTL) Fischer-Tropsch (FT) reactor model**

In recent years, gas-to-liquid (GTL) technology has received considerable attention as a means to monetize natural gas resources at stranded gas fields and associated gas at offshore facilities, which account for almost 40 % of the world's gas reserves. GTL technology converts natural gas to longer chain hydrocarbons and eventually produces clean liquid synthetic crude oil [7]. Conventional GTL processes, especially those of onshore facilities, use a circulating fluidized bed reactor, bubbling fluidized bed reactor, or slurry bubble column for the Fischer-Tropsch (FT) synthesis [8]. However, when it comes to the FT synthesis in floating systems at offshore facilities, conventional FT reactors do not fit well as their typical tall column design is not suitable for operation under possible frequent impacts of sea waves. Additionally, the designed production capacities of conventional FT reactors are far larger than the needs of small- to medium-sized gas fields. Accordingly, a novel type of reactor that can stably operate under the frequent impacts of sea waves and has production capacity suitable for FT synthesis applications at offshore facilities is sought, such as microchannel reactors [9].

Microchannel reactors have emerged as a novel technology for FT synthesis applications due to their short diffusion distance and low heat and mass transfer resistances [10-12]. Reduced mass and heat transfer distances enhance process intensification, making it suitable for a highly active FT catalyst [11].

Additionally, the microchannel reactor is considered to be a highly integrated, compact, portable, and safe technology [13], making it ideal for applications in offshore and remote production facilities. Moreover, small-scale sources for synthesis gas like municipal waste and biomass waste can also leverage the advantages of small-scale microchannel technology for their waste and biomass-to-liquid fuel conversion processes [14]. Several authors [10-13, 15] have experimentally demonstrated the feasibility and effectiveness of microchannel reactors for FT synthesis applications.

However, the use of highly active modern iron- and cobalt-based catalysts, coupled with the high heat generation (165 kJ/mol CO) of FT synthesis, have resulted in the problem of a high-temperature gradient along the channel length. One method to address this problem is to use highly effective commercially available thermal fluids such as Melotherm<sup>TM</sup> and saturated water as coolants, as explored by Deshmukh et al. and Tonkovich et al. [14, 15] in their experimental study, and Kshetrimayum et al. in their simulation study [16, 17]. However, thermal fluids can be expensive and saturated water can be difficult to handle in actual operation compared to cheaper and single-phase coolant-like subcooled water. Another method to avoid a high thermal gradient and maintain a minimum thermal gradient along the channel is to divide the entire reactor length into a number of discrete zones and load different amounts of catalyst in each zone, a method at this moment called the method of discrete dilution.

However, a non-optimized method of discrete dilution would not necessarily guarantee an optimal reactor performance. On the other hand, an optimal number of discrete zones, zone length, and dilution ratio are expected to prevent abnormally high FT reactions and consequently undesirably high heat generation at any region inside the reaction channel. For instance, applying an optimized discrete dilution method can prevent the FT reaction temperatures from becoming abnormally high near the channel inlet by distributing the reaction rates, and consequently the heat generation, more uniformly to all regions of the reaction channel. The method can be optimized to achieve maximum overall reactant conversion and product selectivity at the reactor channel exit. However, the optimization of discrete dilution is a very challenging problem because it usually contains multiple objectives and non-convex constraints.

The method of catalyst dilution to control reaction rates and prevent excessively high-temperature peaks inside reactors has been considered in existing works on a catalyst-packed tubular reactor [18-21] for other highly exothermic reactions. For instance, Hwang and Smith [22] employed the combined effect of catalyst dilution and feed-stream distribution to achieve optimal control of the temperature profile inside their multi-bed multi-tubular reactors for the hydrogenation of nitrobenzene and oxidation of ethylene.



In the past few years, many authors have used computational fluid dynamics (CFD) to simulate FT synthesis in microchannel reactors, to either supplement or replace expensive and difficult experiments involving the FT synthesis [3, 17, 23-28]. Recently, Kshetrimayum et al. [16] evaluated the effect of coolant type and wall boiling condition on the temperature profile of a low-temperature FT synthesis in a microchannel reactor block based on CFD simulations. Jung et al. [29] used CFD for their optimal design of guiding channel geometry in a U-type coolant layer manifold for a large-scale microchannel reactor. Other works that do not use CFD tools have appeared, too. For instance, Park et al. [30, 31] proposed a cell decomposition method to model and simulated the FT synthesis for a large scale microchannel reactor without having to employ a rigorous CFD model and intensive computation. They evaluated the thermal performances of various reactor configurations in microchannel reactor blocks. However, these authors have not explored the application of the method of discrete dilution in FT microchannel reactors for optimal operation of such a reactor. An important criterion to evaluate the performance of such microchannel reactors for FT synthesis is to measure its ability to optimize  $C_{5+}$  while minimizing temperature gradient along the channel length. Accordingly, in this context, to achieve multiple targets, a multi-objective optimization needs to be formulated and solved. However, to our knowledge, such work has not been presented.

In this work, a CFD model of a single microchannel reactor for FT synthesis is first built using the commercial CFD software ANSYS FLUENT, and the simulation results are validated with experimental data from the literature.

### **2.2.1. 2D axisymmetric computational fluid dynamics (CFD) based Fischer-Tropsch microchannel reactor single-channel model**

In this section, we present model equations and parameters that were used in constructing the rigorous CFD model of the microchannel FT reactor.

### **2.2.1.1. FT catalyst and reaction kinetics**

To simulate the FT synthesis, the reaction kinetics of using the cobalt-based catalyst of Oxford Catalyst, LTD (OCL) was employed. Kshetrimayum et al., Lee et al., and Park et al. [16, 24, 30] have also used the reaction kinetics in their simulation works. The reaction kinetics consists of 6 reactions describing the entire FT reaction pathway in a microchannel. To ensure the convergence of the model within a reasonable amount of time,  $C_5$  and higher carbon chains are lumped in  $C_{5+}$  (in reaction,  $C_{5+}$  averaged to  $C_{14}H_{30}$ ). Distribution profiles for various chemical components inside the microchannel reactor can be obtained, which is not possible with a single lumped reaction describing FT synthesis [32]. In Table 2-1, the physical properties of the catalyst and reaction kinetics are shown.

**Table 2-1.** Physical properties and reaction kinetics of FT synthesis catalyst.

(a) Catalyst Physical Properties			
	Effective thermal conductivity ( $k_{\text{eff}}$ )	300 kW/mK	
	Mean particle diameter ( $D_p$ )	280 $\mu\text{m}$	
	Bed void fraction ( $\epsilon$ )*	0.48	
	Bulk packing density ( $\rho_{\text{bulk}}$ )	1054 kg/m <sup>3</sup>	
	Specific heat capacity	473 J/kg K	
(b) Reaction Kinetics and Parameters in rate Expressions			
ID	Reactions and Rate Expression	Kinetic parameters	
		$k_i$ [rate in kmol/(kg-cat s)]	$E_i$ (J/kmol)
	$3\text{H}_2 + \text{CO} \rightarrow \text{H}_2\text{O} + \text{CH}_4$		
1	$R_{\text{CH}_4} = k_1 \exp\left(-\frac{E_1}{RT}\right) C_{\text{H}_2}$	$2.509 \times 10^9$	$1.30 \times 10^8$
	$5\text{H}_2 + 2\text{CO} \rightarrow 2\text{H}_2\text{O} + \text{C}_2\text{H}_6$		
2	$R_{\text{C}_2\text{H}_6} = k_2 \exp\left(-\frac{E_2}{RT}\right) C_{\text{H}_2}$	$3.469 \times 10^7$	$1.25 \times 10^8$
	$7\text{H}_2 + 3\text{CO} \rightarrow 3\text{H}_2\text{O} + \text{C}_3\text{H}_8$		
3	$R_{\text{C}_3\text{H}_8} = k_3 \exp\left(-\frac{E_3}{RT}\right) C_{\text{H}_2}$	$1.480 \times 10^7$	$1.20 \times 10^8$
	$9\text{H}_2 + 5\text{CO} \rightarrow 4\text{H}_2\text{O} + \text{C}_4\text{H}_{10}$		
4	$R_{\text{C}_4\text{H}_{10}} = k_4 \exp\left(-\frac{E_4}{RT}\right) C_{\text{H}_2}$	$1.264 \times 10^7$	$1.20 \times 10^8$
	$\text{H}_2\text{O} + \text{CO} \rightarrow \text{H}_2 + \text{CO}_2$		
5	$R_{\text{CO}_2} = k_5 \exp\left(-\frac{E_5}{RT}\right) C_{\text{CO}} C_{\text{H}_2\text{O}}$	$2.470 \times 10^7$	$1.20 \times 10^8$
	$29\text{H}_2 + 14\text{CO} \rightarrow 14\text{H}_2\text{O} + \text{C}_{14}\text{H}_{30}$		
6	$R_{\text{FT}} = \frac{k_6 \exp\left(-\frac{E_6}{RT}\right) C_{\text{H}_2} C_{\text{CO}}}{\left[1 + k_{\text{ad}} \exp\left(-\frac{E_{\text{ad}}}{RT}\right) C_{\text{CO}}\right]^2}$	$3.165 \times 10^4$ $k_{\text{ad}} = 63.5$	$8.0 \times 10^7$ $E_{\text{ad}} = 8.0 \times 10^7$

\* Assuming uniform spheres with cubic packing

### 2.2.1.2. FT microchannel reactor

A single channel FT microchannel reactor, modeled as an axisymmetric 2D CFD model based on a finite volume method, was considered for the present study. The catalyst-packed reaction channel was assumed to be a porous medium, packed with the spherical catalyst of diameter 280  $\mu\text{m}$ . The Ergun Equation [2-1] was used to obtain the parameters of the porous medium for a packed bed reactor [33].

$$\left| \frac{\Delta p}{L} \right| = \frac{150\mu}{D_p^2} \frac{(1-\epsilon_{cat})^2}{\epsilon_p^3} \mathbf{v}_\infty + \frac{1.75\rho}{D_p} \frac{(1-\epsilon_{cat})}{\epsilon_p^3} \mathbf{v}_\infty^2 \quad [2-1]$$

Equation [2-1] is a semi-empirical equation that can be applied to many types of packing and over a wide range of Reynolds numbers. Because the bed pipe Reynolds number obtained for the size of catalyst particle considered in the present study falls in the range 10 – 100, the flow inside the reaction channel is assumed laminar, and the Ergun equation can be safely applied.

To describe the 2D CFD model of the reactor, a 2D axisymmetric coordinate is used where the x-direction is set as the symmetric axis. The 2D axisymmetric coordinate expands the 2D geometry to 3D with the same quantity of angle direction. Thus, it can calculate mass transfer, heat transfer, and other physical phenomena in 3D. A critically different result comes out when physical quantities such as temperature and flow velocity are critically different through the angle direction. However, our reactor model, microchannel reactor, usually does not need to consider that because the channel width and height are too

short to cause asymmetric physical quantities through the angle direction. Since the flow is laminar, turbulence effects are not considered, and the porous resistance is independent of angle because we assume that the catalyst is packed uniformly. Porous media resistance is modeled as a source term in the momentum conservation equation, and the 2D axisymmetric momentum conservation equation appears as force terms ( $F_x$ , and  $F_r$ ) in the axial and radial directions respectively, as shown in Equation [2-2]

$$\begin{aligned}
& \frac{\partial}{\partial t}(\rho v_x) + \frac{1}{r} \frac{\partial}{\partial x}(r \rho v_x v_x) + \frac{1}{r} \frac{\partial}{\partial r}(r \rho v_r v_x) = -\frac{\partial p}{\partial x} + \\
& \frac{1}{r} \frac{\partial}{\partial x} \left( r \mu \left( 2 \frac{\partial v_x}{\partial x} - \frac{2}{3} (\nabla \cdot \vec{v}) \right) \right) + \frac{1}{r} \frac{\partial}{\partial r} \left( r \mu \left( \frac{\partial v_r}{\partial r} + \frac{\partial v_r}{\partial x} \right) \right) + F_x \\
& \frac{\partial}{\partial t}(\rho v_r) + \frac{1}{r} \frac{\partial}{\partial x}(r \rho v_x v_r) + \frac{1}{r} \frac{\partial}{\partial r}(r \rho v_r v_r) = -\frac{\partial p}{\partial r} + \\
& \frac{1}{r} \frac{\partial}{\partial r} \left( r \mu \left( 2 \frac{\partial v_r}{\partial r} - \frac{2}{3} (\nabla \cdot \vec{v}) \right) \right) + \frac{1}{r} \frac{\partial}{\partial x} \left( r \mu \left( \frac{\partial v_r}{\partial x} + \frac{\partial v_x}{\partial r} \right) \right) - \frac{2 \mu v_r}{r^2} + \\
& \frac{2}{3} \frac{\mu}{r} (\nabla \cdot \vec{v}) + F_r
\end{aligned} \tag{2-2}$$

$$\nabla \cdot \vec{v} = \frac{\partial v_x}{\partial x} + \frac{\partial v_r}{\partial r} + \frac{v_r}{r}$$

The continuity equation is given by Equation [2-3]

$$\frac{\partial \rho}{\partial t} + \frac{\partial}{\partial x}(\rho v_x) + \frac{\partial}{\partial r}(\rho v_r) + \frac{\rho v_r}{r} = 0 \tag{2-3}$$

Syngas and products of the FT reaction are defined as mixture components in the species transport equation with a volumetric reaction term. The species transport equation with the finite-rate chemistry method of volumetric reaction is given by Equation [2-4]

$$\frac{\partial}{\partial t}(\rho Y_c) + \nabla \cdot (\rho \vec{v} Y_c) = -\nabla \cdot \vec{J}_c + R_c \quad [2-4]$$

Reaction rates of each chemical component are represented by  $R_i$ . Multi-component diffusion of each component is represented by the diffusive mass flux ( $J_i$ ) calculated using the Maxwell-Stefan equation [34].

The energy equation inside the reaction channel with homogeneous porous medium is given by Equation [2-5],

$$\begin{aligned} \frac{\partial}{\partial t}(\epsilon_{cat} \rho_{flu} E_{flu} + (1 - \epsilon_{cat}) \rho_{sol} E_{sol}) + \nabla \cdot (\vec{v}(\rho_{flu} E_{flu} + \\ p)) = \nabla \cdot (\mathbf{k}_{eff} \nabla T - (\sum_i \mathbf{h}_c \vec{J}_c) + (\bar{\tau} \cdot \vec{v})) + S_{flu} \end{aligned} \quad [2-5]$$

Where index f means the fluid part and s means the solid part of the reactor;  $\epsilon_{cat}$  and  $k_{eff}$  are the porosity and the effective thermal conductivity of the porous medium inside the microchannel reactor. Source term ( $S_{flu}$ ) of the energy equation is the volumetric heat generation rate due to the exothermic FT reaction, which is calculated using enthalpy values of the components at the reactor's operating temperature and pressure. The values of viscosity and thermal conductivity of each component at operating temperature and pressure were calculated using the Aspen HYSYS 8.8 physical property database, and enthalpy data were calculated using the Peng-Robinson equation of state.

Using the Nusselt number equation of [35], the heat transfer coefficient in the porous medium was calculated and thermal non-equilibrium in porous



media was simulated to consider the exact heat flow between catalyst and continuous flow, which is given in Equation [2-6].

$$\text{Nu} = 2 + 1.1\text{Re}^{0.6}\text{Pr}^{\frac{1}{3}} \quad [2-6]$$

Capillary phenomenon and other micro-physics phenomena which are driven by rarefied flow with high Knudsen number are ignored as the microchannel reactor length scale in the present study are between 1-10 mm and the pressure above 20 bar. This condition does not meet the condition for rarefied flow. Furthermore, the turbulence effect on reaction rate and turbulence viscous model is also ignored. The incompressible ideal gas law was used for calculating the mixture fluid density.

We choose the base geometry of the single channel reactor as a long b type reactor of [14] which has a width of 6 mm, a height of 1 mm, and a length of 616 mm. To apply axisymmetric modeling, the width and height were converted to the hydraulic diameter, whose value is 1.7143 mm. The thickness of the stainless reactor wall is 0.5 mm, and the outer cooling wall boundary condition was set to a fixed wall temperature of 210°C, which is the same as the inlet temperature (Figure 2-1). Although sudden pressure rise and flow deceleration are expected at the beginning of catalyst packing, we assume that the CFD reactor model just simulates the catalyst packing zone and the inlet condition is already stabilized with constant velocity. Moreover, the Ergun Equation [2-1] can predict the porous media resistances.

The mesh quality was represented by minimum orthogonal quality 0.60983 and maximum orthogonal skewness 0.065823, the number of nodes is 88986, and the number of cells is 82,919. The syngas consists of hydrogen, carbon monoxide, and nitrogen, with an  $\text{H}_2/\text{CO}$  molar ratio of 2.0. The molar fraction of nitrogen in the feed gas is 16.5%. The feed gas inlet temperature is 210°C, operating pressure 24 bar, and contact time 290 ms, based on the catalyst bed volume. The inlet boundary condition is set as a velocity inlet (fixing the superficial velocity of the syngas), and the outlet boundary condition is set as a pressure outlet (fixing the outlet pressure as the operating pressure).

In the pressure-velocity coupling solver, the SIMPLE method is used for pressure correction to ensure mass conservation. For spatial discretization of the gradient, pressure, momentum, and species transport, the Green-Gauss node-based, PRESTO!, second-order upwind, and second-order upwind algorithms were used respectively.

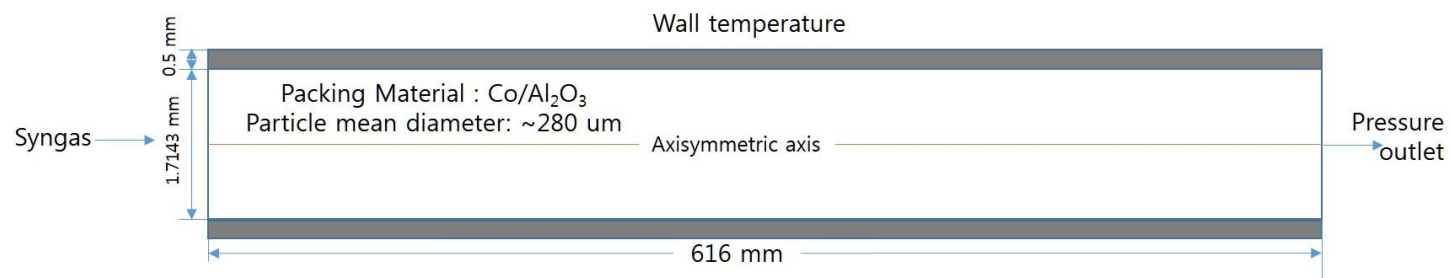


**Figure 2-1.** Validation CFD model geometry and boundary conditions.

### **2.2.1.3. CFD model validation**

Simulation is carried out using the commercial CFD software ANSYS FLUENT 17.0 with parallel computing using 16 cores of Intel Xeon E5-2667v3 (3.2 GHz) processor. For model validation, we compared the simulation results of the CFD reactor model with experimental data on CO conversion and CH<sub>4</sub> selectivity of [14, 15] having the same operating conditions of GHSV, same contact time, and inlet syngas temperature.

Figure 2-2 shows the trends of CO conversion and methane selectivity as predicted by the developed CFD model over a range of temperatures considered. CO conversion is predicted with high accuracy at almost all values of the temperature range considered while the original experimental data from [15] that we used changed the temperature from 206.6°C to ~263°C and GHSV to maintain ~70% conversion. Thus, the fact that our model can predict ~70% conversion through temperature verifies the model performance. Although methane selectivity is overestimated at the lower temperature range, the model predicted the methane selectivity reasonably well at higher temperatures. The reasons why methane selectivity is apparently significantly different from the empirical data at low inlet temperatures can be classified in three big reasons. First, we assume that the coolant wall temperature does not change through the axial direction and time. However, in a realistic reactor, the coolant channel profile can be changed because of inefficient heat exchanger geometry or

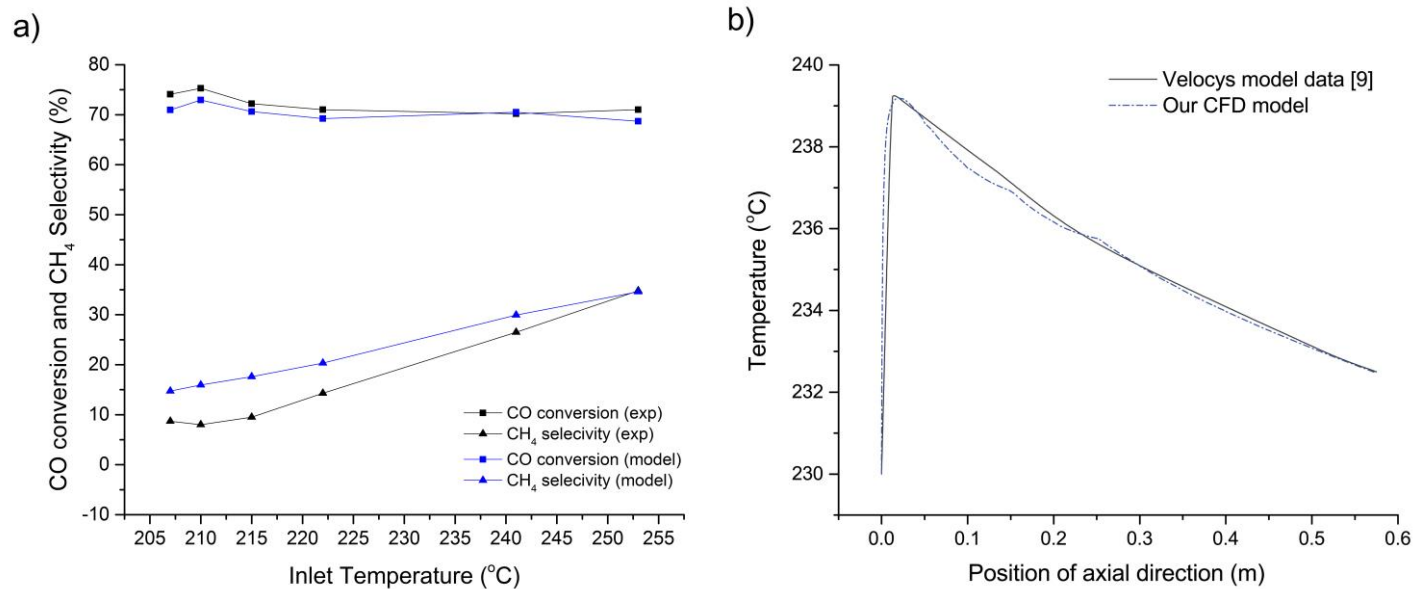
insufficient coolant capacity. Secondly, although we use the reaction kinetics and experiment data from the same literature, the parameter estimation procedure are not shown in the literature. Thus, the activation energy of reaction ID 1 can be different for our reactor model. It is possible that we are forced to increase activation energy to decrease the temperature dependency of methane generation. Then, the slope of methane selectivity through temperature decrease helps to fit our model data to experimental data. However, parameter estimation is not within the scope of this paper, so we used the original kinetics. Finally, some experiments were performed in a multichannel reactor with multiple layered fins in the reactor channel. Thus, the temperature profile of each reactor channel can be different. Despite the weak point of methane selectivity estimation at low temperature, we think it is possible to use our model for this study because the model can predict CO conversion with various temperature and GHSV. Moreover, for optimization, the temperature dependence tendency is more important than the actual value of methane selectivity. Experimental data and our model show that methane selectivity follows a monotonic increase function through temperature. Thus, we can conclude that a low-temperature error does not affect to an optimal value and our model is sufficient to use for the purpose of optimization.

Figure 2-2 also compares the reactor core temperature profile through the axial direction. Our model can predict the maximum temperature and peak

position. Since patent data does not give exact model formulation and coolant wall profile, it is hard to assume the coolant wall profile. Thus, we apply a non-constant coolant wall temperature assuming a temperature profile, and we can fit our model to the patent data successfully. However, it is not necessary to use an imprecise non-constant coolant wall temperature profile for fitting the plot. Firstly, for optimizing catalyst dilution zone divisions, the maximum temperature and its location are more important than the exact temperature profile and our model can predict those pretty well (maximum temperature: 239.6°C, peak position: 0.01 m). Furthermore, the error in CO conversion between the constant coolant wall temperature model and patent data is about 2%. Secondly, it is impossible to get exact coolant wall temperature unless we use a coolant channel model simultaneously which is not within the scope of this paper.

Temperature, species molar concentration, reaction rates, CO conversion, and CH<sub>4</sub> selectivity profiles at the centerline in the axial direction of the reaction channel are shown in Figure 2-3. Since the Fischer-Tropsch reaction is highly exothermic, the temperature of the inlet reactor region can increase to a very high value developing a hot spot in the region. As a result, loss of selectivity of C<sub>5+</sub>, catalyst deactivation, and thermal runaway can occur [36]. The profile indicates that our CFD reactor model can capture the temperature increase effect due to high reaction rates at the inlet region of the reactor. Furthermore,

unlike a 1-dimensional model [30], all physical variables are calculated at the radial, and axial positions of the reactor and reaction kinetics are updated with those variables. Thus, the developed CFD model can accurately predict reactor performance and hence can be applied to the optimization problem to obtain the optimum number of catalyst packing zones and the length of each zone to maximize  $C_{5+}$  selectivity and minimize  $\Delta T_{\max}$ .



**Figure 2-2.** Graph of model validation with a)comparing CO conversion and CH<sub>4</sub> selectivity between the experimental data and FTS microchannel reactor models and b)comparing temperature profile of reaction channel between Velocys model data [15] and proposed CFD reactor model with non-constant coolant wall temperature.



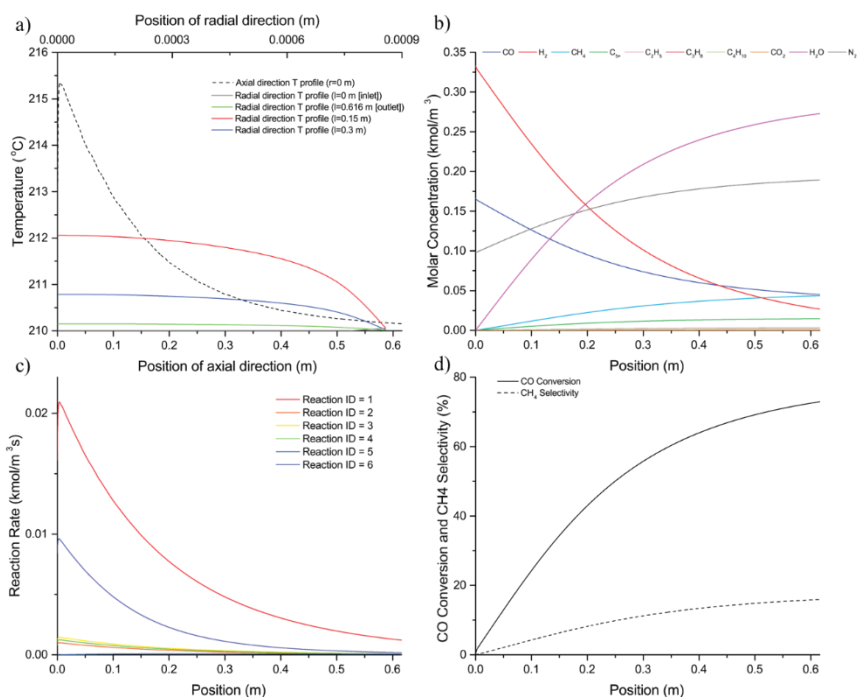


**Figure 2-3.** (a) Temperature profile, (b) species molar concentration, (c) reaction rate, (d) CO conversion and CH<sub>4</sub> selectivity at the center of the reaction channel of the base case simulation.

### **2.2.2. 3D CFD based Fischer-Tropsch microchannel reactor multi-channel model**

Driven by both environmental and economic reasons, the development of small to medium scale GTL(gas-to-liquid) process for offshore applications and for utilizing other stranded or associated gas has recently been studied increasingly. Microchannel GTL reactors have been preferred over the conventional GTL reactors for such applications, due to its compactness, and additional advantages of small heat and mass transfer distance desired for high heat transfer performance and reactor conversion. In this work, the multi-microchannel reactor was simulated by using commercial CFD code, ANSYS FLUENT, to study the geometric effect of the microchannels on the heat transfer phenomena. A heat generation curve was first calculated by modeling a Fischer-Tropsch reaction in a single-microchannel reactor model using Matlab-ASPEN integration platform. The calculated heat generation curve was implemented to the CFD model. Four design variables based on the microchannel geometry namely coolant channel width, coolant channel height, coolant channel to process channel distance, and coolant channel to coolant channel distance, were selected for calculating three dependent variables namely, heat flux, the maximum temperature of coolant channel, and maximum temperature of process channel. The simulation results were visualized to understand the effects of the design variables on the dependent variables. Heat flux and maximum temperature of cooling channel and process channel were

found to be increasing when coolant channel width and height were decreased. Coolant channel to process channel distance was found to not affect the heat transfer phenomena. Finally, total heat flux was found to be increasing and maximum coolant channel temperature to be decreasing when coolant channel to coolant channel distance was decreased. Using the qualitative trend revealed from the present study, an appropriate process channel and coolant channel geometry along with the distance between the adjacent channels could be recommended for a microchannel reactor that meets the desired reactor performance on heat transfer phenomena and hence reactor conversion of a Fischer-Tropsch microchannel reactor.

### **2.2.2.1. Model description**

In order to analyze the tendency of temperature and heat flux according to the structural effect of the 3-D FT microchannel reactor, we use sequential methodologies shown in Figure 2-4. First, the reaction rate equation of a microchannel fixed bed reactor based on cobalt-based catalyst is expressed by a mathematical modeling for a single channel, and the operation condition and reactor structure to be analyzed by CFD are set as parameters. Thus, the heat of reaction given in the longitudinal direction is obtained as an algebraic function. Then, all the other structural variables are obtained by CFD with the fixed heat of reaction, and the values of  $T_{pmax}$ ,  $T_{cmax}$ , and  $Q$  are obtained while varying the four design variables  $C_w$ ,  $C_H$ ,  $CC_D$ , and  $CP_D$ . This is to fix the variables related to the reaction by fixing the reaction heat to increase the calculation speed and tolerance of the flow analysis model and to only see the influence on the reactor structure. Finally, the tendency of the results is visualized to conduct physical analysis and suggest optimal geometric design variables.

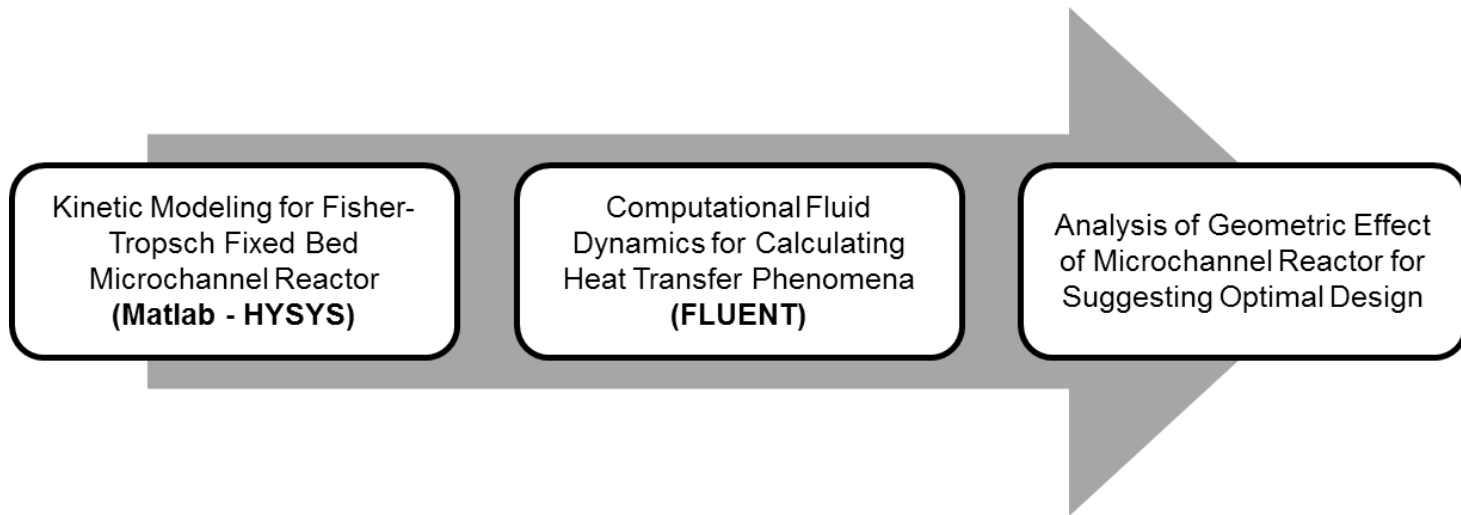


**Figure 2-4.** Sequential methodology for understanding and suggesting the optimal design of FT microchannel reactor.

- **Single microchannel fixed bed reactor model**

Since the FT reaction is a high exothermic reaction, a high reaction heat is generated at the front end of the reactor. Therefore, it should not be assumed that the heat of reaction is the same at any position of the reactor, and it should be expressively expressed as a tendency of the heat of reaction in the longitudinal direction of the reaction channel so that the temperature and heat transfer analysis can be accurately performed. Thus, a linear regression model is used as single channel heat of reaction profile. The single channel model is formulated based on Knochem et al. [37] which consists of mass balance, heat balance, and CoRe/ $\gamma$ -Al<sub>2</sub>O<sub>3</sub> 1<sup>st</sup> order reaction kinetics. In general, empirical equations are used to show that the Fischer-Tropsch reaction is proportional to the H<sub>2</sub> concentration when expressed by the 1<sup>st</sup> order rate equation. Activation energy ( $E_A$ ) is 120 kJ mol<sup>-1</sup> and heat of reaction is assumed as -170 kJ mol<sub>CO</sub><sup>-1</sup> [38].

$$-r_{CO} = kC_{H_2} \quad [2-7]$$

$$k = k_0 \exp\left(-\frac{E_A}{RT}\right) \quad [2-8]$$

For numerically adopting molar bulk concentration, molar weight, mixed gas thermal conductivity, and etc. which changing dynamically through reaction, we use the integrated model to calculate the information based on the Peng-Robinson equation of states, which is often used in GTL FT reactions, by transferring the response information to HYSYS, and then transferring the

calculated information to the Matlab model. Parameters and conditions are given in Table 2-2 in detail.

**Table 2-2.** Compositions of natural gas feed and refrigerant.

Process channel geometry	Width( $P_W$ ) : 1 mm
	Height( $P_H$ ) : 3 mm
	Length( $P_L$ ): 17 mm
Feed operating conditions	Temperature( $T$ ) : 230 °C
	Pressure( $P$ ) : 20 bar
	Molar composition : $H_2:CO:N_2=0.64:0.32:0.04$
	Velocity( $u_{in}$ ) : 0.00281 m/s
	WHSV : 400 ml/hr·gcat
Packed bed properties	Particle thermal conductivity( $k_p$ ) : 0.3 W/m·K
	Particle mean diameter( $D_p$ ) : 250 $\mu$ m
	Bed void fraction( $\epsilon$ ) : 0.3630
	Catalyst density( $\rho_{cat}$ ) : 1.232 x 103 kg/m <sup>3</sup>
	Catalyst weight( $m_{cat}$ ) : 0.076 g



- **Multi-microchannel fixed bed reactor model**

The commercial CFD program, ANSYS Fluent, is used for analyzing the effect of reactor design variables with the fixed heat of reaction curve. The base structure of the cubic style microchannel reactor is shown in Figure 2-5. There are 2 reaction channel layers, and 10 channels exist at each layer. There are 3 cooling channel layers, and 8 channels exist at each layer. Since the reactor is symmetrical with respect to the XZ plane when there is no biased disturbance, a symmetrical plane is created and analyzed to facilitate calculation of the simulation.

Governing equation of CFD model is set to simulate the fixed bed reactor especially understanding the fluid dynamics in the reactor. At each reaction channels, species transport with no reaction is used. SST  $k-\omega$  model (This model is similar to  $k-\omega$ , but it is expressed by blended with  $k-\epsilon$ , where  $k-\omega$  is used near the wall, and  $k-\epsilon$  is used for the rest) is used for turbulence model because it gives relatively accurate heat transfer and shear stress calculation simultaneously at the near wall region than other Reynolds-averaged Navier-Stokes equation (RANS) [39]. Moreover, Peng-Robinson equation of state is used which is usually used for FT reaction [40-42]. Coolant is set to marlotherm® SH and  $u_{cin}$  of the base case is set to 0.1 m/s. Thus, the volumetric flow rate of all coolant channel is fixed at that value. This is because the recycle

unit of the refrigerant is operated in a state where the volumetric flow rate is fixed.

The important governing equations are summarized in Table 2-3. In momentum conservation equation, gravity acceleration ( $\vec{g}$ ) is 9.81 m/s<sup>2</sup> through the inlet direction of the reaction channel,  $+\vec{x}$ . In the energy conservation equation, heat source term ( $S_h$ ) from the heat of reaction is set as the linear function of reactor length for regressing the high reaction heat in the front stage and less in the rear. For calculating the porous media by catalyst packing, Ergun equation with  $\alpha$ (permeability) and  $C_2$ (inertial resistance factor) is used, and equations are given by Equations [2-9] and [2-10]

$$\alpha = \frac{d_p^2}{150} \frac{\varepsilon^3}{(1-\varepsilon)^2} \quad [2-9]$$

$$C_2 = \frac{3.5}{d_p} \frac{1-\varepsilon}{\varepsilon^3} \quad [2-10]$$

$T_{cmax}$ ,  $T_{pmax}$ , and  $Q$  are obtained by varying the four variables of  $C_w$ ,  $C_h$ ,  $CP_D$ , and  $CC_D$  through a total of 11 cases including the base case. Base case. Because we fix the length of the reaction channel, the number of the coolant channel and the total size of the reactor module can be changed with varying the geometry of the coolant channel. Each case is summarized in Table 2-4.

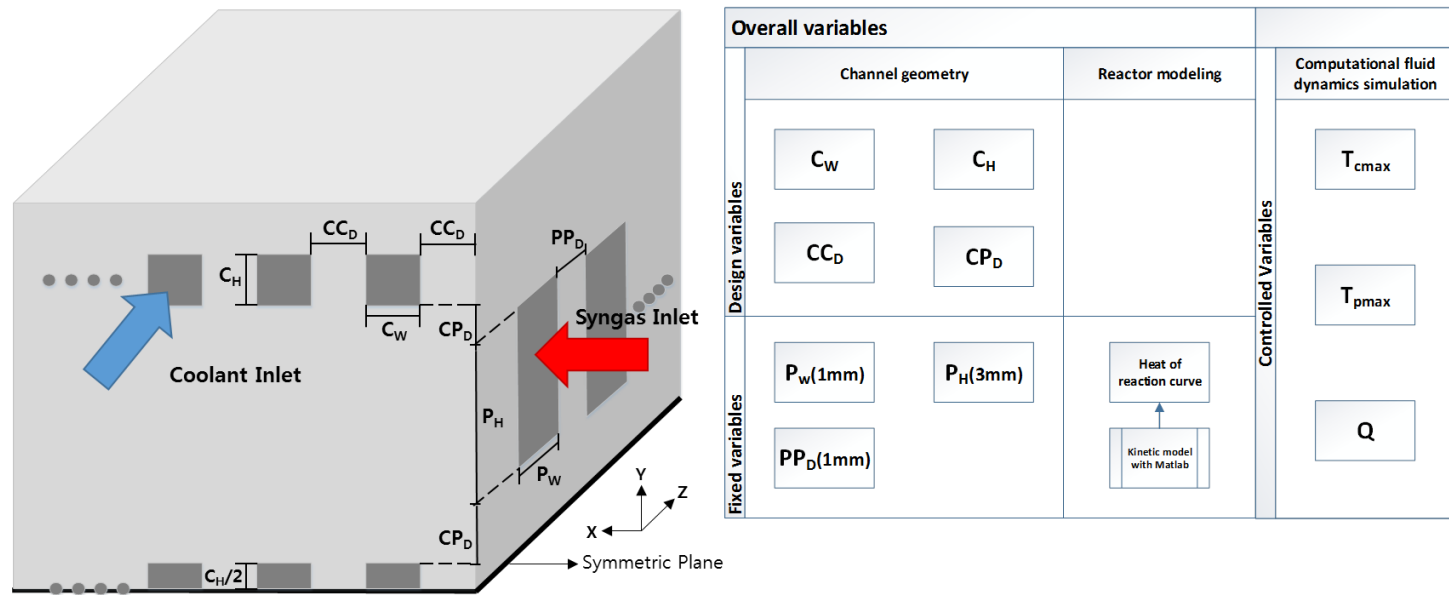


**Figure 2-5.** General geometry of microchannel reactor with variables identification.

**Table 2-3.** Module and governing equations for CFD modeling.

Module name	Governing equation	Remarks
Conservation & continuity	$\frac{\partial \rho}{\partial t} + \nabla \cdot (\rho \vec{v}) = 0$	Mass
	$\frac{\partial \rho \vec{v}}{\partial t} + \nabla \cdot (\rho \vec{v} \vec{v}) = -\nabla P + \rho \vec{g}$	Momentum
	$\frac{\partial \rho E}{\partial t} + \nabla \cdot (\vec{v}(\rho E + P)) = \nabla \cdot \left[ k_{eff} \nabla T - \sum_j h_j \vec{J}_j + \vec{\tau}_{eff} \vec{v} \right] + S_h$	Energy with heat source (S <sub>h</sub> )
Porous media	$S_i = -\left( \frac{\mu}{\alpha} v_i + C_2 \cdot \frac{1}{2} \rho  v  v_i \right)$	Packed bed reactor

**Table 2-4.** Case specifications.

<b>Case</b>	<b>Base</b>	<b>1</b>	<b>2</b>	<b>3</b>	<b>4</b>	<b>5</b>	<b>6</b>	<b>7</b>	<b>8</b>	<b>9</b>	<b>10</b>
<b>Variables</b>		<b>C<sub>W</sub></b>		<b>C<sub>H</sub></b>		<b>CP<sub>D</sub></b>			<b>CC<sub>D</sub></b>		
CW (mm)	1.000	2.200	0.600	1.000	1.000	1.000	1.000	1.000	1.000	1.000	1.000
CH (mm)	1.000	1.000	1.000	2.000	0.500	1.000	1.000	1.000	1.000	1.000	1.000
CPD (mm)	1.000	1.000	1.000	1.000	1.000	5.000	2.000	0.500	1.000	1.000	1.000
CCD (mm)	1.000	1.000	1.000	1.000	1.000	1.000	1.000	1.000	2.600	1.571	0.636

### **2.2.2.2. Result and discussion**

Fixed heat of reaction curve with linear regression function in single FT microchannel reactor is shown in Figure 2-6. Since the reaction rate is proportional to the concentration of  $H_2$  by [2-7], it can be expected that the reaction will be faster at the front of the reactor, which can be observed linearly as reaction heat. Conversion based on the CO is about 0.773, which is appropriate for usual FT reaction. The reason why we use the linear function for regression is a feasible computational time of the CFD with heat source  $S_h$ .  $R^2$  value is about 0.993, and it is sufficient to use for the surrogate model.

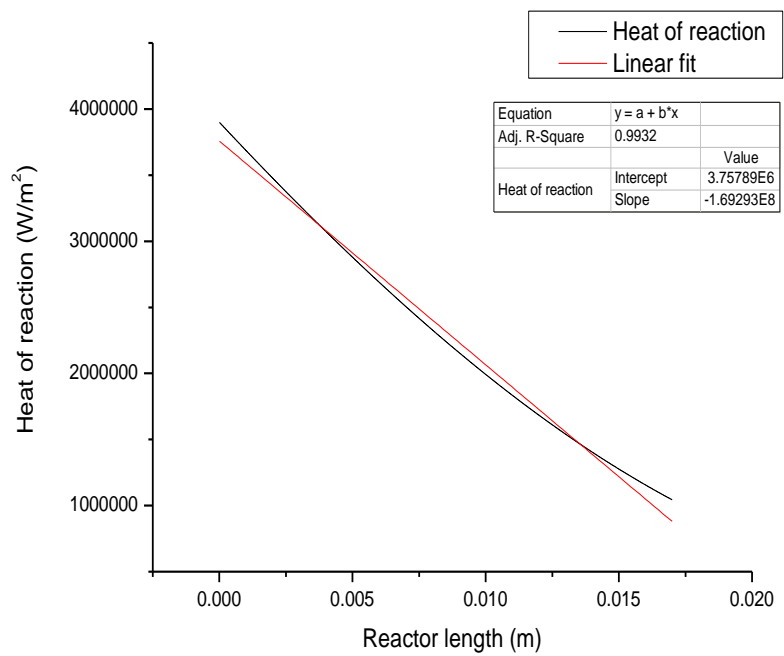


**Figure 2-6.** The heat of reaction curve with a linear fit approximation.

The tendency of the multi microchannel reactor model analyzed by CFD is analyzed for  $Q$ ,  $T_{pmax}$ , and  $T_{cmax}$ . In the case of  $Q$ , the average heat flux over the area through the area weighted average and the area-weighted integral are absorbed into the cooling channel total heat flux is analyzed separately. This model is implemented through steady-state analysis, and we try to minimize the numerical error by equalizing the residual limits of each variable in all cases.

About the 4 design variables, total heat flux which flows to the coolant channel and average heat flux is shown in Figure 2-7. It is found that shorter the  $C_w$ , the more average and total heat flux increased. This is because the surface area does not change because the length of the reaction channel is fixed even if the surface area of the cooling channel fluctuates. However, since the volumetric flow rate is fixed, the flow velocity becomes faster as the area forming the vertical vector of the flow velocity becomes smaller, and it makes the flow velocity gradient between the wall and the center of the refrigerant larger than when it is slow. It also increases the temperature gradient. Thus, more heat can be removed. On the contrary, in the case of  $C_H$ , the shortening of the surface area is disadvantageous to the heat removal due to the reduced surface area, but it seems to be able to remove the high heat due to the effect on the flow rate. All of them remove the higher heat of reaction when the channel is small, which resulted in the effect of the flow rate and the small channel causing a rapid mixing effect of the refrigerant to achieve high heat exchange.



In  $CP_D$ , the highest total heat flux is shifted in the base case, but it decreased as the thickness increased. However, the  $CP_D$  showed a decrease of 0.5 mm, and the variation is much small compared to other parameters. In fact, it is observed to have little effect. The heat transfer resistance due to the microchannel structure assumed to be stainless steel do not have such a great influence when it is predicted that the most critical resistance factor in the heat exchange between the reaction channel and the cooling channel is the resistance caused by the film produced by the fluid flow. On the other hand, the  $CC_D$  shows a tendency toward channel spacing, and the total heat flux and the average heat flux are observed to show the opposite tendencies. Shortening the length between cooling channels increases the surface area of the cooling channels per unit length, which acts as a power to remove more total heat flux, but if the total heat flux is not so large, it can be rather large because the amount of heat to be removed per unit area increases.

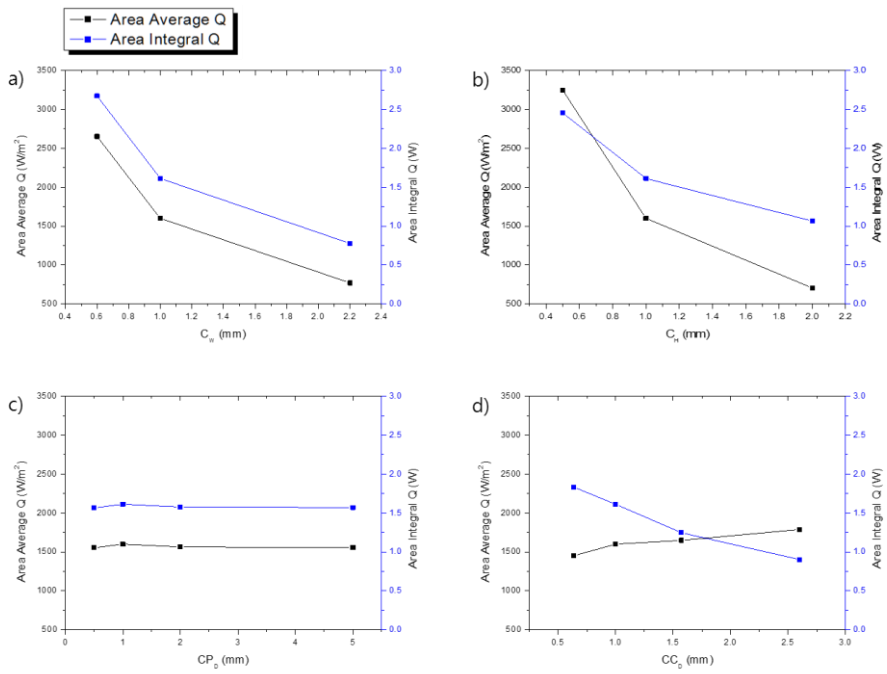


**Figure 2-7.** Overall coolant wall heat flux trends with a)  $C_w$ , b)  $C_H$ , c)  $CP_D$ , d)  $CC_D$ .

In Figure 2-8, the temperature of the highest fluid ( $T_{\text{cmax}}$ ,  $T_{\text{pmax}}$ ) of the cooling channel and the reaction channel, respectively, is plotted for each variable to confirm the tendency of temperature fluctuation. In the case of  $C_W$  and  $C_H$ , absolute temperature decreases and the temperature difference increases when variables increase. Since the heat of reaction and the initial inflow temperature are not changed during the simulation, it is considered that the temperature should be lowered when the total flow rate is removed. In this case, however, the result is opposite. This phenomenon is possible because, even if more heat is removed, the temperature can be observed higher at a specific part due to its position and structural effect. In the case of marlotherm® SH used as a refrigerant, the heat capacity is  $2.22 \text{ kJ/kg}\cdot\text{m}^3$ . However, since heat capacity of stainless steel is  $0.5 \text{ kJ/kg}\cdot\text{m}^3$ , if the ratio of the refrigerant to the overall volume of the reactor is increased, the absolute temperature can be lower even if the higher heat quantity is removed. Therefore, it is confirmed that the maximum temperature of the channel is lowered when the variable moves in the direction of increasing the volume of the cooling channel. However, in the case of  $C_W$ , the proportion of the trade-off relation is not so large, and it is considered that there is almost no change in temperature. In the case of  $CP_D$ , there is no structural change in the cooling channel, so only a large amount of heat removal would result in lower maximum temperature, but the maximum temperature is also found to be unchanged because of less effect of total flow rate. In the case of  $CP_D$ , as the cooling channel spacing is reduced,

the total amount of heat is also removed, and the volume ratio of the refrigerant to the entire reactor is also increased so that the maximum temperature also decreases.

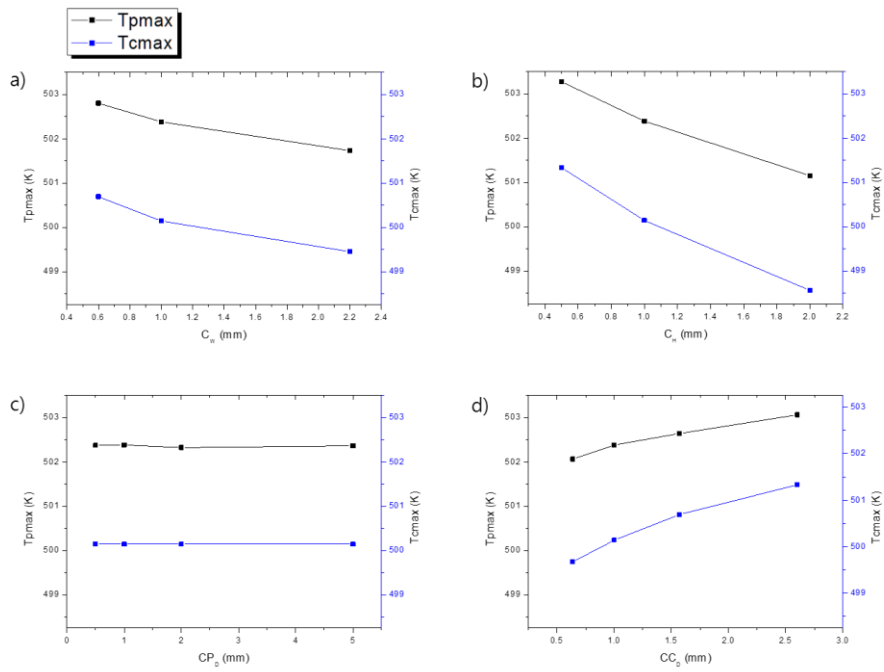


**Figure 2-8.** Maximum temperature trend with a)  $C_w$ , b)  $C_H$ , c)  $CP_D$ , d)  $CC_D$ .

In this study, only the structural parameters of the reactor are changed to confirm the thermal flow tendency. However, as a result, it is confirmed that the tendency may change depending on the external variables such as the difference between the heat capacity of the reactor skeletal metal and the refrigerant, and the degree of the reaction heat of the reaction channel. However, it is expected that most of the fixed values will not escape the extreme tendency because they are introduced by advanced companies such as Velocys® to the same level as proposed in actual patents and papers.

### 2.2.2.3. Conclusion

Parametric study of  $Q$ ,  $T_{cmax}$ , and  $T_{pmax}$  through the multi FT microchannel reactor design variables,  $C_w$ ,  $C_H$ ,  $CP_D$ , and  $CC_D$  is performed using the Matlab-Aspen HYSYS integrated systems for understanding the heat of reaction curve and the ANSYS Fluent for CFD. As a result of simulating the fixed bed reactor, the following conclusions are obtained when the reaction channel and the cooling channel flow through the cross flow.

- The tendency of the heat of reaction is high at the front end of the reaction channel and almost linearly decreased toward the back, and the conversion rate at a given condition is observed to be about 0.733.
- As the cooling channel width ( $C_w$ ) and height ( $C_H$ ) become shorter, the total heat flux and the average heat flux become higher, and the maximum cooling channel temperature ( $T_{cmax}$ ) and the reaction channel maximum temperature ( $T_{pmax}$ ) also become higher.
- The gap between the cooling channel and the reaction channel ( $CP_D$ ) has not been found to have a significant effect on heat transfer
- It is confirmed that the total heat flux and the average heat flux increase as the distance between the cooling channel and the cooling channel became shorter and that the maximum cooling channel temperature

( $T_{\text{cmax}}$ ) and the maximum reaction channel temperature ( $T_{\text{pmax}}$ ) decrease.

- $C_W$  and  $C_H$  have a trade-off relation with the maximum temperature, while a slight change has a great effect on the heat transfer. However, in the case of the  $CC_D$ , it does not give a rapid change as  $C_W$  and  $C_H$ . It also has a design effect that reduces the maximum temperature.
- In this study, it is suggested that  $C_W$ ,  $C_H$ , and  $CC_D$  could be proposed for designing a multi microchannel reactor for Fischer-Tropsch synthesis without any design limit and it is expected that it can be used as a basic data of the reactor design optimization study in the future.



### **2.3. Carbon Capture, Utilization, and Storage (CCUS) multiphase carbonation reactor model**

The national greenhouse gas emission target is set at 640 million ton in 2014 and 540 million ton in 2020. Although the target date for the national greenhouse gas reduction target is 30% compared to BAU by 2020, the development of CCS technology suitable for domestic conditions is not completed. At present, a 10 MW CO<sub>2</sub> capture demonstration plant is operating in Boryeong and Hadong, but CO<sub>2</sub> storage technology has not been developed, and most of the captured CO<sub>2</sub> is released to the atmosphere. The existing carbonation research focuses on the capture of CO<sub>2</sub> using the reaction, but it is difficult to link it with the achievement of greenhouse gas reduction because of limitations in storing the conversion product. In addition to collecting CO<sub>2</sub> directly and finalizing the final storage, it is necessary to develop technologies for mass capture and construction materials with a CO<sub>2</sub> storage potential of over 7,000,000 ton/yr CO<sub>2</sub>

In line with this, many companies around the world are doing their utmost to develop this technology. In the case of Novacem in the UK, the development and commercialization of carbon dioxide cement are underway. The CO<sub>2</sub> production technology using cement produces 1.5 tons of CO<sub>2</sub> reduction effect per ton of cement in the entire production process. In the case of Calera in the US and Canada, the company is recovering carbon dioxide and developing a

substitute for cement and has completed operation of 50 ton/day by-products. Currently, a 10MW pilot plant is in operation. MCI (Mineral Carbonation International) is in the process of researching the CO<sub>2</sub> capture and construction material conversion technology pilot plant and is preparing to commercialize it.

In this study, the authors intend to design a 40 tonCO<sub>2</sub>/day CO<sub>2</sub> carbonation reactor. The process required for reactor design was based on computer-aided engineering (CAE). First, kinetics studies have been carried out for the analysis of reaction systems. Secondly, CFD - based reactor models have been developed to test the performance of the reactors under various conditions.

## **2.3.1. Rigorous reaction kinetics for carbonation based CCUS reactor**

### **2.3.1.1. Introduction**

The first thing to do to design a CCUS reactor is to identify the definite kinetics and perform parameter estimation to predict the reactivity well under various conditions. Ultimately, kinetics should be identified for specific drugs such as waste. However, since all of the reactions are based on calcium hydroxide ( $\text{Ca(OH)}_2$ ), the kinetics of the reaction of  $\text{Ca(OH)}_2$  with the exhaust gas can be easily obtained. Therefore, in this study, the kinetics of  $\text{CO}_2$  gas reaction is investigated for  $\text{Ca(OH)}_2$  and sodium hydroxide ( $\text{NaOH}$ ) solutions.

Several previous studies have attempted to investigate the kinetics of  $\text{CO}_2$  response to  $\text{Ca(OH)}_2$ -based solutions but did not simulate dynamic changes in bubble and particle diameter [43]. Dynamic bubble and particle diameter changes must be performed because mass transfer of  $\text{CO}_2$  and dissolution of  $\text{Ca(OH)}_2$  in water are among the most critical of the reaction. In addition, mass transfer of  $\text{CO}_2$  gas to water and simulation of the equilibrium state of acid bases in aqueous solution must be rigorously performed so that reactor simulations can be successfully carried out.

### **2.3.1.2. Model formulation & development**

The CCUS reaction can be roughly divided into three parts. First, the carbonation part is a reaction that produces various carbonate ions and carboxylic acids while forming an acid-base equilibrium while the  $\text{CO}_2$  is dissolved in water. Since these reactions are strongly involved in pH, they need to be calculated accurately. In the case of  $\text{CO}_2$  bubbles, the size of the bubble will decrease as it dissolves, which must have a great influence on mass transfer and it should be calculated exactly. The next category is the reaction of  $\text{Ca(OH)}_2$  and  $\text{NaOH}$  as an aqueous solution to make a reaction agent. This reaction determines the pH of the initial solution and simulates the unreacted solid particles to dynamically calculate the continuous dissolution as the pH gradually drops. Finally, it is a series of reactions that occur as precipitation to produce calcium carbonate ( $\text{CaCO}_3$ ). Since they remove ions and precipitate in solid form, it is essential to remove ions from the system.

The solid particles and bubble disappear when they are completely dissolved. To introduce this discrete event into an ordinary differential equation (ode) in the form of hybrid systems, a differential algebraic equation (DAE) must be used. In addition, we need to use a stiff solver because the difference in kinetic parameter values between the several reactions is significantly different on the  $10^8$ - $10^9$  scale (Refer to Table 2-5 and reference for more kinetic parameter values and information). Therefore, kinetics is coded based on ode15s and

ode23s solver of MATLAB. Overview of the reaction mechanism is given in Figure 2-9.

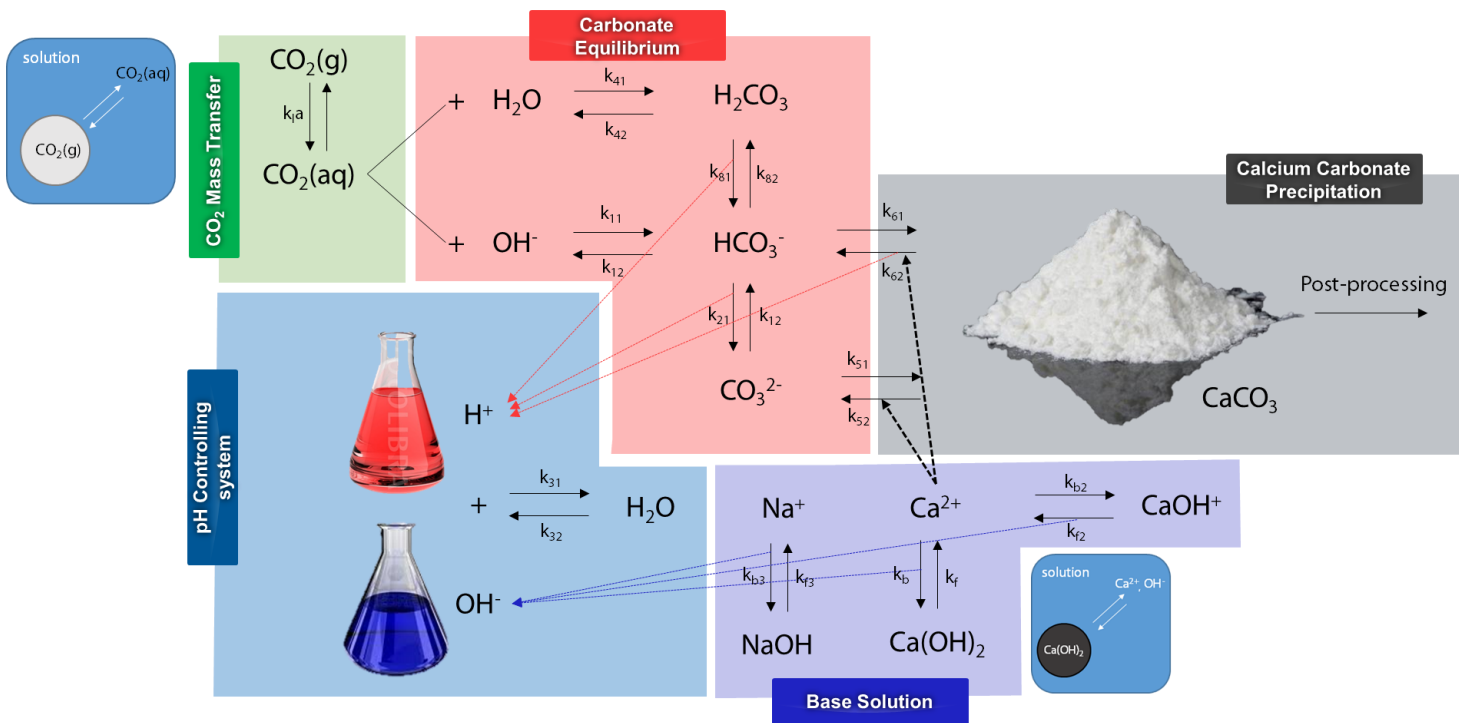


**Figure 2-9.** Overview of reaction mechanism for carbonation reaction in CCUS reactor.

**Table 2-5.** Reaction kinetics and related parameters with references.

#	Class	Reaction	Parameter	Reference
R1	Carbonate	$\text{CO}_2(\text{aq}) + \text{OH}^- \rightleftharpoons \text{HCO}_3^-$	$k_{11}, k_{12}$	[43]
R2	Carbonate	$\text{HCO}_3^- + \text{OH}^- \rightleftharpoons \text{CO}_3^{2-} + \text{H}_2\text{O}$	$k_{21}, k_{22}$	[43]
R3	Carbonate	$\text{OH}^- + \text{H}^+ \rightleftharpoons \text{H}_2\text{O}$	$k_{31}, k_{32}$	[43]
R4	Carbonate	$\text{CO}_2(\text{aq}) + \text{H}_2\text{O} \rightleftharpoons \text{HCO}_3^- + \text{H}^+$	$k_{41}, k_{42}$	[43]
R5	Mass transfer	$\text{CO}_2(\text{g}) \rightleftharpoons \text{CO}_2(\text{aq})$	$k_{1a}, E, H, d_b$	[44] [45]
R6	Base solution	$\text{Ca}(\text{OH})_2 \rightleftharpoons \text{Ca}^{2+} + 2\text{OH}^-$	$k_f, k_b, A$	[46]
R7	Base solution	$\text{CaOH}^+ \rightleftharpoons \text{Ca}^{2+} + \text{OH}^-$	$k_{f2}, k_{b2}$	[46]
R8	Base solution	$\text{NaOH} \rightleftharpoons \text{Na}^+ + \text{OH}^-$	$k_{f3}, k_{b3}$	
R9	Precipitation	$\text{Ca}^{2+} + \text{CO}_3^{2-} \rightleftharpoons \text{CaCO}_3$	$k_{51}, k_{52}$	[47]
R10	Precipitation	$\text{Ca}^{2+} + \text{HCO}_3^- \rightleftharpoons \text{CaCO}_3 + \text{H}^+$	$k_{61}, k_{62}$	[47] [48]
R11	Carbonate	$\text{H}_2\text{CO}_3 \rightleftharpoons \text{H}^+ + \text{HCO}_3^-$	$k_{81}, k_{82}$	[43]

Equations [2-11]-[2-19] represent the time-dependent changes of all the ions participating in the reaction in the form of differential equations. If this is the only place to end here, you can interpret it as an ODE system. However, because of Equation [2-20]-[2-27] which are activated only when bubble and solid particle exist, and it contains the algebraic equation, it is interpreted as a DAE system.

$$\begin{aligned} \frac{d[CO_2(aq)]}{dt} = & -k_{11}[CO_2(aq)][OH^-] + \\ & k_{12}[HCO_3^-] - k_{41}[CO_2(aq)] + k_{42}[HCO_3^-][H^+] + \\ & k_l a E (H^{CO_2} RT [CO_2(g)] - [CO_2(aq)]) \end{aligned} \quad [2-11]$$

$$\begin{aligned} \frac{d[CO_2(g)]}{dt} = & -k_l a E (H^{CO_2} RT [CO_2(g)] - \\ & [CO_2(aq)]) \end{aligned} \quad [2-12]$$

$$\begin{aligned} \frac{d[OH^-]}{dt} = & -k_{11}[CO_2(aq)][OH^-] + k_{12}[HCO_3^-] - \\ & k_{21}[HCO_3^-][OH^-] + k_{22}[CO_3^{2-}] - k_{31}[OH^-][H^+] + \\ & k_{32} + 2A(k_f - k_b[Ca^{2+}][OH^-]^2 f^6) + \\ & k_{f2}[CaOH^+] - k_{b2}[Ca^{2+}][OH^-] + k_{f3} - \\ & k_{b3}[Na^+][OH^-] \end{aligned} \quad [2-13]$$

$$\begin{aligned} \frac{d[H^+]}{dt} = & -k_{31}[OH^-][H^+] + k_{32} + k_{41}[CO_2(aq)] - \\ & k_{42}[HCO_3^-][H^+] + k_{61}[Ca^{2+}][HCO_3^-] - k_{62}[H^+] + \\ & k_{81}[H_2CO_3] - k_{82}[H^+][HCO_3^-] \end{aligned} \quad [2-14]$$

$$\begin{aligned} \frac{d[HCO_3^-]}{dt} = & k_{11}[CO_2(aq)][OH^-] - [HCO_3^-] - \\ & k_{21}[HCO_3^-][OH^-] + k_{22}[CO_3^{2-}] + k_{41}[CO_2(aq)] - \\ & k_{42}[HCO_3^-][H^+] - k_{61}[Ca^{2+}][HCO_3^-] + k_{62}[H^+] + \\ & k_{81}[H_2CO_3] - k_{82}[H^+][HCO_3^-] \end{aligned} \quad [2-15]$$

$$\begin{aligned} \frac{d[CO_3^{2-}]}{dt} = & k_{21}[HCO_3^-][OH^-] - k_{22}[CO_3^{2-}] - \\ & k_{51}[Ca^{2+}][CO_3^{2-}] + k_{52} \end{aligned} \quad [2-16]$$



$$\begin{aligned} \frac{d[Ca^{2+}]}{dt} = & A(k_f - k_b[Ca^{2+}][OH^-]^2f^6) - \\ & k_{51}[Ca^{2+}][CO_3^{2-}] + k_{52} + k_{f2}[CaOH^+] - \\ & k_{b2}[Ca^{2+}][OH^-] - k_{61}[Ca^{2+}][HCO_3^-] + k_{62}[H^+] \end{aligned} \quad [2-17]$$

$$\frac{d[CaOH^+]}{dt} = k_{b2}[Ca^{2+}][OH^-] - k_{f2}[CaOH^+] \quad [2-18]$$

$$\frac{d[Na^+]}{dt} = k_{f3} - k_{b3}[Na^+][OH^-] \quad [2-19]$$

$$\begin{aligned} r_{mass\ transfer} = & k_l \left( \frac{6n_B}{d_B} \right) E \left( H_w RT \left[ \frac{n_{CO_2}}{V_g} \right] - \right. \\ & \left. [CO_2(aq)] \right) \end{aligned} \quad [2-20]$$

$$V_g = \frac{(n_{CO_2} + n_{N_2})RT}{P} \quad [2-21]$$

$$n_B = \frac{V_g^0}{\frac{4}{3}\pi \left( \frac{d_B^0}{2} \right)^3} \quad [2-22]$$

$$d_B = 2 \left( \frac{V_g}{\frac{4}{3}\pi n_B} \right)^{\frac{1}{3}} \quad [2-23]$$

$$r_{solid\ dissolution} = A(k_f - k_b[Ca^{2+}][OH^-]^2f^6) \quad [2-24]$$

$$V_{particle} = \frac{V_{Ca(OH)_2}}{n_{particle}} \quad [2-25]$$

$$d_{particle} = 2 \left( \frac{3V_{particle}}{4\pi} \right)^{\frac{1}{3}} \quad [2-26]$$

$$A = n_{particle}(4\pi) \left( \frac{d_{particle}}{2} \right)^2 \quad [2-27]$$

All of the above expressions were coded in MATLAB R2016b based on ode15s and ode23s, and a dynamic system was constructed. Since there is a possibility that there is a gap between actual system and kinetics, validation and parameter estimation were carried out through a 500 ml reactor. Experimental set uses 16 experimental sets selected through the orthogonal array to use the design of experiment to simultaneously reflect the influence of various variables as much as possible. The parameters used in this experiment were operating temperature, CO<sub>2</sub> vol%, Ca (OH)<sub>2</sub> wt%, NaOH wt%, GHSV (hr<sup>-1</sup>), and CO<sub>2</sub> flow rate (L / min). Parameter estimation was performed by adjusting the CO<sub>2</sub> outlet (vol%) and pH, and the mean squared error of the experimental and model values was calculated. Solver algorithm was Dividing hyper-RECTangle (DIRECT), and target parameters were gas hold up, bubble initial diameter, mass transfer coefficient for the bubble, mass transfer coefficient for solid, Ca(OH)<sub>2</sub> dissolution factor, enhancement fact, and solid particle initial diameter. The exact values for each experiment set are shown in Table 2-6.

**Table 2-6.** Experiment set using an orthogonal array for the design of the experiment.

Exp #	Temperature °C	CO <sub>2</sub> vol%	Ca(OH) <sub>2</sub> wt%	NaOH wt%	GHSV hr <sup>-1</sup>	CO <sub>2</sub> flow rate L/min
1	25	2.00%	1.00%	0.00%	60	0.5
2	25	10.00%	1.50%	1.00%	120	1
3	25	20.00%	2.00%	2.00%	180	1.5
4	25	30.00%	3.00%	3.00%	240	2
5	40	2.00%	1.50%	2.00%	240	2
6	40	10.00%	1.00%	3.00%	180	1.5
7	40	20.00%	3.00%	0.00%	120	1
8	40	30.00%	2.00%	1.00%	60	0.5
9	55	2.00%	2.00%	3.00%	120	1
10	55	10.00%	3.00%	2.00%	60	0.5
11	55	20.00%	1.00%	1.00%	240	2
12	55	30.00%	1.50%	0.00%	180	1.5
13	70	2.00%	3.00%	1.00%	180	1.5
14	70	10.00%	2.00%	0.00%	240	2
15	70	20.00%	1.50%	3.00%	60	0.5
16	70	30.00%	1.00%	2.00%	120	1

### **2.3.1.3. Result and Discussion**

In Figure 2-10, we can see how the CO<sub>2</sub> removal rate is for various experiments. It can be seen that the curves exhibit significantly different tendencies under various conditions. In general, NaOH was dissolved in almost all water, and high pH was obtained. It was found that the initial CO<sub>2</sub> removal rate was high in the case of NaOH containing experiment. However, when the effect of NaOH was over, and CO<sub>2</sub> was removed only by the basicity of Ca(OH)<sub>2</sub>, the CO<sub>2</sub> removal rate dropped sharply. Therefore, it was found that the addition of NaOH is essential for obtaining a very high CO<sub>2</sub> removal rate directly for a single reactor.

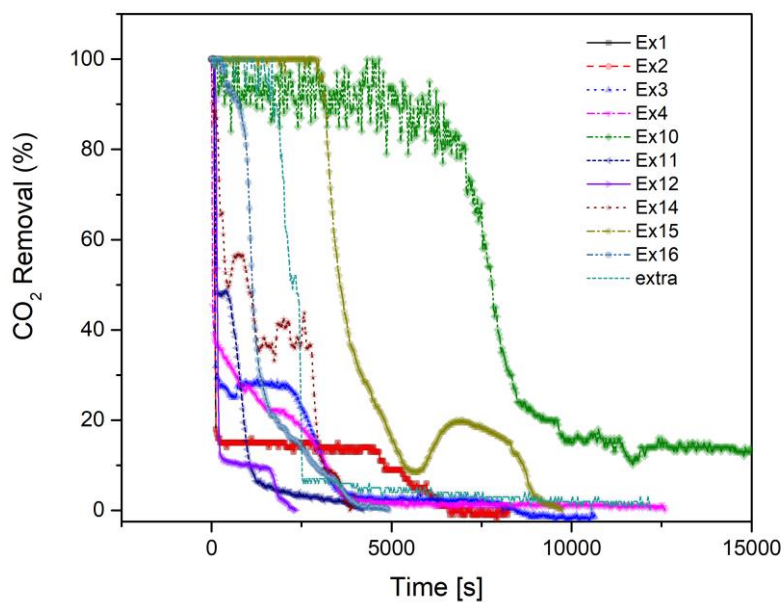


**Figure 2-10.** CO<sub>2</sub> removal rate over different experiment set.

The results of the parameter estimation for the 10th experiment are plotted in Figure 2-11. The model determined by the parameters referring to several documents at the beginning and arbitrarily inserted parameters seem to show a great difference from the experiment. The results obtained with the optimized parameter set through the DIRECT global NLP algorithm show that the experiment is almost exactly matched. In the case of the conventional model, the pH fitting was calculated to be very slowly dropped. However, for the optimal model, we confirmed that the experiment curve follows almost exactly.

Finally, in order to find out what kind of changes are observed under various conditions, we try to show the tendency of simulation by changing the operating temperature of the reactor and the amount of the initial NaOH (Figure 2-12). It can be seen that the CO<sub>2</sub> outlet volume fraction is formed at a higher level when the temperature is first raised. It is not so sensitive to temperature until all of the NaOH is consumed, but once consumed, the pH is determined by the solubility of Ca(OH)<sub>2</sub> and the CO<sub>2</sub> removal rate is determined accordingly. However, when the temperature is high, it is confirmed that Ca(OH)<sub>2</sub> is less soluble and thus the CO<sub>2</sub> removal rate is lowered. Similarly, in the case of NaOH, the CO<sub>2</sub> removal rate remained very high for more time, indicating that the outlet volume reaction remained close to zero. The interesting thing is that this curve does not just go up to the same slope, but shows that NaOH goes up

more steeply. This is probably due to the effect of the product, which causes the  $\text{CO}_2$  to dissolve slightly more.

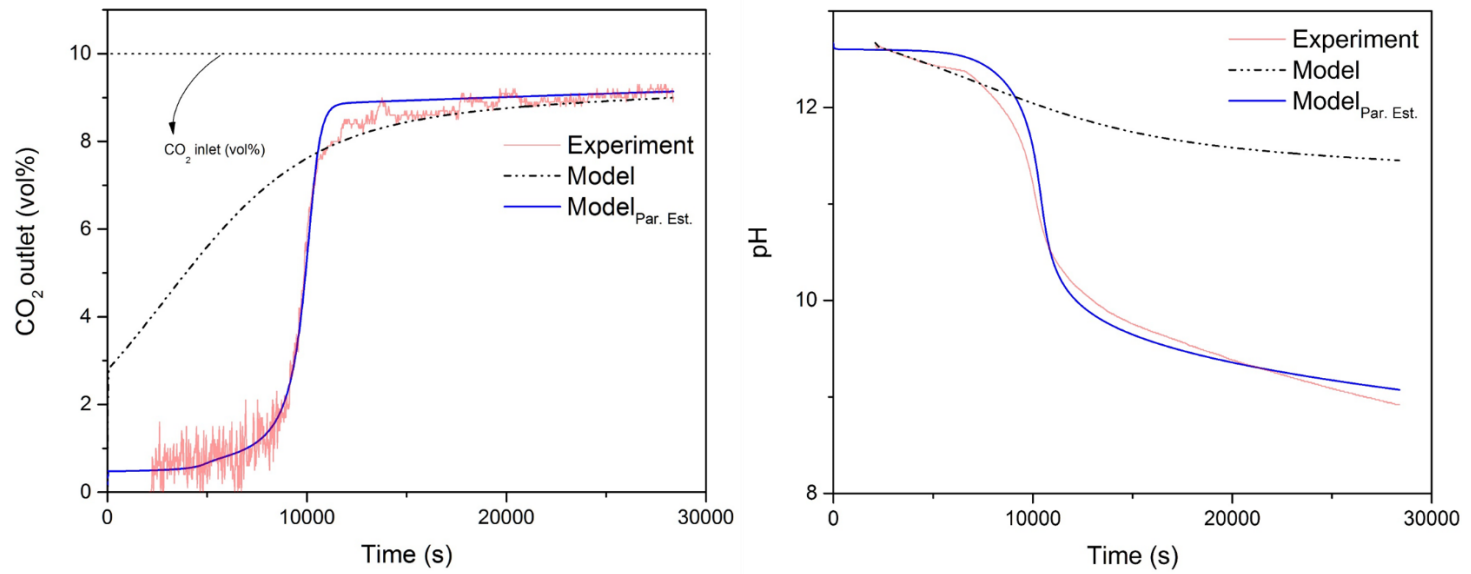


**Figure 2-11.** The result of parameter estimation.



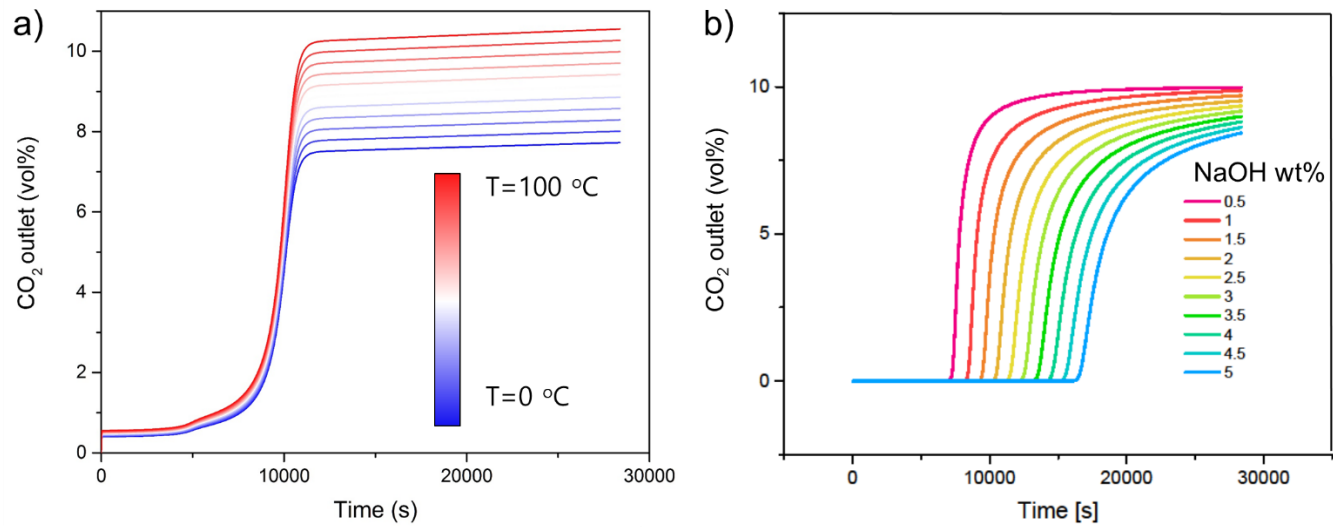


**Figure 2-12.** Sensitivity analysis for CO<sub>2</sub> outlet volume fraction with a) temperature fluctuation and b) NaOH weight fluctuation.

## **2.3.2. Eulerian multiphase model for carbonation reactor**

### **2.3.2.1. Introduction**

As can be seen in 2.3.1, since the reaction is a very fast acid-base reaction, the rate of the overall reaction of this system is governed by the rate of mass transfer, such as the rate of dissolution of the gas and solid reactants. Among them, the dissolution process of the solid reactants is generally regarded as the rate determining step [49]. Many studies have been conducted on chemical factors such as additives, temperature, pressure, reaction conditions such as concentration, particle size of solid reactants, etc., which can increase the dissolution rate. However, there are research that the mass transfer rate has a great influence not only on these chemical factors but also on physical factors such as velocity fields, turbulence intensities, shear stress distributions, and volume fraction of various phases [50]. Despite the fact that proper reactor designs can improve physical factors to increase mass transfer rates, little research has been done on reactors in this process.

It is very important to ensure that the reactant distribution within the reactor is evenly distributed through appropriate reactor design. Uneven distribution of reactants means that reactants and some of the reactors are not utilized properly, which can lead to an increase in the cost of the process. Large-Scale reactors are designed using empirical correlations or empirical laws based on laboratory

experiments [51]. In the case of agitated reactors, there are correlations for predicting solid suspension in solution using various solutions [52, 53]. However, there is a limitation that the shape of the reactor is not applicable as the size or the deviation from the standard becomes larger.

In this study, we investigate the correlation between the dispersion of the solid reactants and the internal design factors in pilot scale stirred tank reactors capable of mineral carbonation of 40 tons of carbon dioxide per day and to propose an appropriate internal structure of the reactor. Although all of the gas-liquid ( $\text{CO}_2$ -solution) and solid-liquid ( $\text{CaO}$ -solution) transport in the target process is involved, this paper deals only with solid-liquid mixing. This is because the solubility rate of the solids is slower first, and secondly, the amount of gas entering the reactor is very large ( $7000 \text{ Nm}^3/\text{hr}$  of gas must be introduced to treat 40 tonnes of  $\text{CO}_2$  per day based on exhaust gas containing 15 vol%  $\text{CO}_2$ ) the reactor structure changes to a flooding regime that has little effect on gas mixing [54]. In this study, CFD technique was used to analyze the flow of the reactor. There have been many studies on the CFD analysis of agitated reactors from the past, and their reliability has been acknowledged by comparison with experimental results [55-58]. However, since the flow is always changed depending on the shape and characteristics of the reactor, the results of the existing studies cannot be applied to the present process. Therefore, in this

paper, we tried to analyze the internal flow, especially solid dispersion, in aqueous mineral carbonation reactor.

### **2.3.2.2. Model description**

The structure of the reactor is shown in Figure 2-1. It is a stirred tank reactor in which three impellers are vertically arranged in the center of a cylindrical tank having a diameter of 4 m and a height of 2.5 m. A gas distributor is disposed between the bottom agitator and the intermediate agitator. In this study, the gas is not discharged from the gas distributor because it does not deal with the gas dispersion, but the structure is described in detail as much as possible because the dispersing device itself can act as a flow obstacle of the liquid or solid. In this study, the reactor modeling range was limited to the head height, so the height of the reactor was considered to be 2.5 m, which is the height of the head.

As a reaction material, a mixture of water and solid calcium oxide of 25 °C, which is a liquid, was set. At this time, the calcium oxide mixture was assumed to have a particle size of 200 mesh, a density of 3,366 kg / m<sup>3</sup>, and a viscosity of 1.5 cP. In addition, the solid reactant occupies a volume fraction of 5 vol% in the total solution.

Design variables such as the number, type, clearance, and diameter of the impeller can have a large influence on the internal flow [59]. This value was reduced to the  $D(\text{impeller diameter})/T(\text{reactor diameter})$  value, which was 0.33 and 0.5 in this study. The rpm representing the number of revolutions per minute can be adjusted after the design and construction of the reactor is

completed, but it is crucial to estimate the operation range in advance because the specifications of the power equipment to be installed are determined according to how to select the rpm range. In this study, 0, 30, 60, and 90 rpm were verified. The type of agitator can be divided into an axial stirrer, which makes a large axial flow, a radial stirrer, which makes a horizontal flow, and a Pitched Blade Turbine (PBT), which produces a mixed flow of axial and horizontal directions. In this study, only the Pitched Blade Turbine (PBT) was discussed. The baffle is advantageous to install four equally spaced as possible [18] if solid dispersion is required, and longer and thicker thicknesses are considered better. However, as the baffle becomes larger and the structure becomes more complicated, the power consumption increases together. The detailed study of various variables and the application of the optimum design theory to the 40 tonCO<sub>2</sub>/day carbonation reactor are explained in detail in Section 4.2, and the description in this chapter is focused on the description of the model.

For the CFD modeling of this study, ANSYS® fluent 16.0 was used. The governing equations and several model equations used in CFD modeling are summarized in Table 2-7. A Euler-Granular multiphase model was used to analyze multiphase flows involving liquids and solids. This model solves the Navier-Stokes equations for coexisting and interpenetrating continuum phases, respectively and that can consider together by including interphase momentum

transfer or interphase mass transfer in the governing equations. There are several types of forces interacting between the liquid and solid, through which interphase momentum transfer is possible. The most important force among them is the drag force, and it has been found by various studies that the remaining interaction forces such as lift force, virtual mass force, and turbulent dispersion terms do not significantly affect the overall flow of the agitating reactor [56, 60, 61]. Therefore, in this paper, only the drag force is considered as the force involved in interphase momentum transfer. As a turbulence model, a realizable  $k$ - $\epsilon$  turbulence model was used for the liquid phase. This was determined by referring to the previous case study of solid dispersion in a stirred reactor [62]. Multiple reference frame (MRF) method was used to model the impeller rotation. No-slip condition boundary conditions were given to all wall surfaces in the reactor such as tank walls, impeller blades, rotary shafts, and gas injector surfaces, and the surface of the rotating shaft was set to rotate at the same speed as the impeller.

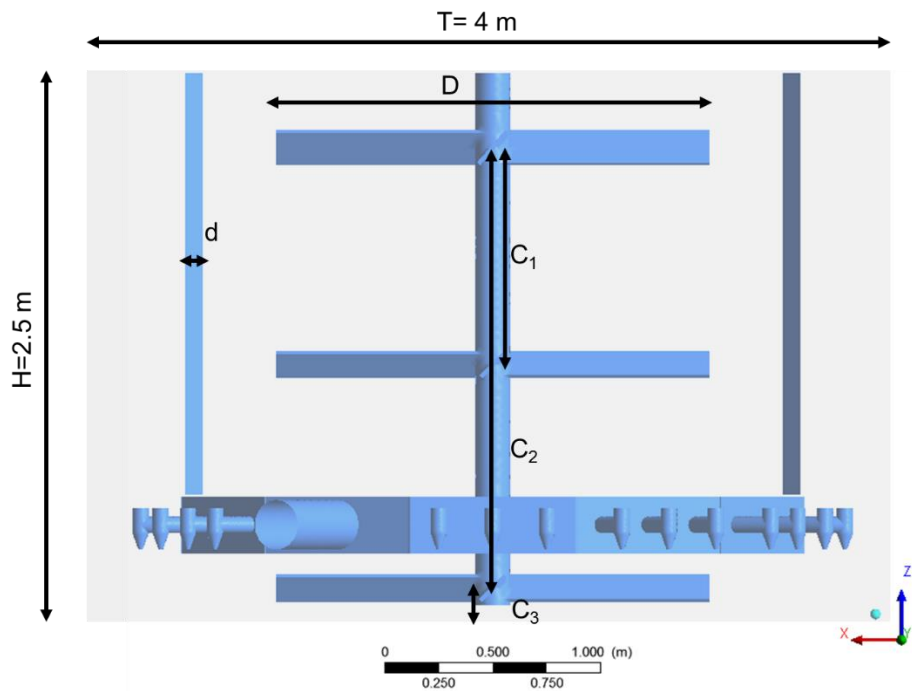


**Figure 2-13.** Reactor geometry with design variables.



**Table 2-7.** Governing equations of the reactor model.

	Governing equations/models	Remarks
Continuity	$\frac{\partial}{\partial t}(\alpha_k \rho_k) + \nabla \cdot (\alpha_k \rho_k \bar{u}_k) = 0$	K=phases(l,s)
Momentum	$\frac{\partial}{\partial t}(\alpha_k \rho_k \bar{u}_k) + \nabla \cdot (\alpha_k \rho_k \bar{u}_k \bar{u}_k) =$ $-\alpha_k \nabla P + \nabla \cdot \bar{\tau}_k + \sum_{k=1}^2 (R_{ls} + \dot{m}_{ls} +$ $\bar{u}_{ls}) + \vec{F}_k$	
Interphase momentum exchange	$R_{ls} = K_{ls}(\bar{u}_l - \bar{u}_s)$	Kls: Gisdaspaw law [23]
Turbulence Model	Realizable k-ε model	

### **2.3.2.3. Result and discussion**

In this study, we made a model for the design of the reactor and proceeded to the point where we simply looked at the tendency to differentiate the flow and solid suspension according to impeller speed and  $D / T$ . Since we wanted to cover more details in Section 4.2, we will look at some cases of how the velocity vector field, the solid volume fraction, and the solid volume fraction of the continuous phase in the reactor change with reactor height.

Figure 2-14 shows velocity vector field according to impeller speed. Obviously, as the impeller speed increases, a stronger vector field appears. It can be seen that a circulation loop is formed between the impeller layer, and a sufficient circulation loop is formed at 60 rpm. The top view shows that the impellers of the three stages are rotating at the same speed so that the speed difference does not seem to be so great. The analysis of this vector field is directly related to the solid suspension ability in Figure 2-15. At 30 rpm, we found that there was insufficient vector field, which resulted in the solid particles not being able to spread throughout the reactor but sinking below. At 60 rpm, we can see that solid particles are spread well enough to be considered as well suspension. However, it was confirmed that when the  $D / T$  decreased to 0.33, the suspension ability was lowered. Particularly, it is confirmed that solid particles are pushed toward the outer wall of the reactor, and then the static

force is lowered. However, since the length and the effective area of the impeller are reduced, low energy is used, and trade-off relationship is formed.

Figure 2-16 shows a little more clearly, depending on the height of the reactor, the solid volume fraction is obviously more evenly distributed as the impeller velocity increases. In this Eulerian multiphase model, it is expected that various analyzes can be made because it is easy to see how the solid particles change in response to other reactor geometry changes or operating conditions changes.

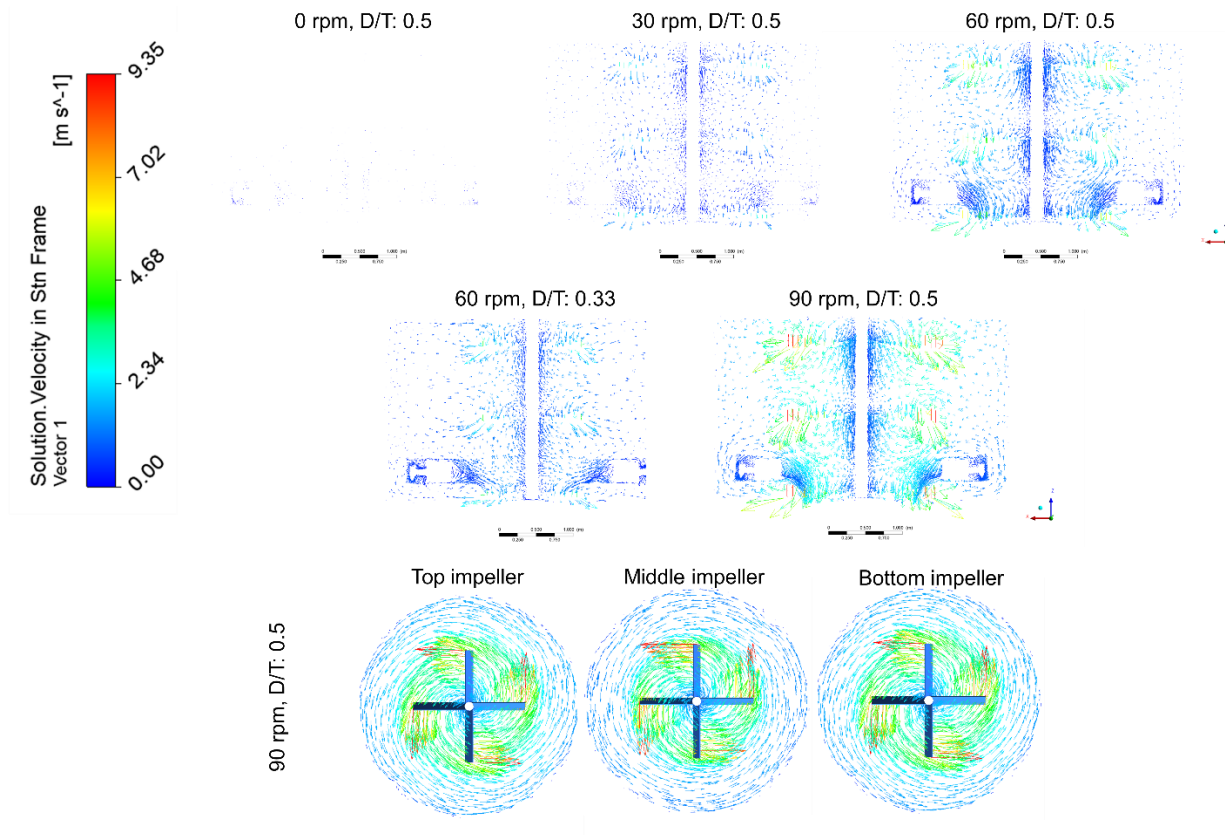


**Figure 2-14.** Velocity vector field of each case.

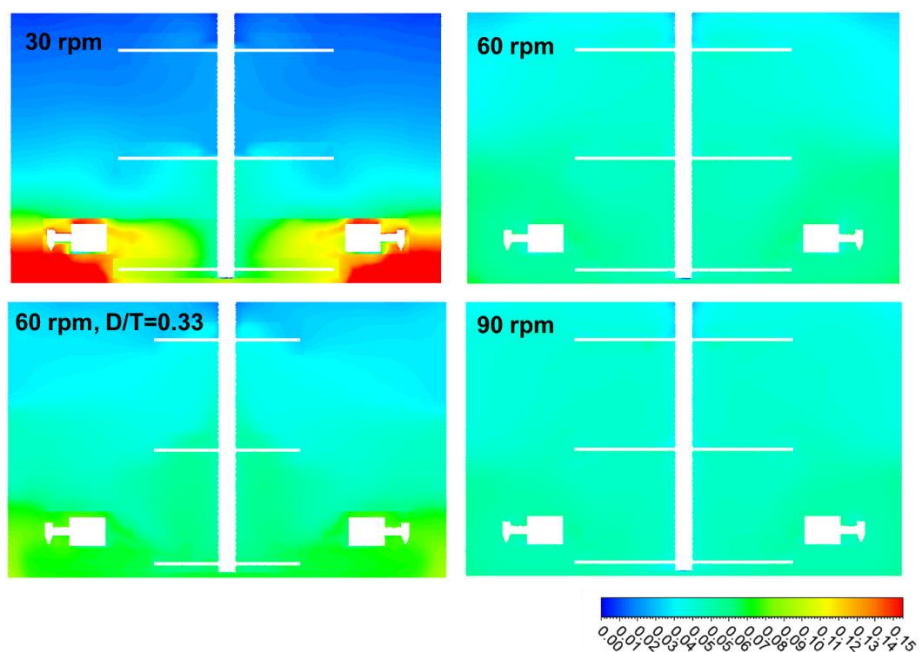


**Figure 2-15.** Solid phase volume fraction for different impeller speed.

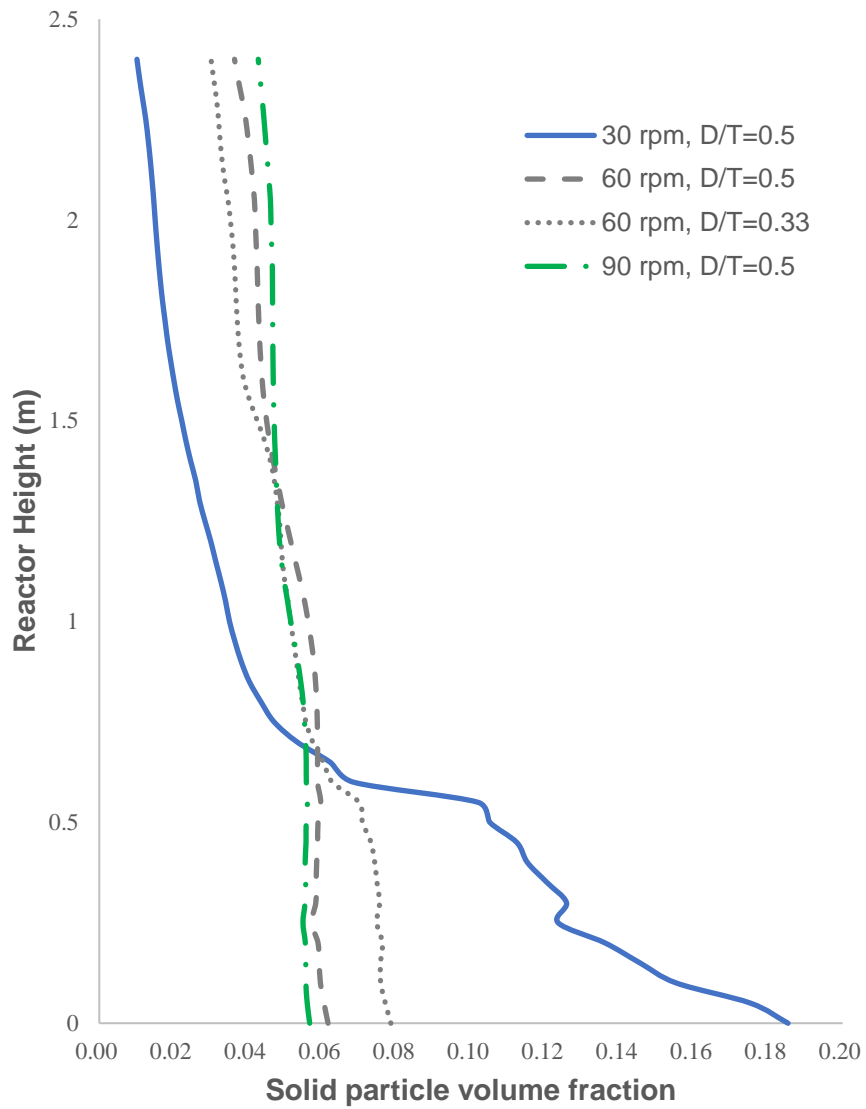


**Figure 2-16.** Solid particle volume fraction plot through reactor height.

## **2.4. CFD-Process integrated platform for simultaneous process and reactor design**

### **2.4.1. Introduction**

In this section, CFD based Fischer-Tropsch multitubular reactor model is integrated with process simulator, especially Aspen Plus, reactor model for implanting the rigorous reactor model to the process simulator and analyzing the reactor performance efficiently. In process systems engineering, there are several steps for designing overall process. Especially, conceptual design step should be performed primarily because it is easy to solve overall design problem when its complexity decreases by dividing the overall problem into sequential sub-problems. However, in detailed design step which is roughly next step of conceptual design, there are no opportunities to change the conceptual design of process and this limitation can block some combinations of process design and detailed design. In this study, we integrated process simulator used for conceptual designing and computation fluid dynamics used for detailed designing simultaneously and applied to multitubular packed bed Fischer-Tropsch Reactor. Several studies tried to develop this kind of reactor or unit modeling such as AML:FBCR with fluent for gPROMS.

### **2.4.2. Model formulation**

In this integrated platform between CFD section and process systems section, ANSYS FLUENT and Aspen Plus that are acknowledged software are used. In CFD section, exact fluid dynamic simulation and rigorous physics phenomena such as multiphase, mass transfer in complex geometry field, non-ideal mixing effect, etc. can be performed effectively which is impossible in process simulator. Moreover, 3D graphics analysis and unit geometry considering can help us to analyze the unit performance more explicitly. Process systems, however, also have advantages targeted at analyzing process systems. Simple 1-d reaction model and thermodynamic calculation with experimental data from NIST and DIPPR help the user to understand and solve the chemical equilibria exactly. Furthermore, systematic approach to overall process systems is possible, unlike CFD section. Hence, these advantages of each section are integrated into the proposed integrated platform which is shown in Figure 2-17.

CFD simulation transfers the information of detailed geometry, fluid dynamics, heat transfer, velocity vector field to the process simulator for considering various parameters. Then, process simulator can calculate the exact value of essential parameters such as heat transfer coefficient as function profile. With exact calculated multi-dimension parameters, process simulator can calculate the rigorous kinetics with its commercial reactor model for obtaining heat of reaction and material properties. These values are transferred to the CFD



simulator to calculate heat transfer and viscosity calculation once again and iterate this calculation until simulation is converged. Therefore, reaction, unit geometry, turbulence effect, non-ideal mixing, and the other physical phenomena are perfectly considered in detailed designing of reaction and systems design simultaneously.

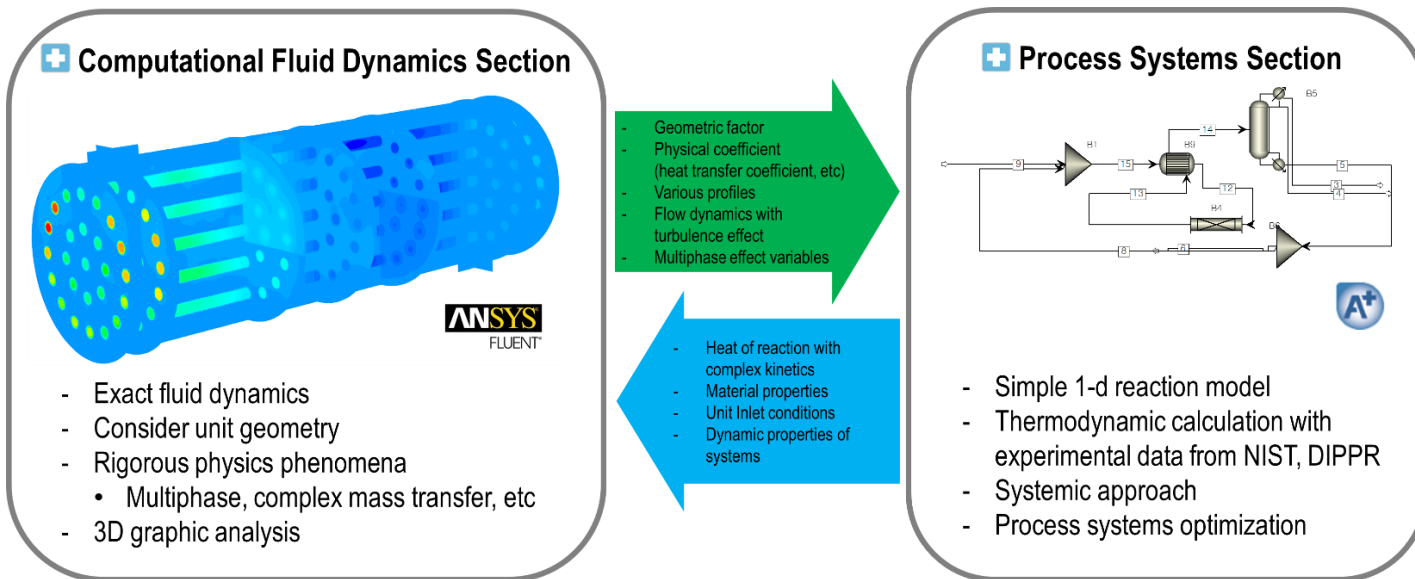


**Figure 2-17.** Diagram of CFD-Process systems integration platform.

In this study, we implant this methodology into the FT multitubular fixed bed reactor shown in Figure 2-18. The reactor has a total of 25 single channel reactor tubes. The coolant enters the shell side as water and conducts heat exchange with the reaction channel through two baffles. The kinetics used in the reaction are the same as in Table 2-1. The calculation process is as follows. First, estimate the heat of reaction curve using the 1-d reactor model in Aspen Plus. The calculated heat of reaction curve is treated with the source term in Fluent's reactor tube to generate heat and the heat exchange capacity is tested through fluid flow. Once the calculations converge to the steady state, the heat transfer coefficient and wall temperature of each tube are extracted and brought to Aspen Plus. In Aspen Plus, the modified heat transfer coefficient and wall temperature values for each tube are entered as profiles, and the heat of reaction is calculated differently for each tube. The source of the heat of reaction curve, which is different from the initial guess, is simulated by Fluent CFD simulation and the process is repeated to the satisfaction level. Detail algorithm is shown in Figure 2-19.

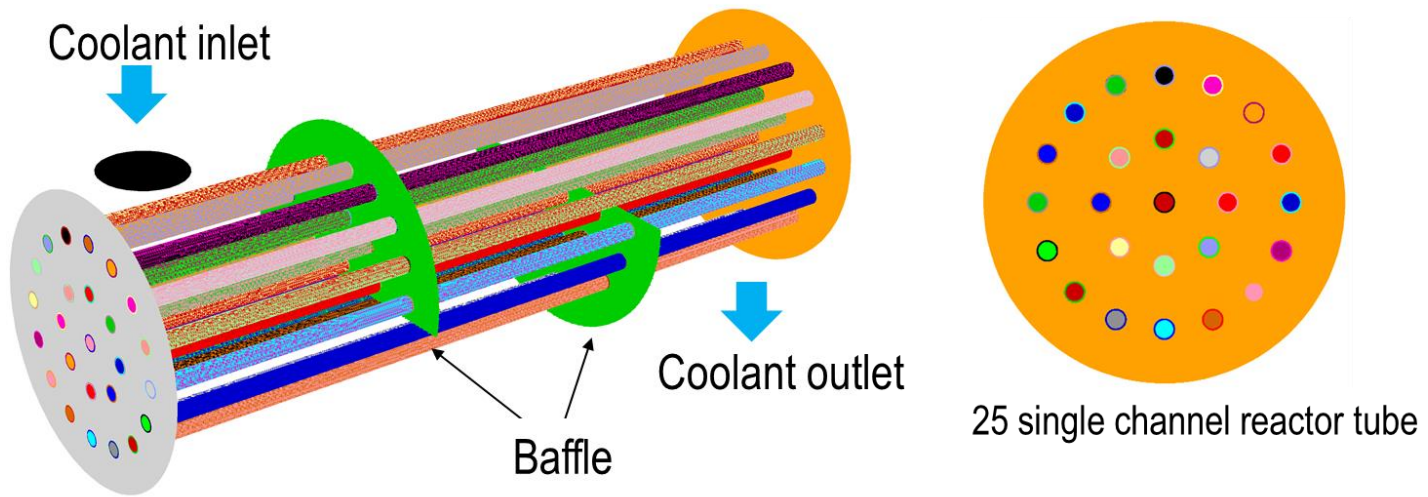


**Figure 2-18.** Geometry of FT multitubular fixed bed reactor.

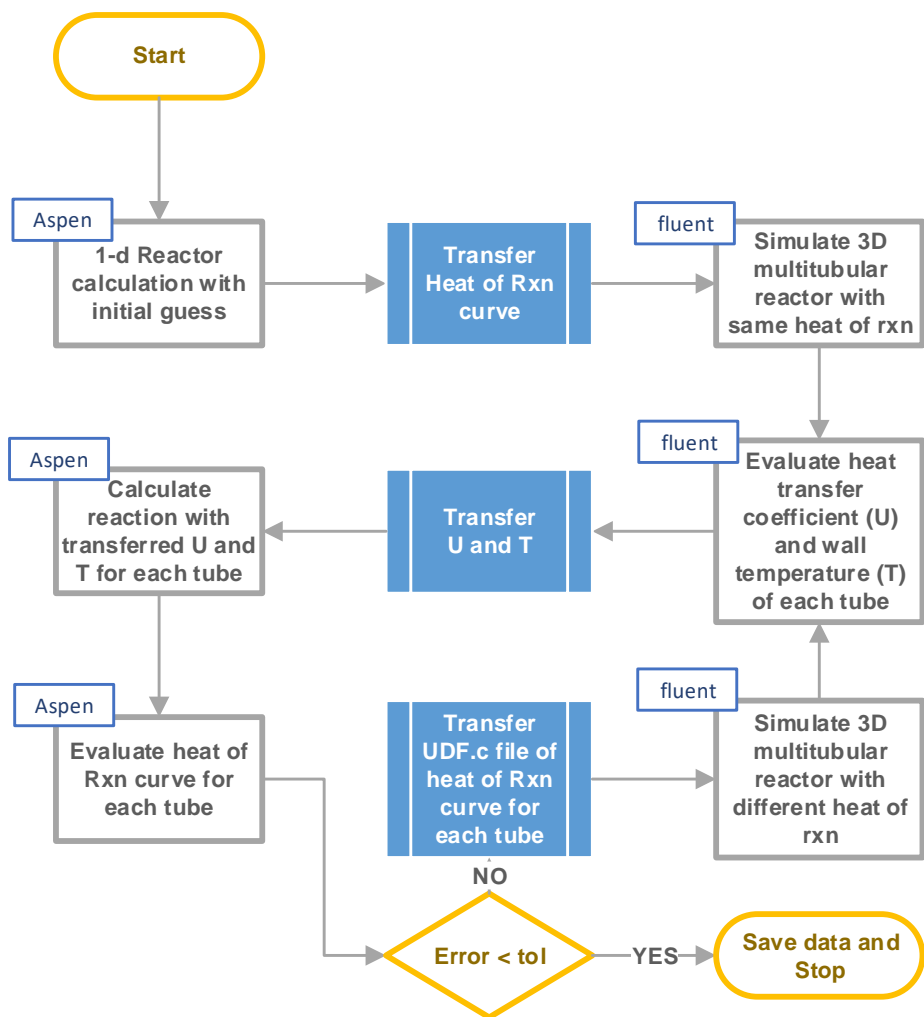


**Figure 2-19.** CFD-Process systems integration algorithm.

### **2.4.3. Result and discussion**

In the conventional model, even if it is multitubular, the heat exchange capacity of each tube cannot be simulated depending on the flow of the shell side fluid or the shape of the reactor. However, the proposed model showed that this is possible.

The coolant velocity profile clearly shows that the flux is higher at the inlet and outlet, which are small in area, and that it is the same in the region where the flow path is narrowed due to the baffle. In case of the rear side of the first baffle, the cooling effect is negligible because there is almost no movement of the fluid at the rear part. In the second baffle, it seems that the outlet is on the side, thus cooling effect exists (Figure 2-20). The front view shows the tendency to vary the convective heat transfer depending on the location of the tube. In case of the tube which is in charge of the coolant inlet, it seems that it is cooled well by obtaining a sufficient coolant flow rate, whereas in the side tube, the coolant is not sufficiently distributed and the flow rate is slow.

This effect can be more clearly seen in the temperature profile. Since the FT reaction is a highly exothermic reaction, it can be seen that there is a considerably high heat generation in the front reactor through the side view and a rise in temperature. It can be seen that the temperature goes higher toward the lower tube, which is more distant from the inlet part. It is thought that this phenomenon occurs because the coolant cannot go down to the bottom and is

passed after the baffle. As you can see from the front view, it can be distinguished. As shown in the front coolant velocity profile, the side tube is not sufficiently cooled, and the reactor temperature is rapidly increased.

In Figure 2-21, wall function heat transfer coefficient of each reaction tube is plotted through reactor length. At first, the wall function heat transfer coefficient of all reaction tubes was given the same as the initial guess heat transfer coefficient. This value does not affect the reactor length, and in fact, it does not have to be arbitrarily determined since it may be some time to design the reactor at first. However, the proposed model can be used to estimate the exact wall function heat transfer coefficient through reactor length. In addition, a revolutionary design methodology has developed because it obtains the reaction kinetics by Aspen Plus and the precise degree of change of reactants by separately calculating the wall function heat transfer coefficient according to the geometry of the tube.

As a result, the proposed integrated platform can be used for process design by analyzing the entire process systems including CFD 3D reactor analysis and reaction kinetics of process simulator.

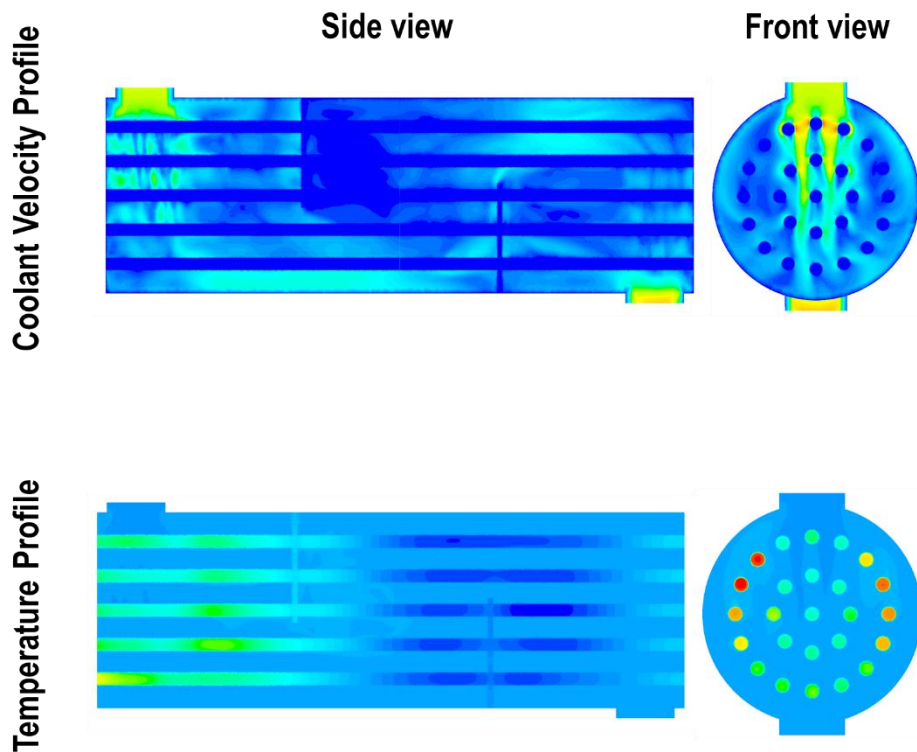


**Figure 2-20.** Coolant velocity profile and temperature profile of the multitubular reactor; side and front view.



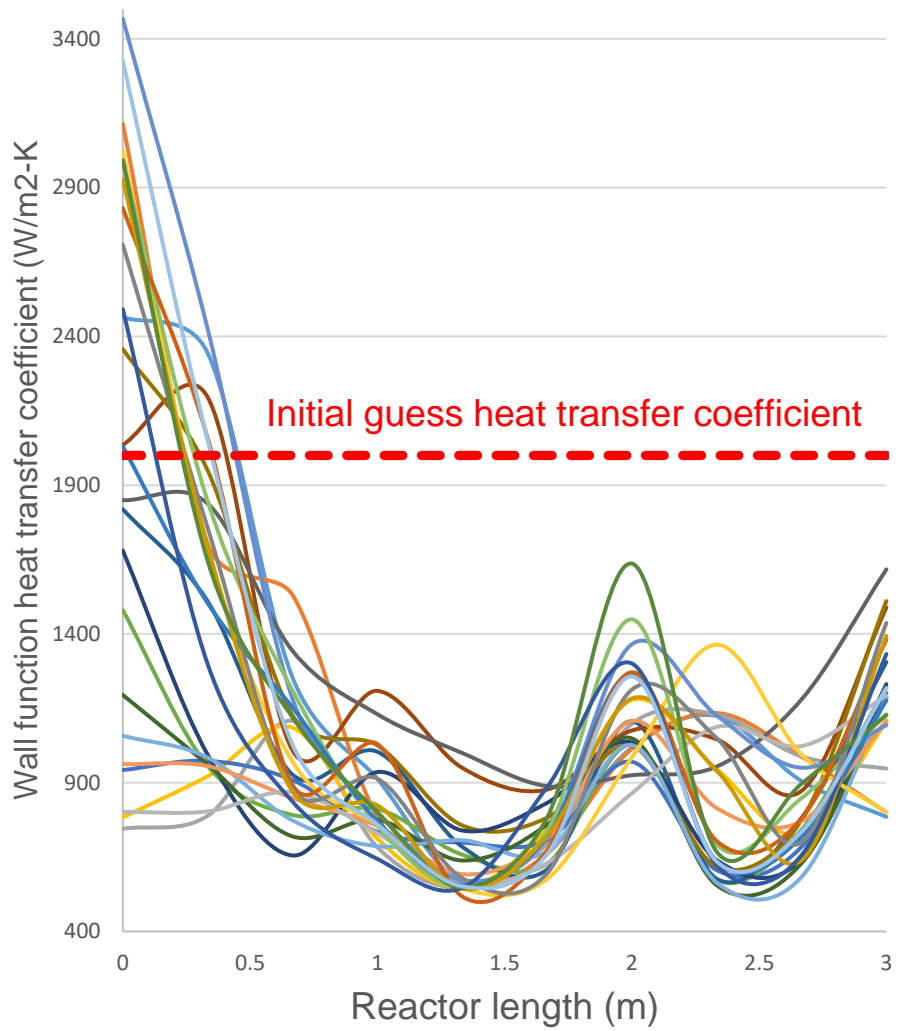


**Figure 2-21.** Wall function heat transfer coefficient for each reaction tube at final converged state.

#### **2.4.4. Conclusion**

In this study, we developed an integration platform that can be used in a design by connecting the chemical reaction formulas calculated in CFD reactor model and process simulator. This enables simultaneous execution of basic design methodologies that sequential process of conceptual process design and detailed unit design. Therefore, it is possible to study the results that can be changed in the detailed design at the conceptual design stage and to find the optimum point at the same time.

## CHAPTER 3. Optimization for the Unit, Process, and Plant-wide Systems

### 3.1. Introduction

What we would like to achieve ultimately on various simulation platforms obtained through advanced modeling as described in CHAPTER 2 is the optimal solution for unit, process, and plant systems. In CHAPTER 3, mathematical programming, derivative-free optimization algorithm, and deep learning, which are used in modern computational science, are combined with CFD and process simulator to propose an optimization strategy for a specific purpose. In particular, by proposing an optimization platform that gradually expands the range of reactor systems, process systems, and plant systems, introduce the optimization methodology for specific applications.

Section 3.2 proposes an optimization methodology on the reactor scale level. For CFD-modeled reactor models, multi-objective optimization was performed to optimize both maximum productivity and minimum  $\Delta T_{\max}$  simultaneously. The contribution of this research is the development of an algorithm that can effectively perform multi-objective optimization for a costly function called CFD and derive the concept of optimum packing division zone.

Section 3.3 discusses optimization methodologies at the level of process systems. Section 3.3.1 discusses the modified Dividing hyper-Rectangle (DIRECT) algorithm, which enables global optimization while effectively

handling hidden constraints that are seriously considered in the generic process simulator. Section 3.3.2 proposes the HENS methodology to analyze how many heat exchangers present in this sustainable process are most economical to construct in any combination of networks. We develop multiple utilities based simultaneous HENS using sub-stage in sustainable process which is multiple utilities system from the various refrigerant to heat source.

Finally, in Section 3.4, we have developed a technology to help safety analysis in a plant-wide system by using data reduction using variational autoencoder with deep convolutional layers. Then, we are developing a real-time leak alarm system by replacing the gas leak simulation of a complex and huge scale plant with a deep neural network based non-linear surrogate model that can perform the real-time calculation.

## **3.2. Reactor systems scale optimization**

### **3.2.1. Multi-objective optimization of microchannel reactor for Fischer-Tropsch synthesis using computational fluid dynamics and genetic algorithm**

Optimization of microchannel reactor is a challenging problem because non-convex functions including differential equations are involved in the model. Typically, derivatives of these equations are very expensive to compute or often impossible to obtain [63]. Thus, derivative-free methods are considered attractive options for problems when numbers of non-convex functions are included in the model. One way to deal with such a complex problem is problem decomposition. In the decomposition method, the original problems are decomposed into the simulation and optimization parts, and the simulation part is externally calculated using a simulator. The optimization is usually carried out using a stochastic solver due to the fact that stochastic solvers are based on function evaluations. Leboireiro and Acevedo [64] used a genetic algorithm with the decomposition approach for optimizing distillation column sequencing. Javaloyes-Antón et al. [65] used a particle swarm algorithm interfaced with Aspen Hysys to optimize a rigorous tray-by-tray distillation column model. Recently, Lee et al. [66] decomposed the MINLP problem to optimize a superstructure for a rigorous rate-based reactive distillation model for capturing CO<sub>2</sub> from flue gas. Alternatively, a surrogate model has also been used for

optimizing microchannel reactors. For instance, Jung et al. [29] used a surrogate model constructed based on an artificial neural network to optimize the guiding channel geometry in a U-Type coolant layer manifold for a large-scale microchannel FT reactor. They used the commercial CFD software ANSYS CFX to generate the flow field data required to construct the surrogate model and used the MATLAB fmincon solver, which is based on sequential quadrating programming, for optimizing the surrogate model.

In this work, a CFD model of a single microchannel reactor for FT synthesis is first built using the commercial CFD software ANSYS FLUENT and the simulation results are validated with experimental data from the literature. Then, we employed the concept of discrete dilution zones in our catalyst-filled microchannel FT reactor and performed a multi-objective optimization study using an  $\epsilon$ -constraint method and genetic algorithm to determine optimal dilution ratios and zone length that maximize  $C_{5+}$  productivity and minimize  $\Delta T_{\max}$  simultaneously.

### 3.2.1.1. Modeling and optimization

The Fischer-Tropsch microchannel reactor design optimization problem can be formulated as a multi-objective MINLP (Equation [3-1]):

$$\begin{aligned} & \min (f_1(\mathbf{x}, \mathbf{y}), f_2(\mathbf{x}, \mathbf{y})) \\ & \text{subject to} \quad g_i(\mathbf{x}, \mathbf{y}) \leq 0, \quad i = 1, 2, 3, \dots, p \\ & \quad h_j(\mathbf{x}, \mathbf{y}) = 0, \quad j = 1, 2, 3, \dots, q \\ & \quad \mathbf{x} \in \mathbf{X} \subset \mathbf{R}^n, \quad \mathbf{y} \in \mathbf{N}^n \end{aligned} \quad [3-1]$$

where  $\mathbf{x}$  and  $\mathbf{y}$  are vectors consisting of  $n$  continuous and integer variables. Continuous variables represent the dilution ratio, and integer variables represent the packing length. In order to avoid technical difficulty with packing the catalyst in different and continuous volume sizes, we assume the packing length has integer values. We discretized the reactor length into 10 zones of equal length allowing us to set the length variable as an integer variable.  $f(\mathbf{x}, \mathbf{y})$ ,  $g(\mathbf{x}, \mathbf{y})$ , and  $h(\mathbf{x}, \mathbf{y})$  represent the objective function, inequality, and equality constraints, respectively. The FT microchannel reactor design involves a large number of equality constraints with differential terms that are used to describe reaction kinetics, heat, and mass and momentum balance equations resulting in a challenging MINLP problem. The resulting MINLP, thus, finds it difficult to find a feasible solution using a deterministic optimization solver because obtaining the gradient is computationally very expensive and it is often impossible to find one.

Herein, we decompose the original MINLP. The decomposition divides the original MINLP problem into sets of sub-problems and explicitly calculates the subsets of constraints. Consequently, the optimization is carried out in the reduced search space. The equality constraints,  $h(x, y)$ , are decomposed as  $h_s(x, y)$  and  $h_o(x, y)$ .  $h_s(x, y)$  includes equations related to reactor design and  $h_o(x, y)$  includes those of optimization. With the decomposition, the MINLP model can be reformulated as Equation [3-2]

$$\begin{aligned}
 & \min f_1(x, y) \\
 & f_2(x, y) \leq \varepsilon \\
 & h_o(x, y) = 0 \\
 & g_i(x, y) \leq 0 \\
 & x \in M, y \in M \\
 & \text{with } M = \{(x, y): h_s(x, y) = 0 \quad \text{for some } x \in X \subset \mathbb{R}^n, y \in \mathbb{N}^n\}
 \end{aligned} \tag{3-2}$$

For considering  $f_1$  ( $C_{5+}$  productivity) and  $f_2$  ( $\Delta T_{\max}$ ) simultaneously, an  $\varepsilon$ -constraint method introduced by Haimes et al. [67] can be applied for  $f_2$  where  $C_{5+}$  represents FT hydrocarbon products with 5 or more carbons and  $\Delta T_{\max}$  is the difference between the inlet temperature and peak temperature inside the reaction channel. If an objective function  $f_1$  and a user-defined  $\Delta T_{\max}$ -controlled scalar  $\varepsilon$  exist in dimension  $M$  such that  $x^*$  and  $y^*$  are optimal solutions to the problem (2), then  $x^*$  and  $y^*$  are weak Pareto optimum points as per the general result of Miettinen [68]. This method has an advantage when the number of objectives is two, and the shape of the Pareto optimal curve is non-convex [69]. The MINLP problem is solved using a stochastic solver



integrated with the CFD model. Stochastic solvers are powerful tools for finding the optimal solution when integrated with an external simulation tool as they do not require a priori mathematical information or gradients of functions.

### 3.2.1.2. MINLP formulation using stochastic solver

The MINLP optimization is carried out using a genetic algorithm (GA) [70]. The objective function of the original problem is defined using Equation [3-3].

$$\max C_{5+} \text{productivity}(l_i, x_i) + P * (\text{abs}(\Delta T_{\max}(l_i, x_i) - \varepsilon) - (\Delta T_{\max}(l_i, x_i) - \varepsilon)) \quad [3-3]$$

Herein, the  $C_{5+}$  productivity is maximized, and  $\Delta T_{\max}$  is minimized.  $\Delta T_{\max}$  is bounded by the  $\varepsilon$ -constraint in Equation [3-4]. For obtaining the Pareto optimal curve, we find the maximum value of  $C_{5+}$  productivity with different  $\varepsilon$  values.

$$\Delta T_{\max} \leq \varepsilon \quad [3-4]$$

The  $\varepsilon$ -constraint is the hidden constraint in this problem whose feasibility cannot be realized before calculating the CFD sub-problem. Therefore, we deactivate the point that does not adjust to the  $\varepsilon$ -constraint, using scalarization of  $\Delta T_{\max}$  with a large penalty factor  $P$ . However, this method is not the weighted-sum or scalarization technique as the difference between  $\Delta T_{\max}$  and  $\varepsilon$  does not affect the objective function.

In Figure 3-1, the FT single-channel reactor length was divided into 10 zones of 50 mm each, where each zone can have different catalyst dilution ratios. Hence, during optimization, the packing length ( $l_i$ ) and dilution ratio ( $x_i$ ) are set as design variables while operating conditions such as the gas hourly space

velocity (GHSV) of syngas and inlet temperature were fixed. Index  $n$  is the number of catalyst packing zones.

$l_i$  is the integer variable that tells how to divide the 10 zones of the reactor into  $n$  packing zones. To illustrate, if  $n$  is 2,  $l_1$  is 3, and  $l_2$  is 7, then the catalyst packing zone will be divided into 2 zones of 3 unit zone length and 7 unit zone length, that is 150 mm and 350 mm. Accordingly, the equality constraint that expresses the sum of  $l_i$  should equal 10 as given in Equation [3-5]. The stochastic solver generates the combinations of  $l_i$  randomly within the variable bounds defined by Equation [3-6].

$$\sum_{i=1}^n l_i = 10 \quad [3-5]$$

$$1 \leq l_i \leq 10 \quad [3-6]$$

Because the FT reaction is fast and highly exothermic, the temperature in the immediate region of the reactor inlet, front zone in this case, tends to go undesirably high. Therefore, it is necessary to strategically apply different dilution ratios over the entire catalyst packing zone; for instance, higher dilution ratios in the front zones and lower dilution ratios in the rear zones. This way, the reaction rate in the front zones, especially in the region of the reactor inlet, can be allowed to limit to a desirable level while still allowing a desirable level of catalyst activity in the middle and rear zones of the reactor. By limiting the reaction rates to the desired level and hence the heat generation rate in the front zones,  $\Delta T_{\max}$  along the channel length can be minimized. The dilution ratio

inequality constraint is given by Equation [3-7] with variable bounds of dilution ratios 0 (all catalyst) to 1 (all diluent) [3-8].

$$x_i \leq x_{i-1} \quad [3-7]$$

$$0 \leq x_i \leq 1 \quad [3-8]$$

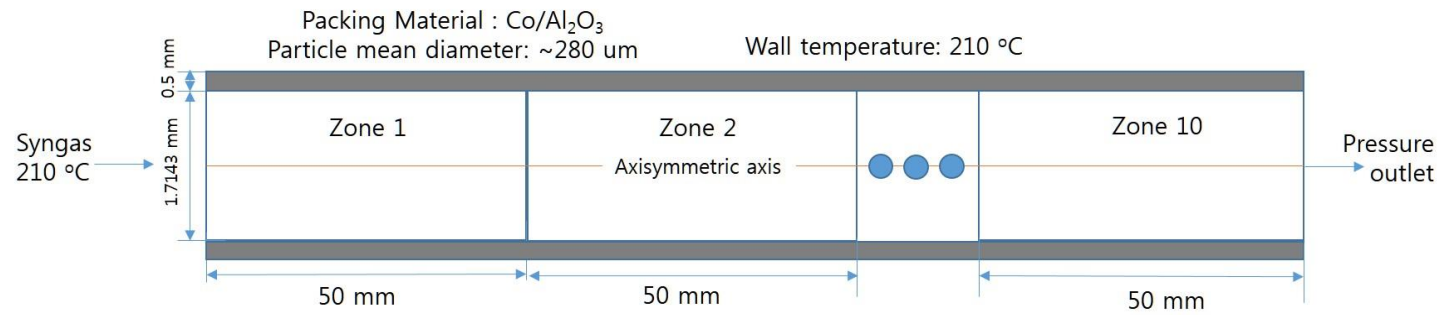


**Figure 3-1.** Superstructure of 500 mm FTS single microchannel reactor for dividing catalyst packing zone optimization.

We built an integrated interface between MATLAB and the commercial CFD software FLUENT, called the GA-CFD optimizer. In this study, the CFD reactor model has inputs of  $d_i$  and  $x_i$ , and outputs of  $\Delta T_{\max}$  and  $C_{5+}$  productivity. The GA algorithm in MATLAB calls FLUENT using ActiveX server communication. With this connection, the input variables of FLUENT can be received from MATLAB, and the output of FLUENT can be sent back to MATLAB, as shown in Figure 3-2. Initially, the input parameters and reaction kinetics data are set, and the CFD reactor model runs with those settings. After that, the GA algorithm generates a population within variable bounds. Each individual in the population is sent to FLUENT through the ActiveX server. Once the output of FLUENT is received in MATLAB, the objective function value is calculated and checked for termination criteria. The maximum population size and six consecutive stall generations are used for the termination criteria. If the termination criteria are not satisfied, a new population is generated through three characteristic steps: selection, mutation, and recombination. The GA solver does not provide a guarantee of optimality. In fact, the convergence rates are different between integer variables and continuous variables. Thus the global solution of a MINLP problem can seldom be found from a stochastic solver. Several studies indicate that stochastic solvers do not allow continuous variables to converge while discrete variables correspond to a global optimum solution [71-73].

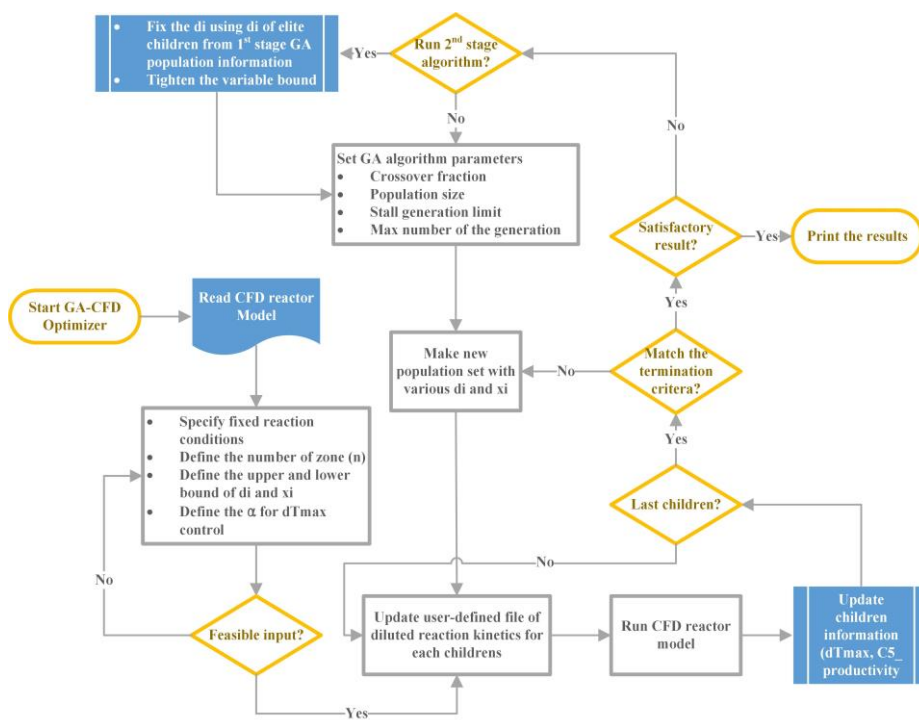


**Figure 3-2.** Block diagram of GA-CFD optimizer algorithm.

Herein, we optimized the MINLP problem in two stages. Several studies used multi-stage optimization of MINLP, either to reduce the complexity or to improve convergence [74-76]. In the first stage optimization, the MINLP problem is solved multiple times with different crossover fractions (0.4, 0.6, and 0.8) until the integer variables have the same solution for all values of the crossover fraction. If the values of integer variables are different in each run, the population size of the problem is increased, and the calculation is repeated. The original MINLP problem is reduced to NLP in the second stage using the integer variable solution found in the first stage. In the second stage GA-CFD, the reduced NLP has optimized once again with the GA. The 2<sup>nd</sup> stage optimization still does not guarantee the global optimum solution; an improved solution can be found in the 2<sup>nd</sup> stage optimization in many cases within a reasonable computation time. Herein, a maximum of 50 generations and  $20 \times n$  individuals for a population are used. Single point crossovers with crossover fractions of 0.4, 0.6, and 0.8, two elite populations, and Gaussian mutation are used in the GA solver. The tournament selection method is used to choose parents for the next generation. Note that we adopt the GA parameters from [77].

We compare the effectiveness of the GA-CFD optimizer with grid search when the number of zones is relatively small. If the number of zones is one and we divide the continuous variable with 0.1 scales, then the near optimum



solution can be calculated within 10 CFD executions. If the number of zones is 2, 3, or 4, the number of function evaluations increases to 405, 4320, and 17640, respectively. Considering that the average function evaluation time is about 1 minute, we did a grid search only for cases having one and two zones and compared the result with the GA-CFD optimizer.

### 3.2.1.3. Optimization result

In Figure 3-3, the results of a grid search, dividing  $x_i$  as 0.1 scales and considering all possible combinations of  $l_i$ , with 1 zone and 2 zones are compared with results from the 1<sup>st</sup> stage GA-CFD optimizer with 2 zones and 3 zones.  $\varepsilon$  was changed to different  $\Delta T_{\max}$  values such as 1, 1.5, 2, 3, and 5 for obtaining the Pareto optimal curve. The meaning of the curve is the correlation between  $\Delta T_{\max}$ , which represents the safety factor, and maximum  $C_{5+}$  productivity, which represents the efficiency of the reactor, at fixed  $\Delta T_{\max}$ . When  $n$  equals 2 and 3, all optimal points calculated by the GA-CFD optimizer through all the temperature ranges are advantageous compared to 1 zone catalyst packing. Optimization results indicate that the discrete dilution method allows distribution of the overall heat of the FT reaction in the most strategic manner to different catalyst packing zones. The 3 zones 1<sup>st</sup> stage GA-CFD optimizer gives the best solution except when  $\varepsilon = 1$ , compared to the solution from a 2 zone total grid search. Although the 2 zones 1<sup>st</sup> stage GA-CFD optimizer gives the same optimal solution as the total grid search in the high  $\Delta T_{\max}$  region, only sub-optimal solutions are obtained in the low  $\Delta T_{\max}$  region. The feasible searching area decreases at low  $\varepsilon$  because the  $\varepsilon$ -constraint tightens the boundary of the feasible searching area. In order to confirm the reproducibility of the GA-CFD results, Table 3-1 that shows multiple execution results of the optimization problem is included. Although a pseudo-random

initialization of the initial population is carried out, the best-found solutions are very close to different numbers of zones and  $\varepsilon$  constraints. Even though the reproducibility of the MINLP GA-CFD optimizer is appropriate to this optimization problem, it is true that the best-found solution cannot be guaranteed to be the optimal solution. Thus, 2<sup>nd</sup> stage NLP GA-CFD optimization is performed to increase the quality of the solution.

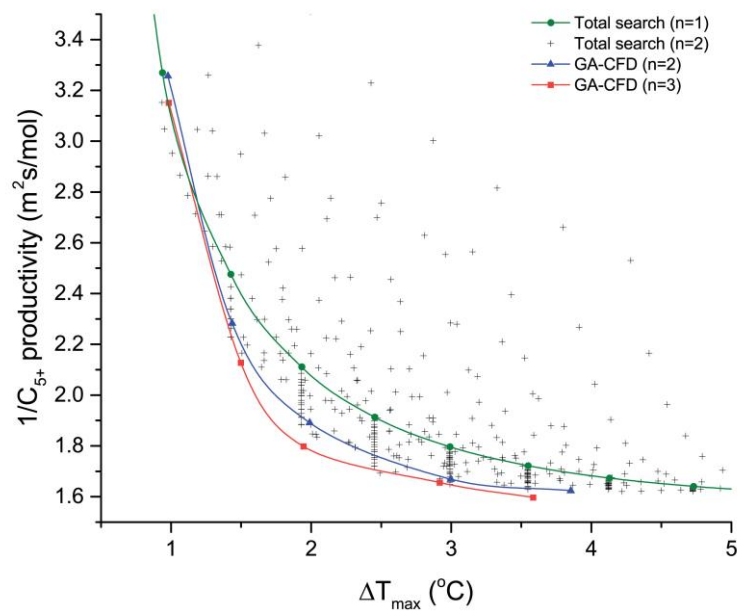


**Figure 3-3.** Pareto optimal curve between  $\Delta T_{\max}$  and  $1/C_{5+}$  productivity of total search and GA-CFD optimizer through  $n=1, 2$ , and  $3$ .

**Table 3-1.** Multiple execution results of the GA-CFD with various crossover fraction.

<b>Crossover fraction</b>	<b>2 zones</b>		<b>3 zones</b>		<b>4 zones</b>	
	$\Delta T_{\max}$ (°C)	$1/C_{5+}$ productivity (m <sup>2</sup> ·s·mol <sup>-1</sup> )	$\Delta T_{\max}$ (°C)	$1/C_{5+}$ productivity (m <sup>2</sup> ·s·mol <sup>-1</sup> )	$\Delta T_{\max}$ (°C)	$1/C_{5+}$ productivity (m <sup>2</sup> ·s·mol <sup>-1</sup> )
<b>0.4</b>	3.985	1.667	1.945	1.798	1.996	2.007
<b>0.6</b>	3.818	1.633	1.928	1.812	1.966	1.919
<b>0.8</b>	3.854	1.623	1.984	1.798	1.921	1.869

When the number of catalyst packing zones increases, the performance of the 1<sup>st</sup> stage GA-CFD optimizer decreases. Unlike 2 zone results, the 4 zone 1<sup>st</sup> stage GA-CFD optimizer gives high performance at low  $\Delta T_{\max}$  and low performance at high  $\Delta T_{\max}$ . To illustrate, 4 zone optimal points are better than 2 or 3 zones at low  $\Delta T_{\max}$  although this is not the case at high  $\Delta T_{\max}$ . A higher number of catalyst packing zones can describe the optimal solution more sensitively than a lower number of catalyst packing zones because with the former the searching area can be expanded. However, the 1<sup>st</sup> stage GA-CFD optimizer has low performance due to the handling method of integer variables and constraints in the GA algorithm. It makes  $n*20$  children in a population with a random combination of each  $l_i$  in its boundary condition without considering the summation constraint (11). For children whose  $l_i$  combination is infeasible, the optimizer gives a penalty value to the objective function and does not evaluate the CFD reactor model function. This algorithm helps the randomness of integer variable combinations but decreases the number of children in a population, and in some cases, it is too low to proceed with the optimization. At 4 zones and further, we observed that there are few feasible children in the population and the optimizer stops iterating at an early stage; the optimizer cannot find a good solution before stall generation. Simply changing the crossover fraction and stall generation were not enough to find a high-quality solution; so a 2<sup>nd</sup> stage GA-CFD was executed. Figure 3-4 shows the absolute advantage, indicated by Pareto optimal curve, of a 4 zone 2<sup>nd</sup> stage

GA-CFD optimization compared to a 3 zone 1<sup>st</sup> stage GA-CFD optimization, which the 4 zone 1<sup>st</sup> stage GA-CFD optimization failed to achieve. The number of function evaluations was 1930, about a 90 % reduction from that of the 4 zone grid search (17640). Information of the best found Pareto optimal curve calculated by the 4 zone 2<sup>nd</sup> stage GA-CFD optimization is given in Figure 3-5. Firstly, all temperature profiles through the position of the axial direction of the reactor are bounded under the temperature constraint successfully. Front sections of each zone show a sudden temperature rise because of the higher catalyst loading, and 4 discrete sections are shown. The reason why the temperature distribution at the high temperature constraint value is less uniform than the low temperature constraint value is that CO and H<sub>2</sub> are already reacted at the front of the reactor, and it is not enough to increase the temperature at the rear section of the reactor. Thus, it does not imply that the optimal solution is not efficient. Although the CO conversion at higher  $\varepsilon$  value is higher than at lower  $\varepsilon$  value because of the possibility of high temperature which accelerates the reaction rate, CH<sub>4</sub> selectivity is lower because methane selectivity increases when the reactor temperature is higher, decreasing the C<sub>5+</sub> productivity. However, the operator does not need to consider this value because each point of the Pareto-optimal curve is maximized for C<sub>5+</sub> productivity solution at that temperature constraint.

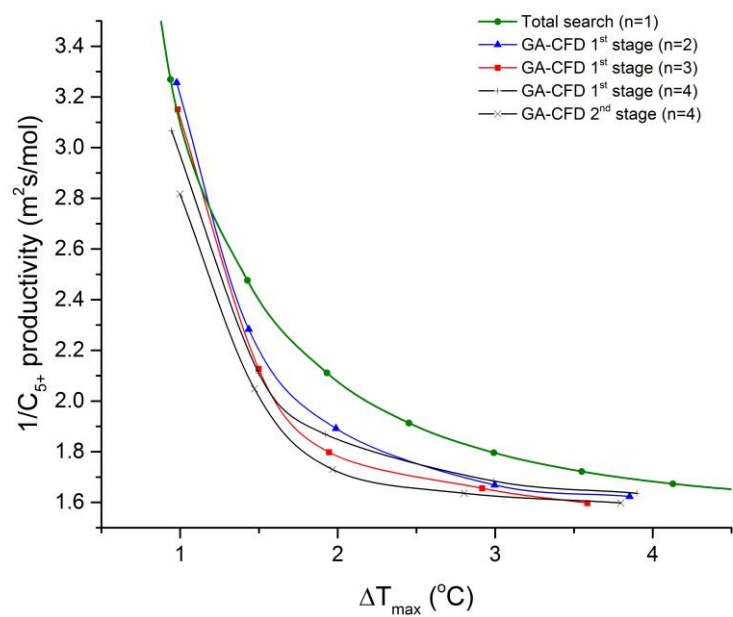


**Figure 3-4.** Comparing Pareto optimal curve with different  $n$  and between 1<sup>st</sup> stage and 2<sup>nd</sup> stages.



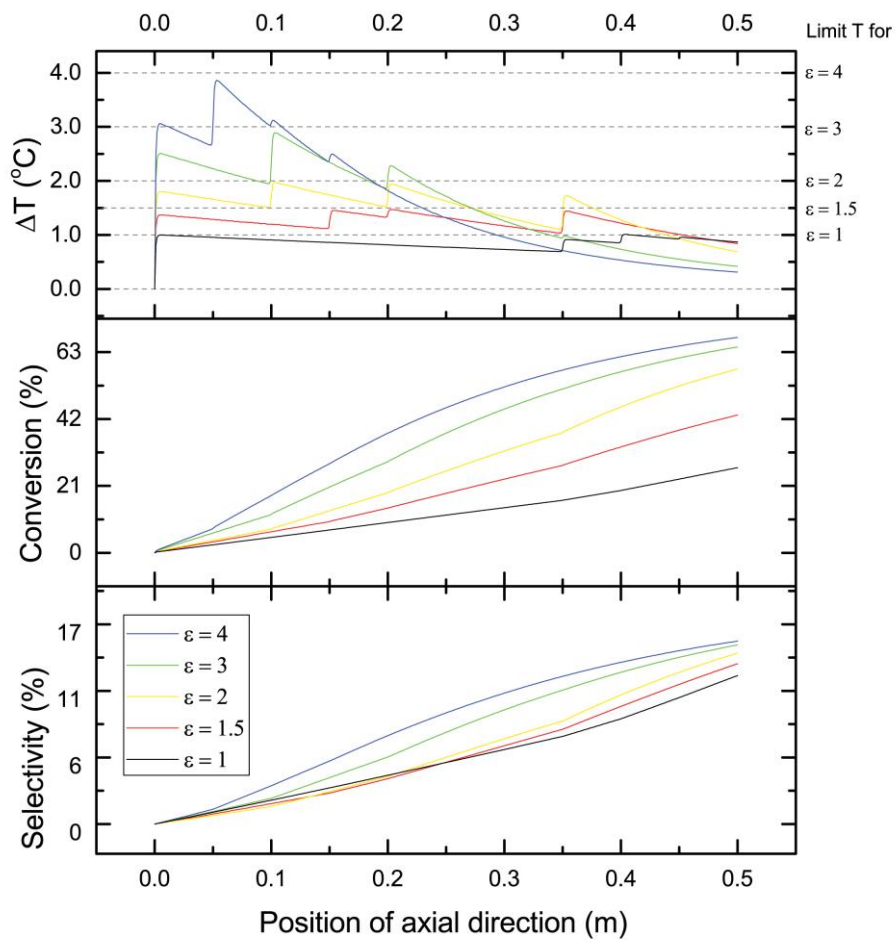


**Figure 3-5.** Profile of  $\Delta T$ , CO conversion, and  $\text{CH}_4$  selectivity of the best found Pareto optimal curve calculated by the 4 zone 2<sup>nd</sup> stage GA-CFD.

In order to clarify the effectiveness of the proposed GA-CFD method, the same objective functions were solved by other traditional non-convex constraint local optimization algorithms such as active-set, interior-point, and sequential quadratic programming (SQP). Integer variables were processed by the bound method. Each sub-optimal result with three different zones (2, 3, and 4) and five different temperature constraints as  $\varepsilon$ -constraints (1, 1.5, 2, 3, 4) is given in Figure 3-6. The GA-CFD optimizer gives a better solution than a local optimization algorithm. Especially, the result of the 2<sup>nd</sup> stage GA-CFD optimizer with 4 zones is always better than any of the other methods. Active-set, SQP, and SQP-legacy algorithms return sub-optimal solutions while the interior-point method cannot find optimal solutions in most trials. Although several local optimization solvers sometimes return a better solution than the 1<sup>st</sup> stage GA-CFD optimizer at the point where the  $\varepsilon$ -constraint equals 1, we strongly believe that the GA-CFD optimizer locates on the dominant position because the convergence rate of the local solver is too low to use generally and the GA-CFD optimizer is developed for derivative-free MINLP, which is not supported in traditional non-convex constraint local optimization algorithms.

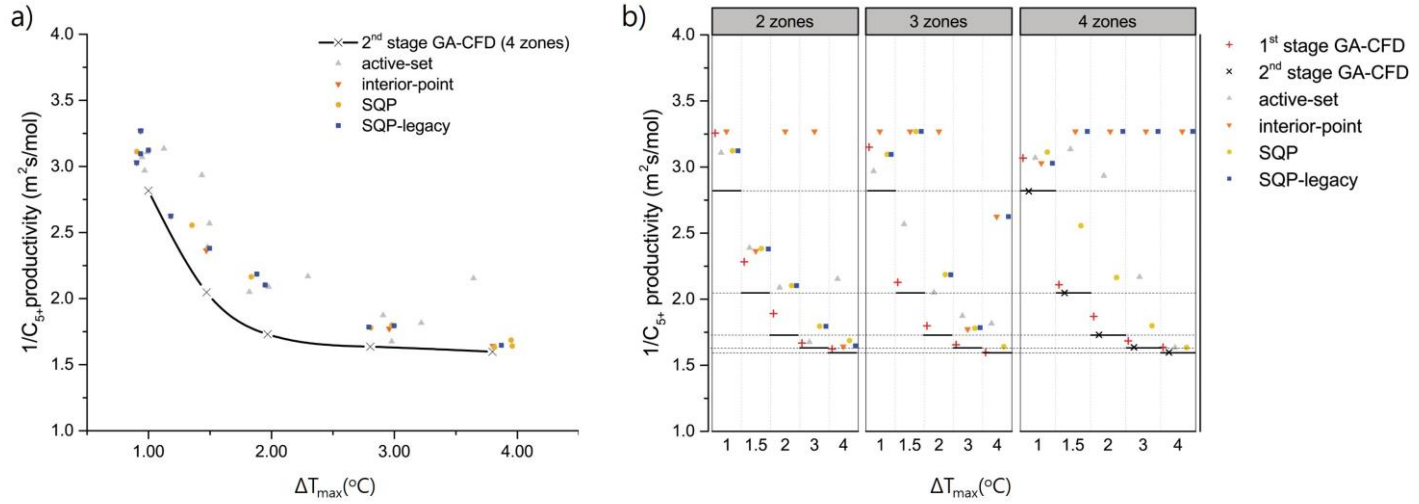


**Figure 3-6.** Comparison diagram of different zones and temperature constraint optimized by traditional non-convex constraint algorithm and proposed algorithm (GA-CFD) form of a) Pareto curve and b) group data chart.

The input parameters and the optimal solutions for several points are given in Table 3-2. The key factor in the decrease in computation cost of GA-CFD optimization is the decrease in the number of function evaluations of the CFD reactor sub-problem, as the CFD reactor sub-problem requires high computational time to solve. In the case of 1<sup>st</sup> stage GA-CFD optimization, the number of function evaluations in most cases was less than 1000 cycles. Although this value is larger than the 2 zone total grid search (405), it is much smaller than the 3 and 4 zone total grid searches (4320 and 17640, respectively).

**Table 3-2.** Result of several optimal points given by GA-CFD optimizer.

	1	2	3	4	5	6	7	8
<b>Objective function</b>								
1/C5+ productivity ( $\text{m}^2\cdot\text{s}\cdot\text{mol}^{-1}$ )	1.62	1.62	1.60	2.11	1.89	1.80	1.87	1.73
dTmax (K)	5.35	3.85	3.59	1.93	1.99	1.95	1.92	1.97
<b>Variables</b>								
$l_1$	10	1	1	10	4	6	2	2
$l_2$		9	2		6	1	2	2
$l_3$			7			3	3	3
$l_4$							3	3
$x_1$	0.000	0.366	0.723	0.600	0.595	0.604	0.724	0.674
$x_2$		0.123	0.367		0.419	0.256	0.667	0.487
$x_3$			0.103			0.052	0.48	0.364
$x_4$							0.157	0.001
$\varepsilon$		4	4		2	2	2	2
<b>n</b>	1	2	3	1	2	3	4	4
<b>Crossover fraction</b>		0.8	0.6		0.8	0.4	0.8	0.4
<b>CPU time (min)</b>		905	570		246	81	78	1428
<b>Number of generation</b>		50	50		24	16	19	30
<b>Function evaluation</b>		1400	686		275	88	94	1930
<b>Stopping criterion<sup>a</sup></b>	0	2	2	0	1	1	1	2
<b>GA-CFD stage</b>		1	1		1	1	1	2

<sup>a</sup> Stopping criterion 0: grid search does not need stopping criterion, 1: maximum stall generation has been reached (5),  
2: maximum number generation has been reached (50) for point 1-7 and (30) for point 8

Analyzing the points that are on the Pareto optimal curve, we realize that the difference in catalyst dilution ratio between the zones is not extreme. It means that a gradual change of dilution ratio is better than a sudden change because a sudden change cannot distribute the reaction rate effectively over the entire catalyst packed zones of the reactor. If the dilution ratios in the front zone are much lower than in the rear zones, most of the reaction occurs at the rear zones and the problem of hot spots appears again, this time at the rear zones. Furthermore, the method of dividing the catalyst packing zone has no advantage when  $\varepsilon$  is high because, at high  $\varepsilon$ , the decreasing effect for  $C_{5+}$  productivity is much larger than the decreasing effect for  $\Delta T_{\max}$ . Hence, this method is most appropriate when safety issues are critical or specific chemical components are highly sensitive to temperature change.

To discuss the difference between pre- and post-optimization performance, a summarized bar graph is shown in Figure 3-7.  $\Delta T_{\max}$  of the best solutions from GA-CFD and the local solvers are lower than the base case (which does not apply the catalyst zone division method) with similar  $C_{5+}$  productivity. GA-CFD can find a better solution than the local solver. Unlike  $\Delta T_{\max}$ , the best found  $1/C_{5+}$  productivity with a similar  $\Delta T_{\max}$  from the local solver does not decrease. The interior-point method cannot find a feasible solution for that search region. However, GA-CFD can decrease the objective function, and we can conclude that GA-CFD had a high advantage over other optimizers. For

analyzing the detail of the reactor interior, two sets of optimal points are selected. In Table 3-2, the first case compares  $\Delta T_{\max}$  among points 1-3 and 8, where  $1/C_{5+}$  productivity is similar ( $1.60\text{-}1.73 \text{ m}^2\cdot\text{s}\cdot\text{mol}^{-1}$ ) for different numbers of zones (1, 2, 3, and 4, respectively). The second case compares  $C_{5+}$  productivity among points 4-6 and 8, where  $\Delta T_{\max}$  is similar ( $1.93 - 1.99 \text{ }^{\circ}\text{C}$ ) for different numbers of the zone (1, 2, 3, and 4, respectively).

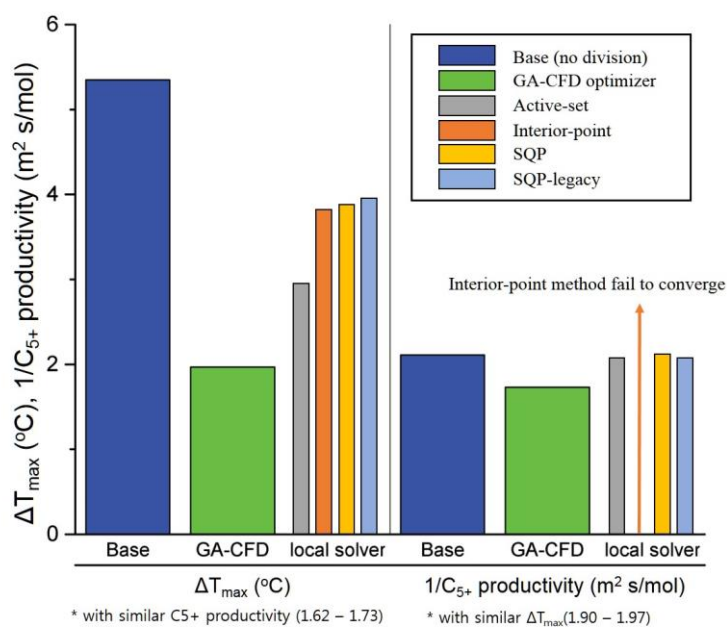


**Figure 3-7.** Summarized result graph of  $\Delta T_{\max}$  and  $C_{5+}$  productivity through single zone packing, GA-CFD, and various local solver.



In Figure 3-8, polar contour graphs of the reactor's  $\Delta T$  profile are given for case 1 where the angle direction is the reactor length, and the radial direction is the reactor radius. Optimal catalyst packing of the 4 zone type reactor results in a 63.2% decrease in  $\Delta T_{\max}$  compared to the optimal catalyst packing of the 1 zone type reactor, for similar  $1/C_{5+}$  productivity ( $1.60\text{-}1.73 \text{ m}^2\cdot\text{s}\cdot\text{mol}^{-1}$ ). In the front zones, reaction rates are lowered and the remaining reactants, thus, manage to react at rear zones under a higher dilution ratio. It is obvious that the Pareto optimal solution calculated by the 2<sup>nd</sup> stage GA-CFD result has an advantage over the sub-optimal points calculated by other methods such as the local solver and even the 1<sup>st</sup> stage GA-CFD by Figure 3-6. Moreover, Figure 3-8 visualizes a better temperature distribution of the Pareto optimal solution. Although the rear position temperature of the 2<sup>nd</sup> stage GA-CFD solution is higher than the other solutions, it reduces the front temperature from rising, which is the main problem of highly exothermic reactors such as the FT reactor. Since the heat of reaction and heat transfer to coolant channel together determine the reactor temperature, mere redistribution of the heat of reaction, using optimal catalyst packing, does not guarantee a good distribution of temperature. Thus, for the proposed GA-CFD optimizer which set the  $\varepsilon$ -constraint as  $\Delta T_{\max}$ , no heat of reaction is proper to optimize the reactor efficiency and safety simultaneously. Finally, we can find points that have similar or even higher  $C_{5+}$  productivity than the points with high averaged catalyst dilution ratio. To illustrate, comparing the point 2 ( $n=2$ ) in Table 3-2

which has the 0.147 averaged catalyst dilution ratio and  $1.66 \text{ m}^2 \cdot \text{s} \cdot \text{mol}^{-1} 1/\text{C}_{5+}$  productivity with the point ( $n=1$ ) which has the same dilution ratio, the  $1/\text{C}_{5+}$  productivity of the 1 zone point is higher ( $1.66 \text{ m}^2 \cdot \text{s} \cdot \text{mol}^{-1}$ ) than the 2 zones point. Therefore, it can be concluded that the temperature profile and component distribution affect the reaction kinetics simultaneously and not only the low dilution ratio, but the dilution zone combination together guarantee the efficiency of the reactor.

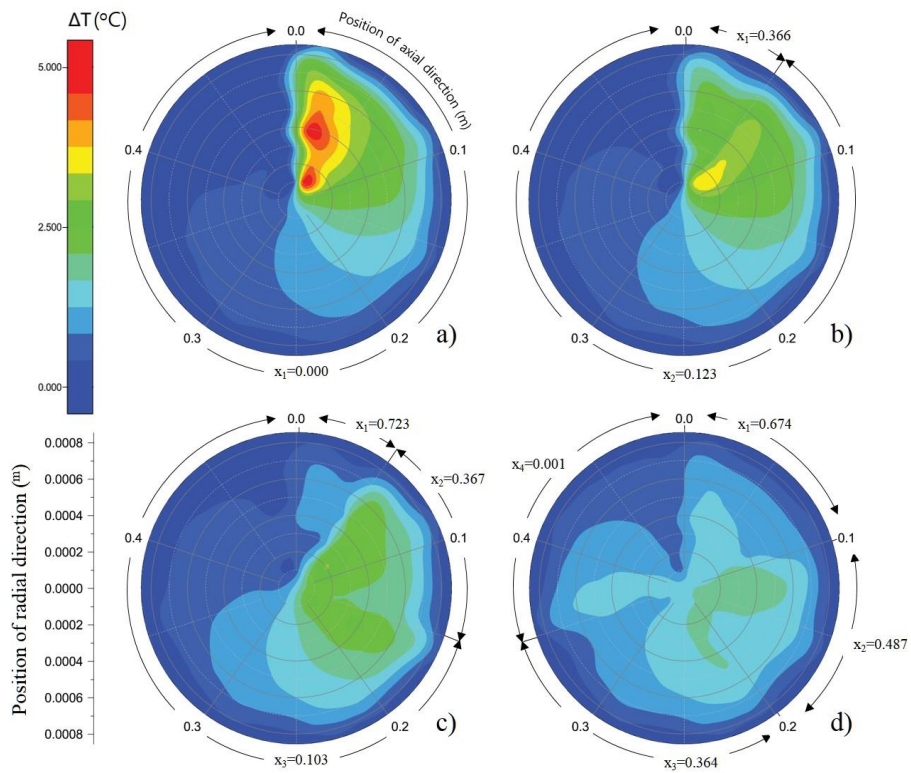


**Figure 3-8.** Polar contour graph of  $\Delta T$  profile under similar  $C_{5+}$  productivity of a) single zone catalyst full packing, b) two zone GA-CFD result, c) three zone GA-CFD result, d) four zone 2<sup>nd</sup> stage GA-CFD result.

\*radial direction is reactor width and angle direction is reaction length.

In Figure 3-9, although  $\Delta T_{\max}$  is similar, it is possible to get more  $C_{5+}$  by high CO conversion and reaction control using catalyst packing zone division. The  $C_{5+}$  productivity of the optimal solution reactor with 4 zones is 22 % higher than that of the 1 zone reactor. A strategy that decreases the reaction rate in the front zones for controlling  $\Delta T_{\max}$  and increases in the middle and rear zones for producing the  $C_{5+}$  at the reactor exit is shown on the Pareto optimal curve. In the case of the 2<sup>nd</sup> stage GA-CFD 4 zone, although the dilution ratio of the front-most zone is higher than the other cases, the dilution ratio of the middle and rear zones are lower for similar values of  $\Delta T_{\max}$  achieved. Finally, CO conversion of the 2<sup>nd</sup> stage GA-CFD 4 zone is 5.8 %, 17.1 %, and 40.7 % higher than the 3 zone, 2 zone, and 1 zone results, respectively for a similar  $\Delta T_{\max}$ .

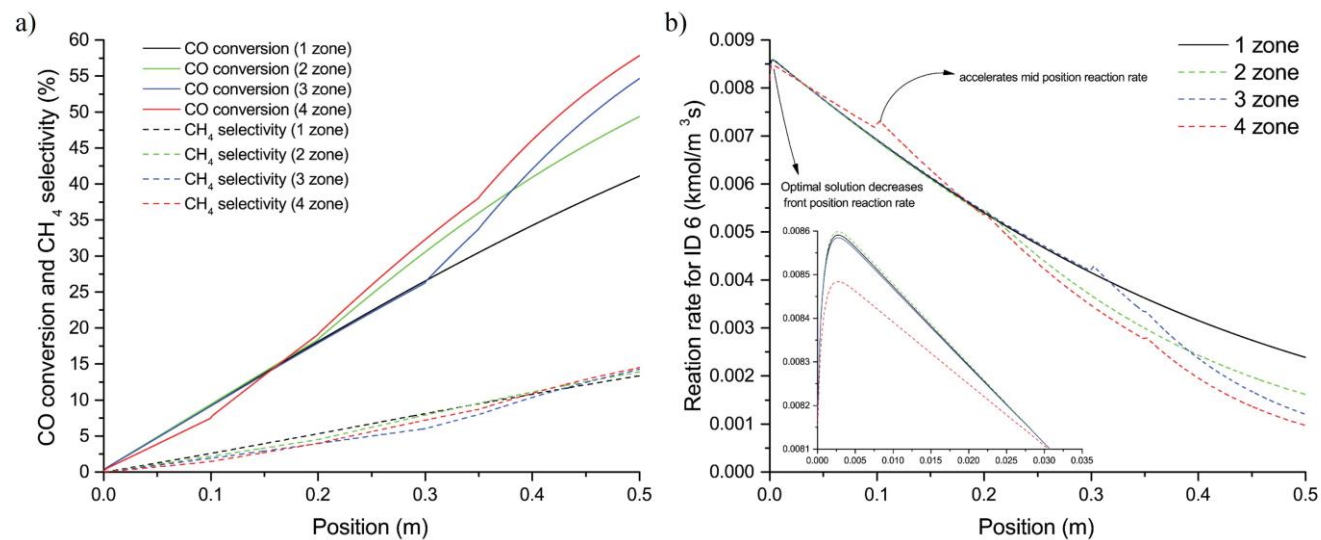


**Figure 3-9.** a) CO conversion and  $\text{CH}_4$  selectivity and b)  $\text{C}_{5+}$  reaction (ID=6) rate under the similar  $\Delta T_{\max}$  point of single zone catalyst packing, two zone GA-CFD result, three zone GA-CFD result, and four zone 2-stage GA-CFD result.

### **3.3. Process systems scale optimization**

#### **3.3.1. A modified DIRECT algorithm for hidden constraints optimization problem**

##### **3.3.1.1. Introduction**

The chemical process systems are troublesome problems to optimize them because of its essential attributes. They have a number of equality constraints such as mass balance and energy balance, and it makes hard to find a feasible solution. Not only the objective function but also the feasible region are generally non-linear, and numerous local optimums exist. To solve these problems, various kinds of optimization algorithms have been developed and applied to the industrial applications [78-85]. Derivative-free optimization, which can optimize the function for which derivative information is unavailable, unreliable, or impractical to obtain because of being expensive to calculate or noisy [86], is the key technique for this purpose. The reason why this kind of technique is important is that many analyzing methodologies used in engineering and science problems are black-box models for which a user cannot get the equations and other specific information being used from either the software or the analyzing machine. Especially, commercial software usually does not give exact equations and derivative information because of calculation methodology or their intellectual property rights. To solve this problem, many researchers have studied derivative-free optimization to optimize their specific engineering or science problems [87-91]. Derivative-free optimization

algorithms can be classified by two types of criteria, which are optimizing directly or indirectly and locally or globally. The direct search method uses the objective function directly for optimization whereas models based on an indirect search method regress the original function into an accurate surrogate model. Specifically, nature-inspired metaheuristic stochastic global search algorithms such as a genetic algorithm (GA), simulated annealing (SA), and particle swarm algorithms (PSO) are different from deterministic algorithm because they involve randomness which does not exist in the deterministic algorithm. Furthermore, algorithms are different depending on whether their target is local or global. A brief classification of derivative-free optimization algorithms originally provided from [86] are listed in Table 3-3 and see [86] for more details.

**Table 3-3.** Classification of derivative-free optimization.

		Local Search	Global Search
<b>Deterministic algorithm</b>	<b>Direct search method</b>	Nelder-Mead simplex algorithm Generalized pattern search (GPS) Generating set search (GSS) Mesh adaptive direct search (MADS) Pattern search methods using simplex gradient	Lipschitzian-based partitioning techniques - Divide a hyper-RECTangle(DIRECT) - Branch-and-Bound(BB) search Multilevel coordinate search (MCS)
	<b>Model-based search method</b>	Trust-region methods Implicit filtering	Response surface methods (RSMs) - Kriging - Analysis of computer experiments (DACE) stochastic model - Efficient global optimization (EGO) - Radial basis functions - Sequential design for optimization (SDO) Surrogate management framework (SMF) Optimization by branch-and-fit
<b>Stochastic algorithm</b>			Hit-and-run algorithms Simulated annealing (SA) Genetic algorithms (GA) Particle swarm algorithms (PSO)



In the case of the chemical engineering industry, commercial process simulators for designing process systems such as Aspen Plus, Aspen HYSYS, and SimSci PRO/II can be classified as black-box models in general. Since they are sequential modular-based simulators, it is hard to get derivative information of the target variables. Furthermore, an optimization tool given by a program usually shows low performance. Hence, for optimizing the process simulator function, an appropriate derivative-free optimization algorithm is necessary. For this reason, much research has been conducted for designing optimal process models with high-performance, derivative-free optimization algorithms by integrating commercial simulators and optimization algorithms. Lee et al. [92] integrated Aspen Plus and a gradient-based optimization method with MATLAB code for maximizing the exergy efficiency of the multi-component organic Rankine cycle (ORC) by changing component composition. Also, Lee et al. [77, 93] used GA for decomposing the MINLP problem to optimize a superstructure of a rigorous rate-based reactive distillation model and green-field post-combustion CO<sub>2</sub> capture process. For optimizing a rigorous tray-by-tray distillation column model, Javaloyes-Antón et al. [94] implanted a particle swarm algorithm into a process model simulated by Aspen HYSYS. Cozad et al. [95] developed the automated learning of algebraic models for optimization (ALAMO) to make a surrogate model of the given derivative-free function, and it can be used for a simulation of model-based derivative-free optimization [96]. Shi and You [97] proposed a novel adaptive surrogate modeling-based

algorithm to solve the integrated scheduling and dynamic optimization problem for sequential batch processes. Quirante et al. [98] used kriging interpolation, one of the response surface methods (RSMs), for rigorous designing of distillation columns where original model is formulated by Aspen HYSYS. Not only that, but also various researchers have tried to optimize the process systems using commercial simulator with external optimization algorithms [99-105].

Especially, liquefied natural gas (LNG), which is a widely used energy source for the remote transportation due to its environmental friendly attributes [106, 107], is the key area for this type of optimization. The liquefaction process for natural gas (NG) is an energy intensive process and therefore many researchers have widely studied about the process design and optimization of a liquefaction process [108-110]. Among the liquefaction technologies, single mixed refrigerant (SMR) liquefaction process is a traditional but still effective process for many projects with small-scale LNG production capacity [111-113]. It uses only single cycle of mixed refrigerant (MR) and therefore its efficiency is limited compared to the advanced processes such as the propane precooled mixed refrigerant (C3MR) or dual mixed refrigerant liquefaction process. However, it has the advantage of simple configuration, which makes the process easy to operate it with lower capital investment. Also, the efficiency of SMR can be improved with proper modification and optimization, and therefore many researchers have studied the SMR process optimization

problems. Shirazi and Mowla modeled optimized the PRICO SMR process by using GA [114]. Xu et al. modeled and optimized the PRICO SMR with Aspen Plus and GA [115]. Khan et al. modeled an SMR liquefaction process with a commercial simulator Honeywell UniSim Design and optimized it with the nonlinear programming [116], particle swarm paradigm [117] and sequential coordinate random search (modeled by Aspen HYSYS) [118]. Moein et al. modeled the APCI SMR process with Aspen HYSYS and optimized it with GA when the ambient temperature is changed [119]. Morosuk et al. modeled PRICO SMR with Aspen Plus and discussed about the evaluation and optimization for improvement [120]. Mehrpooya and Ansarinassab modeled and compared Linde and APCI liquefaction process based on exergy and cost analysis with Aspen HYSYS [121]. Park et al. modeled and optimized SMR using Aspen HYSYS and particle swarm algorithm with varying ambient temperature [122].

Previous optimization methods for a process simulator usually used a stochastic solver and surrogate model-based optimization because their implementation is simple compared to deterministic algorithms. Especially, nature-inspired metaheuristic algorithms were applied to the general purpose of a significant number of process systems studies, and they gave fine best-found solution in general [93, 115, 123-130]. However, when optimizing a process with a methodology that has been traditionally used, the following problems may arise. In the case of stochastic solvers, the algorithms highly depend on

tuning parameters, and the convergence rate of the objective function is slower with improper parameters. In addition, because these parameters are so numerous, finding an appropriate parameter set can be another problem. If the objective function has a high computation cost, it can be very inefficient because additional evaluation must be applied. Moreover, because of the features of the stochastic solver, randomness, even if the same initial conditions such as population for GA and swarm for PSO are set the same, it can be optimized along with other trajectories, thus causing reproducibility problems. There is also a problem because the initial population itself can have a large impact on optimization and does not guarantee that solvers converge into a global optimal solution. Moreover, although model-based search methods have been developed by machine learning technology, it is difficult to consider hidden constraints, especially complicated shape constraints that should be calculated in a process simulator. In fact, in order to solve these problems, stable noisy optimization by branch-and-fit (SNOBFIT) which can solve the hidden constraints in a robust way have been developed [131]. It is necessary to develop a handling method because it is hard to consider the possibility of hidden constraint when forming surrogate with a conventional regression model. Although several studies were performed with systematic optimization using the explicit function of liquefaction process [132-135], explicit process modeling makes lots of works, and complicated mathematical expression such as differential algebraic equation for kinetics can decrease the convergence rate.

Conclusively, most compatible optimization algorithms for process modeling should need a global search algorithm, hidden constraints handling, robustness, and a consistent result. As can be seen in Table 3-3, typical algorithms that satisfy these properties are Lipschitzian-based partitioning techniques. Among these, DIRECT-type algorithm is an appropriate algorithm for solving general engineering problems [136-143]. It is proved by Jones and Finkel and Kelley [144, 145] that if objective function is a deterministic and Lipschitzian continuous, then convergence to the global optimum is guaranteed. Since DIRECT does not require a Lipschitzian constant, there is no need to predict or compute it, so the parameter is actually only a Jones factor, and even this value has found an appropriate value [144]. Thus, deterministic and robust optimization can be performed. However, several improvements should be performed to apply the DIRECT algorithm to the process optimization. The DIRECT algorithm does not have a specific interpretation for handling hidden constraints [146]. Thus, if we want to integrate a derivative-free optimization scheme effectively with an unknown infeasible region with hidden constraints of the process simulator function, then we should develop an effective hidden constraint-handling algorithm. Therefore, in this study, we developed a subdividing step as a hidden constraint handling method to apply the DIRECT algorithm to process systems optimization. By applying this method to the SMR liquefaction process modeled by Aspen HYSYS, the performance of the algorithm was validated.

The paper is organized as follows. A brief introduction to the original DIRECT method is described. The proposed modified DIRECT algorithm that has a sub-dividing step to handle hidden constraints is explained and compared with the previous methods of the barrier approach and neighborhood assignment strategy (NAS) [138]. To test the performance of the modified DIRECT algorithm with a sub-dividing step, a simple single mixed refrigerant (SMR) process for natural gas liquefaction with 3 hidden constraints modeled by Aspen HYSYS V8.8 is utilized. Finally, the optimized process is compared with the conventional DIRECT algorithms (barrier approach, neighborhood assignment strategy), the stochastic global search algorithms (GA, PSO, SA), the model based global search algorithm (SNOBFIT), and the several local search methods (GPS, GSS, MADS, SQP, active-set, interior-point)

### **3.3.1.2. DIRECT Algorithm with Hidden Constraints**

The DIRECT algorithm is based on Lipschitzian-based partitioning techniques, and it can handle non-linear and non-convex functions globally [86]. Since many functions of process systems engineering in chemical engineering are calculated by commercial software assumed to be black-box models for users, and as the equations are highly non-linear and non-convex, a deterministic derivative-free global optimization algorithm is appropriate. Moreover, after they evaluate the simulation, commercial process simulators give error messages because of convergence errors or a physically infeasible region. Thus, we should consider hidden constraints that do not give information of infeasibility before evaluating a function. In this research, we suggest a modified DIRECT algorithm to handle hidden constraints by using a sub-dividing step based on the original DIRECT algorithm.

### 3.3.1.3. Basic Ideas of the Original DIRECT algorithm

The mathematical description of the original DIRECT algorithm was developed by Jones et al. [144]. Two critical ideas were implemented in Shubert's algorithm for applying it to derivative-free optimization problems without the Lipschitz constant. First, hyper-rectangular partitions based on  $N$ -dimensional trisection are suggested. This can decrease the computational cost by evaluating the function at the center of the hyper-rectangle and not at all extreme points. Since the center point solution of the hyper-rectangle is conserved, unnecessary overlapped function calculations are not performed after partitioning. Second, the decision criteria regarding which hyper-rectangles should be divided are decided based on the concept of potentially optimal hyper-rectangles. At the iteration step, all hyper-rectangles are identified that are potentially optimal and only potentially optimal hyper-rectangles will be divided before passing to the next iteration. The brief description of the potentially optimal condition based on [144] is given in Definition 1.

**Definition 1** Let  $i$  and  $j$  be the index of the hyper-rectangle and  $c_i$  and  $c_j$  be the center of hyper-rectangles  $i$  and  $j$ , respectively.  $d_j$  is a measure for this hyper-rectangle such as the distance from the center of hyper-rectangle  $i$  to its vertices. Let  $\varepsilon$  called Jones factor be a positive constant and let  $f_{\min}$  be the minimum



function value so far iteration. A hyper-rectangle  $j$  is called potentially optimal if positive  $\tilde{K}$  exists such that

$$f(c_j) - \tilde{K}d_j \leq f(c_i) - \tilde{K}d_i \quad \text{for } \forall i \quad [3-9]$$

$$f(c_j) - \tilde{K}d_j \leq f_{\min} - \varepsilon|f_{\min}| \quad [3-10]$$

The step of identifying hyper-rectangles is performed at every iteration repeatedly. Thus, resolution of the searching area near the locally or globally optimal solution increases sequentially. A brief description of the DIRECT algorithm is shown in Algorithm 1.

---

**Algorithm 1** DIRECT(upper and lower bound of variables,  $f$ ,  $\varepsilon$ , termination criteria)

---

Normalize the searching space to be the unit hyper-rectangle.

Evaluate the function at the center of hyper-rectangle ( $c_1$ ) and  $f_{\min}=f(c_1)$ .

**while** termination conditions such as reaching the number of max iteration and function evaluation are activated

    Identify which hyper-rectangles are the potentially optimal hyper-rectangles.

        Divide all potentially optimal hyper-rectangles.

        Evaluate the function value at the center of new hyper-rectangles.

        Update  $f_{\min}$ .

**end while**

---

#### **3.3.1.4. Modified DIRECT Algorithm for Hidden Constraints**

The DIRECT algorithm does not have a constraint-handling mechanism, and its searching area consists of the upper and the lower bound of each variable. However, a constraint-handling mechanism should be needed to solve engineering application problems. Three constraint-handling methods were proposed which are the barrier approach, L1 penalty function [147], and the neighborhood assignment strategy (NAS) [138]. However, the L1 penalty function approach is not appropriate for hidden constraints because it requires a predefined explicit constraint. If a commercial process simulator diverges at an infeasible point, then it is impossible to use the L1 penalty function because it has no function value. Furthermore, although the barrier approach can handle the hidden constraint, it was not an appropriate method with DIRECT with hyper-rectangles with a large feasible area, but an infeasible center [148]. Thus, the function should be evaluated by checking whether the point is either in the hidden constraint or not and whether it can be effectively handled by NAS. NAS sets the enlarged rectangle whose center is an infeasible point and determines the surrogate value from the already evaluated feasible points. Thus, it does not need a penalty parameter or constraint function value. However, because NAS does not use information of constraints such as the shape of the constraint or constraint violations, its performance can decrease greatly when the shape of the constraints is highly non-convex [149].

To solve this problem, we suggest a sub-dividing step for infeasible hyper-rectangles that do not satisfy the hidden constraints. If the points are identified as infeasible points, then the function assigns a penalty value like the barrier approach. In the sub-dividing step, all infeasible hyper-rectangles are divided after dividing potentially optimal hyper-rectangles, and the center values of the new hyper-rectangles generated by the sub-dividing step are calculated. After the sub-dividing step, the new minimum function value is updated and goes back to the next iteration. A brief introduction of this algorithm is shown in Algorithm 2.

---

**Algorithm 2** modified-DIRECT(upper and lower bound of variables,  $f$ ,  $\varepsilon$ , termination criteria)

---

Normalize the searching space to be the unit hyper-rectangle.  
Evaluate the function at the center of the hyper-rectangle ( $c_1$ ).  
**if**  $f(c_1)$  is feasible  
     $f_{\min}=f(c_1)$ .  
**else**  
    Divide the first hyper-rectangle.  
**end if**  
**while** termination conditions such as reaching the number of max iterations and function evaluations are activated  
    Identify which hyper-rectangles are the potentially optimal hyper-rectangles.  
    **if the** sub-dividing step is activated  
        Identify which hyper-rectangles have an infeasible function value  
    **end if**  
    Divide all potentially optimal hyper-rectangles  
    Evaluate the function value at the center of the new hyper-rectangles.  
    **if the** sub-dividing step is activated  
        Divide all infeasible hyper-rectangles  
        Evaluate the function value at the center of the new hyper-rectangles.  
    **end if**  
    Update  $f_{\min}$   
**end while**

---

To illustrate the sub-dividing algorithm, Figure 3-10 shows a geometric graph of the DIRECT algorithm with a sub-dividing step at the third main iteration. Unlike the barrier approach, the sub-dividing step can decompose the edge of the hidden constraints and expand the feasible searching area. Thus, it is possible to consider complicated shape constraints with high skewness such as a non-convex shape. Although the calculation cost is higher than the original DIRECT algorithm because of the sub-dividing step, if sub-dividing steps are performed at the proper iteration, then performance can be increased effectively within computational limitations. For validating the performance of a simple problem with a hidden constraint, the Goldstein-Price test function, which is given by the Equation [3-11], is used [150].

$$f(x_1, x_2) = [1 + (x_1 + x_2 + 1)^2(19 - 14x_1 + 3x_1^2 - 14x_2 + 6x_1x_2 + 3x_2^2)][30 + (2x_1 - 3x_2)^2(18 - 32x_1 + 12x_1^2 + 48x_2 - 36x_1x_2 + 27x_2^2)], \{x_1, x_2\} \subset D \cap D_{hidden} \quad [3-11]$$

where the pre-defined feasible region  $D$  and hidden constraint  $D_{hidden}$  are defined as Equation [3-12] and [3-13].

$$D = \{(x_1, x_2) \mid (-2, -2) \leq (x_1, x_2) \leq (2, 2)\} \quad [3-12]$$

$$D_{hidden} = \{(x_1, x_2) \mid [(x_1 + 1)^2 + (x_2 + 1)^2 \geq 1.1] \cap [(x_1 - 1)^2 + (x_2 - 1)^2 \geq 0.9]\} \quad [3-13]$$

We assume that we do not know the value of  $D_{hidden}$ , thus only the function can determine that the point is feasible or infeasible and the optimization

problem is  $\min_{x_1, x_2 \in D \cap D_{hidden}} f(x_1, x_2)$ . The sub-dividing step is activated at iterations 5 and 15. The barrier approach and NAS are also evaluated with a limited function evaluation number set to 2000 for comparing the algorithm performance in the same manner.

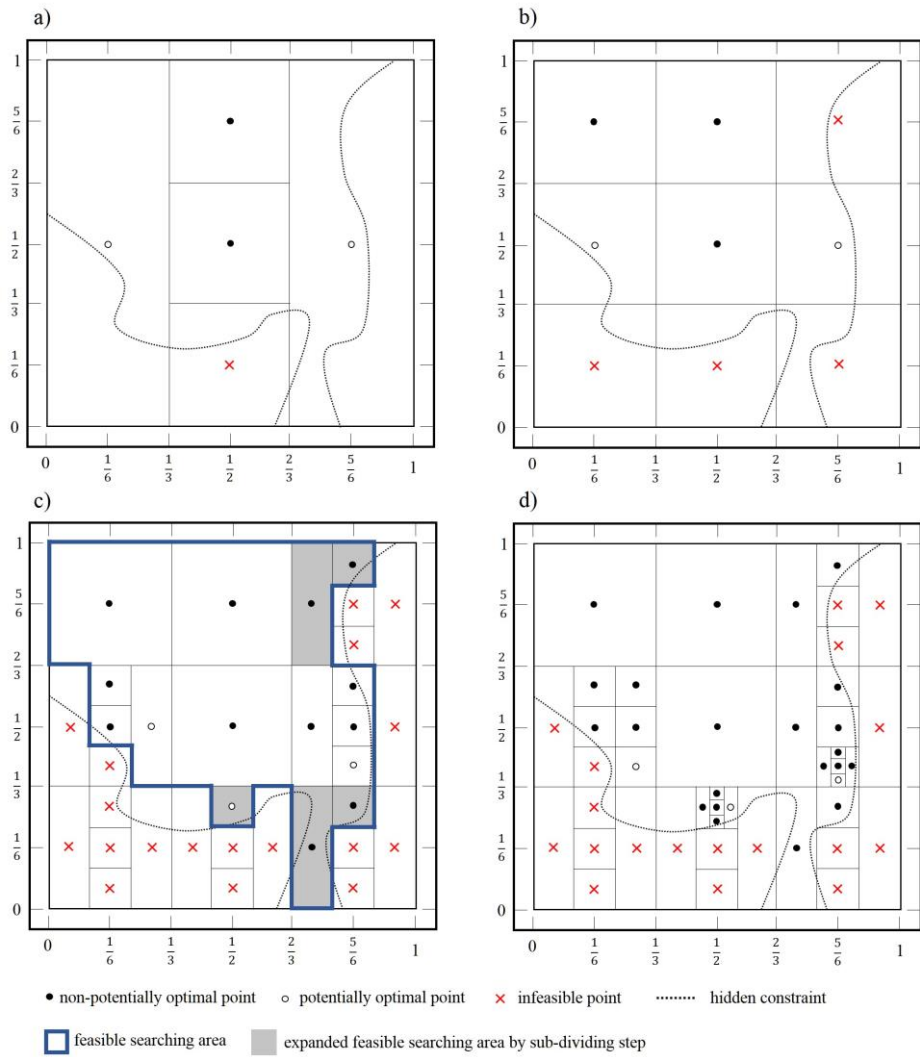


**Figure 3-10.** Geometric interpretation of potentially optimal point and infeasible point using DIRECT with sub-dividing step algorithm on two dimension hidden constraints problem at a) the first iteration, b) the second iteration, c) the third iteration with the first sub-dividing step, d) the fourth iteration.



The objective function values versus function evaluation are illustrated in Figure 3-11. Convergence speed of the barrier approach, NAS, and the sub-dividing step are similar at the early stage, but the optimal values are different. The final optimal values are 14.4, 4.3, and 3.5, respectively. Moreover, NAS shows a second decreasing phase at about the 1700 function evaluation number point. It seems that NAS finds the feasible points in the enlarged rectangle with a surrogate model at that stage. In Figure 3-12, the barrier approach and NAS show convergence values of feasible points at (0.22, -0.87) which is far from the infeasible circle hidden constraints while the sub-dividing step has convergent points at (0.049, -0.99) which is almost at the edge of the hidden constraints. Although NAS has a second set of convergent points at (0.074, -0.97), it is also farther from the hidden constraints than the sub-dividing step. The reason for the inefficiency of the barrier approach is that the barrier approach deactivates the infeasible hyper-rectangle and that rectangle cannot be divided until optimization is over. Thus, the resolution of feasible rectangles near the hidden constraint is very low, and we can see a rectangle barrier in Figure 3-12. There is a possibility that NAS gives a low performance when NAS fails to consider the shape of the hidden constraint and estimates the function value of an infeasible point from the surrogate model.

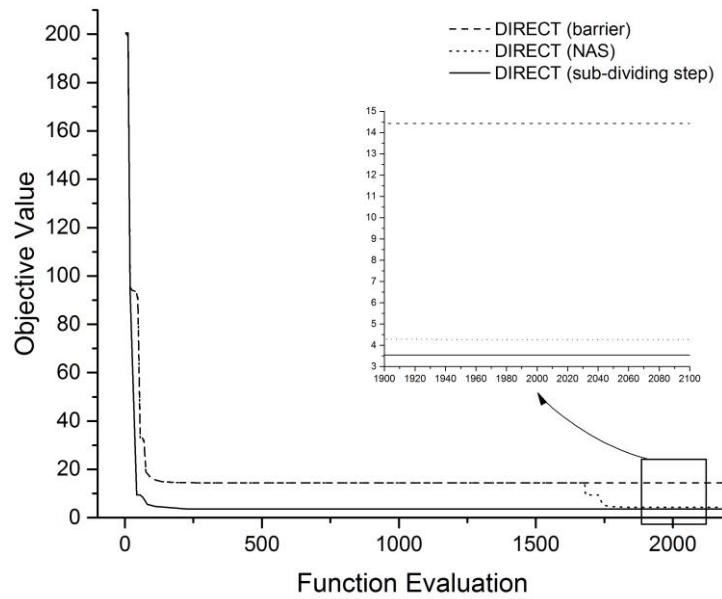


**Figure 3-11.** DIRECT with barrier, NAS, and sub-dividing step iteration for Goldstein-Price test function.

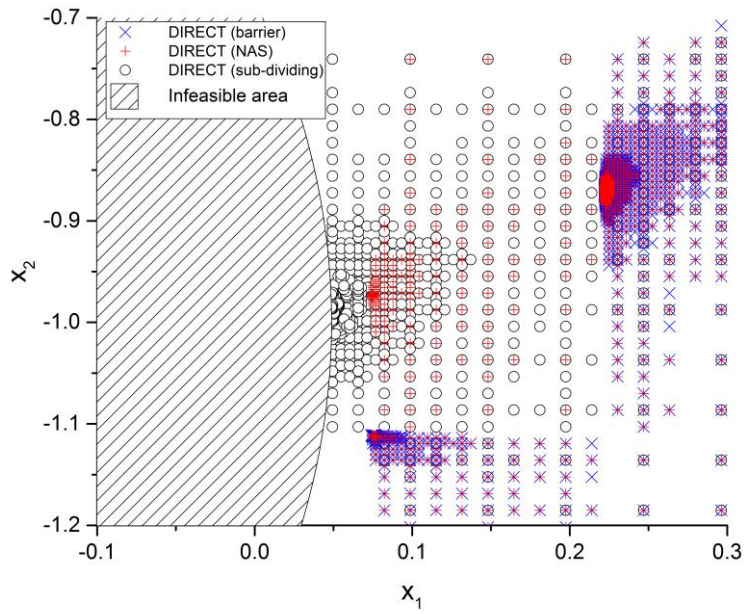


**Figure 3-12.** The points where Goldstein-Price test function is evaluated with barrier, NAS, and sub-dividing step at 2000 function evaluation.

### **3.3.1.5. SMR Liquefaction Process for Natural Gas**

The single mixed refrigerant (SMR) liquefaction process is one of the famous cryogenic mixed refrigerant processes because of its simplicity. The basic structure of the SMR process consists of a single stage cold box, a Joule-Thomson valve, and 4 series compressors with after-cooling. Although SMR processes are theoretically inefficient in exergy compared to advanced liquefaction processes, such as the dual mixed refrigerant (DMR) cycle and the propane pre-cooled mixed refrigerant (C3MR) cycle [133], they have been used because of their simple structure and network connections, which guarantee easy control, operation, and low capital cost. In this study, the base case of the SMR process was selected from [151] which consists of two multi-stream heat exchangers, a phase separator, three compressors, and after-cooling heat exchangers.

### **3.3.1.6. Process Model and Design Variables**

The process is modeled by Aspen HYSYS V8.8, which is a qualified commercial process simulator in the LNG industry. The process flow diagram and the name of each unit and stream are given in Figure 3-13. Table 3-4 lists the simulation basis and feed conditions in the SMR process. The base operating condition and assumptions are provided from the literature, and the readers should refer to [34]. The mixed refrigerant consists of nitrogen, methane, ethane, propane, and n-butane, and the composition of NG is nitrogen, methane, ethane, propane, i-butane, n-butane, and i-pentane. Peng-Robinson EOS is used for calculating thermodynamic properties. The production rate of NG and the minimum temperature approach (MTA) were fixed as 26.38 kg/h and  $3 \pm 0.15\text{K}$ , respectively. In fact, liquefaction process performance should be evaluated by not only exergy and compressor shaft work but also by capital cost. However, it is difficult to scalarize the operating cost and the capital cost in the same dimension such as cost. Thus, we bound MTA as  $\pm 5\%$  of 3K for keeping off the catastrophe, infinite area of the heat exchanger and set the minimum MTA of LNG-100 and LNG-101 of the base case as 2.85 K for comparison purposes. Centrifugal compression energy is calculated by the Schultz polytrophic method with 80% adiabatic efficiency. The pressure drop across the heat exchanger, flash drum, and mixer is ignored. Table 3-5 lists the 9 design variables, which are 4 types of pressure variables and 5 types of refrigerant

composition, and their bounds. LP, MP1, MP2, and HP are the pressure of stream 1-start, 2a, 2c, and 2, respectively, which are connected to the compressors. Especially, LP is connected to the after stream of the Joule-Thomson valve, VLV-101, which directly affects exergy efficiency and the MTA of the cold box. Although LP can be changed to the temperature of stream 7 as in previous research [117], we selected this pressure variable for preserving the consistency of variable type. Although the mixed refrigerant is mixed with 5 pure chemical compounds, compositions of 4 of the compounds are enough to set the optimization problem because of the composition constraint, which limits the sum of composition equal to 100%. Previous researches [117, 118] usually selected the bounds based on the preceding process knowledge, process designer experience, and sensitivity analysis of variables. However, that method is not efficient for the general purpose of optimization for various processes. Because the proposed optimization method can handle predefined constraints and hidden constraints simultaneously, the user does not need to find the nice bounds. In this research paper, the upper and lower bound of each variable is set to  $\pm 90\%$  of the base set of the design variables.

**Table 3-4.** Base operating condition of SMR process and NG feed composition.

<b>Property</b>		<b>State</b>
NG feed		
Temperature (K)		300
Operating pressure (bar)		65
Flow rate (kg/h)		26.38
Composition (mol%)	Nitrogen	4.0
	Methane	87.5
	Ethane	5.5
	Propane	2.1
	i-Butane	0.3
	n-Butane	0.5
	i-Pentane	0.1
Minimum temperature approach at LNG-100 and LNG-101 (K)		2.85
Intercooler outlet temperature (K)		305
Compressor adiabatic efficiency (%)		80

**Table 3-5.** The lower and upper bounds of design variables.

Property	Lower bounds	Upper bounds
Pressure variables (bar)		
LP	0.300	5.700
MP1	0.750	14.250
MP2	1.875	35.625
HP	4.675	88.825
Composition variables (%)		
Nitrogen	0.859	16.321
Methane	2.597	49.343
Ethane	2.541	48.279
Propane	3.911	74.309
n-Butane	dependent	



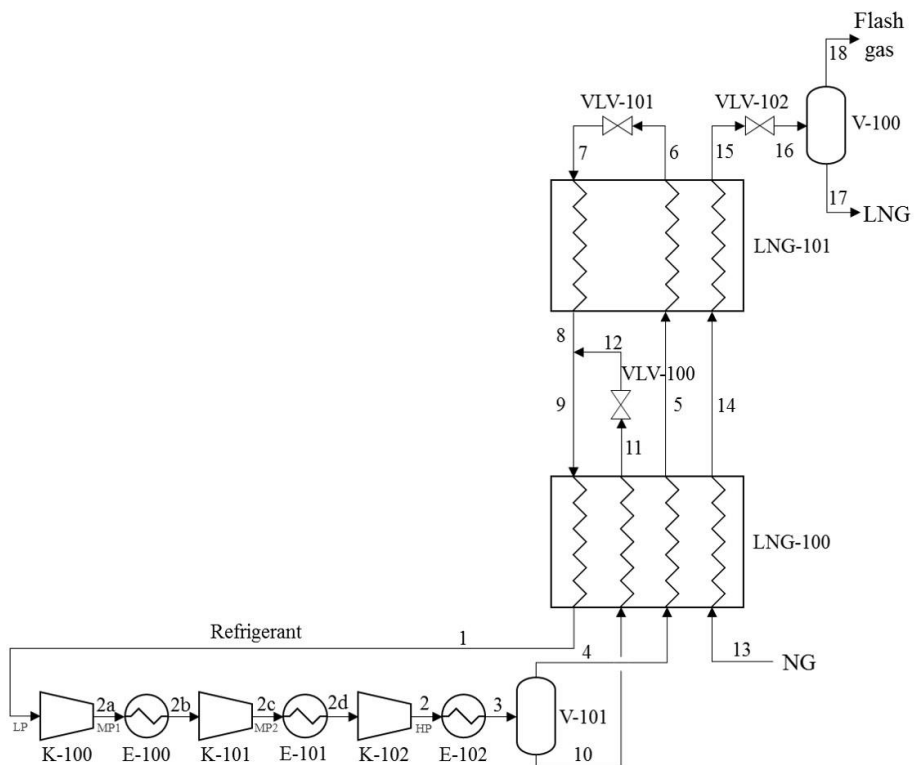


**Figure 3-13.** Process flow diagram of single mixed refrigerant (SMR) natural gas liquefaction process.

**Table 3-6.** Base operating condition of SMR process and NG feed composition.

Property		State
NG feed		
Temperature (K)		300
Operating pressure (bar)		65
Flow rate (kg/h)		26.38
Composition (mol%)	Nitrogen	4.0
	Methane	87.5
	Ethane	5.5
	Propane	2.1
	i-Butane	0.3
	n-Butane	0.5
	i-Pentane	0.1
Minimum temperature approach at LNG-100 and LNG-101 (K)		2.85
Intercooler outlet temperature (K)		305
Compressor adiabatic efficiency (%)		80

For automating the connection between Aspen HYSYS V8.8 and the MATLAB optimization algorithm, the Aspen HYSYS SMR process case is set by objective function and ActiveX server communication technology is used and block diagram of combined algorithm and process simulation function is shown in Figure 3-14. Therefore, we can manage the process simulation as the function of MATLAB. Overall optimization algorithm is coded in the MATLAB and hidden constraints feasibility is also checked by external in-house code. Because of technical problems with the software, composition is changed by controlling the molar flow rate of pure component streams and the molar flow rate is determined by matching the temperature of 1-start and 1-end using the adjustment unit ADJ-1 with the secant method. Aspen HYSYS SMR process model, MATLAB-Aspen HYSYS ActiveX server interaction structure, and in-house objective function are provided at supplementary.

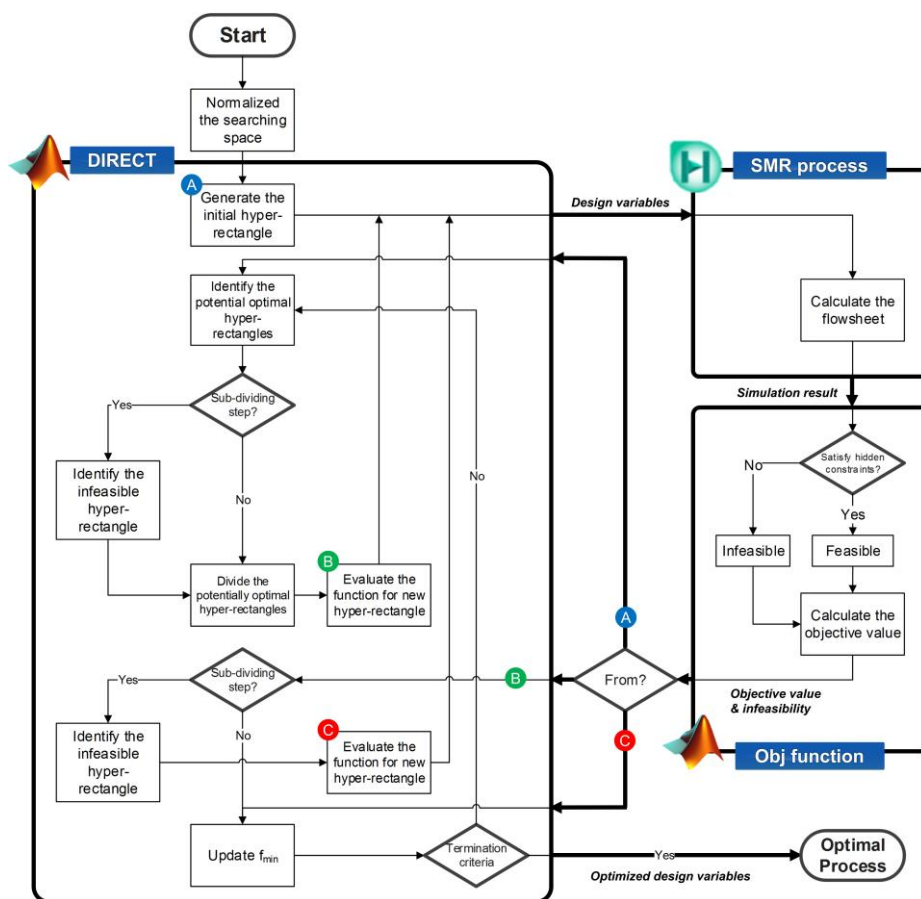


**Figure 3-14.** Block flow diagram of optimization platform for DIRECT algorithm with sub-dividing step method for hidden constraint handling method and interconnection between optimization algorithm and Aspen HYSYS SMR process model.

### 3.3.1.7. Optimization Formulation

There are three types of constraints for process systems equations which are defined by the process simulator ( $h_p(x)$ ), predefined constraints ( $g_i(x)$ ,  $h_j(x)$ ) and hidden constraints ( $s_k(x)$ ). We should distinguish those constraints for different considerations. Brief optimization problem is given in Equation [3-14].

$$\begin{aligned}
 & \min_{x \in \mathbb{R}^{1 \times n}} f(x) + \gamma p(x) \\
 & \text{subject to} \\
 & g_i(x) \leq 0 \quad i = 1, 2, 3 \\
 & h_j(x) = 0 \quad j = 1 \\
 & h_p(x) = 0 \quad p = 1, 2, 3, \dots, m \\
 & p(x) = \begin{cases} 0 & \text{if } s_k(x) = 0 \text{ and } g_i(x) \leq 0 \text{ and } h_j(x) = 0 \quad k = 1, 2, \dots \\ 1 & \text{if } s_k(x) \neq 0 \text{ or } g_i(x) > 0 \text{ or } h_j(x) \neq 0 \quad k = 1, 2, \dots \end{cases} \\
 & LB \leq x \leq UB
 \end{aligned} \tag{3-14}$$

First,  $h_p(x)$  such as the mass and heat balance equation, several thermodynamics equations, and other numerical equation systems are already defined by the process simulator. Thus, at the optimization platform, users do not need to consider those type equations precisely. Since the second type of constraints is predefined, it is possible to do not evaluate the function at out of constraints. Thus, if the variables set do not fit  $g_i(x)$  and  $h_j(x)$  which are linear constraints, a penalty function ( $p(x)$ ) will be activated in the objective function and penalty parameter ( $\gamma$ ) which is usually large value as barrier increases objective function. Thus, the process simulation function does not need to be evaluated. Predefined inequality constraints,  $g_i(x)$ , mean that the series connection of compressors should increase the pressure of each of the streams

which is given in Equation [3-15]. Predefined equality constraint,  $h_j(x)$  means that the mole fraction ( $m_k$ ) summation of overall chemical components mole fraction should be equal to 100% because of its definition Equation [3-16]

$$P_{LP} \leq P_{MP1} \leq P_{MP2} \leq P_{HP} \quad [3-15]$$

$$\sum m_k = 100\%, \quad k \in \text{all chemicals in SMR} \quad [3-16]$$

In this SMR process, there are three types of physically infeasible regions, which are 1) a case with no solution (divergent system), 2) a case with a temperature crossing point at LNG-100 and LNG-101, or MTA is not in  $3 \pm 0.15^\circ\text{C}$ , and 3) a case that the liquid stream enters the compressors. However, it is impossible to know which design variable sets are in the infeasible regions before running the process simulator, which are also called hidden constraints. Thus, we judge this region as an infeasible hyper-rectangle for evaluating the process simulator function. With these three types of constraints, we integrated the process simulator with the modified DIRECT algorithm and the sub-dividing step using Aspen HYSYS and MATLAB. If the variable sets do not satisfy the pre-defined constraints and the hidden constraints, those points will be divided at the sub-dividing step. As in  $g_i(x)$  and  $h_j(x)$ ,  $p(x)$  is activated, and the penalty parameter is added to the objective function value. The objective function,  $f(x)$  is the specific power required for NG liquefaction (kJ/kg-LNG) which is the total energy consumption of the compressor over the LNG product mass flow rate in stream 17. Since LNG should not be obtained as a multiphase

form and vapor fraction of LNG must equal to 0, stream 17 after V-100 to measure the mass flow for liquid phase through flash calculation is selected

For validating the performance of the proposed algorithm, the algorithms given in Table 3-7 are tested. There are three types of the stochastic global search algorithm, GA, PSO, and SA, which are the most famous nature-inspired metaheuristic algorithm. For a fair comparison, population size for GA, swarm size for PSO, and reanneal interval for SA are set to 40. SNOBFIT is deterministic but model-based search method, and it has been known as robust and flexible for hidden constraints. GPS, GSS, and MADS are deterministic and direct search method but local search method based on pattern search. Finally, conventional constrained non-convex local optimization solver, active-set, interior-point, and SQP are tested with default option in MATLAB. In order to compare with the DIRECT algorithm under the same conditions, we tried to compare the values at the same computation cost based on the function evaluation. However, in the case of the local solver, the operation is stopped with the terminal criterion when the local optimum is lost and the operation is no longer meaningful. In the case of the DIRECT algorithm, barrier approach and the NAS for hidden constraint handling method are also calculated to compare the performance of the proposed method, the sub-dividing step. In order to compare the experiments under the same conditions, we try to compare the values at the same computation cost based on the function evaluation. However, in the case of the local solver, the operation is stopped with the

terminal criterion when solver fall into the local optimum, and the operation is no longer meaningful.



**Table 3-7.** List of Algorithms for comparing the performance.

<b>Solver</b>	<b>Global/Local</b>	<b>Deterministic / Stochastic</b>	<b>Constraints</b>	<b>Options</b>
<b>GA</b>	Global	Stochastic	Yes	'PopulationSize'={40} 'CrossoverFraction'={0.5} 'EliteCount'={2}
<b>PSO</b>	Global	Stochastic	Yes	'SwarmSize'={40}
<b>SA</b>	Global	Stochastic	No	'AcceptanceFcn'=@modified_BoltzmannProbabilityDensity 'ReannealInterval'={40}
<b>SNOBFIT</b>	Global	Deterministic	Yes	Default
<b>GPS</b>	Local	Deterministic	Yes	'PollMethod'='GPSPositiveBasisNp1'
<b>GSS</b>	Local	Deterministic	Yes	'SearchMethod'=@GPSPositiveBasisNp1 'PollMethod'='MADSPositiveBasisNp1'
<b>MADS</b>	Local	Deterministic	Yes	'SearchMethod'=@GSSPositiveBasisNp1 'PollMethod'='MADSPositiveBasisNp1'
<b>Active-set</b>	Local	Deterministic	Yes	'SearchMethod'=@MADSPositiveBasisNp1
<b>Interior-point</b>	Local	Deterministic	Yes	Default (fmincon option)
<b>SQP</b>	Local	Deterministic	Yes	

### **3.3.1.8. Optimization Result and Discussion**

The optimization results of the SMR process are listed in Table 3-8. Since the objective function we have taken is the specific power required for NG liquefaction, results can be compared based on this value, and see how close the objective value approaches the constraint by looking at the MTA values of LNG-100 and LNG-101. For comparing each algorithm fairly, in the case of global search algorithm, the maximum number of iterations of the process simulator function is limited to 20,000 times. Meanwhile, the maximum number of iterations for local search algorithm is also limited to 20,000 times, but all of them stop before it because of falling into the local optima. From the conclusion, the DIRECT algorithm with sub-dividing step successes in obtaining the most optimal value in the determined computation cost. This value is an energy saving effect of 18.9% for the base case, and 13% on average in comparison with other algorithms. Objective function value versus function evaluation of each algorithm is given in Figure 3-15.

**Table 3-8.** Optimization result of SMR process.

Property	Base case	DIRECT sub-dividing step	DIRECT barrier	DIRECT NAS	GA	PSO	SA	SNOBFIT	GPS	GSS	MADS	Active-set	Interior-point	SQP	
Total compression power (kW)	8.27	6.71	6.82	7.39	8.03	7.67	7.41	6.77	8.25	7.91	7.97	8.27	8.27	8.27	
Specific power required for NG liquefaction (kJ/kg-LNG)	1170	949	965	1045	1136	1085	1048	958	1167	1118	1128	1170	1170	1170	
Minimum temperature approach at LNG-100 (K)	3.01	3.00	3.02	3.00	3.05	3.00	2.99	3.00	3.01	3.00	3.00	3.01	3.01	3.01	
Minimum temperature approach at LNG-101 (K)	2.85	2.85	2.96	3.27	2.87	2.93	3.53	2.88	2.85	2.88	2.85	2.85	2.85	2.85	
Design variables															
Pressure (bar)	LP	3.12	3.87	3.07	3.00	3.58	2.87	4.39	5.70	3.12	3.44	3.41	3.12	3.12	3.12
	MP1	7.50	7.27	6.50	4.50	11.22	8.56	10.22	9.40	8.88	9.87	8.41	7.50	7.50	7.50
	MP2	18.75	13.10	9.17	7.50	24.35	19.82	17.08	16.07	22.75	23.26	17.88	18.75	18.75	18.75
	HP	46.75	28.05	24.93	18.70	47.15	37.99	39.85	38.32	46.75	47.10	47.32	46.75	46.75	46.75
	Nitrogen	8.59	8.58	7.83	8.59	8.91	6.93	11.25	11.93	8.59	8.68	8.63	8.59	8.59	8.59
Composition (mol%)	Methane	25.97	25.78	24.24	25.97	26.62	25.66	25.03	25.91	25.97	26.42	26.35	25.97	25.97	25.97
	Ethane	25.41	30.68	30.49	25.41	27.12	26.29	32.21	35.09	25.41	29.46	29.57	25.41	25.41	25.41
	Propane	39.11	15.64	15.64	15.64	34.21	34.40	19.03	10.47	39.11	29.86	30.11	39.11	39.11	39.11
	n-Butane	0.92	19.32	21.80	24.39	3.13	6.72	12.49	16.60	0.92	5.58	5.34	0.92	0.92	0.92
Computation cost (the number of process simulator function evaluation)		-			20000					336	811	438	51	47	103

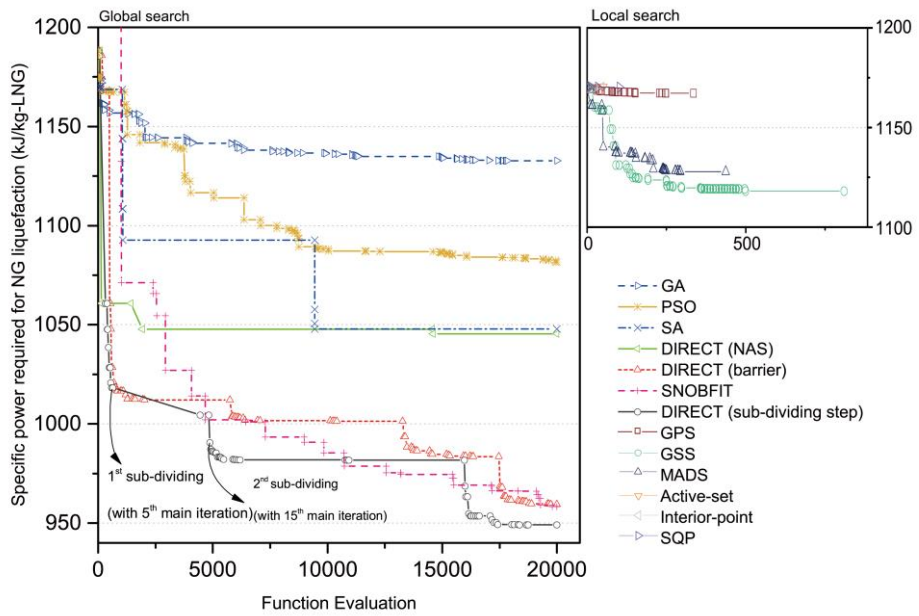


**Figure 3-15.** Objective function value versus function evaluation of GA, DIRECT algorithm with barrier approach, NAS, and sub-dividing step.

First of all, in case of DIRECT type solver, the specific power required for NG liquefaction from the sub-dividing step optimal solution is 1.7% and 9.2% lower DIRECT with the barrier approach, and NAS, respectively. Surprisingly, the result of the barrier approach is better than NAS. In Figure 3-15, a graph of the barrier approach and NAS shows similar movement at the early stage; NAS cannot find a much better solution within the limited function evaluation whereas the barrier approach finds a better solution. It seems that the hidden constraint handling method of NAS is not appropriate for highly non-convex constraints or functions because its surrogate model assumes the neighborhood function value linearly, such as  $F + \delta|F|$ , where  $F$  is the low function value in the neighborhood around the infeasible center  $c$ . Since a physically feasible process, condition is very sensitive to design variables with non-convex hidden constraints, many populations and many iterations are needed to achieve a better solution. However, the solution fails when limited by the computational cost. Thus, the performance of NAS for an SMR process function is low and rather the barrier approach and DIRECT with the sub-dividing step is better. Obviously, the sub-dividing step shows better performance than the barrier approach because sub-dividing step divide the edge of the hidden constraints and solution can approach closer to the edge.

In case of stochastic solver, GA, PSO, and SA, best-found solutions are 16.4%, 12.5%, 9.4% higher than DIRECT with sub dividing step respectively. First, GA does not produce better results than expected. This seems to be due

to the fact that the initial population selection has a great influence in the process of finding solutions. In the SMR process, the range of hidden constraints is quite wide, so if there is no initial procedure such as enumeration and the initial population is given randomly, there is a case where there is no feasible solution in the generation. This confirms the problem that most of calculations occur within an infeasible region even after significant generation. A total of 20,000 operations are performed five times and two initial population failure are detected. Among the others, the best performance trial is shown in Figure 3-15. Although improved optimal solution can be found by changing various GA parameters such as crossover fraction, It is a disadvantage to do such additional operations. Similarly, in case of PSO, if all the swarms of the initial particles exist only in the infeasible region, the problem seems to occur because the direction or velocity of the particles cannot be calculated properly. However, unlike GA, 2 times are infeasible during 4 times, but 2 are better than GA. In case of giving several points which converged in DIRECT with initial swarm, it is about 4% better than DIRECT. However, this is another problem that determines what the initial swarm is given. Also, because there is a randomness tendency, it is not always possible to reproduce the solution in the same way. Therefore, it is can be said that the higher computation cost is needed. In case of SA, the Boltzmann probability density function, which is the default acceptance function, is used and since the penalty factor is increased, the temperature of the algorithm is drastically lowered and reannealing is prevented.

Hence, we modify the algorithm to make the reannealing forcibly if the temperature is too low and continue the constant iteration at one point. The results show that SA shows similar performance to the DIRECT with NAS method. Overall, it seems that the stochastic solvers do not perform well in this optimization problem. Sometimes, however, solver can show nice solution with several trials because of their randomness characteristics and if initial procedure is well performed then solver can calculate the great solution. Despite probability of the great solution, it is impossible to guarantee that stochastic solver gives the best optimal solution deterministically. Thus, if the objective function is the case of high cost function, it is very inefficient and risky.

SNOBFIT, a deterministic and global solver, is a model based search method, but it is known to be an algorithm designed to handle hidden constraints very well. SNOBFIT gives the second best optimal solution following the DIRECT with sub-dividing step. However, because error between quadratic subproblem of SNOBFIT and original SMR process simulation function is relatively high up to about 5000 function evaluation, convergence rate is relatively slow than other algorithms. Even though SNOBFIT shows better optimal value at short interval, 12,000-16,000, DIRECT with sub-dividing step gives better optimal solution at the other intervals and has better early stage convergence speed.

Local solver gives a very bad solution overall. Even though the function evaluation is forced to 20,000, it fall into the local optimum, and the further operation became meaningless and stopped. Base case is given for initial point

of local solver, which is the main factor of difference between the pattern search (GPS, GSS, MADS) and conventional constrained non-convex solver (active-set, interior-point, SQP). Since the base case itself is precisely adjacent to the MTA hidden constraint ( $\geq 2.85$  °C), if the LP rises even a little, the penalty function is activated because MTA of LNG-101 decreases. Because conventional constrained non-convex solvers change the main problem to the subproblem for handling the constraint effectively using the gradient information, they have tried to move through the gradient but they fail to find the better solution because of the discontinuity of hidden constraints. Thus, the final solutions of three solver are just same as base case. Unlike conventional constrained non-convex solvers, GPS, GSS, and MADS try to investigate the pattern of larger searching area and success to find better solution than base case. However, their solutions are 18.7%, 15.1%, and 15.9% higher than DIRECT with sub-dividing step respectively, which is terrible performance compared to global search algorithm. Herein, some reasons why solution might be considered as local optimum are explained. The results of the high-performance solvers in the global solver show that the n-butane content is significantly increased (more than 15%) and the HP pressure is significantly reduced (less than 40 bar) compared to the base case, which decrease the compressor power. However, if the change is continuously simulated on the simulator, it is impossible to converge continuously which means there are



some discontinuous hidden constraints. In the case of the local solvers, they fails to pass the hidden constraints barrier during iteration and stops.

The optimal design of an SMR process has lower HP pressure and propane composition and higher n-butane composition than the base case. In fact, the process simulator convergence of LNG-100 and LNG-101 highly depends on the composition of refrigerant, LP, and HP. Thus, the DIRECT with hidden constraint handling method can the point to where low HP pressure decreases the total compressor work ensuring convergence by changing the refrigerant composition. In Figure 3-16, the hot and cold composite curve of LNG-100 and LNG-101 shows that the composite curve of the optimal case from DIRECT with the sub-dividing step adjoin closer to each other than the base case. Thus, we can conclude that exergy efficiency, which represents the efficiency of the overall liquefaction process, of the optimal case is better than the base case. Furthermore, in Figure 3-17, the overall  $\Delta T$  profile of the optimal case is lower on average than the base case and the maximum  $\Delta T$  of the optimal case is 24.8 K while the base case is 46.9 K. Thus, although the minimum temperature approach of the two cases is the same, the optimal solution can have high efficiency. Finally, the heat exchanger separation line, which is the discrete heat flow line between LNG-100 and LNG-101, moves to the right in the optimal solution. The overall heat flow quantity of the optimal solution increases and most of that quantity is allocated to LNG-100 because the  $\Delta T$  profile of LNG-100 is better than for LNG-101.

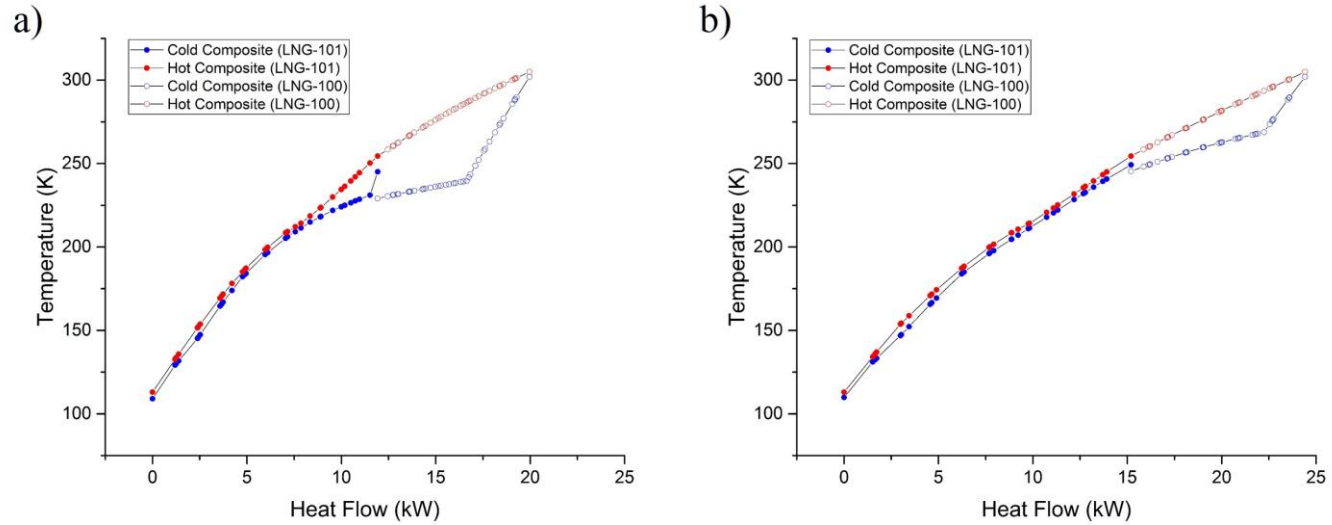


**Figure 3-16.** Hot and cold composite curve of a) base case and b) optimal solution of DIRECT algorithm with sub-dividing step.

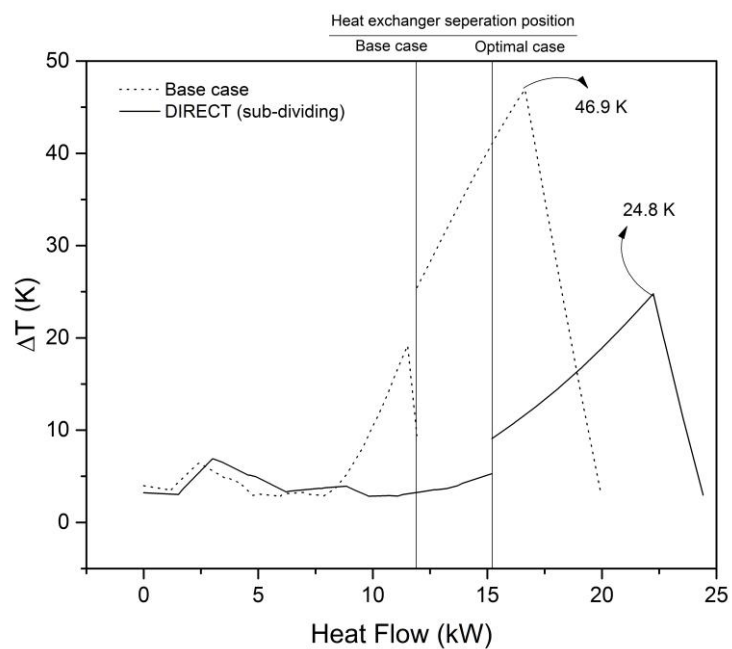


**Figure 3-17.**  $\Delta T$  profile in the cold box of base case optimal and DIRECT algorithm with sub-dividing step.

### 3.3.1.9. Conclusion

The modified DIRECT algorithm using sub-dividing steps is suggested as a means to handle hidden constraints. Unlike conventional methods such as the barrier approach and NAS, the sub-dividing step method can consider non-convex shape hidden constraints efficiently by partitioning the edge of the constraints. Thus, the DIRECT algorithm can search an expanded feasible searching area better than other methods. The DIRECT with sub-dividing step optimization decreases HP and increases n-butane content for lower compression specific power demands compared to the base case. To illustrate, the SMR NG liquefaction process with a commercial process simulator is optimized and provided a 18.9% better solution than the base case. In comparison with GA, PSO and SA, the proposed algorithm solves the problems of reproducibility and initial procedure of stochastic solver based on deterministic characteristics and efficiency of algorithm itself and DIRECT with sub dividing step provides 16.4%, 12.5%, 9.4% better solution respectively. The result is even 1.7% and 9.2% better than the DIRECT algorithm with other hidden constraint handling methods, the barrier approach and NAS, respectively. We strongly believe that the proposed algorithm has advantages for optimizing chemical processes, not only SMR process, but also many processes developed in a commercial simulator such as the Aspen HYSYS because of its non-linearity and non-convexity with a large hidden

constraints area. However, significant improvements on the original DIRECT algorithm and DIRECT with a sub-dividing step are required for a numerically robust and reliable solution. The proposed methodology cannot guarantee that which iterations are the best for the sub-dividing step. Moreover, not all infeasible hyper-rectangles but rather selected hyper-rectangles located in the edge of the hidden constraints should decrease the computation cost. Finally, if the DIRECT algorithm is modified for considering integer variables, then it can be applied for mixed integer non-linear programming (MINLP) problems such as mixed refrigerant selection, superstructure optimization of process design, and heat exchanger network synthesis (HENS).

### **3.3.2. Simultaneous synthesis of a heat exchanger network with multiple utilities using utility substages**

#### **3.3.2.1. Introduction**

In the last half-century, optimization of process synthesis with process integration has been applied in most important fields of research and industry for increasing price competitiveness. In particular, there has been a focus on heat exchanger network synthesis (HENS) designed for energy integration of utilities and process streams. A significant portion of annualized cost, which includes capital cost and operating cost, can be minimized by HENS. One of the main approaches with HENS is the sequential method, which applies heuristics or physical intuitions for dividing a problem into subproblems; this is represented by pinch technology. The other is the simultaneous method, which solves the problem using mathematical programming techniques such as mixed-integer non-linear programming (MINLP) without dividing a problem [152]. Recently, HENS has developed to the point of achieving global optimal solutions not only mathematically but also in reality; for instance, addressing uncertainty, non-isothermal mixing, and bypass streams [153, 154]. Thus, the research trend is focused on generalizing and expanding HENS models, which combine the optimization of simultaneous methods with the heuristics and realistic factors of sequential methods while reaching the global optimum in a feasible amount of computing time.

In general processes, multiple utilities should be considered for generating optimal networks. To illustrate this, a steam cycle with a CO<sub>2</sub> post-combustion capture process can use various low-pressure, medium-pressure, and high-pressure (LP, MP, and HP) utilities as heat sources for stripping columns, decrease reboiler stream cost relative to using just a single utility. Furthermore, using various working fluids in an organic Rankine cycle can reduce irreversibilities, decreasing compressor operating costs. However, most conventional HENS algorithms cannot synthesize networks with multiple utilities because they consider a single utility when composing the HEN [155].

HENS that consider multiple utilities were allegedly developed in several projects related to graphical techniques in the sequential method and mathematical techniques in the simultaneous method. In the sequential method field, Shenoy et al. [156] proposed a multiple-utility model based on the pinch method. Total annual cost (TAC) is minimized by calculating the optimal minimum approach temperature and utility combination. Other graphical technique research considers stream temperature versus enthalpy plot supertargeting (STEPS) for optimizing the minimum approach temperature [157]. For utility targeting in the sequential method, a non-graphical procedure using rigorously calculated process stream thermodynamic properties was suggested [158] in order to consider realistic situations. These kinds of sequential models have the advantages of simple calculations, intuitive

graphical visualization, and industrial feasibility. However, they contain the critical limitations inherent to sequential methods: inability to consider heat flows cross the pinch point and lack of a guarantee of a globally optimal network.

In the simultaneous methods field, Isafiade and Fraser [159] suggested an interval-based MINLP model with multiple utilities, but the assumption of fixed utility end site superstructure could not be surmounted. Moreover, by expanding stagewise superstructure, the modified model could place utilities anywhere else [160]. The proposed superstructure has new splitting streams, which involve multiple utilities in each conventional stage. Although modified HENS implements optimization with multiple utilities, it is hard to converge in many stages and analyzing a structure that contains subsequently arranged utilities is difficult because of inefficient superstructure geometry. Huang and Karimi [161] introduced generalized stagewise superstructure with cross flows and the model could nearly calculate a globally optimal network. However, even with the four utility simplification constraints, the problem had numerous discrete variables and constraints, which hampered calculations. Thus, in some examples, they set the time limitation on a solver related to global solver concepts such as BARON.

In this work, a new methodology is presented for solving HENS considering multiple utilities by using utility substages. The most important problems in



previous methods, namely a search area too large to find an optimal solution in a feasible amount of computing time and inefficient superstructure network, can be solved by using a modified superstructure. Using the utility substage concept, series connection of multiple utilities can be taken into account in one stage. Also, fixing positions of utilities heuristically in order of temperature in the modified superstructure can decrease the number of discrete variables. A reduced model size results and can enhance solution quality in the same number of stages or less compared to previous models.

### 3.3.2.2. Utility substage superstructure

The overall problem statement is similar to those of previous simultaneous HENS methods: finding the optimized structure of a heat exchanger network by using  $N_H$  hot streams and  $N_C$  cold streams along with possible combinations of input temperatures and heat capacity flow rates [155]. Basic assumptions and constraints for the superstructure such as constant heat capacity and flow rates, infeasible combinations of the same set of streams ( $N_H$ ,  $N_C$ ), and isothermal mixing are derived from conventional HENS problems considering multiple utilities. Several new sets and constraints related to utility substages are added to the model formulation because the model should describe the geometrical connection of a modified utility substage superstructure with multiple utilities. Five indices, namely  $i$ ,  $j$ ,  $m$ ,  $n$ , and  $k$ , representing hot streams, cold streams, hot utilities, cold utilities, and stages, respectively, are imposed on the model description to formulate the model effectively. Moreover, the superstructure properties, number of stages (NOK), number of hot utilities (NOM), and number of cold utilities (NON), are defined as scalar parameters and are fixed before solving a problem. Based on this discussion, each set is defined as:

$$HP = \{i | i \text{ is a hot process stream}\}$$

$$CP = \{j | j \text{ is a cold process stream}\}$$

$$HU = \{m | m \text{ is a hot utility, } m = 1, \dots, \text{NOM}\}$$

$CU = \{n|n \text{ is a cold utility, } n = 1, \dots, NON\}$

$ST = \{k|k \text{ is a stage in the superstructure, } k = 1, \dots, NOK\}$

$ST' = \{k|k \text{ is a stage in the superstructure, } k = 1, \dots, NOK+1\}$

To illustrate the modified superstructure, Figure 3-18 that contains a 2 by 2 stream system and m by n utility stream with 2 stages is shown. Existing between each conventional stage, the utility substage is the core idea of this modified superstructure. Series connection of multiple utilities via utility substages can easily consider the continuous connection of utilities and provides an opportunity to rapidly approach the global optimal solution. Although thermodynamic efficiency between the utility-stream heat exchanging system, which accounts indirectly for network preference owing to low heat exchanger area cost, is better than stream- stream heat exchanger systems, stream- stream heat exchangers should be considered because of the trade-off between utility cost and heat exchanger investment cost. Thus, vague situations, such as splitting one stream into two streams and designating one for stream/stream heat exchanger and another for stream/utility heat exchanger, have only a marginal chance of reaching an optimized solution. Therefore, it is better to expand the feasible search area to consider a large number of stages than to resort to conventional algorithms through deleting ambiguous network structure and adding high-probability structure. Even if the number of utilities increases, the number of stages would not increase because of the utility

substage. Moreover, the increasing number of variables and constraints is linear in the present approach, while previous research necessitated increasing the number of stages for considering utilities connected in series [160].

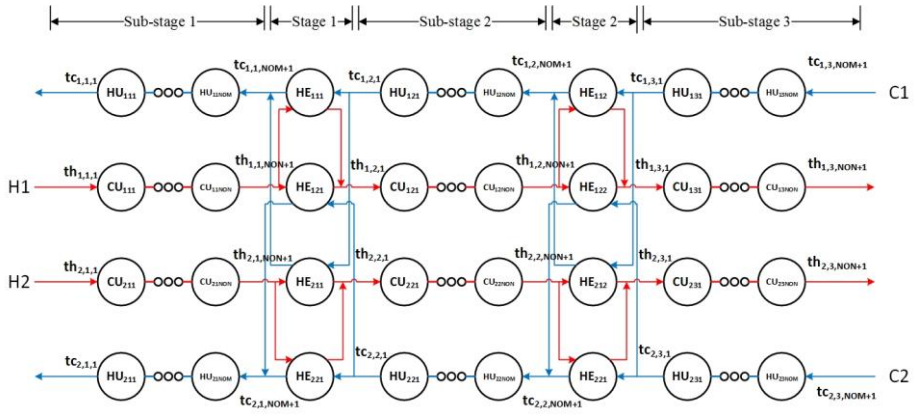


**Figure 3-18.** Utility substage superstructure.

Each of the multiple utilities that are connected by utility substages has a fixed location according to the order of its temperature. This heuristic structure is based on preceding research that suggested low-quality utilities be used prior to high-quality utilities to increase thermodynamic efficiency with decreasing operating cost [156]. Therefore, in the case of a hot utility, a low-temperature utility such as a low-pressure steam should be located before a high-temperature utility such as a high-pressure steam. On the contrary, in the case of a cold utility, a high-temperature utility such as hot oil should be located first, followed by a low-temperature utility such as chilled water. Hence, the series connection property of utility substages does not have a random combination, as it decreases the number of constraints and variables considered. Furthermore, it is possible to use the existing stage temperature variables  $th_{i,k,n}$  and  $tc_{j,k,m}$ , instead of using new variables for the utility substage, which only adds linear constraints (except for the heat exchanger area function).

### 3.3.2.3. Model formulation

Since utility substages are added to established conventional superstructure, the model formulation is also changed. Indices such as m and n are added to each variable of constraint to describe the utility substage. Moreover, binary variables, which express the existence of various utilities and heat exchangers, should be changed to three-dimensional variables involving the type of stream, stage number, and type of utility. The series connection property of utility substages presents linear constraints of added temperature variables except for the heat exchanger area function, which contains non-convexity.

#### - Overall heat balance for each stream

$$(TIN_i - TOUT_i)F_i = \sum_{j \in CP} \sum_{k \in ST} q_{i,j,k} + \sum_{k \in ST} \sum_{n \in CU} q_{cu,i,k,n} \quad i \in HP \quad [3-17]$$

$$(TIN_j - TOUT_j)F_j = \sum_{i \in HP} \sum_{k \in ST} q_{i,j,k} + \sum_{k \in ST} \sum_{m \in HU} q_{hu,j,k,m} \quad j \in CP \quad [3-18]$$

Overall heat balance is calculated by Equations [3-17] and [3-18] by multiplying the heat capacity flow rate, assuming constant temperature difference between inlet and outlet streams and constant total sum of heat being exchanged through all heat exchangers in the superstructure. It should be noted that additional terms of heat exchange between multiple utilities and stream ( $q_{hu,j,k,m}$ ,  $q_{cu,i,k,n}$ ) are linear.

- **Heat balance at each stage**

$$(th_{i,k,NON+1} - th_{i,k+1,1}) F_i = \sum_{j \in CP} q_{i,j,k} \quad i \in HP, k \in ST \quad [3-19]$$

$$(tc_{j,k,NOM+1} - tc_{j,k+1,1}) F_j = \sum_{i \in HP} q_{i,j,k} \quad j \in CP, k \in ST \quad [3-20]$$

A utility substage and a conventional stage can be connected by the temperature  $th_{i,k,n}$  between utility substage  $n-1$  and  $n$  of the cold utility at stage  $k$  and the temperature  $tc_{j,k,m}$  between utility substage  $m-1$  and  $m$  of the hot utility at stage  $k$ . Thus, Equations [3-19] and [3-20] can describe temperature balance on the overall superstructure continuously even if a conventional stage and utility substage are disconnected at a certain point, for instance, because of geometry. In other words, the last temperature of stage  $k$  equals the first temperature of utility substage  $k$ , and the last temperature of utility substage  $k$  equals the first temperature of stage  $k+1$ .

$$(th_{i,k,n} - th_{i,k,n+1}) F_i = qcu_{i,k,n} \quad i \in HP, k \in ST, n \in CU \quad [3-21]$$

$$(tc_{j,k,m} - tc_{j,k,m+1}) F_j = qhu_{j,k,m} \quad j \in CP, k \in ST, m \in HU \quad [3-22]$$

In the utility substage, the location of the utility is fixed in order of temperature, which is represented by the order of indices  $m$  and  $n$ . When the index number is higher, operating temperature of a utility is lower. Furthermore, heat balance can be simply formulated by Equations [3-21] and [3-22]. The temperature difference because of series connection property and model does not need additional hot and cold utility load constraints.



**- Assignment of superstructure temperatures and feasibility of temperatures**

$$th_{i,1,1} = TIN_i \quad i \in HP \quad [3-23]$$

$$tc_{j,1,1} = TOUT_j \quad j \in CP \quad [3-24]$$

$$th_{i,NOK+1,NON+1} = TOUT_i \quad i \in HP \quad [3-25]$$

$$tc_{j,NOK+1,NOM+1} = TIN_j \quad j \in CP \quad [3-26]$$

Inlet temperatures and outlet temperatures of streams are interlocked with the superstructure end site temperature in Equations [3-23]-[3-26]. Unlike previous single-utility superstructure, which has the asymmetric structure property, it is not necessary to add an end-site utility temperature constraint (Yee and Grossmann, 1990).

$$th_{i,k,n} \geq th_{i,k,n+1} \quad i \in HP, k \in ST', n \in CU \quad [3-27]$$

$$tc_{j,k,m} \geq tc_{j,k,m+1} \quad j \in CP, k \in ST', m \in HU \quad [3-28]$$

$$th_{i,k,n} \geq th_{i,k+1,1} \quad i \in HP, k \in ST \quad [3-29]$$

$$tc_{j,k,m} \geq tc_{j,k+1,1} \quad j \in CP, k \in ST \quad [3-30]$$

Temperature order at the utility substage can be described by the ordering of  $m$  and  $n$  with inequality constraints. Conventional stage temperature order is easily described by the ordering of  $k$ . Equations [3-27]-[3-30] describe the feasibility of temperatures.

- **Logical constraints**

$$q_{i,j,k} - M z_{i,j,k} \leq 0 \quad i \in \text{HP}, j \in \text{CP}, k \in \text{ST} \quad [3-31]$$

$$q_{cu_{i,k,n}} - M z_{cu_{i,k,n}} \leq 0 \quad i \in \text{HP}, k \in \text{ST}', n \in \text{CU} \quad [3-32]$$

$$q_{cu_{i,k,n}} - M z_{cu_{i,k,n}} \leq 0 \quad i \in \text{HP}, k \in \text{ST}', n \in \text{CU} \quad [3-33]$$

The binary variable  $z_{i,j,k}$  denotes existence of a heat exchanger between hot stream  $i$  and cold stream  $j$  at stage  $k$ . If the value of  $z_{i,j,k}$  is zero, then  $q_{i,j,k}$  will also be zero because a heat exchanger does not exist. When  $z_{i,j,k}$  is unity, the “big  $M$ ” constraint will be activated for calculating  $q_{i,j,k}$  within the upper bound,  $M$ . To shrink the search area as much as possible during consideration of the feasible search area containing the optimal point, the value of  $M$  is defined as  $\min \left( (TIN_i - TOUT_i) F_i, (TIN_j - TOUT_j) F_j \right)$ . Therefore,  $q_{i,j,k}$  can be calculated within the physical maximum heat exchange rate between hot stream  $i$  and cold stream  $j$ ; this is represented in Equation [3-31]

Additionally,  $z_{hu_{j,k,m}}$  and  $z_{cu_{i,k,n}}$  are the binary variables, which denote the existence of hot and cold utilities, respectively. The value of zero indicates that the hot or cold utility does not exist, and when the value is unity, the solver searches for the optimal  $q_{hu_{j,k,m}}$  and  $q_{cu_{i,k,n}}$  within the upper bound constraint. In the utility case, it is assumed that there is no limitation of the heat exchange rate on utilities. Hence, it is possible to fix the upper bound constraint as

$(TIN_i - TOUT_i) F_i$  and  $(TIN_j - TOUT_j) F_j$ . In this feasible search area,  $qhu_{j,k,m}$  and  $qcu_{i,k,n}$  are calculated by Equations [3-32] and [3-33].

$$\sum_{m \in HU, n \in CU} zcu_{i,k,n}, zhu_{j,k,m} = \theta \quad i \in HP, j \in CP, k \in ST' \quad [3-34]$$

Optionally, it is possible to accelerate calculation speed by restricting the maximum number of multiple utilities to  $\theta$ . If the number of opportunities to connect the utility in series is low, Equation [3-34] can be implemented to construct multiple utilities practically.

#### - Calculation of approach temperatures

$$dth_{i,j,k} \leq th_{i,k,NON+1} - tc_{j,k,NOM+1} + \gamma_{i,j} * (1 - z_{i,j,k}) \quad i \in HP, j \in CP, k \in ST \quad [3-35]$$

$$dtr_{i,j,k} \leq th_{i,k+1,1} - tc_{j,k+1,1} + \gamma_{i,j} * (1 - z_{i,j,k}) \quad i \in HP, j \in CP, k \in ST \quad [3-36]$$

$$dthu_{j,k,m} \leq TINhu_m - tc_{j,k,m} + \gamma_{j,m} * (1 - zhu_{j,k,m}) \quad j \in CP, k \in ST', m \in HU \quad [3-37]$$

$$dthu_{j,k,m+1} \leq TOUThu_m - tc_{j,k,m+1} + \gamma_{j,m} * (1 - zhu_{j,k,m}) \\ j \in CP, k \in ST', m \in HU \quad [3-38]$$

$$dteu_{i,k,n} \leq th_{i,k,n} - TOUTcu_n + \gamma_{i,n} * (1 - zcu_{i,k,n}) \\ i \in HP, k \in ST', n \in CU \quad [3-39]$$

$$dteu_{i,k,n+1} \leq th_{i,k,n+1} - TINcu_n + \gamma_{i,n} * (1 - zcu_{i,k,n}) \\ i \in HP, k \in ST', n \in CU \quad [3-40]$$

$$dth_{i,j,k}, dtr_{i,j,k}, dthu_{j,k,m}, dteu_{i,k,n} \geq EMAT \quad [3-41]$$

For defining the temperature driving force of heat exchangers, each approach temperature can be formulated using Equations [3-35]-[3-41].

Because of the discontinuous network of a conventional stage, the approach temperature of a stream/stream heat exchanger should be modified as the approach temperature on the left and right sides in Equations [3-35] and [3-36]. As with other mixed-integer constraints, the upper bound method is used to activate and deactivate each constraint.  $\gamma$ , which denotes  $M$  in the upper bound constraint method, represents the maximum approach temperature between two streams including the multiple utilities, which constitute the heat exchanger. Thus, the model can efficiently cover all of the feasible search area. Moreover, the exchanger minimum approach temperature (EMAT) can be set by Equation [3-41] when the user wants to define the approach temperature boundary. An important note is that even when a user-set EMAT is provided for some value, the optimal solution EMAT might not have been exactly the value that the user set initially, but rather some value that optimizes the objective functions. Inlet and outlet approach temperatures for each utility are set separately and can be formulated continuously because of the series connection with fixed positions.

#### **- Objective function and heat exchanger area function**

Chen's approximation, which is one of the most popular logarithmic mean approximations in the HENS area, is used for comparing efficiency of the present model with that of previous algorithms [162]. This log mean temperature difference (LMTD) has been used for describing heat exchanger area function in recent simultaneous HENS models involving multiple utilities.

$$LMTD_{i,j,k} = \left[ (dtl_{i,j,k}) (dtr_{i,j,k}) \left( \frac{dtl_{i,j,k} + dtr_{i,j,k}}{2} \right) \right]^{\frac{1}{3}} \quad [3-42]$$

$$A_{i,j,k} = \frac{q_{i,j,k} \left( \frac{1}{h_i} + \frac{1}{h_j} \right)}{LMTD_{i,j,k}} \quad [3-43]$$

Heat exchanger area can be calculated by Equations [3-42] and [3-43] using a constant heat transfer coefficient for each stream, constant rate of heat exchange between the two streams, and LMTD. The area of hot and cold utility heat exchangers can be calculated in the same way as for stream heat exchangers. Therefore, the objective function, also called total annualized cost, is expressed by summation of utility cost and investment cost as in Equation [3-44]:

$$\begin{aligned} \min_{x_H \in \Omega_H} & \left( \sum_{i \in HP} \sum_{k \in ST'} \sum_{n \in CU} CCU_n q_{i,k,n} + \sum_{j \in CP} \sum_{k \in ST'} \sum_{m \in HU} CHU_m q_{j,k,m} \right) \\ & + \left( \sum_{i \in HP} \sum_{j \in CP} \sum_{k \in ST} CF_{i,j} z_{i,j,k} + \sum_{i \in HP} \sum_{k \in ST'} \sum_{n \in CU} CFC_{i,n} zcu_{i,k,n} \right. \\ & \quad \left. + \sum_{j \in CP} \sum_{k \in ST'} \sum_{m \in HU} CFH_{j,m} zhu_{j,k,m} \right) \\ & + \left( \sum_{i \in HP} \sum_{j \in CP} \sum_{k \in ST} C_{i,j} A_{i,j,k}^{\beta} + \sum_{i \in HP} \sum_{k \in ST'} \sum_{n \in CU} CC_{i,n} Acu_{i,k,m}^{\beta_{cu}} \right) \\ & \quad + \sum_{j \in CP} \sum_{k \in ST'} \sum_{m \in HU} CH_{j,m} Ahu_{j,k,n}^{\beta_{hu}} \end{aligned} \quad [3-44]$$

### **3.3.2.4. Numerical application**

Since the suggested model in this paper presents a non-convex MINLP considering multiple utilities, model size is bigger than in the conventional, single-utility SYNHEAT model. However, the utility substage model can provide a better result with fewer continuous variables, discrete variables, and constraints than the other simultaneous multiple-utility models presented by Ponce-Ortega et al. [160] and Haung and Karimi [161]. Although some cases yield larger TAC than in the non-isothermal mixing model because the present model is based on isothermal mixing and stream splitting, this model has several advantages; for instance, its small model size expands the feasible search area, especially in cases of numerous utilities and scenario analysis for various conditions. To validate the efficiency of the utility substage model, several examples are presented. In terms of mathematical programming, BARON/GAMS and LINDOglobl/GAMS, which are deterministic global algorithms based on branch-and-bound methods, and DICOPT/GAMS, which divides the MINLP problem into NLP-MIP subproblems using outer approximation, are used as solvers. The programming language used is GAMS 24.2.1 and MINLP subsolvers are CONOPT 3 (NLP solver) and Cplex 12.6 (MIP and LP solver).

### - Example 1

This is a classical problem from Shenoy et al. [156] and other researchers who invented the modified HENS model considering multiple utilities and has been used to validate their respective models. In this example, two hot streams, one cold stream, a hot utility for HP, MP, and LP steam, and chilled water for a cold utility should be combined to make an optimal network system. Table 3-9 summarizes stream information and parameters for example 1 and Figure 3-19 shows the optimized HEN. The obtained TAC is \$96,076, which is a lower cost than in any previous literature. The main factor of this result comes out from considering many stages with small model size, helping to expand the search area. Comparing model size with the result in Table 3-12, the number of constraints and variables are reduced by 45% and 70%, respectively, compared with results in recent literature. In fact, part of the utility cost is reduced further compared with the solution of Ponce-Ortega et al. [160] because they use two types of hot utility while this model uses three types of hot utility, distributing heat duty more efficiently. Moreover, comparing this model with model of Huang and Karimi [163], considering a number of stages with feasible model size can easily expand the network connecting heat exchangers with utilities. Thus, right side of network is totally different and it decreases more utility cost with little increasing of investment cost by efficient heat load distribution. From the efficiency of the utility sub stage super-structure in considering many stages,

it is evident that small model size helps to converge the solution near to the global optimum.



**Table 3-9.** Stream information and cost function for example 1.

Stream	TIN (oC)	TOUT (oC)	F (kW K-1)	h (kW m <sup>2</sup> K-1)	Cost (\$ kW-1 yr-1)
H1	105	25	10	0.5	-
H2	185	35	5	0.5	-
C1	25	185	7.5	0.5	-
HP Steam	210	209	-	5.0	160
MP Steam	160	159	-	5.0	110
LP Steam	130	129	-	5.0	50
Chilled water	5	6	-	2.6	10
Exchanger capital cost = 800 (area)					
Annualization factor = 0.298					

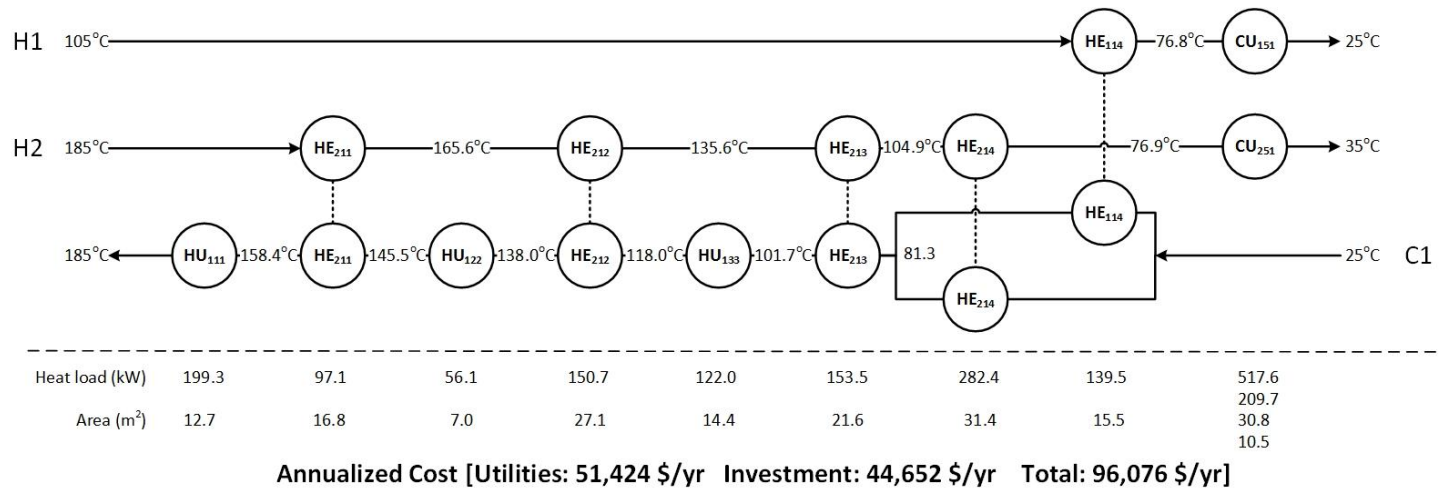


**Figure 3-19.** Optimized HEN with heat load, heat exchanger area, and annualized cost data for example 1.

## - Example 2

Like example 1, this example is also a representative problem from Shenoy et al. [156] and has been solved in various projects related to multiple-utility HENS. The solution depends strongly on the efficiency of the model related to superstructure because the model size of problem is quite large, consisting of two hot streams, three cold streams, three types of hot utility (HP, MP, and LP steam), and two types of cold utility (chilled water and air cooling). Table 3-10 summarizes stream information and parameters for example 2. The model can expand its search area to consider non-isothermal mixing and to expand the number of stages. Although, the utility substage model assumes isothermal mixing for stream splitting, because of its heuristically efficient superstructure, series connection of multiple utilities, and temperature-order fixed position, the model can consider a large number of stages with few variables and constraints. For global-search solvers such as BARON/GAMS and LINDOglobal/GAMS, convergence of MINLP problems depends strongly on model size and convexity; the present model has characteristics that accelerate for the case of equal upper and lower bounds. Figure 3-20 describes the optimized HEN of example 2. Table 3-12 compares this model, with which the minimum TAC is obtained, with other isothermal mixing multiple-utility HENS models. Even though the competing models are based on non-isothermal mixing, such as the work by Huang and Karimi [164], the utility substage model gives a better

solution than when the model is solved with commercial solvers such as BARON, DICOPI, and SBB. Only the non-isothermal mixing models produce slightly better TAC when they use modified solvers with the newly proposed outer approximation algorithm.

**Table 3-10.** Stream information and cost function for example 2.

Stream	TIN (oC)	TOUT (oC)	F (kW K-1)	h (kW m <sup>2</sup> K-1)	Cost (\$ kW-1 yr-1)
H1	155	85	150	0.5	-
H2	230	40	85	0.5	-
C1	115	210	140	0.5	-
C2	50	180	55	0.5	-
C3	60	175	60	0.5	-
HP Steam	255	254	-	0.5	70
MP Steam	205	204	-	0.5	50
LP Steam	150	149	-	0.5	20
Cold water	30	40	-	0.5	10
Air cooling	40	65	-	0.5	5
Exchanger capital cost = 13000 + 1000 (area) <sup>0.83</sup>					
Annualization factor = 0.322					

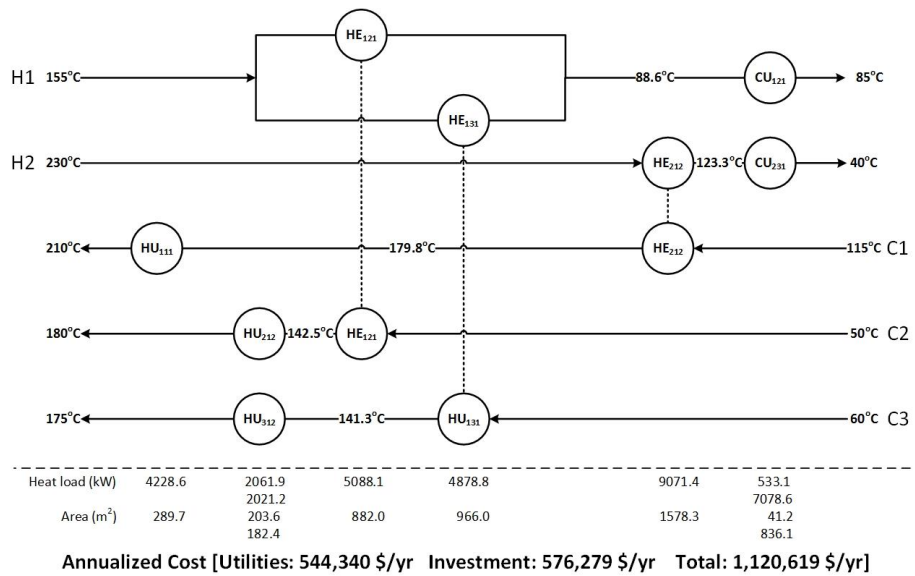


**Figure 3-20.** Optimized HEN with heat load, heat exchanger area, and annualized cost data for example 3.

### - Example 3

Example 3 is a newly proposed problem in this paper for illustrating how direct series connection of multiple utilities can help to reach the optimum. In fact, the utility substage superstructure has the power to present series connection of utilities because of its geometric characteristics. Thus, this example emphasizes the advantages of using the utility substage superstructure. Table 3-11 describes the stream information and the cost function. Imagining the composite curve, expensive HP or MP steam should be replaced by cheap LP steam or hot oil. Moreover, if the number of hot utilities increases and fixed costs of heat exchangers decrease, then series connection of the hot utilities will be attractive. To verify this alternative, we compared with the conventional simultaneous method, SYNHEAT, and modified a multiple-utility models, which considers only one utility at one stage, similar to the previous model, with the utility substage model proposed in this paper. In this example, Paterson's LMTD approximation described in Equation [3-45] is substituted into the objective function [165]. The reason for using this LMTD is that Huang et al. [153] found Paterson's LMTD to be the best, it is used by and recent simultaneous models.

$$\text{LMTDP}_{i,j,k} = \left[ \frac{1}{6} (\text{dtl}_{i,j,k} + \text{dtr}_{i,j,k}) + \frac{2}{3} \left( (\text{dtl}_{i,j,k})(\text{dtr}_{i,j,k}) \right) \right]^{\frac{1}{2}} \quad [3-45]$$

As a result in Figure 3-21, TAC is reduced by 45.6% compared with the result from SYNHEAT and by 21.0% compared with one utility in the one-stage model under the same calculation conditions (e.g., using three stages) on the GAMS/BARON solver. This phenomenon occurs when utility cost is the major cost in the TAC and various utilities can be used as alternatives. Since the utility substage model is optimized for considering series connection of utilities, it is possible to obtain very effective solutions even considering small stages. If a cheap but low-quality utility and an expensive but thermally effective utility were interlaced with a trade-off relation, it is difficult to analyze using only the composite curve. However, the simultaneous multiple-utility model can consider all combinations with a wide search area for reaching the optimal solution. An optimal utility system is constructed, dividing the heat duty of HP steam and LP steam to less expensive MP steam and hot oil, respectively and it is easily seemed in Figure 3-22. Although the utility substage model synthesizes a network in which heat duty of cold utilities is higher than in other networks, it is possible for it to reach the lowest annualized cost because this example is a hot-utility-dominated case. Theoretically, it is possible to construct an optimal structure (Figure 3-21c) with two stages by using the utility substage model. However, previous models such as Ponce-Ortega et al. [160] need at least seven stages to synthesize the same optimal structure. Because of MINLP problem characteristics, it is difficult to converge within a feasible computation time.



**Table 3-11.** Stream information and cost function for example 3.

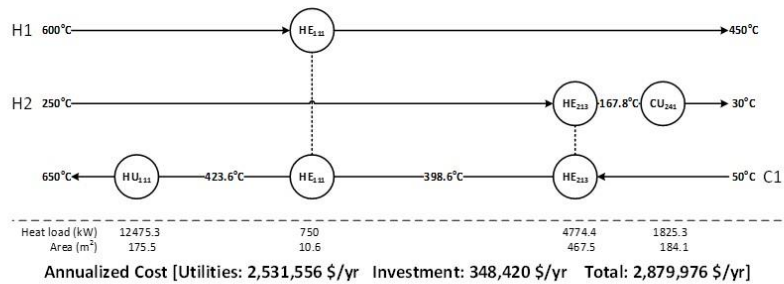
Stream	TIN (°C)	TOUT (°C)	F (kW K <sup>-1</sup> )	h (kW m <sup>2</sup> K <sup>-1</sup> )	Cost (\$ kW <sup>-1</sup> yr <sup>-1</sup> )
H1	600	450	5	0.5	-
H2	250	30	30	0.5	-
C1	50	650	30	0.5	-
HP Steam	680	680	-	5	200
MP Steam	630	630	-	5	150
LP Steam	400	400	-	5	45
Hot Oil	330	300	-	5	10
Chilled water	20	25	-	1	20
Stream exchanger capital cost = 500 (area)					
Cold utility exchanger capital cost = 500 (area)					
Hot utility exchanger capital cost = 100 (area)					

**Table 3-12.** Solution comparison for examples 1-3 regarding total annualized cost and model size.

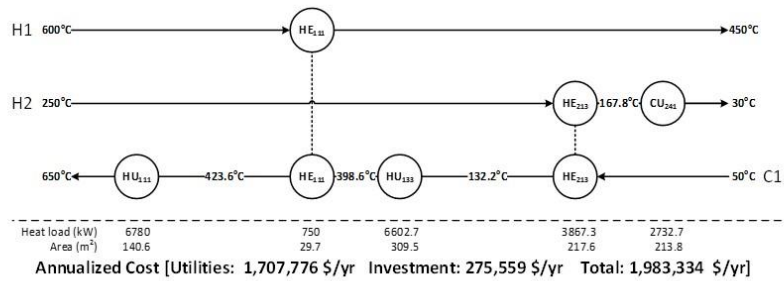
Example	TAC (\$)		Model size (equations, continuous variables, discrete variables)	
	This work	Literature	This work	Literature
1	96,076	96,937 <sup>a</sup> 97,079 <sup>b</sup> 97,211 <sup>c</sup> 98,263 <sup>d</sup>	(291, 184, 48)	(511, 501, 120) <sup>b</sup>
2	1,120,619	1,115,705 <sup>e</sup> 1,120,271 <sup>e</sup> 1,120,711 <sup>e</sup> 1,135,773 <sup>e</sup> 1,121,175 <sup>e</sup> 1,150,460 <sup>c</sup> 1,158,500 <sup>d</sup>	(827, 475, 114)	(2236, 889,38) <sup>e</sup> (320, 174, 25) <sup>e</sup> (1391, 1442, 360) <sup>b</sup>
3	1,567,144	-	(253, 151, 30)	-

a: [163], b: [160], c: [159], d: [156], e: [164]

a)



b)



c)

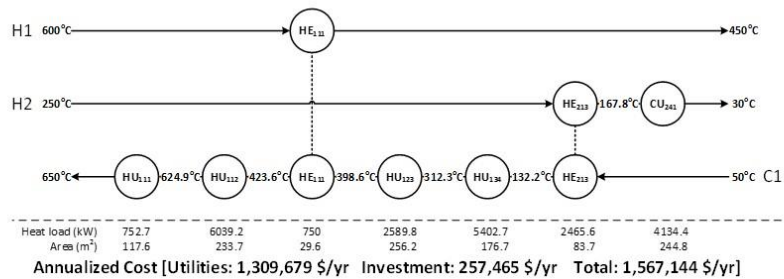


**Figure 3-21.** Optimized HEN with heat load, heat exchanger area, and annualized cost data for example 4 calculated by a) SYNHEAT, b) restricting series connection of utility, and c) utility substage superstructure.

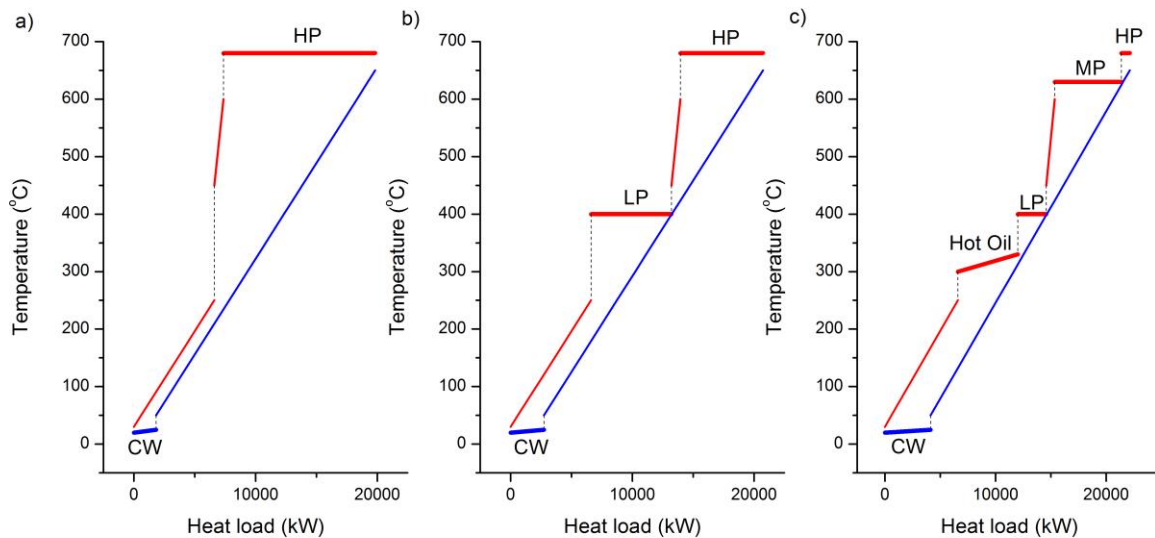


**Figure 3-22.** Composite curve for example 4 calculated by a) SYNHEAT, b) restricting series connection of utility, and c) utility substage superstructure.

### **3.3.2.5. Conclusion**

Developing an effective simultaneous model with multiple utilities for application to various process syntheses is a highly challenging area of process integration research. In previous literature, there have been several limitations to synthesis of multiple-utility HEN, including pinch method limitations, single-utility simultaneous model, and very large size of multiple-utility simultaneous models. In this work, the utility substage superstructure, which features temperature-order fixed position of multiple utilities with series connection, is suggested. The new algorithm obtains even smaller model size than in previous algorithms and a better heat exchanger network solution. From assessing the TAC and the number of variables and constraints, it is verified that the heuristics and modified factors of the utility substage superstructure are effective. Furthermore, it is verified in the case of existing various utilities and low fixed cost that series connection of multiple utilities can be effective for decreasing TAC, especially utility operating cost; our algorithm is optimized for solving problems of this kind. Considering the same number of stages, TAC is reduced by 45.6% compared with the SYNHEAT model result and 21.0% compared with the single utility result in the single-stage model.

Although several problems remain, which preclude a guarantee of the global optimum in cases requiring consideration of stream bypassing and non-isothermal mixing, the present research demonstrates the significant power of

the utility substage algorithm in treating multiple utilities effectively with small model size, which is the most important issue for multiple-utility problems.

### **3.4. Plant-wide systems scale modeling and optimization**

#### **3.4.1. Toxic gas release modeling for real-time analysis using variational autoencoder with convolution neural networks**

As the chemical engineering industry grows steadily, concerns about catastrophic accidents in chemical plants have increased. Among the various types of accidents in chemical processes, toxic gas leaks are particularly critical owing to the wide range of the risks involved. When toxic gas dispersion occurs, a toxic gas cloud is generated and remains in the accident area. If the concentration of the toxic gas is above a certain level, the local population is subjected to serious health hazards. When an accident occurs in a densely populated area, e.g., an urban area, the risk becomes even higher. On December 3, 1984, for example, a methyl isocyanate gas leak accident caused at least 3800 deaths and about 100,000 permanently disabled in Bhopal, India [166]. Therefore, methods for predicting gas dispersion in accidents in urban areas are essential. However, toxic gas dispersion experiments are difficult to implement owing to cost, risk, and technical requirements.

To resolve this, computer simulation has been developed to model gas dispersion. There are two-dimensional integral models, viz. the Box model and Gaussian dispersion models, [167] and simulators (ALOHA and PHAST), which can be used in emergency owing to their short computation time. They

are fairly accurate in the case of flat terrain without three-dimensional obstacles. However, they have low accuracy in the case of three-dimensional obstacles, such as mountains and buildings, as these obstacles are ignored. Moreover, they do not change dynamically, as they are based on the steady state. Thus, it is difficult to use these tools in actual emergency situations [168, 169].

Computational fluid dynamics (CFD) is widely used to accurately simulate the dispersion of toxic chemicals in urban areas. CFD has the highest accuracy because it takes into account geographic information and gas characteristics. The CFD model in urban areas has been developed in various studies. Hanna et al. [170] described and compared five CFD models using gas dispersion experimental data from Madison Square Garden in Manhattan (MSG05). Hanna et al. [171] simulated a hypothetical chlorine railcar accident in the Chicago urban area using FLACS and compared the results with those obtained by simpler models, such as SLAB, HGSYSTEM, and ALOHA. Likewise, Long et al. [172] compared a gas dispersion CFD model (AcuSolve) and the Urban Dispersion Model (HPAC) in regions with large obstacles. Xie et al. [173] modeled gas flow and dispersion in London using large eddy simulation.

However, CFD-based simulation models have a critical disadvantage, i.e., computation cost. Most accident scenarios require more than 1 h for simulation in CFD-based tools, such as FLACS, Fluent, and OpenFOAM [171, 174, 175]. When a toxic gas spill occurs, the simulation time must be at least less than the



golden time, also known as golden hour, to effectively predict the extent of the accident and evacuate the population. However, there are currently no CFD-based tools for simulating accidents faster than the golden time. Hence, these tools cannot practically be used in real-time alarm systems. Therefore, there is a need for computationally efficient methods that are as accurate as CFD. Therefore, research on surrogate or meta-models has been conducted to simplify complex models and shorten computation time. Palmer and Realff [176] and Caballero and Grossmann [177, 178] used surrogate models based on kriging functions to optimize flowsheet simulation. Gomes et al. [179] used kriging models for real-time process optimization. Chen et al. [180] applied meta-models of complex process simulations with time-space-dependent output adopting Gaussian process regression. Moreover, Wang et al. [181] achieved data reduction using segPCT-PCA and Gaussian process regression (GPR) meta-models. Loy et al. [182] developed and compared two surrogate models for consequence analysis based on CFD, i.e. a non-linear global surrogate model (least squares support vector machine) and a linear piece-wise surrogate model (linear nearest neighbor interpolation). Research for developing a meta-model has been steadily progressing, and methods such as kriging (Gaussian process model) and support vector machines have been primarily used. In addition, Kajero et al. [183] has reviewed other methods for this meta-modeling.

Three steps are required for designing a surrogate model based on large amounts of data: data reduction, data regression, and data reconstruction. In most of the studies mentioned above, since data reduction uses a linear method such as PCA, it is often difficult to distinguish nonlinear manifolds or to store image information with complex nonlinearities. Therefore, a training technique for the representation of an unlabeled data set through an autoencoder has been developed. An autoencoder is a learning system based on artificial neural networks that can efficiently learn and compress input information. Autoencoders are composed of an encoder (recognition network), a decoder (generative network), and hidden layers (internal representation). Since autoencoders are based on neural networks and can operate in various combinations, they achieve sufficient dimensionality reduction even for data sets with strong nonlinearity. Moreover, when combined with a convolutional neural network (CNN), they can perform powerful feature detection, which is a significant performance improvement [184]. Finally, a variational autoencoder that extends to a generative model based on the latent space generated by features of the training set has been developed as a powerful model that can generate images by extracting definite features and changing their values [185]. Therefore, it would be a powerful meta-modeling, with the addition of the regression process that performs the mapping between the important variable and the encoded data or the latent space from the autoencoder.

In regard to regression, various methods are used, such as linear regression and artificial neural networks. Recently, various methods have been introduced to deep neural networks (DNN) and resolved the issues of vanishing gradient, excessively low learning speed, and overfitting the training set [186]. For example, initialization methods have been introduced [187, 188]. Moreover, the ReLU activation function, which exhibits better performance than the sigmoid activation function, and the Mother Nature activation function appeared in the theory of deep networks. In addition, non-saturating activation functions, such as the leaky ReLU, ELU, and SeLU, were introduced, improving performance. It is obvious that these methods can reduce the vanishing and exploding gradient problems at the beginning of training state; however, these may occur during the learning state. To resolve this, zero-centering and normalization of the input are required before the activation function through the Batch Normalization (BN) method proposed by [189] and subsequent scaling and shifting of the results. Moreover, techniques such as momentum optimization, Nesterov Accelerated Gradient, AdaGrad, RMSProp, and Adam optimization have been developed to optimize machine learning. Adam (Adaptive Momentum Estimation) optimization is performed by combining Momentum optimization and the RMSProp algorithm [190]. Therefore, it is highly likely to develop high-performance surrogate models using this state-of-the-art deep learning technique for data reduction with high-quality feature extraction, data

regression of highly non-linear manifold, and generation or reconstruction of the image data by means of generative models.

In this study, a gas leak model of industrial-scale was developed for the Mipo complex in the city of Ulsan, Republic of Korea, using FLACS. Moreover, a surrogate model was constructed for real-time applications, namely, a real-time alarm system within golden time. Initially, for the scenario where three variables (wind speed, wind direction, release rate) were randomly applied, the data was obtained by CFD and the probability of death factor ( $P_{\text{death}}$ ) was expressed as a 2D image. Subsequently, using a variational autoencoder with deep convolutional layers, the resulting data of dimension 30,400 was compressed into a 32-dimensional latent space. Through the deep neural network architecture designed by the authors, the variable space was mapped into the latent space to predict the 32-dimensional latent space with 3 variables. Finally, a surrogate model was constructed that can generate the predicted contour of  $P_{\text{death}}$  through three variables only. The effectiveness and applicability of the model was demonstrated by comparison with several other methods of regression. It was shown that the model does not merely memorize the  $P_{\text{death}}$  contour but rather extracts features and smoothly generates the image.

### **3.4.1.1. Toxic gas dispersion model**

In this study, FLACS (Flame Acceleration Simulator) is utilized as a gas dispersion CFD tool. The version of FLACS used is v10.4 released in July 27th, 2015 and developed by Gexcon. FLACS was originally developed for explosion simulation. However, FLACS may also simulate gas dispersion and fire models. A number of studies have been conducted to verify the accuracy of the atmospheric dispersion model of FLACS used in this study. Hanna [171] modeled an actual chlorine leakage accident in an urban area and compared the results with the accident data. In addition, Yang et al. [175] compared the hydrogen fluoride leakage accidents in the Gumi area in Korea with the FLACS simulation results. In addition, several studies have been carried out to validate gas diffusion experiments performed under various conditions, not actual accidents, with FLACS [174, 191-193]

#### **- Model description**

The Mipo complex in the city of Ulsan, Republic of Korea, has a large number of industrial plants as well as a residential area nearby. Thus, this region has a high potential of not only gas leakage accidents but also considerable damage in case of such an accident. Therefore, it was selected as a virtual gas leakage accident site. In the model, seen on the left side of Figure 3-23, flat terrain with thousands of buildings was assumed. The size of the entire domain

is about 4,000 m in the  $x$ -direction, 3,000 m in the  $y$ -direction, and 80 m in the  $z$ -direction (from ground level). The CAD image inside FLACS can be seen on the right side of Figure 3-23. As more than 500 simulation data points are required, a uniform grid resolution of  $20\text{ m} \times 20\text{ m} \times 20\text{ m}$  was used to reduce computation cost.

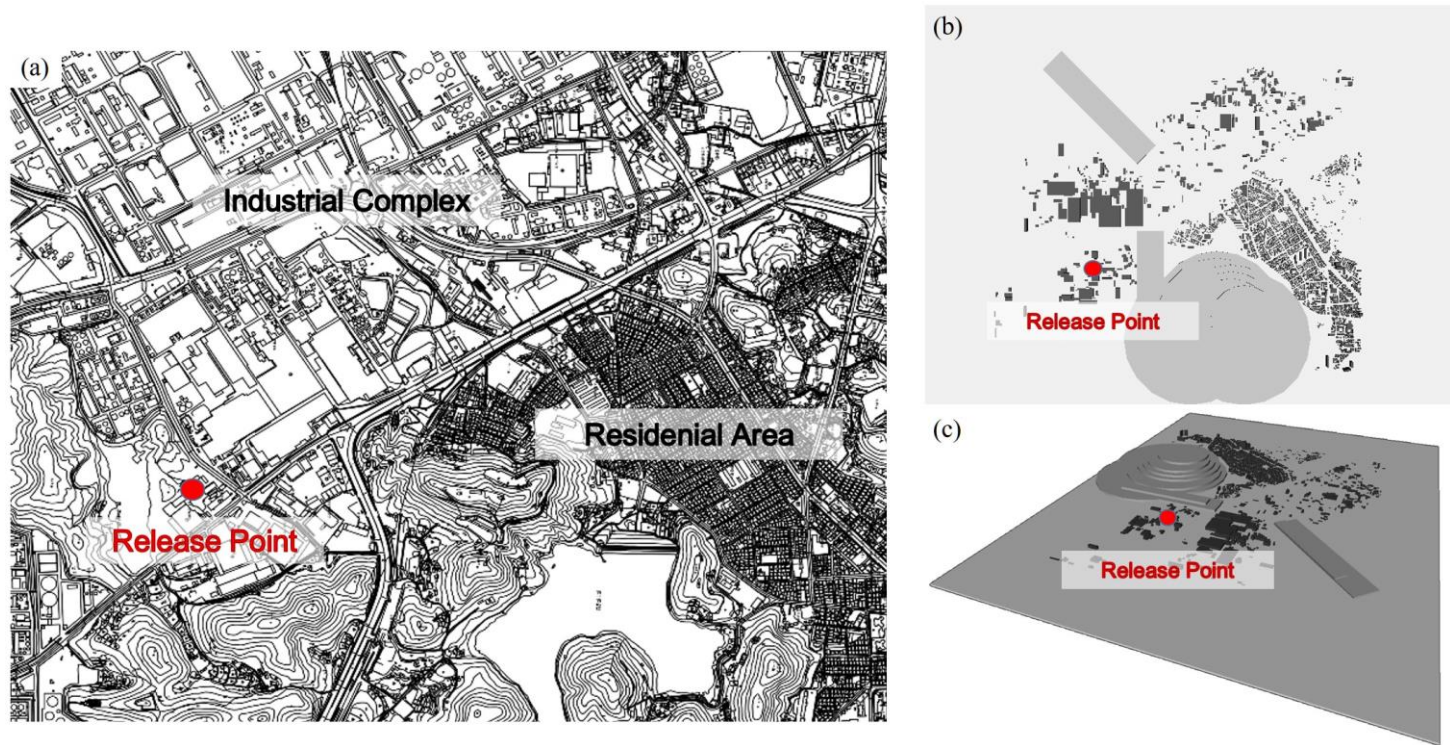


**Figure 3-23.** (a) The geometry of Mipo complex in Ulsan, (b) top view of CAD image, and (c) 3D view of CAD image in FLACS.

As liquefied chlorine is used on a large scale in this area for industrial purposes, chlorine was chosen as the material of the hypothetical release scenario. To generate distinct simulation samples, three main variables were randomly selected within a certain boundary. Wind direction was chosen within  $0 - 2\pi$ , wind speed within 0.5~5 m/s, and release rate within 10~100 kg/s. All other variables were fixed, including release duration (60 s), release point, release material, and temperature (20° C). The entire simulation time in all cases was set to 1000 s. The conditions of the simulation are summarized in Table 3-13.



**Table 3-13.** Scenario conditions

Variable	Unit	Value
Ambient temperature	°C	20
Ambient pressure	Bar	1
Wind direction	rad	0 - $2\pi$
Wind speed	m/s	0.5 – 5
Discharge rate	kg/s	10 – 100
Discharge direction	-	+Y
Release duration	s	60
Total simulation time	s	1000
Pasquill class	-	None

## - Mathematical formulation

FLACS calculates the compressible fluid flow using conservation equations for mass, energy, and momentum. It solves the three-dimensional Reynolds-averaged Navier–Stokes (3D RANS) equations, which are widely used in CFD, based on the  $k$ - $\varepsilon$  turbulence model [194] on a non-uniform Cartesian mesh. The  $k$ - $\varepsilon$  model is an eddy viscosity model with turbulent kinetic energy transport and dissipation of the turbulent kinetic energy equation. In particular, FLACS uses distributed porosity concepts [195] to efficiently calculate the effect of obstacles smaller than the sub-grid on fluid flow. This approach not only considers small obstacles but also reduces computational cost. In this study, two governing equations for compressible fluid flow are used: conservation of mass and momentum equation. The conservation of mass equation can be written as

$$\frac{\partial}{\partial t}(\beta_v \rho) + \frac{\partial}{\partial x_j}(\beta_j \rho u_j) = \frac{\dot{m}}{V}, \quad [3-46]$$

where  $\beta_v$  denotes volume porosity and  $\beta_j$  area porosity in the  $j$ -direction. Here,  $j$  is any of the directions determined by the Cartesian coordinates  $x$ ,  $y$ , and  $z$ . The momentum equation can be written as

$$\begin{aligned} \frac{\partial}{\partial t}(\beta_v \rho u_i) + \frac{\partial}{\partial x_j}(\beta_j \rho u_i u_j) = & -\beta_v \frac{\partial P}{\partial x_i} + \frac{\partial}{\partial x_j}(\beta_j \sigma_{ij}) + \\ & F_{o,i} + \beta_v F_{w,i} + \beta_v (\rho - \rho_0) g_i, \end{aligned} \quad [3-47]$$

where  $F_{o,i}$  is the flow resistance created by sub-grid obstacles,  $F_{w,i}$  is the flow resistance created by the walls, and  $\sigma_{ij}$  is the stress tensor. Here,  $F_{o,i}$  and  $\sigma_{ij}$  are defined by

$$F_{o,i} = -\rho \left| \frac{\partial \beta}{\partial x_i} \right| u_i |u_i| \quad [3-48]$$

$$\sigma_{ij} = \mu_{eff} \left( \frac{\partial u_i}{\partial x_j} + \frac{\partial u_j}{\partial x_i} \right) - \frac{2}{3} \delta_{ij} \left( \rho k + \mu_{eff} \frac{\partial u_k}{\partial x_k} \right) \quad [3-49]$$

where  $\mu_{eff}$  is the effective viscosity, defined as follows:

$$\mu_{eff} = \mu + \rho C_\mu \frac{k^2}{\varepsilon} \quad [3-50]$$

where  $k$  is the turbulent kinetic energy and  $\varepsilon$  its dissipation. The second term is the turbulent viscosity or eddy viscosity.

#### - **Lethality calculation**

Chlorine is a highly toxic material. There are a number of indicators that can be used to assess the risk of exposure to toxic gases. Among these, AEGLs (Acute Exposure Guideline Levels), ERPGs (Emergency Response Planning Guidelines), and TEELs (Temporary Emergency Exposure Limits) are widely used. Moreover, there is a method from Withers and Lees [196, 197] to quantitatively calculate the probability of death using the probit function. This

method is a vulnerability model for describing the average fatal effects due to chlorine release. The equation of this method can be written as

$$Pr = a + b \ln \int c^n dt \quad [3-51]$$

$$P_{death} = 0.5 + \left( 1 + \frac{\text{erf}(Pr-5)}{\sqrt{2}} \right) \quad [3-52]$$

where  $Pr$  is the probit,  $c$  is the concentration by volume (in ppm), and  $a$ ,  $b$ ,  $n$  are constants. In the case of chlorine,  $a$  is -0.829,  $b$  is 0.92, and  $n$  is 2 [198]. In this study, the probit value is integrated up to 10 minutes after the onset of the leak. As the toxic gas flows into the residential area for about 10 min during the pre-simulation stage, 10 min is considered the golden time.

#### - Numerical setup

FLACS solves the conservation equations for each cell of a 3D Cartesian grid using the finite volume method. The numerical time step algorithm that is used in FLACS is based on the implicit first-order backward Euler method. Time steps in transient simulations should be set so that the solution evolves smoothly and stably in time. The Courant-Friedrich-Levy (CFL) number provides a solver-specific criterion for the maximum time step that yields a stable solution in the compressible solver of FLACS. Two CFL numbers are used to determine the maximum time steps: CFLV and CFLC. CFLV is based

on fluid velocity, whereas CFLC is based on sound velocity. The CFD solver chooses the minimum value between CFLV and CFLC.

$$\Delta t_v = \frac{\text{CFLV}}{\max(\frac{u_i}{\Delta x_i})} \quad [3-53]$$

$$\Delta t_c = \frac{\text{CFLC}}{\max(\frac{c}{\Delta x_i})} \quad [3-54]$$

$$\Delta t = \min(\Delta t_v, \Delta t_c) \quad [3-55]$$

where  $\Delta x_i$  represents the length of the cell in  $i$ -direction and  $\Delta t$  denotes the time step. In this study, CFLV is fixed at 1.0 and CFLC is fixed at 10, which are common values in dispersion simulations. Each simulation is performed by parallel computing with 12 CPU threads. The computer used in this study has a 24-core Intel Xeon E5-2697v2 (2.7 GHz) processor and 256 GB DDR3 RAM.

#### - Data sampling and preprocessing

To create a surrogate model using a neural network, hundreds of sample data points are required for training. However, it is costly to manually acquire large amounts of data; thus, an automated process is used to generate them. This is carried out by linking Python code with FLACS. Moreover, it is difficult to directly use the results obtained from FLACS in surrogate model training.

Therefore, it is necessary to preprocess them. The flow chart for this process can be seen in Figure 3-24.

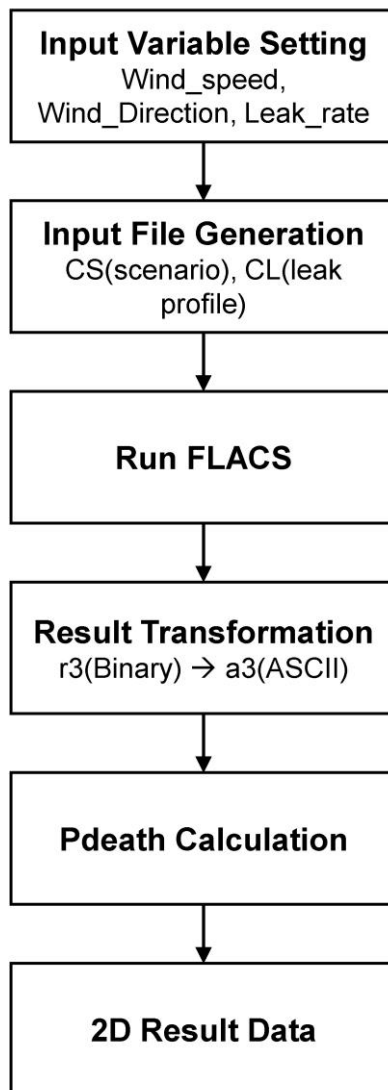


**Figure 3-24.** Data sampling and preprocessing flow chart

Initially, among the input variables applied to each sample, three variables (wind speed, wind direction, and release rate) are randomly selected within a certain range. Using these selected variables, the cs and cl files are created. To initiate the FLACS calculation, the cs (scenario), cl (leak), co (geometry), cg (grid), and cp (porosity) files are required. Among them, the co, cg, and cp files are fixed because the simulation is performed with a single geometry. As the variables in the cs and cl files only are changed, they are generated for each sample. Once the FLACS simulation is complete, the resulting r3 file (binary form) can be converted to an a3 file (ASCII form) using the FLACS utility. The result thus obtained is four-dimensional data ( $x$ ,  $y$ ,  $z$ , and time). Subsequently,  $P_{\text{death}}$  is calculated by integrating over time up to 10 min. Only the data at the point  $z = 2$  m, which is the height directly affecting the population, is extracted from the reduced 3D data and becomes 2D data ( $150 \times 200$ ), which is the  $P_{\text{death}}$  value corresponding to the  $x$  and  $y$  coordinates. 550 samples are thereby generated.



### 3.4.1.2. VAEDC-DNN surrogate model

Most of the previous studies on the reduced-order model for chemical engineering problems, such as reactor modeling, gas dispersion modeling, and process data monitoring, used principal component analysis (PCA) for data reduction and feature extraction [199-205]. However, as deep autoencoders exhibit superior performance in nonlinear data reduction compared with PCA and shallow autoencoders [206], well configured deep autoencoder are employed in the present case. Even though PCA can effectively reduce linearly correlated data in certain cases, and there are several applications of PCA, such as kernel-PCA for nonlinear dimensionality reduction or manifold learning, an autoencoder is the nonlinear generalized version of PCA. Furthermore, autoencoders can be applied to the generative model owing to their theoretical relationship with the latent variable model [207].  $P_{\text{death}}$  images generated from CFD gas dispersion models are highly nonlinear owing to complicated geometric factors (buildings, mountains, and loads), and it is considerably difficult to extract features from them. Thus, a surrogate model based on a variational autoencoder [185] is introduced for compressing the output image data  $x \in \mathbb{R}^{152 \times 200}$  to the latent space  $z \in \mathbb{R}^{1 \times N_z}$ , where  $N_z$  is the number of latent variables, using a probabilistic encoder ( $q_\phi(z|x)$ ) and a probabilistic decoder as generator ( $p_\theta(x|z)$ ) by means of variational Bayes that let the prior over the latent variables be the centered isotropic multivariate Gaussian

$(\mathcal{N}(z; 0, 1))$ . Finally, the latent space  $z$  is mapped by the variable space  $v \in \mathbb{R}^{1 \times 3}$  for reconstructing the image with  $v$  only.

For developing the surrogate model ( $f^*(v)$ ) of the CFD gas release model ( $f(v)$ ) employed by FLACS, a variational autoencoder with deep convolutional layer (VAEDC) and a fully connected deep neural network (DNN) involving batch normalization layers are used. The input of the original CFD model and the VAEDC-DNN surrogate model is represented by  $v \in \mathbb{R}^{1 \times 3}$ , that is, wind velocity (m/s), wind direction (rad), and gas release rate (kg/s). The output of the models is represented by  $x \in \mathbb{R}^{152 \times 200}$ , which is the contour image of  $P_{\text{death}}$ . Thus, the problem can be defined as developing a high performance, minimum mean squared error, surrogate model  $f^*(v): \mathbb{R}^{1 \times 3} \rightarrow \mathbb{R}^{152 \times 200}$  of the original CFD model  $f(v): \mathbb{R}^{1 \times 3} \rightarrow \mathbb{R}^{152 \times 200}$  using the pre-calculated data set of  $f(v)$ . 500 data points are used as training set ( $v^{\text{train}}, x^{\text{train}}$ ) and validation set ( $v^{\text{validation}}, x^{\text{validation}}$ ). 50 data points are used for testing ( $v^{\text{test}}, x^{\text{test}}$ ) the final metric (mean squared error) between the generated image data of ( $x^{\text{test}}_{\text{gen}}$ ) and  $x^{\text{test}}$ .

## - **Model architecture**

The proposed surrogate model, VAEDC-DNN, consists of two parts. The first part constructs the encoder and decoder using a variational autoencoder with deep convolutional layers (VAEDC). The second part maps the variable space ( $v$ ) to the latent space ( $z$ ) using deep neural networks. This two-stage method enables the proposed model to efficiently regress the  $P_{\text{death}}$  image ( $x$ ) with the variable ( $v$ ).

The detailed VAEDC architecture of the encoder and decoder for the surrogate model is shown in Figure 3-25. Three convolutional layers with a kernel size of (3,3), stride of 1, He initialization, ReLU activation function, and padding of the same dimension are used. After each convolutional layer, a max pooling layer with (2,2) filters and stride 2 is used for dimension reduction. Subsequently, the input layer dimension ( $152 \times 200$ ) is reduced to  $19 \times 25$ , which is one-fourth of the width and height of the image. Then, the  $19 \times 25 \times 8$  (number of filters) layer is reshaped into  $1 \times 3800$  vectors for constructing a 3800-128-64 fully connected dense layer with the ReLU activation function. The  $\mu$  and  $\log(\sigma^2)$  layers in parallel represent the mean and log of variance, respectively, of the latent variables. Thus, the dimension of the  $\mu$  layer,  $\log(\sigma^2)$  layer, and  $z$  layer is  $1 \times N_z$ , where  $N_z$  is the number of the latent variables. After the encoding process is finished, the decoding process is started, which is the inverse of the encoding process. Finally, the loss function, which

is represented by the variational lower bound, is calculated using  $x^{\text{train}}$  and  $x_{\text{gen}}^{\text{train}}$  at the variational layer.

The detailed DNN configuration for mapping the latent space from VAEDC and the variable space (wind velocity, wind direction, and gas release rate) is shown in Figure 3-26. A 5-layer fully connected deep neural network with batch normalization, ReLU activation function, and He initialization is used for mapping the variable space into the latent space. In the training phase, the network is trained using 400 resampled training sets ( $x^{\text{train}'}, v^{\text{train}'}$ ) and 100 validation sets ( $x^{\text{validation}'}, v^{\text{validation}'}$ ). The mean of the latent variables designated as output in this supervised learning is extracted using the encoder part of the VAEDC that has already been trained. The variable set  $v^{\text{train}'}$ , mapped in one-to-one correspondence, is used as input. Finally, in the generating phase, the model uses a test set that was not used as training or validation set in both VAEDC and DNN.  $z^{\text{test}}$  is predicted by  $v^{\text{test}}$  and the trained DNN, and  $x_{\text{gen}}^{\text{test}}$  is generated by the decoder of the trained VAEDC. Performance can be assessed by comparing the mean squared errors between  $x_{\text{gen}}^{\text{test}}$  and  $x^{\text{test}}$ .

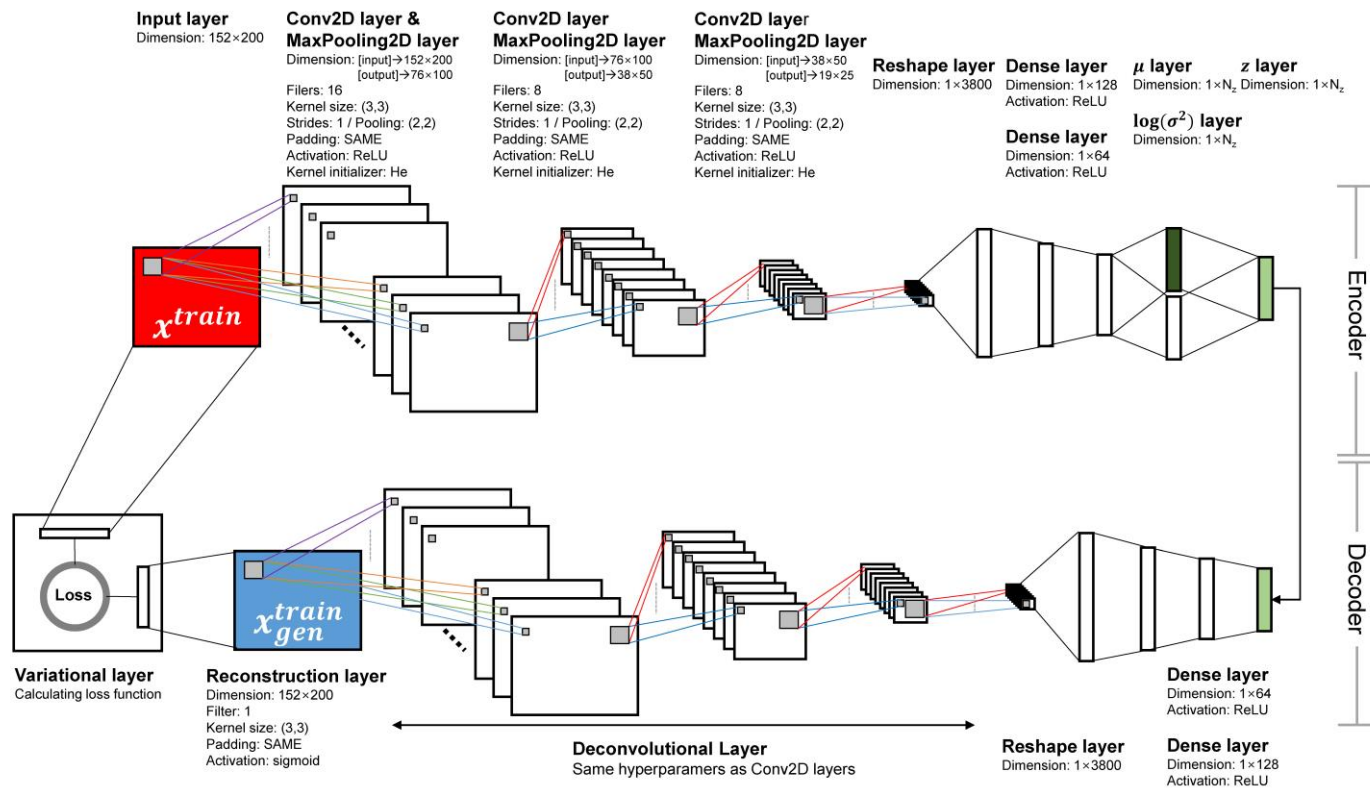
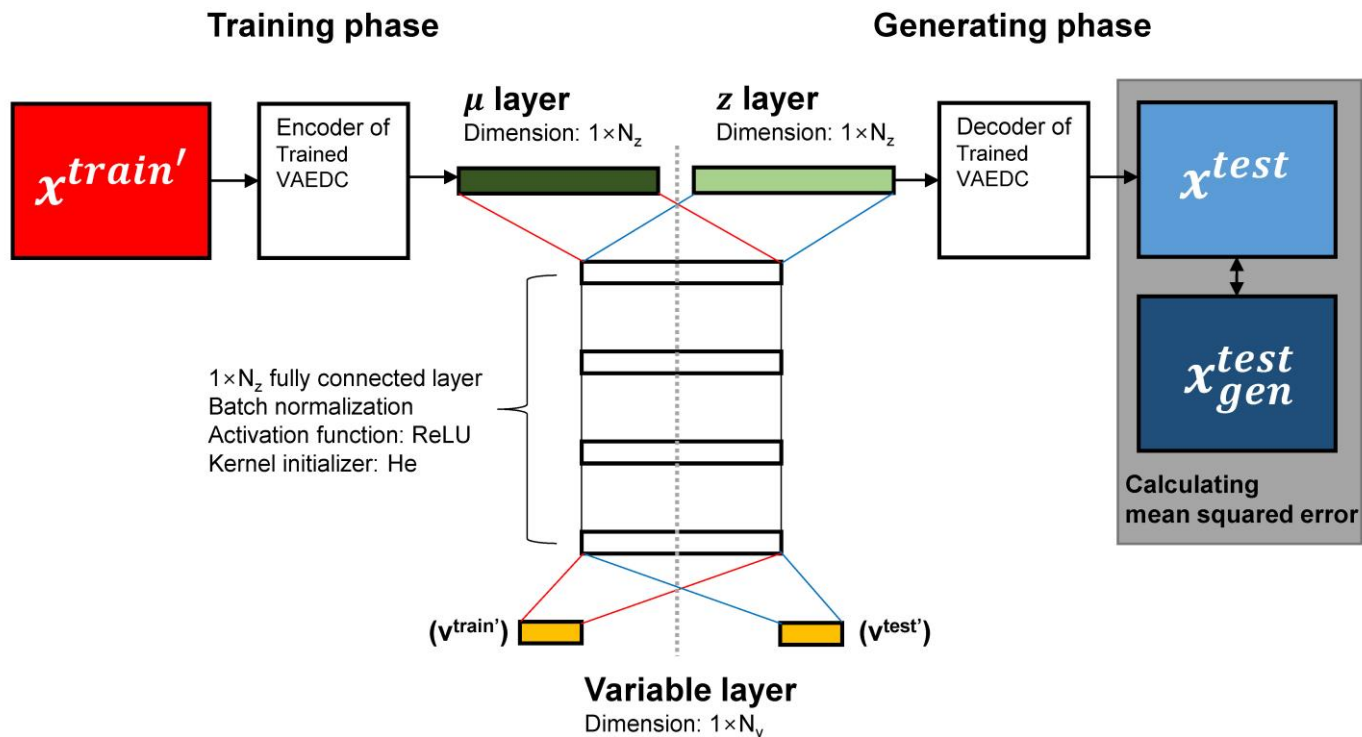


Figure 3-25. VAEDC architecture



**Figure 3-26.** DNN architecture for combining with VAEDC

- **Latent space and variational lower bound estimator**

The loss function is one of the most important settings for constructing efficient autoencoders. In this study, the variational lower bound on the marginal likelihood proposed by [185] is used. The lower bound is given by the following equation:

$$\mathcal{L}(\theta, \phi; x^{(i)}) = -D_{KL}(q_{\phi}(z|x^{(i)})||p_{\theta}(z)) + \mathbb{E}_{q_{\phi}(z|x)}[\log p_{\theta}(x^{(i)}|z)] \quad [3-56]$$

where  $D_{KL}$  denotes Kullback–Leibler divergence,  $p_{\theta}(x|z)$  is the probabilistic decoder with generative parameter  $\theta$ , and  $q_{\phi}(z|x)$  is the probabilistic encoder with variational parameter  $\phi$ . Training consists in maximizing the variational lower bound on the marginal likelihood of the data point  $i$  through the variational parameter  $\phi$  and generative parameter  $\theta$ . To use this statistical approach in a neural network framework, the loss function is defined as  $l(\theta, \phi; x^{(i)}) = -\mathcal{L}(\theta, \phi; x^{(i)})$  for converting the maximization problem to a minimization problem. Furthermore, to generate samples from  $q_{\phi}(z|x)$  and reparametrize  $\phi$  as a multivariate Gaussian with diagonal covariance structure with mean ( $\mu$ ) and standard deviation ( $\sigma$ ) of the approximate posterior, the following equation is applied to sampling.

$$z^{(i)} = \mu^{(i)} + \sigma^{(i)} \odot \epsilon \quad \text{and} \quad \epsilon \sim \mathcal{N}(0,1). \quad [3-57]$$

This sampling is performed at the  $z$  layer which is located after the  $\mu$  and  $\log(\sigma^2)$  layers in Fig. 3. Previous studies [185] proved that the KL divergence

can be calculated and differentiated without estimation, and the second term of the variational lower bound can be treated as a binary crossentropy loss function. Finally, the proposed loss function for VAEDC and the data point  $x^{(i)}$  is given by

$$l(\theta, \phi; x^{(i)}) \simeq -\frac{0.5}{N_z} \sum_{j=1}^{N_z} (1 + \log((\sigma_j^{(i)})^2) - (\mu_j^{(i)})^2 - (\sigma_j^{(i)})^2) + \frac{152 \times 200}{N_{\text{train}}} \sum_{i=1}^{N_{\text{train}}} (x^{(i)} \cdot -\log p_{\theta}(x^{(i)}|z) + (1 - x^{(i)}) \cdot -\log(1 - p_{\theta}(x^{(i)}|z))) \quad [3-58]$$

#### - Performance evaluation and numerical setting

It is very important to evaluate the performance of the proposed surrogate model correctly. Evaluating the performance using the value of the loss function of VAEDC or DNN is inappropriate. The purpose of the surrogate model is to predict the  $P_{\text{death}}$  image correctly using the variable space, rather than merely encode and decode the image data or map the variable space into the latent space. Therefore, it is necessary to determine whether the latent space accurately reflects the features representing the  $P_{\text{death}}$  image and whether the variable space and the generated image data are in one-to-one correspondence. That is, it should be ensured that the image data is not simply memorized in the latent space or overfitting. Thus, the performance of the surrogate model is not evaluated by each loss function of VAEDC and DNN but rather using the mean



squared error between  $x_{\text{gen}}^{\text{test}}$  and  $x^{\text{test}}$ , where the test set was not used as training or validation set in both VAEDC and DNN. Furthermore, for comparing the model performance with other types of surrogate models based on autoencoder neural networks, a neural network with one hidden layer (NN) without autoencoder, a deep neural network with three hidden layers and batch normalization (DNN) without autoencoder, NN with simple autoencoder (AE-NN), NN and DNN with deep autoencoder (DAE-NN, DAE-DNN), NN and DNN with deep convolutional autoencoder (DCAE-NN, DCAE-DNN), DNN with simple variational autoencoder (VAE-DNN), and DNN with variational autoencoder with deep convolutional layers (VAEDC-DNN) are compared using the same hyperparameters (Table 3-14). Detailed architectures and summaries are provided in the supplementary file.

To compare the models fairly, the number of epochs of both the autoencoder and neural network was set to 1,500, and the size of the latent space ( $N_z$ ) was set to 32 for all models. The size of the variable space ( $N_v$ ) was set to 3, i.e., wind velocity (m/s), wind direction (rad), and release rate (kg/s). The *Adam* optimizer [190] was used for optimizing loss functions. All models were coded using the Python deep learning library Keras with the Tensorflow backend. Training was carried out using NVIDIA GeForce GTX 1070 with 8 GB GDDR5.

**Table 3-14.** Summary of various models for comparison (architecture, loss function, number of parameters); detailed descriptions are shown in the supplementary file.

Autoencoder									
	NN	DNN	AE-NN	DAE-NN	DAE-DNN	DCAE-NN	DCAE-E-DNN	VAE-DNN	VAEDC-DNN
Description	-	-	One fully connected dense layer	5 fully connected hidden layers	2D convolutional layers, 3 max pooling layers, and 3 up-sampling layers	5 fully connected hidden layers, 7 2D convolutional layers, 3 max pooling layers, and a variational layer	9 fully connected hidden layers, 7 2D convolutional layers, 3 max pooling layers, 3 up-sampling layers, and a variational layers		
Loss function	-	-		binary cross entropy			- variational lower bound		
Parameters	-	-	1,976,032	7,833,696	1,001,881	15,620,352	1,003,961		
NN regression									
Description	One fully connected hidden layer	Three fully connected hidden layers with BN	NN	NN	DNN	NN	DNN	DNN	DNN
Loss function					mean squared error				
Parameters	30,434,400	3,933,056	1,184	1,184	3,680	1,184	3,680	3,680	3,680

### 3.4.1.3. Results and discussion

Various training aspects of the models will be examined through the change of each loss function concerning the epoch (Figure 3-27). The maximum epoch for all training is set to 1500. If this number does not fit, the training may be underfitting or overfitting. This can be determined by comparing the loss function of the validation set with the loss function of the test set. As the number 1500 is set through trial and error, the entire training process is considered appropriate for all models. In the case of NN, a significantly unstable training process manifests itself as the epoch rises over 70. The prediction of a higher dimension from a considerably lower dimension in a fully connected dense hidden layer results in an unstable training process because the number of parameters (30,434,400) is excessively large and no additional normalization process is added. However, it may be used for comparison because the process appears to stabilize to some extent as the epoch exceeds 800. Considering DNN, which has three hidden layers and batch normalization applied after each layer to alleviate the vanishing gradient problem of deep networks, the training process is more stable, without overfitting, and exhibits fast convergence. Regarding AE-NN, the autoencoder part and the NN or DNN parts should be considered separately. In the autoencoder training process, represented by the blue line, overfitting occurs slightly after the epoch 100 only in the case of DAE. However, in AE, DCAE, VAE, and VAEDC, the value of the loss function at

the end of training is highly satisfactory. NN, represented by the red line, exhibits a highly stable training process, unlike NN without autoencoder. Moreover, there is no difference between the training error and the validation error. Therefore, there is no overfitting. In the case of DNN, there is a slight vibration in the second half. Nevertheless, it appears to be well trained because it exhibits a monotonically decreasing training process, and there is almost no difference between the validation error and the test error. However, the lower validation error compared with the training error is attributed to the fact that the randomly extracted validation sets,  $x^{\text{validation}'}$  and  $v^{\text{validation}'}$ , contain a predictable subset.

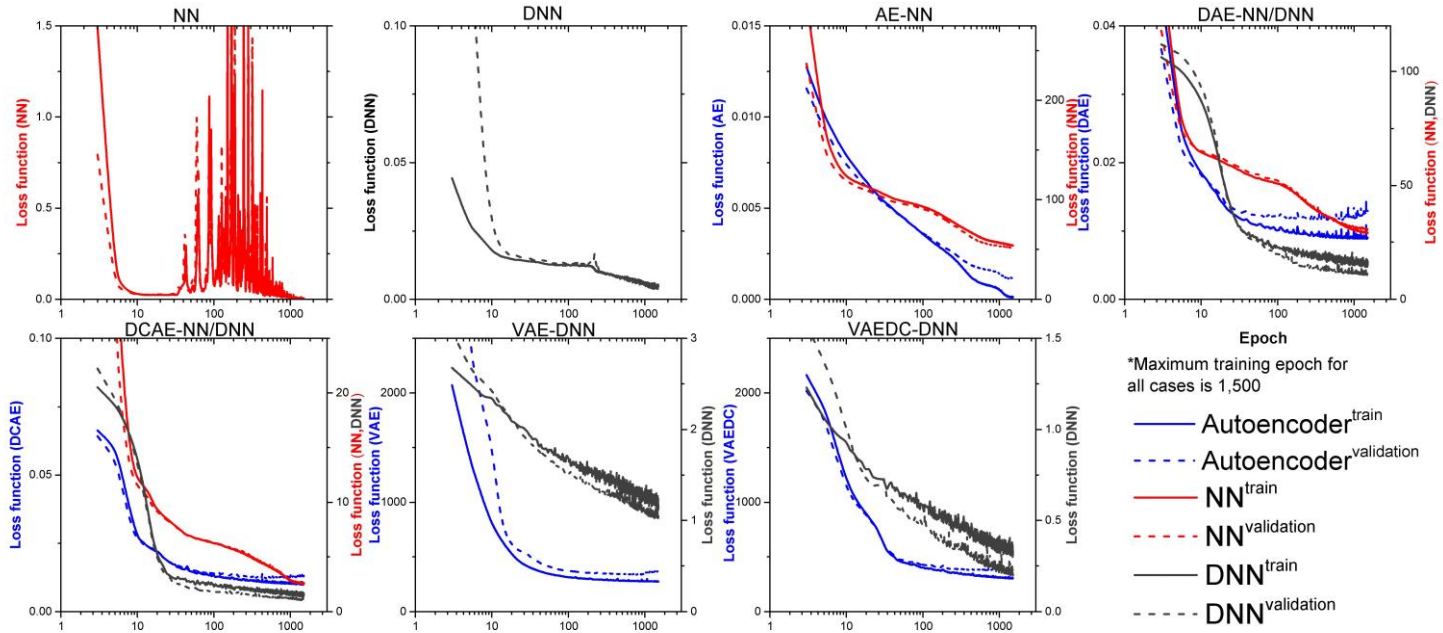


**Figure 3-27.** Comparison of epoch vs. loss function graphs for NN, DNN, AE-NN, DAE-NN, DAE-DNN, DCAE-NN, DCAE-DNN, VAE-NN, and VAEDC-DNN models.

In **Figure 3-28**, the mean squared error between  $\mathbf{x}_{\text{gen}}^{\text{test}}$  and  $\mathbf{x}^{\text{test}}$  for each of the 50 newly extracted test data sets ( $\mathbf{x}^{\text{test}}$ ,  $\mathbf{v}^{\text{test}}$ ) is shown. The mean and standard deviation for all test data sets with Gaussian distribution fitting is also provided. The surrogate model constructed using the proposed VAEDC-DNN exhibits the highest performance. The mean value is the lowest, at 0.00246, and the standard deviation of 50 test data sets is considered the narrowest. That is, VAEDC-DNN does not merely memorize the Pdeath image information obtained from the training set, but rather has the ability to extract features in the most suitable form for the latent space and to map it explicitly to the variable space. When NN is used, it can be seen that regardless of the effectiveness of the autoencoder compression, performance drops considerably. It can be seen that the relationship between the latent space and the variable space is not captured clearly. However, performance increases when encoding is such that each variable stored in the latent space clearly exhibits nonlinear correlation with the variable space. It can be confirmed that performance is improved even when NN is used in the order of VAE, DCAE, DAE, and AE. In conclusion, the best performance is achieved when VAE-based autoencoder and convolutional layers are used. In the case of NN without autoencoder, the number of parameters is 30,434,400, whereas in VAEDC-DNN it is 1,007,641, which is 3.31% of the former. The superior performance may be attributed to efficient training and feature extraction with a small number of parameters.

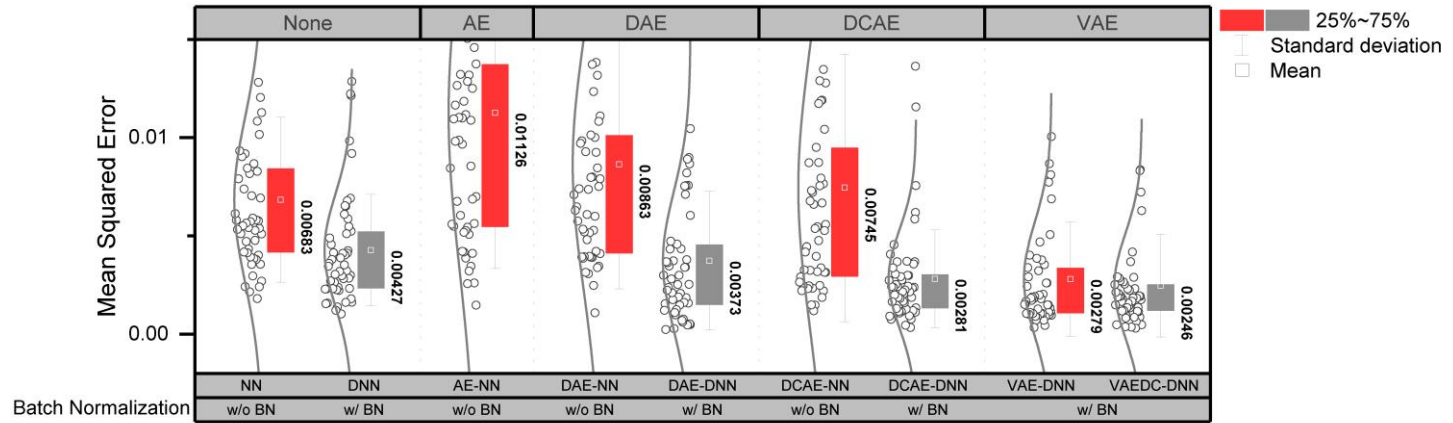


**Figure 3-28.** Mean squared error of test set data

It should be noted that in terms of the mean squared error, NN and DNN without autoencoder appear to perform better compared with several combinations of autoencoders and NN. However, if  $x_{\text{gen}}^{\text{test}}$  is drawn directly in the contour graph, NN and DNN without autoencoder are shown to exhibit severe noise. To visualize this, a contour graph of five randomly selected  $x_{\text{gen}}^{\text{test}}$  generated from FLACS (CFD), which is the ground zero result, NN, AE-NN, DAE-DNN, ACAE-DNN, and VAEDC-DNN are shown in Figure 3-29. If NN or DNN without autoencoder are used, severe noise appears. This is because it is difficult to efficiently extract only the features of the image during the training process. Hence, other training data images are memorized and reflected in the results. Moreover, owing to the characteristics of highly nonlinear images, it is difficult to predict the entire image using the variable space only. Thus, the result is quite misleading in some cases, such as the 1<sup>st</sup>, 3<sup>rd</sup>, and 5<sup>th</sup> columns in Fig. 7. The noise disappears from the prediction after data compression by the autoencoder. However, failure to extract features by the autoencoder and map the variable space into the latent space by NN results in deterioration of the surrogate model performance. Such phenomena can be observed directly in AE-NN. The disappearance of noise is important; however, only the approximate trends are predictable. In the case of the 2<sup>nd</sup> column data, prediction is considerably inaccurate, whereas in the 5<sup>th</sup> column data it is highly accurate. At this point, it becomes apparent that the introduction of the DNN model with



batch normalization model is necessary for improving overall performance. Feature extraction should be activated through the deep convolutional layer and image compression should be accurately performed with the latent space by predicting the posterior distribution through the variational autoencoder. Between the two best-performing models, i.e., VAEDC-DNN and DCAE-DNN, VAEDC-DNN provides superior prediction compared with FLACS (CFD). In the 1<sup>st</sup> column,  $P_{\text{death}}$  spreads out slightly to the upper side; it cannot be detected by DCAE-DNN, whereas VAEDC-DNN detects it. In the 3<sup>rd</sup> column, VAEDC-DNN is nearly matched although the other models cannot clearly predict width and size. In 4<sup>th</sup> and 5<sup>th</sup> column data, superior feature extraction is exhibited even though the shape is complex with many cracking features. Finally, it can be seen that a cracked, non-convex, complex image is predicted as well.

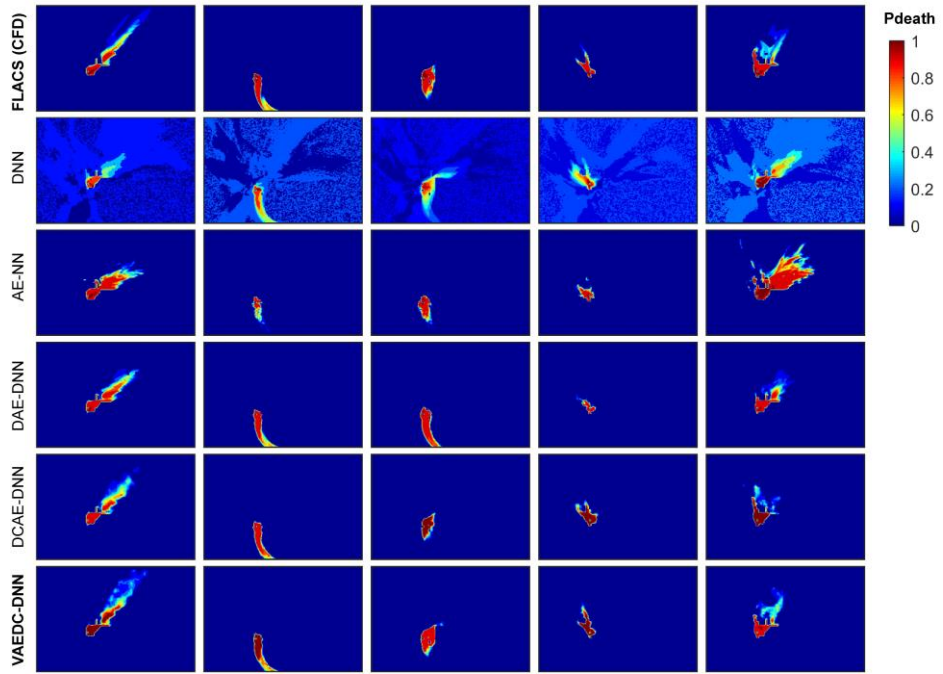


**Figure 3-29.** Comparison of generated  $P_{\text{death}}$  image ( $x_{\text{gen}}^{\text{test}}$ ) using  $v^{\text{test}}$  with FLACS (CFD), which is ground truth, DNN, AE-NN, DAE-DNN, DCAE-DNN, and VAEDC-DNN.

As can be seen by the sentence “walking in the latent space” from [208], understanding the landscape of the latent space is highly important because it is possible to detect memorization through walking in the latent space. If there is sharp image transition, which implies that the latent space is collapsed, the model fails to learn relevant and interesting representations. In this study, as the variable space has already been mapped into the latent space, “walking in the variable space” is suitable for determining whether the manifold is learned. The results are shown in Figure 3-30.

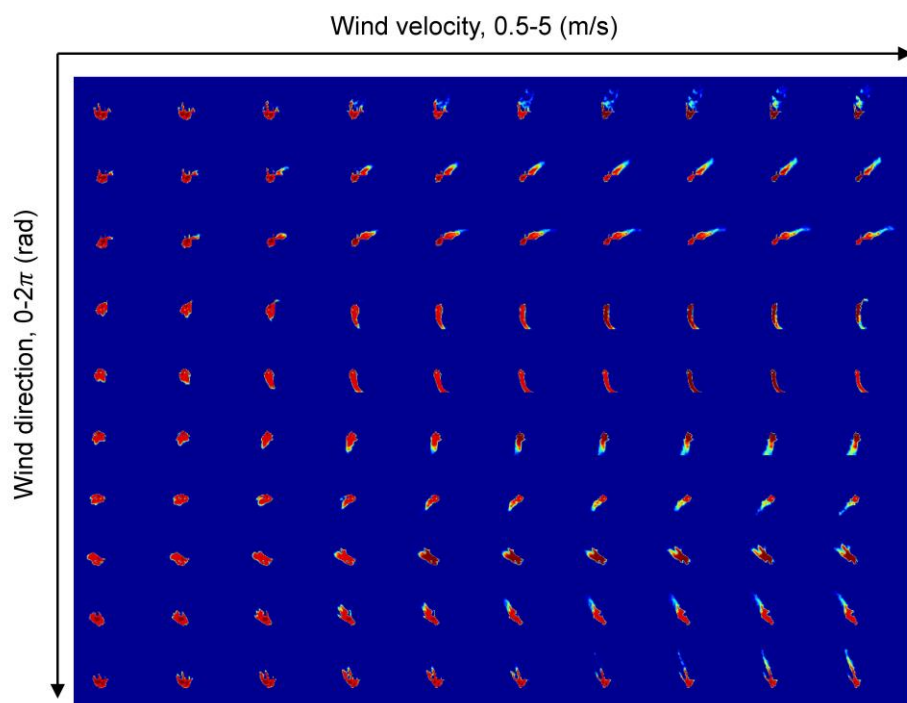


**Figure 3-30.** “Walking in the variable space” of a VAEDC-DNN.

As the variable space ( $v$ ) is three-dimensional, the toxic gas release rate (discharge rate) is fixed at 50 kg/s, and  $P_{\text{death}}$  is visualized as a linear series of 10 points in wind velocity and wind direction. Smooth transitions in all directions are observed.  $P_{\text{death}}$  spreads wider as wind velocity increases, and the diffusion direction of  $P_{\text{death}}$  varies smoothly with wind direction, and the topography and obstacles of the region are reflected by the asymmetrical movement. Fig. 8 shows that VAEDC-DNN accurately extracts the  $P_{\text{death}}$  features, as it is trained not to merely interpolate and symmetrically rotate the wind direction.

Comparison of computational time, storage space for saving the model, and use in real-time alarm systems between the CFD model and VAEDC-DNN is given in Table 3-15. In the case of real-time alarm systems, if a chemical release accident occurs, then wind velocity, wind direction, and release rate are provided to the alarm system from external sensors. Subsequently,  $P_{\text{death}}$  or concentration of toxic chemicals should be calculated. When using the CFD model for calculating  $P_{\text{death}}$ , CPU time is over 700 s using 16 cores of the Intel Xeon E5-2667v3 (3.2 GHz) processor; thus, it is impossible to obtain this information before golden time (10 min). Moreover, it is difficult to pre-calculate all scenarios in advance because the storage requirement for saving CFD data is on the GB scale per case, and results are usually non-linear via the variable space, owing to the complexity of the geometry. Thus, VAEDC-DNN

is particularly helpful for developing the surrogate model with a minimum amount of pre-calculated CFD data. After training, up to 1 s of CPU time with a single core is required. As mentioned above, the non-linear correlation between the  $P_{\text{death}}$  distribution and the geometry effect via the variable space is achieved by the variational autoencoder. Hence, with hundreds of pre-calculated CFD results, VAEDC-DNN successfully predicts the  $P_{\text{death}}$  contour via any variable space.

**Table 3-15.** CPU computational time, storage space for saving the model, and use in real-time alarm systems.

CPU time		Storage	Use in real-time alarm systems
CFD model	~700 s with 16 cores	GB scale	Thousands of cases are required for predicting all variables.
VAEDC-DNN	< 1 s with single core	KB scale	With hundreds of cases, the surrogate model can predict all variables.

#### 3.4.1.4. Conclusions

In this study, the CFD model was reduced, and regression was introduced through a surrogate model for fast calculation. A variational autoencoder with deep convolutional layers was used to extract only key features without noise from high-dimensional image data. Thereby, the CFD result data was reduced, and features were extracted into the latent space  $z$ . Moreover, a surrogate model for mapping the variable space  $v$  to  $z$  using a deep neural network with batch normalization was designed. The integrated model, a variational autoencoder with deep convolution layers interconnected with a deep neural network (VAEDC-DNN), was finally proposed, and the results were remarkable. To verify the performance of the proposed surrogate model, a toxic gas release scenario in the Mipo complex in the city of Ulsan, Republic of Korea, modeled by the commercial CFD software application FALCS was used. CFD modeling was based on CAD, reflecting the complex geometry of real industrial complexes, and the distribution of the probability of death ( $P_{\text{death}}$ ) was obtained as a 2D contour graph by varying  $v$ . 500 randomly sampled training sets, and 100 validation sets were used for training. Furthermore, 50 randomly sampled test sets, which were not used for training, were used for performance evaluation by comparing the results of the ground truth CFD and those of the proposed surrogate model via the mean squared error of  $P_{\text{death}}$ . For objectivity, NN without autoencoder, DNN without autoencoder, AE-NN, DAE-NN, DAE-



DNN, DCAE-NN, DCAE-DNN VAE-DNN, and VAEDC-DNN were compared using the same hyperparameters. The mse of VAEDC-DNN was 0.00246, which is on average 47.7% as low as that of the other models. Moreover, the model yields a fairly accurate prediction of the nonlinearity of image cracks and topography. Finally, it is confirmed that image generation is not overfitting by data memorization through the smoothness of image transition in the variable space.

The proposed regression methodology has considerable advantages for developing the surrogate model when the dimension of the training data is very large, which may result in problems related to noise or feature extraction. Furthermore, it leads to high-quality surrogate models when the computational cost of the original model, such as a CFD-based model, is overly high for real-time analysis. Therefore, when constructing an early warning system for chemical accidents, or when the dynamics of a virtual plant is required at real time in the form of a 2D or 3D contour image of the concentration of chemicals or temperature profile, compressing the pre-calculated CFD results and developing a surrogate model using VAEDC-DNN is expected to have a considerable effect. In future work, it is expected that state-of-the-art generative models, such as boundary equilibrium generative adversarial networks (BEGAN), will be used for generating images with sharp edges for more complex features.

## CHAPTER 4. Industrial Applications

### 4.1. Optimal Design and Operation of Fischer-Tropsch Microchannel Reactor for Pilot Scale Compact Gas-to-Liquid Process

A pilot scale (1.0 BDP) compact GTL process comprising of reforming section, CO<sub>2</sub> separating section and Fischer -Tropsch (FT) synthesis section is presented. Systematic design procedure adopted for the design of a modular 0.5 BPD microchannel FT reactor block design consisting of 528 process channels is described. On average 98.27% CH<sub>4</sub> conversion to syngas in reforming section comprising of a pre-reformer unit and a tri-reformer unit, CO<sub>2</sub> separation rate of 36.75 % along with CO/H<sub>2</sub> reduction from 2.67 to 2.08 in CO<sub>2</sub> membrane separation section comprising of three membrane separators, for the entire plant operation duration of 450 hr demonstrated successful and stable operation of pre-processing sections of the present pilot-scale compact GTL process. Parallel operation of FT microchannel reactor and multitubular fixed bed type FT reactor proved failure for latter due to reaction runaway, while the former showed stable operation with high CO conversion of 83% and successful temperature control (at 220 °C, 230 °C, and 240 °C during the 139 hr operation), which demonstrated the appreciable performance of KOGAS-SNU novel microchannel FT reactor.

#### **4.1.1. Pilot scale compact GTL process**

The present KOGAS-SNU collaboration project "GTL Pilot Plant Operation and Technology Enhancement Project" works on technology development for compact GTL process mainly targeting for offshore and small to mid-scale gas field application. The process consists of syn-gas reformer units, CO<sub>2</sub> membrane separator units, NG supply tanks (supplied from LNG storage tank in Incheon, South Korea), and an integrated FT reactor that produces synthetic crude oil through FT reaction. FT reactor being at the core of GTL process, the main focus of the work was on the design of modular FT microchannel reactor block suitable for small- to medium-sized gas fields where one reactor module can produce FT product up to 0.5 BPD. Accordingly, a novel modular microchannel FT block reactor was developed in-house following a rigorous design procedure. The microchannel block reactor is expected to miniaturize FT synthesis with nearly 100 times heat exchange capacity compared to the conventional fixed bed type FT reactor, as supported by several literatures [12-14, 209]. Like Velocys®, the pioneer company for microchannel FT reactor based small-scale GTL process, the capacity of present pilot scale compact GTL process can be scaled up by numbering up the the block reactor modules. This allows microchannel reactors to have flexibility in their desired production capacity. Additionally, block-type micro-channel reactors are also effective for reactor scale-up in offshore environments where ocean wave motion can affect

the reaction performance [9]. The tri-reformer section in the present compact GTL process however used a vessel type reformer, but since the total height is designed to be within  $\sim 3$  m, the tri-reformer unit does not nullify the advantageous feature of block-type microchannel reactors in the context of offshore application.

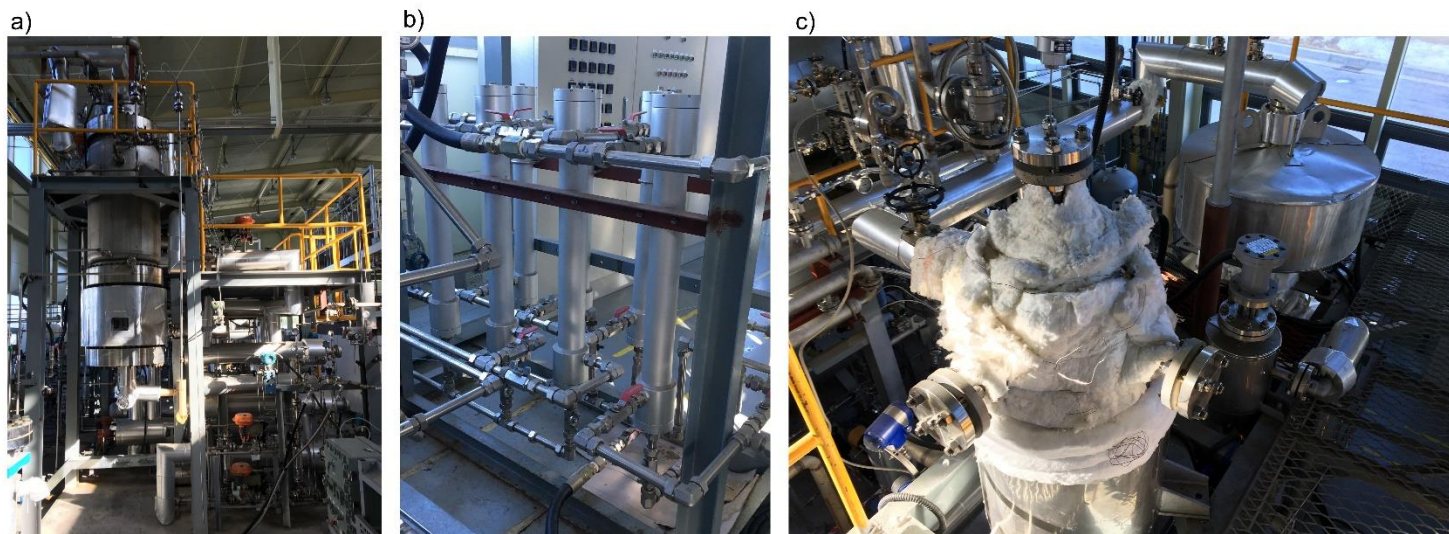


**Figure 4-1.** Overview of KOGAS compact GTL pilot plant (1 barrel per day) involved a) reformer section, b) CO<sub>2</sub> membrane separation section, and c) FT reactor section.

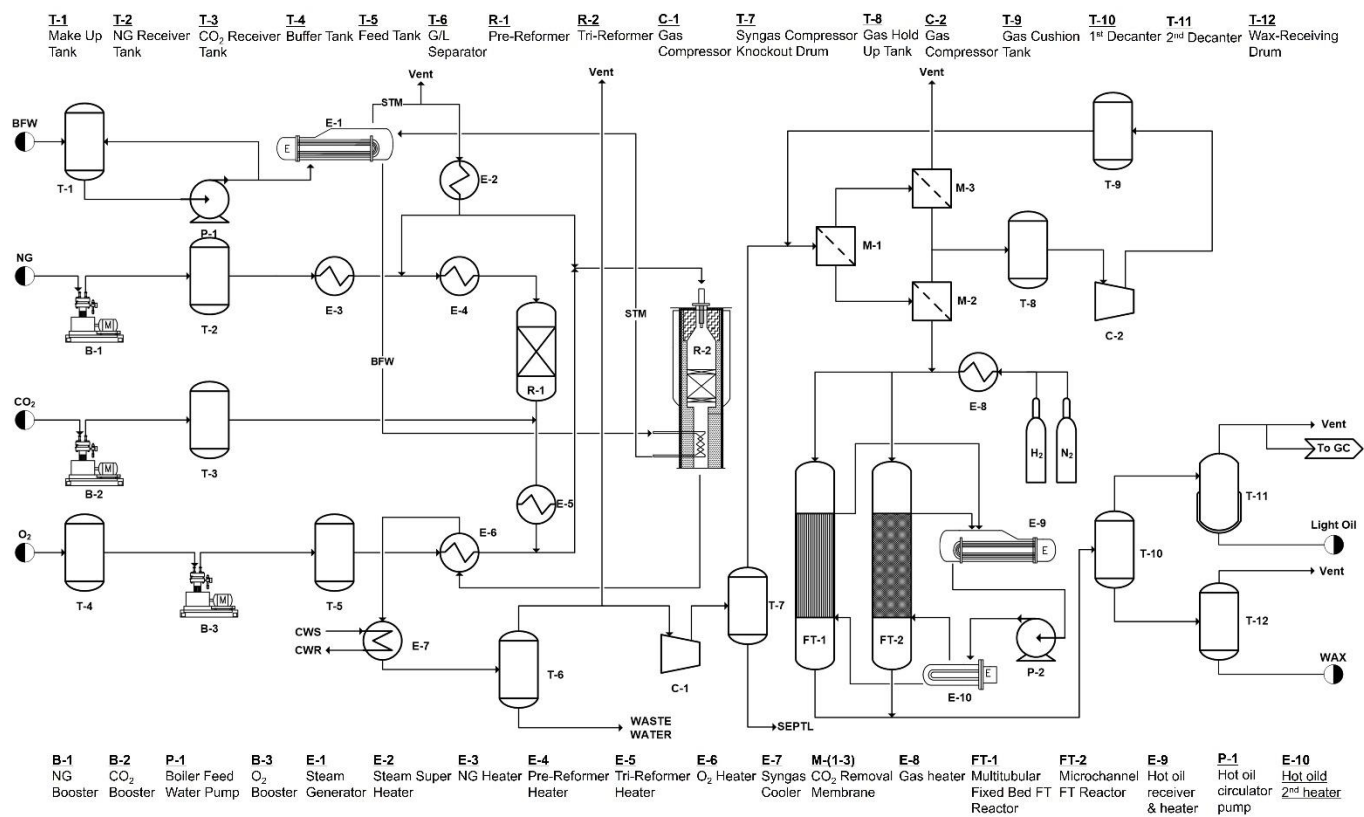
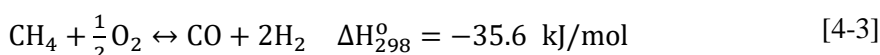
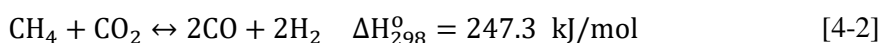
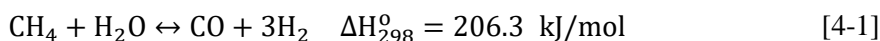


**Figure 4-2.** Process flow diagram of the compact GTL process which involves unit processes of reformer, CO<sub>2</sub> separation, and FT reaction process.

Overview of the KOGAS GTL pilot plant is shown in Figure 4-1 and Figure 4-2 shows the process flow diagram of the overall compact GTL process. The process can be divided into three processing sections, namely, reforming section, CO<sub>2</sub> separating section, and FT reaction section. Boiler feed water, natural gas, CO<sub>2</sub>, and O<sub>2</sub> are the feed materials. These feed materials are converted to syngas (mixture of CO and H<sub>2</sub>) by the reforming section which is then passed as feed to the FT reaction section after removing CO<sub>2</sub> in the CO<sub>2</sub> membrane separator section. The reforming section consists of pre-processing units (B-1, B-2, B-3, T-1, T-2, T-3, E-1, E-2, E-3) to heat up, mix and pressurize the feed natural gas, and a pre-reformer and a tri-reformer unit to convert feed natural gas to syn-gas (mixture of CO and H<sub>2</sub>). First, boiler feed water (BFW) is received by a make-up tank (T-1) which is then pumped (by P-1) to the steam generator (E-1) where it subsequently becomes steam after passing through a waste heat boiler located at the bottom of the tri-reformer. Natural gas is supplied from an LNG storage tank located outside the pilot plant facility at KOGAS and is mixed with steam at the upstream of pre-reformer. CO<sub>2</sub> and O<sub>2</sub> supplied to the reformer section requires booster (B-2, B-3) to increase flow pressure to that of feed gas stream to tri-reformer in order to mix with the feed gas stream before entering the tri-reformer. O<sub>2</sub> supply in this case does not require an electric heater as it exchanges heat in heat exchanger (E-6) with the hot stream coming out from tri-reformer. Equations [4-1]-[4-3] show the reactions in the conventional process of steam reforming of methane (SRM),

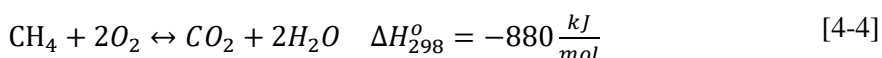
the carbon dioxide reforming of methane (CDR), and the partial oxidation of methane (POM), respectively.



The tri-reforming process of methane (TRM) proposed by Song and Pan [210] is considered suitable for GTL process, because in their case, the three reforming reactions occur simultaneously making it easier to control syngas ratio ( $\text{H}_2/\text{CO}$ ) in tri-reformer product. Inappropriate  $\text{H}_2/\text{CO}$  ratio is the main factor for coke formation that can occur in processes that use syngas as feed, such as dimethyl ether (DME) production, GTL, biomass-to-liquid (BTL) and coal-to-liquid (CTL) [210-213]. In the present compact GTL process, boiler feed water converted to steam along with natural gas,  $\text{CO}_2$ , and  $\text{O}_2$  are reacted in the pre-reformer with ReforMax 100 (Sud-Chemie catalyst) and the tri-reformer with KDN-1 (Ni-Mg/Ce-ZrO<sub>2</sub>/γ-Al<sub>2</sub>O<sub>3</sub> based tri-reformer catalyst) developed by KOGAS to produce the syngas. The reaction temperature of the pre-reformer was maintained between 400-420 ° C and the temperature of the heterogeneous zone of the tri-reformer was maintained between 900-1000 ° C. High-temperature of the tri-reformer product is reduced to a much lower temperature (~25 oC) suitable for  $\text{CO}_2$  membrane separating section by first exchanging heat with  $\text{O}_2$  supply to reforming section and then subsequent cooling using chilled water.



In the tri-reformer, in addition to SMR, CDR and POM reactions, methane combustion also occur at the high reaction temperature of tri-reformer. This lead to excess CO<sub>2</sub> in the tri-reformer product stream.



However, in the FT reaction, excessive CO<sub>2</sub> act as an inert gas, like N<sub>2</sub> in the CO/Al<sub>2</sub>O<sub>3</sub> based catalyst, and the reaction conversion gets dominated by undesired methanation reaction [209]. Syngas feed to the FT reactor along with excess CO<sub>2</sub> would require reactor size to increase drastically, in addition to promoting undesired methanation reaction. Therefore, CO<sub>2</sub> membrane separator section is introduced to lower the CO<sub>2</sub> concentration to less than 10 mol%. Three membrane units (M-1, M-2 and M-3) are connected in tree fashion so that the permeate of M-1 is transferred to M-3 and the retentate is transferred to M-2. The permeate of M-3 which contains excess CO<sub>2</sub> gas is vented out. Alternatively, the permeate of M-3 can be recycled to the tri-reformer unit by combining with the main CO<sub>2</sub> feed stream to tri-reformer. The retentate of M-3 and the permeate of M-2 are combined and recycled to M-1 using the gas compressor to minimize H<sub>2</sub> and CO losses. Finally, the retentate of M-2 showed a CO<sub>2</sub> removal efficiency of the CO<sub>2</sub> membrane separation section upto 36.8-39.4% leaving the syngas stream composition with an average CO<sub>2</sub> content of ~ 10%. The syngas purified using the CO<sub>2</sub> membrane separation section of the pilot plant has H<sub>2</sub>/CO ratio ~2, which is a necessary condition for high FT reaction conversion and desired selectivity [214]. The purified syngas enters

the FT reaction section of the pilot plant comprising of a microchannel block FT reactor and a multitubular fixed bed type FT reactor connected in parallel for performance comparison. Both microchannel FT reactor block and a multitubular fixed bed type FT reactor were maintained at the same operating conditions of 20bar, 220 °C and GHSV = 2500 hr<sup>-1</sup>. A hydrogen (H<sub>2</sub>) gas cylinder is connected to reaction system to reduce the FT catalyst needed for FT reaction. A nitrogen (N<sub>2</sub>) gas cylinder is also connected to the reaction system to act a diluent and to be used in the calculation of CO conversion and CH<sub>4</sub> selectivity by gas chromatography later. Both H<sub>2</sub> and N<sub>2</sub> are heated to the FT reactor operating temperature through a gas heater (E-8). Cobalt based catalyst with alumina support (12 wt% Co /  $\gamma$ -Al<sub>2</sub>O<sub>3</sub>), developed by KOGAS, was used for the FT reaction along with alumina ball as inert packing material. In lab-scale experiment, incipient wetness impregnation (IWI) was performed to produce the catalyst in gram scale (detail information of catalyst with reaction kinetics is reported in [31]). However in pilot scale operation, because of necessity of industrial scale production, spray coating method was used for producing the catalyst in kilogram scale. Products of the FT reaction were collected as light oil, wax and gas after passing through 1<sup>st</sup> and 2<sup>nd</sup> decanter (T-10 and T-11 for light oil and gas) and wax-receiving drum (T-12 for wax). The gas is then sent to GC analyzer for analyzing the gaseous products.

In addition to the development of an integrated and compact GTL process, present work also includes the design of a corrugated fin-type microchannel FT

reactor block suitable for the process. Therefore, the present GTL technology development requires consideration of both process and reactor design along with the analysis for optimal operating conditions for the reactor. Furthermore, to our knowledge, literature on combined work for design, fabrication and operation of pilot scale microchannel reactors is limited. Therefore, it is imperative to organize the sequence of studies conducted in the design process. In the next section, we explain the design procedure followed in the present study to achieve the final design of microchannel FT reactor block used in the pilot plant demonstration.

### **4.1.2. Microchannel FT reactor design**

The work presented in Chapter 4.1.2 has been submitted to *Chemical Engineering and Processing: Process Intensification* with KS. Kshetrimayum (joint first author). Furthermore, this section was used in Ph.D. thesis of KS. Kshetrimayum (“Modeling, Simulation, and Design Procedure Development of Micro-channel FT Reactor using Computational Fluid Dynamics”). Thus, I exclude this Chapter in my thesis. Especially, specific data (Figure 4-5 and Figure 4-6) are shared with him under his consent.

### 4.1.3. Pilot plant experiment

#### - Pilot plant setup

The pilot scale GTL process experiment was performed through three operating sections reformer section, CO<sub>2</sub> membrane separation section, and FT Synthesis section. Tri-reformer for the reformer section was made by stainless steel with shell side and jacket side. Al<sub>2</sub>O<sub>3</sub> ball was packed on the top of the reactor, KDN-1 (Ni-Mg/Ce-ZrO<sub>2</sub>/γ-Al<sub>2</sub>O<sub>3</sub> based tri-reformer catalyst developed by KOGAS) was packed in the middle of the reactor, and Al<sub>2</sub>O<sub>3</sub> ball was packed at the outlet region of the reactor. Operation temperature and pressure were set to 900-1000°C and 25 bar respectively. Average pressure drop was 25 kPa through the overall Tri-reformer section. In case of pre-reformer, Al<sub>2</sub>O<sub>3</sub> ball was packed on the top of the reactor, ReforMax 100 (Sud-Chemie) was packed on the middle of the reactor, and Al<sub>2</sub>O<sub>3</sub> ball was packed on the bottom of the reactor. Operation temperature and pressure were set to 400-420°C and 27 bar respectively. Total operation time of reformer section, including the reformer ignition start up time, was 450 hr. At the ignition condition, GHSV was about 1567 hr<sup>-1</sup>, mass flow rate of steam was 9.8 kg/hr, and volumetric flow rate of natural gas and oxygen were 4.8 and 4.5 Nm<sup>3</sup>/hr respectively.

In the case of CO<sub>2</sub> membrane separation section, total operation time was 188 hr for microchannel reactor and 134 hr for multitubular packed bed reactor.

Average pressure of M-1 retentate, M-2 permeate, M-3 retentate, and M-3 CO<sub>2</sub> exhaust were 22.5 bar, 6.0 bar, 6.5-7.0 bar, and 0-0.1 bar respectively. For increasing the CO<sub>2</sub> removal efficiency, recycle loop with gas hold up tank (T-8), gas compressor (C-2), and gas cushion tank (T-9) was designed and stream was merged into the inlet stream of M-1. Target syngas ratio after membrane section was set to about 2.0.

Two FT reactor, microchannel (FT-2) and multitubular fixed bed type (FT-1), were installed in parallel for comparing the performances. Microchannel FT reactor core was made by 316L stainless steel with 285×295×460 mm. There were 528 reaction channels in total, and the specification of each channel was 5 mm in height, 10 mm in width and 460 mm in length. Both the inlet and outlet region (about 30 mm on both sides) of the reactor was filled with Al<sub>2</sub>O<sub>3</sub> balls, and GL-3000S (12 wt% cobalt catalyst supported on 1 mm  $\gamma$ -Al<sub>2</sub>O<sub>3</sub> developed by KOGAS) was prepared for packing 400 mm of reaction channel. Multitubular fixed bed FT reactor core was made by stainless steel for shell side and high pressure steel pipe for tube side. Diameter of the reactor core was 300 mm and total length was 1815 mm. Diameter of each tube was 33.4 mm and length was 1200 mm and the number of the tube was 33. The inlet and outlet region of the reactor was filled with Al<sub>2</sub>O<sub>3</sub> balls, and GL-3000S was prepared for packing at the middle of the reactor. Target operating temperature and pressure were set as 220-240°C and 20 bar respectively. For the cooling system,

silicon based cooling oil, Syltherm 800®, was circulated at the flow rate of 200 L/min with non-seal hot oil circulating pump (P-2). Hot oil receiver with 9 kW heater (E-9) and 9 kW hot oil 2<sup>nd</sup> heater heated up the coolant. Gas chromatography (YoungLin YL6100GC) with the 45/60 molecular sieve 13X, 80/100 PORAPAK N 10 ft×1/8 in, thermal conductivity detector (TCD) and flame ionization detector (FID) was installed after the 2<sup>nd</sup> decanter (T-11) for analyzing the gaseous components (CO, N<sub>2</sub>, CH<sub>4</sub>, and CO<sub>2</sub>) of the FT reaction products. Locations of the thermocouples installed in the microchannel FT reactor for sensing the local temperature inside the reactor are indicated in the front view of the reactor, as shown in Figure 4-3. For reducing and rinsing the catalyst, H<sub>2</sub> and N<sub>2</sub> were supplied from a H<sub>2</sub> cylinder and a N<sub>2</sub> cylinder kept near the reactor set-up. Downstream end section of the compact GTL process consisted of decanter (T-10, T-11) and wax receiving drum (T-12)

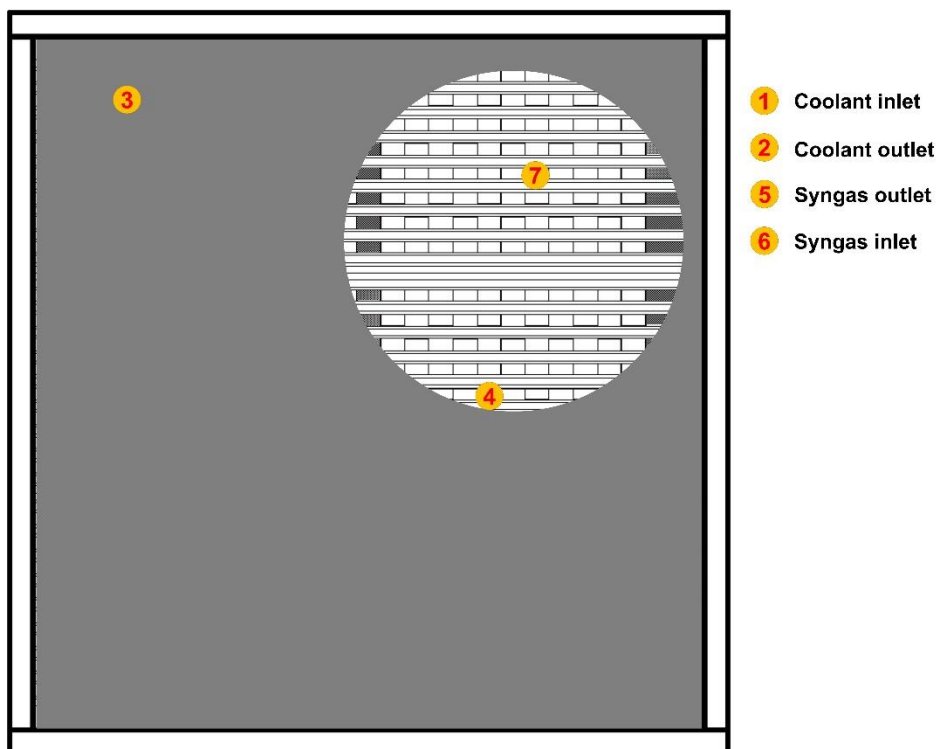


**Figure 4-3.** Location and index of the thermocouples (TC-(1-7)) in the front view of the reactor.



#### 4.1.4. Result and discussion

First, the composition of the syngas stream coming out from reformer section and passing through CO<sub>2</sub> membrane separation section is checked before feeding to the FT reaction section. The temperature data from three thermocouples (TC-RE1, TC-RE2, and TC-RE3) located in the heterogeneous zone of the tri-reformer is shown in Figure 4-4. It can be seen that after the auto ignition reaction (AIR) was successfully performed and stabilized, the thermocouple located in the heterogeneous zone of tri-reformer shows temperature between 900-1000 °C. From the composition data of tri-reformer exit, it can be seen that an average of 98.27% CH<sub>4</sub> is converted to syngas (mixture of H<sub>2</sub> and CO) with syngas ratio (H<sub>2</sub>/CO) as 2.67 on average. In fact, H<sub>2</sub>/CO ratio in the initial AIR reaction is 9.34, but once the tri-reforming process is stabilized (after 24 hr operation), the H<sub>2</sub>/CO ratio decreases to an average value of 2.67 and remain static for rest of the operating hours, as can be seen in Figure 4-4. The average CO<sub>2</sub> molar composition at the tri-reforming exit is 16.44%. This percentage of CO<sub>2</sub> in the syngas stream is unsuitable for FT reaction and should be removed through the CO<sub>2</sub> membrane separation section. The average CO<sub>2</sub> molar composition in the exit stream from CO<sub>2</sub> membrane separation section is 10.58%, showing a CO<sub>2</sub> removal rate of about 36.75%. In this particular CO<sub>2</sub> separation process, non-polar CO<sub>2</sub> is removed by the selective permeability of the membrane. However, non-polar H<sub>2</sub> also gets

removed at the same time through a small portion of the membrane, thereby reducing the overall  $H_2/CO$  ratio to an average value of 2.08, which is appropriate value for low-temperature FT reaction. And, as can be seen from Figure 4-4, the reforming section and the  $CO_2$  separation section, which are the pre-processing sections for the FT reaction section, were operated stability till 280 hr without large variations while FT reaction section was operated from 140 hr to 270 hr. This clarifies the fact that syngas supply to the FT reaction unit was stable during the entire duration of FT reactor operation.

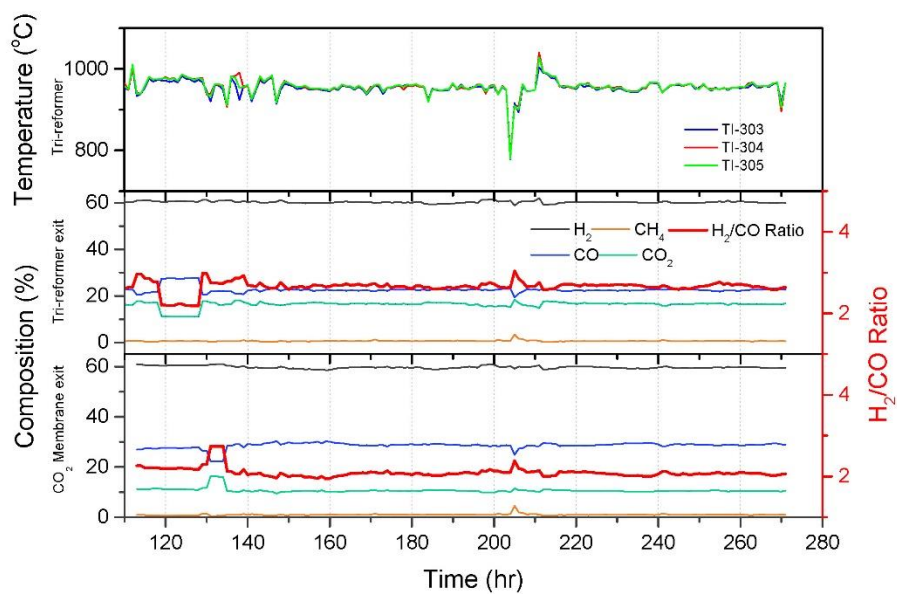


**Figure 4-4.** Temperature and composition profile after starting the operation of reformer and CO<sub>2</sub> membrane separation sections.

To compare the performance of the two types of FT reactors based on the thermal control, data from thermocouples installed inside the microchannel reactor (TC- (1-7)) as indicated in Figure 4-3 and data from the thermocouples installed inside the central tube of the multitubular fixed bed reactor (TC-FB1 and TC-FB2 located at the 2nd and 3rd segments of the 10 segments divided along the longitudinal direction of the tube) are compared, as shown in Figure 4-5. First, the temperature of the microchannel reactor was increased to 220 °C, followed by step increase to 230 °C and 240 °C in order to determine whether the runaway reaction occurred or not. Even though the syngas inlet temperature (TC-6) is higher than the target reactor temperature (by more than 10 °C), the enhanced heat transfer capability of the microchannel reactor system can easily bring down the syngas temperature to the target reactor temperature before entering the reactor core. It is noteworthy that because TC-3, TC-4, and TC-7 are installed at the entrance of the reactor, reactor area is large since it is a pilot scale, uniform gas inlet distribution fails, and with the highly exothermic nature of FT reaction, it is possible that temperature fluctuation could occur with large heat generation, but temperature shows fluctuation within 1 °C. The syngas outlet (TC-5) temperature profile is similar to that of other temperature sensors and is much lower than the syngas inlet, which is an evidence that there was no undesired heterogeneous heating phenomena near the position of the thermocouples. Moreover, no runaway reaction occurred even when the operating temperature was increased to 240 °C and inlet syngas temperature to

250 °C, which indicates that developed microchannel FT reactor is robust even at high temperature operation. However, in the multitubular fixed bed FT reactor, unlike microchannel FT reactor, hot spot at the front region of the reactor was observed, as shown by the thermocouple (TC-FB1) data in Figure 4-5, indicating a condition of runaway reaction. When the operating temperature was increased from 220°C to 230°C, TC-FB1 showed rapid rise in temperature to about 395°C indicating a surge in exothermic reaction at that condition. Even when the temperature of the coolant supplied to the multitubular fixed bed reactor was kept much lower compared to that of coolant supplied microchannel reactor, the low heat removal efficiency of multitubular fixed bed reactor system could not prevent the runaway reaction from appearing. During the runaway reaction, the catalyst inside the multitubular fixed bed reactor got deactivated resulting to the eventual disappearance of FT reaction in the reactor. Accordingly, multitubular fixed bed reactor was shut down for safety and economic reason.

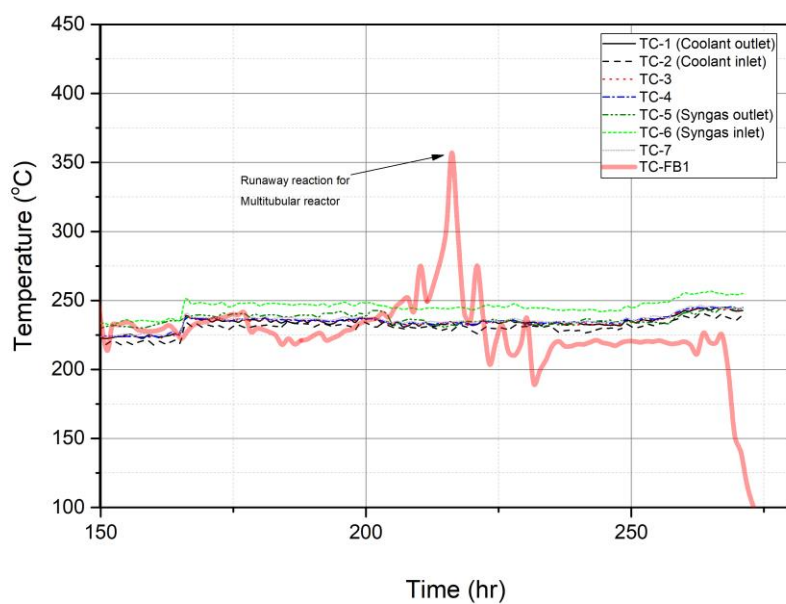


**Figure 4-5.** Reactor temperature of the microchannel FT reactor and multitubular fixed bed FT reactor as given by thermocouples installed inside the reactors.

Therefore, it can be understood that temperature data from multitubular fixed bed reactor suggest that smaller tube diameter (smaller than 5mm diameter of the present tube) may provide higher heat removal capacity needed to control reactor temperature of multitubular type FT reactor. Also, in the coolant oil circulation system of the present FT reaction section, there is no cooling facility in the hot oil return line. This can prove to be a disaster in the reactor operation should the temperature of the catalyst layer rises rapidly due to a rapid exothermic reaction as the reaction heat cannot be removed abruptly. Therefore, it is necessary to provide additional cooling facility in the hot oil return line or dilute the catalyst loading to avoid excessively high reaction rate. On the other hand, temperature data from microchannel reactor operation showed safe and stable operation, adequate control of reactor temperature, while still achieving high CO conversion for the entire duration of reaction operation (140 hr to 270 hr), as shown in Figure 4-6. Microchannel FT reactor, therefore, proved to be more advantageous compared to multitubular fixed bed FT reactor in terms of FT reactor performance. Accordingly, a microchannel FT reactor may be used to achieve efficient and safer operation of small scale compact GTL plant. Additionally, although not conducted, in the present pilot scale demonstration set-up, since both microchannel FT reactor and multitubular fixed bed type reactor are installed in parallel, replacing the latter with second module of the former should make the productivity of 1 BPD (two 0.5 BPD modular microchannel reactor in parallel).

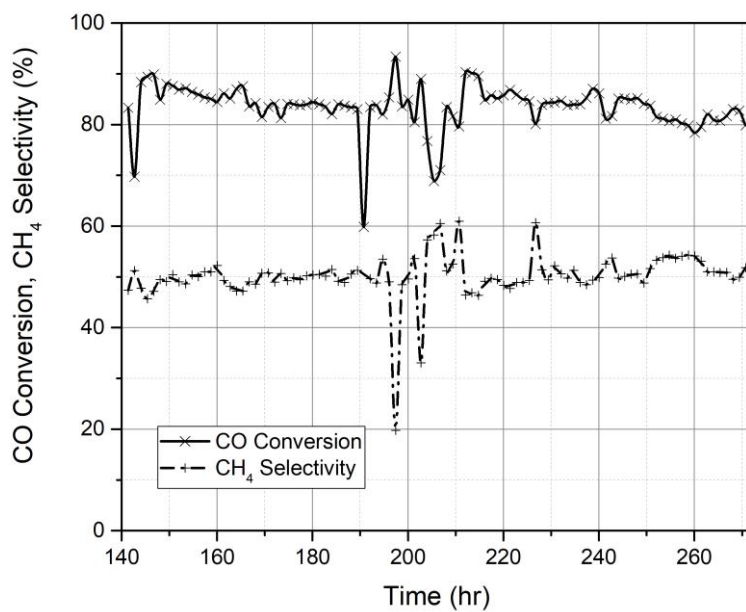


**Figure 4-6.** CO conversion and CH<sub>4</sub> selectivity of compact GTL pilot plant with microchannel FT reactor in the FT reaction section.



Finally, we evaluate the performance of the microchannel FT reactor based on CO conversion and CH<sub>4</sub> selectivity. The CO conversion is calculated by indirect measurement of the absolute molar composition of CO at the inlet and outlet of the reactor given by the GC analyzer and using inert N<sub>2</sub> gas from the GC data as the baseline. The average CO conversion is estimated to be about 83.54%. Although temperature affects the CO conversion [2, 16, 24, 215], in the present pilot plant operation, it is difficult to notice the effect of operating temperature change on CO conversion as there are no clear cut shift in the value of CO conversion time series data. There are several peaks with low conversion, but the reason for the existence of these peaks is believed to be due to the fluctuations in flow and conversion rates in the reformer section. However, the conversion rate in the present pilot plant operation (83.54 %) is higher than the values (65 - 78 %) reported from both commercial and lab scale FT synthesis operation. This higher value of CO conversion achieved in the present pilot plant operation may be due to the fact that the syngas injection rate into the reactor (GHSV = 2500 hr<sup>-1</sup>) was much lower than the GHSV value of 4000 ml/gcat · h used in the simulation [31]. Experiments using the same catalyst showed a conversion rate of 42.00% at 4000 ml / gcat · hr at 220 °C on a lab scale [31]. However, in the KOGAS compact GTL pilot plant, due to the efficiency and design limitations of the reformer and the CO<sub>2</sub> membrane section, the space velocity set to 2500 ml / gcat · hr. This GHSV is low but the conversion is overwhelmingly high. Consequently, heat produced by the

exothermic reaction would be higher. Assuming that the total enthalpy change is directly proportional to the mole of CO converted, rate of heat produced for the GHSV used in the present pilot plant operation can be obtained as  $\dot{n}_{CO} \times X_{CO} \times 165 \frac{\text{kJ}}{\text{mol CO}}$  [14] which gives around 15 kW. But because heat removal performance of the in-house designed microchannel FT reactor is efficient, the reactor temperature control was excellent in the pilot plant experiment. Although operation with higher values of GHSV was not conducted due to high operation cost (approximately 100,000 USD per run), we expect that there will be no heat removal problem with the present microchannel FT reactor block even if FT synthesis operation were carried out with increased value of GHSV. However, it is possible to have an argument for the unchanged conversion although thermocouple indicated increased temperature because there can be uncontrolled reactions at any location inside the reactor. Even though all thermocouples show no high temperature that indicates hot spot or runaway reaction, hot spots or runaway reaction can develop somewhere inside the reactor which is likely to be missed by the thermocouples installed at the front region of the reactor. Moreover imperfect distribution of inlet syngas can accelerate the uncontrolled kinetics because we did not performed the optimal design simulation of the inlet part of the reactor. Thus, in the future research, penetrated method for sensing the temperature of the reaction channel and the

method or simulation for checking the gas distribution performance should be performed.

In the case of CH<sub>4</sub> selectivity, the average selectivity is 50.13% much higher than value of 10-20% obtained in our lab scale experiments [31]. Compared with lab scale, the higher CH<sub>4</sub> selectivity can be obtained on a normal pilot scale, but the CH<sub>4</sub> selectivity obtained in this experiment is undesirably high and needs to be lowered. Multiple reasons exist for the CH<sub>4</sub> selectivity in the present pilot-scale experiment to be undesirably higher than that of our lab scale experiments. One obvious reason is the fact that the residence time for the syngas flow in the present pilot plant operation was much lower compared to the our lab-scale experiment. If the residence time is insufficient, the CH<sub>4</sub> selectivity is expected to increase as there is no sufficient time for the carbon chain growth [216]. Second reason could be the fact that in our lab scale experiment, incipient wetness impregnation (IWI) was used for producing the catalyst in gram scale. However, in pilot scale, because of necessity of industrial scale production, spray coating method was used for producing the catalyst in kilogram scale. And the third reason could be that Al<sub>2</sub>O<sub>3</sub> support diameter of pilot scale operation was about 1 mm, which is much bigger than the diameter of Al<sub>2</sub>O<sub>3</sub> support used in our lab scale (100 μm scale). This difference in catalyst support diameter can make approximately 10 times difference in the catalyst surface area per unit volume, thereby reducing the catalyst activity significantly.

Additionally, the bigger catalyst support size does not allow Co particles to sufficiently penetrate into the support pores. Therefore, due to low effective residence time of syngas, less effective method of catalyst material coating and bigger catalyst support size, much higher value of CH<sub>4</sub> selectivity was obtained although nearly constant value of GHSV and CO mass fraction was maintained during the entire operating hours. Yet another reason could be the fact that the plant was operated at conditions corresponding to high CO conversion. As commonly known with FT reaction, CO conversion and the product selectivity are strongly related to the process operating conditions. In the present pilot plant operation, operating time at 220 °C was relatively low compared to that of 230 °C and 240 °C, thereby making overall CO conversion unreasonably high. And it is generally agreed that high CH<sub>4</sub> selectivity is generated for high CO conversion [217] .

The final reason for obtaining undesirably high CH<sub>4</sub> selectivity in the present pilot plant operation is expected to be the improper method of catalyst reduction. In the present pilot plant experiment, the catalyst was reduced at 300 °C using only H<sub>2</sub>. However, D.B. Bukur et al. [218] identified with their Fe-based FT catalyst that more CH<sub>4</sub> and gaseous hydrocarbons are obtained if the catalyst is reduced only with H<sub>2</sub> reduced compared to that of carbon monoxide or syngas reduced catalysts. In Co-based FT catalyst too, it is reported that lower CH<sub>4</sub> selectivity, and good catalyst stability can be achieved by using

syngas rather than pure  $H_2$  for catalyst reduction prior to actual FT reaction [219]. Moreover, it is also reported that low catalyst reduction temperature cannot reduce catalyst sufficiently. In our present pilot plant experiment, to avoid excessive vaporization and subsequent increase in pressure over 20bar of the coolant medium, temperature was not increased over 300 °C during the catalyst reduction process. Therefore, assuming that all the reasons discussed are applicable to the present method of catalyst preparation, catalyst pre-processing and reactor operation in order to reduce high  $CH_4$  selectivity following practices are recommended; 1) reducing the catalyst with syngas, 2) increasing the reduction temperature above 300 °C, 3) producing the catalyst with IWI method, and 4) operating with moderate value (below 80 %) of CO conversion.

#### 4.1.5. Conclusion

A pilot scale compact GTL process is operated using an in-house designed microchannel reactor block as the FT synthesis unit. Process description of the present pilot scale compact GTL process comprising of reforming section, CO<sub>2</sub> separating section and FT synthesis section are presented. Systematic computer aided engineering design procedure adopted for a modular 0.5 BPD microchannel FT reactor block design (285 mm × 295 mm × 460 mm) consisting of 528 process channels is described in the form of design procedure flow-chart. Reforming section comprising of a pre-reformer unit followed by a tri-reformer unit achieved an average value of 98.27% CH<sub>4</sub> conversion to syngas. CO<sub>2</sub> membrane separation section comprising of three membrane separators achieved separation rate of 36.75% along with successful reduction of CO/H<sub>2</sub> ratio from 2.67 to 2.08, a value desired in low temperature FT synthesis. Temperature data from thermocouples installed inside both 0.5 BPD modular microchannel and packed bed type FT reactors operated in parallel showed stable temperature control for microchannel FT reactor for the entire plant operation up to 270 hr, while the multitubular fixed bed type FT reactor operation failed due to reaction runaway. From the modular microchannel FT reactor operation, although undesirably high value of CH<sub>4</sub> selectivity (50.13%) was obtained from the plant operation, high CO conversion of 83% and stable temperature control at 220 °C, 230 °C and at 240 °C during the entire pilot plant

operation (140 hr to 270 hr ) demonstrated the appreciable performance of KOGAS-SNU novel microchannel FT reactor. Reasons for undesirably high value of  $\text{CH}_4$  selectivity are mostly reactor operation related rather than the design related. Accordingly, following practices are recommended to achieve appreciable CO conversion with low  $\text{CH}_4$  selectivity: reducing the catalyst with syngas, increasing the reduction temperature above 300 °C, producing the catalyst with IWI method, and operating with moderate value (below 80%) of CO conversion. Furthermore, penetrated thermocouple for sensing reactor inside temperature should be developed for microchannel reactor for understanding precise temperature profile and further study related to distribute inlet syngas uniformly which can be related to uniform packing of catalyst must be performed for more controllable reactor. Further, the compact GTL process described, the systematic modular microchannel reactor design procedure and pilot plant operation data presented in the present paper may serve as a general guideline in similar future works on pilot scale reactor model development, design and operation.

## **4.2. Industrial scale (40 tonCO<sub>2</sub>/day) CCUS carbonation reactor geometry design optimization**

Using the reactor modeling in Section 2.3, the design of the CCUS direct carbonation reactor, a 40 tonCO<sub>2</sub>/day class, was carried out with Daewoo E&C. It is aimed to find the optimal reactor structure design and operating condition by analyzing the base case for reactor designed with approximate heuristic through various computer-aided engineering techniques. The design specifications sought by the reactor must first satisfy the inlet gas flow rate of 7000 Nm<sup>3</sup> / hr and the temperature inside the reactor to 80 °C. Also, the CO<sub>2</sub> concentration is 15 mol%, which is higher than the general incinerator and seems to be about the average of coal-fired power plants. The solid concentration before the reaction is 28.7 wt% of the total reaction agent, and after the reaction is completed, including the amount of precipitated calcium carbonate, solid concentration is increased to 36.1 wt%. The resulting solution is an opaque white liquid with a density expected to be about ~ 1.3 tonnes / m<sup>3</sup>. We tried to find the maximum value of the solid suspension by fixing these external conditions and taking into consideration various variables such as the speed, position, number and baffle of the stirrer, and addition of the slope structure under the reactor.

To evaluate the degree of solid suspension, which is the primary purpose of this paper, it is necessary to measure quantitatively the solid suspension degree.



As a measure of these, just-suspension speed ( $N_{js}$ ), solid distribution, and cloud height are often used [220].  $N_{js}$  is the impeller's speed (rpm) that ensures that all solids stay on the floor for a second or more. However, even though there are no settled solid particles, further analysis of the solid distribution is necessary because the distribution throughout the reactor may be uneven. Also, because the height at which a solid can be maximally floated is limited, its height is expressed as cloud height ( $H_c$ ). Cloud height is defined as the point at which the liquid-solid mixture is separated from the clean liquid. As a concrete value, the average height is calculated as the maximum height of the isosurface where the average solid fraction is achieved [55]. If the cloud height is explicitly present, the cloud height is maximized, and the efficiency of the reaction can be increased since it is the dead space above which no reaction occurs. In this study,  $N_{js}$ , which cannot be directly measured using normal-state CFD calculations, was not analyzed, but solids distribution and cloud height were directly measured and analyzed. First, we set 50 height points (0 m to 2.45 m at 0.05 m intervals) in a 2.5 m height reactor, calculate the average solid fraction at each height point, and calculate the standard deviation (STD) for quantifying the solid distribution. If the deviation of the solid fraction along the height direction is large, the STD value becomes large. For example, in Figure 2-16, the STD value decreases as the solid volume fraction changes with reactor height. Also, the cloud height was determined by measuring the highest height

of the isosurface (Figure 4-7), which achieved 5% of the total solid volume fraction throughout the reactor.

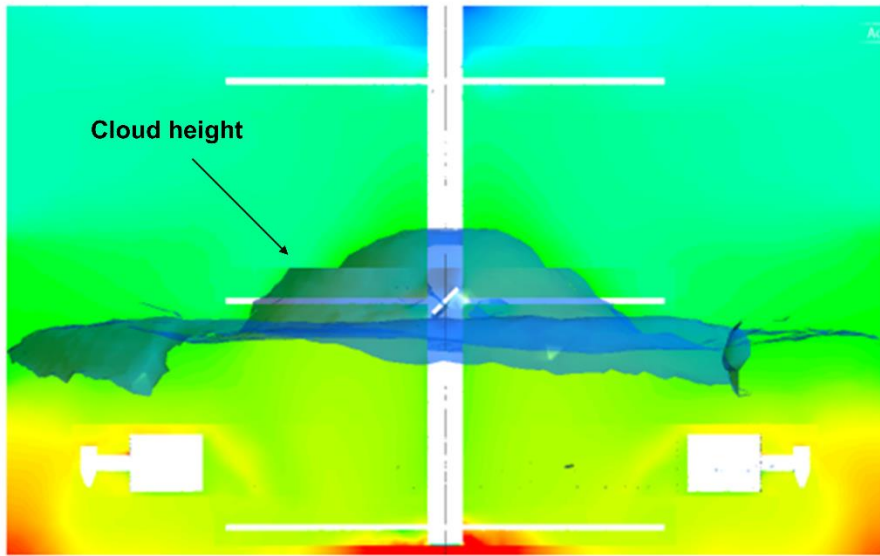


**Figure 4-7.** Visualization of cloud height of solid-liquid multiphase reactor

### **4.2.1. Design procedure and simulation set-up**

To optimize the design of the reactor, the method used in this study is computer-aided engineering, the 3D geometry is computerized, meshing is performed, and the reactor is analyzed by CFD model. In this process, reactors of various structures and conditions can be tested, and the reactor with the best performance can be selected. In this research, solid suspension, bubble dispersion, and bubble residence time are the most important design objectives. All of these values must be high enough for the reactor to have maximum  $\text{Ca(OH)}_2$  dissolution and  $\text{CO}_2$  mass transfer.

In order to accomplish this, we tried to find the optimal combination by conducting the screening work for the second time. First, we analyze the influence of the overall design variables on the 22 cases of the first order, select the conditions that showed the best performance among them, and make a new combination to perform the second design analysis.

The core design variables are 1) impeller geometry involving axial type which gives vertical flow, radial type which gives horizontal flow, and pitched blade type which gives horizontal and vertical flow at the same time. 2) The  $D/T$  ratio, which is the diameter ratio of the stirrer to the diameter of the reactor, is also one of the most important design parameters. 3) The number of the impeller layer is also very important. The number of impellers involved has a great influence on the back mixing and affects the retention of the reactants.

Also, 4) the spacing between the impeller layers is also important. If the spacing is too long, the effect of the multi-layer impeller is significantly deteriorated. If the spacing is too short, the mixing loop is broken, and the flow becomes ineffective. 5) The impeller angular velocity is the most important value that can be overestimated without too much emphasis. 6) Finally, the presence of the baffle and the length are important, and they must be analyzed because the internal reactor flow forces them to have a rising fluid flow that affects the ability of solid particles to rise upwards. The combination of each variable is shown in Table 4-1.

The Eulerian-granular multiphase model (2.3.2) was used for the solid-liquid model and the Eulerian multiphase model for the gas-liquid model.

**Table 4-1.** Variables specification.

Type	#	Impeller			Baffle
		Clearance	D/T	Rpm	
Radial	Triple*	Low <sup>a</sup>	Small <sup>c</sup>	30*	Base*. <sup>e</sup>
Mix				60	Long <sup>f</sup>
PBT*	Dual	Base*	Base*. <sup>d</sup>	90	Long & Wide <sup>g</sup>

\*indicates the values constituting the base case, <sup>a</sup>C<sub>1</sub>=0.46T, C<sub>2</sub>=0.21T, <sup>b</sup>C<sub>1</sub>=0.54T, C<sub>2</sub>=0.29T, <sup>c</sup>D=0.33T, <sup>d</sup>D=0.5T, <sup>e</sup>h=1.95 m, d=100 mm, <sup>f</sup>h=2.5 m, d=100 mm, <sup>g</sup>h=2.5 m, d=250 mm, all variables are describe in Figure 2-13

### 4.2.2. Result and Discussion

The results are introduced first in the 1st design case and then in a way to explain the new 2nd design case selected. Table 4-2 shows the results of all 1<sup>st</sup> design cases.

First, the analysis results of gas-liquid fluid dynamics are as follows. Eight models with changes in RPM (0 rpm, 30 rpm, 90 rpm), impeller type change (PBT, Radial impeller), impeller diameter change ( $D / T = 0.33, 0.5$ ), impeller clearance change did not have a meaningful effect on residence time. Turning the RPM to 60 rpm or more causes surface vortex, which reduces the residence time and also the gas dispersion inside the reactor. If we lower the clearance, decrease the  $D / T$  to 0.33, or change it to a radial impeller, the surface vortex disappears, but the residence time or gas dispersion is worse than the 0, 30rpm model. When the power consumption, residence time, and gas dispersion were taken into consideration, the model with the rpm reduced to 30 rpm in the base case and the model with the  $D / T$  reduced from 0.5 to 0.33 were most suitable.

Overall, gas-liquid systems do not seem to need special consideration in the 2nd design case because there is no phenomenon that the impeller speed is so fast that the vortex phenomenon does not occur and that the gas dispersion does not change significantly due to other factors.

**Table 4-2.** 1<sup>st</sup> Design result of each case.

	Impeller				Diffuser		Baffle		Solid suspension					Bubble characteristics			Impeller Power						
	rpm	D/T	type	#	clearance	position	length	width (mm)	top	mid	bot	STD	Cloud Height (m)	Dispersion (STD)	residence time (s)	Surface Vortex	(top, mid, bot) (kW)	Sum (kW)					
Base case	60	0.5	PBT	3	base	base	base	100	6%	9%	10%	0.008	1.078	0.1183	2	O	(7.74, 6.01, 7.62)	21.37					
1	0	0.5	PBT	3	base	base	base	100	0%	7%	100%	0.114	0.452	0.095	2.27	X	(0, 0, 0)	0					
2	30	0.5	PBT	3	base	base	base	100	5%	8%	13%	0.014	1.037	0.102	2.28	X	(1.32, 0.96, 1.13)	3.41					
3	60	0.5	PBT	3	base	base	base	100	6%	9%	10%	0.008	1.078	0.1183	2	O	(7.74, 6.01, 7.62)	21.37					
4	90	0.5	PBT	3	base	base	base	100	7%	8%	9%	0.005	0.954	0.149	1.59	O	(20.7, 20.1, 17.5)	58.3					
5	60	0.33	PBT	3	base	base	base	100	5%	8%	13%	0.016	1.142	0.104	2.29	X	(1.66, 1.28, 1.82)	4.76					
6	90	0.33	PBT	3	base	base	base	100	7%	8%	11%	0.008	1.062	0.112	1.97	O	(10.1, 6.26, 7.52)	23.88					
7	30	0.5	PBT	3	base	base	long	100	5%	8%	13%	0.014	1.081										
8	30	0.5	PBT	3	base	base	long	250	6%	8%	11%	0.01	1.134										
9	60	0.5	PBT	3	base	base	base	400	6%	9%	10%	0.009	1.239										
10	30	0.5	PBT	3	low	base	base	100					0.113	2.22	X	(3.43, 3.06, 4.14)	10.63						
11	60	0.5	radial	3	base	base	base	100															
12	30	0.5	radial	3	base	base	base	100															
13	30	0.5	radial	3	base	base	long	100															
14	30	0.5	radial	3	base	base	long	250	5%	8%	16%	0.018	0.964	0.1105	2.07	X	(9.78, 5.60, 8.18)	23.56					
15	60	0.5	radial	3	base	base	base	400	16%	8%	5%	0.001	1.303										
16	30	0.5	PBT	2	base	base	base	100															
17	30	0.5	radial	2	base	base	base	100															
18	30	0.5	radial	2	low	base	base	100															
19	30	0.5	mix	2	base	base	base	100	8%	8%	9%	0.001	1.266	0.1105	2.07	X	(9.78, 5.60, 8.18)	23.56					
20	30	0.5	mix	2	low	base	base	100	6%	8%	13%	0.015	1.016										
21	30	0.5	mix	3	base	base	base	100	5%	8%	16%	0.017	0.889										
22	60	0.5	PBT	3	low	base	base	100															



The degree of dispersion of solid particles is very important in this reactor. The rate of dissolution of the solid drug, which is the rate-determining step of the reaction, is greatly influenced by how uniformly the solid drug particles are dispersed. Therefore, it is important to select a model in which the volume fraction distribution of the solid particles is maximally uniform, and the cloud height is maximized.

Part of the graph that can be analyzed is the particle volume fraction gradient (denoted by gradient contour), cloud height (denoted by the dense isosurface portion of the reactor, rather than the perfect suspension), and velocity vector field. The result of changing the impeller rotation speed at 0, 30, 60, and 90 rpm in the 3 layer impeller with pitched blade turbine (PBT) as the base case is shown in Figure 4-8. The particle volume fraction was found to be 60 and 90 rpm, which is well mixed (volume fraction is uniform throughout). However, at 30 rpm, the solid concentration is high on both sides and at the bottom of the impeller. This part is a part that does not contact with the gas, and provides a room for reducing the reactivity. However, we tried to design a structure that can be appropriately suspended at 30 rpm as the power usage is proportional to the cube root of impeller speed. As a result of analyzing the flow field of the internal liquid, it can be seen that the impeller has three separate flow loops in three-layer impeller. In the case of the top impeller at the top, there is not enough space above and below, and the circulation loop of the liquid is distorted.

This suggests that energy is not being used efficiently. In addition, the structure of the diffuser located at the bottom prevents the bottom impeller from generating a flow, which is a bad shape that generates only a weak upward flow.

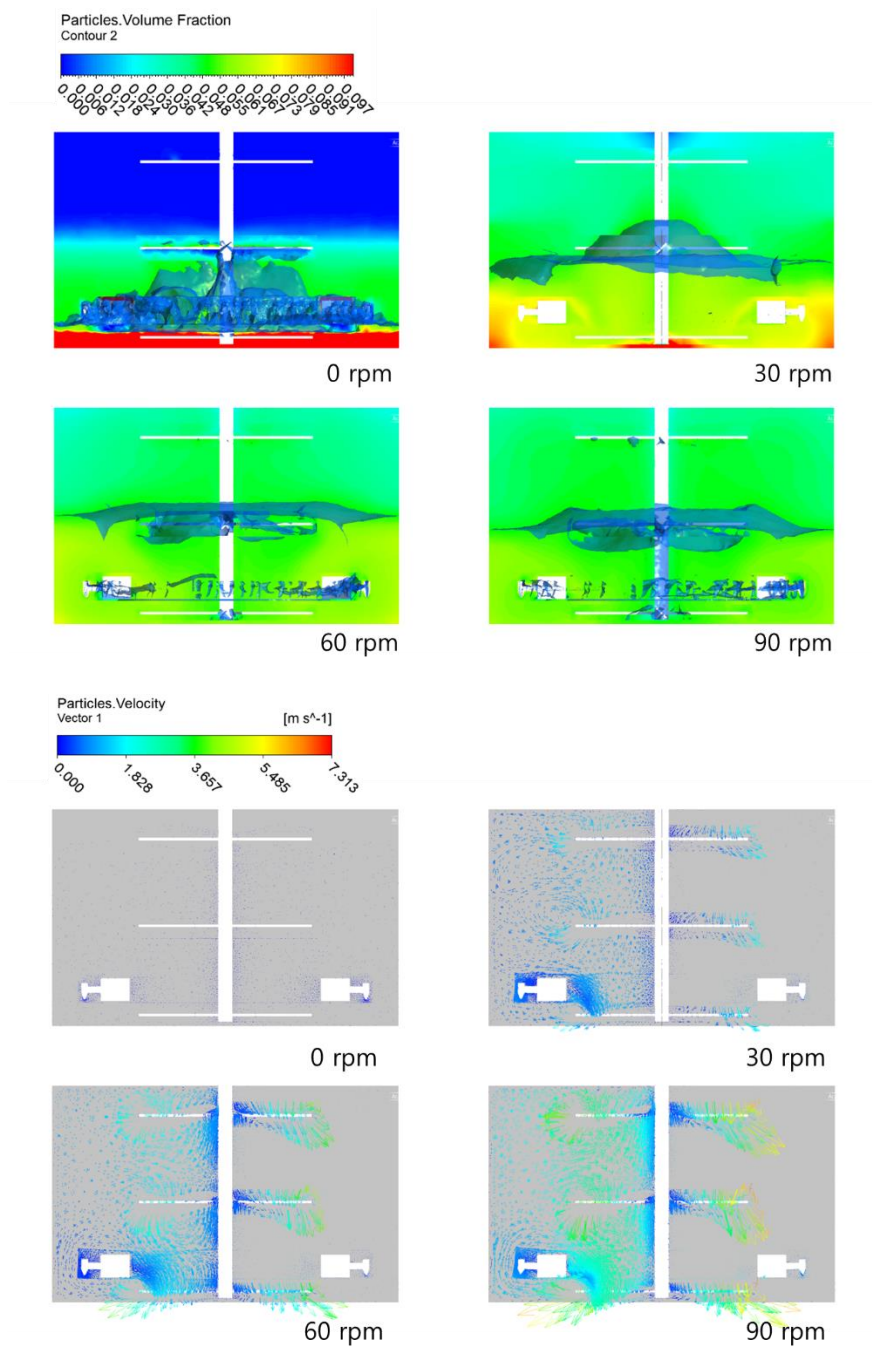
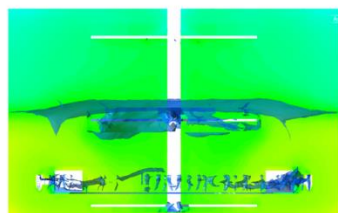
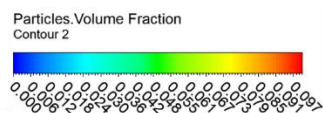
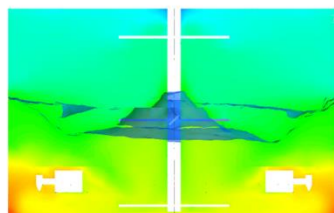


**Figure 4-8.** Particle volume fraction and velocity vector field of different impeller speed.

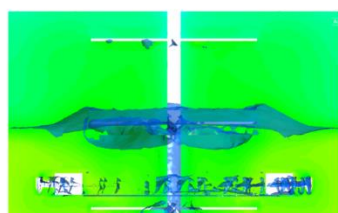
We also wanted to see if there is sufficient suspension effect at high rpm (60, 90) even when the impeller diameter is reduced (Figure 4-9). As the  $D / T$  decreases, the solid suspension is not good because the force and energy that make the flow as a whole decrease. However, it was confirmed that when  $D / T = 0.33$  when the speed was increased up to 90 rpm, the suspension shape was almost similar to  $D / T = 0.5$  of 60 rpm. In other words, it was confirmed that the change of  $D / T = 0.5 \rightarrow D / T = 0.33$  was equivalent exchange by raising about 30 rpm when hit by rpm. As discussed above, since the outermost angular velocity decreases as the  $D/T$  decreases, the energy transfer force decreases, and the velocity vector field weakens as a whole.



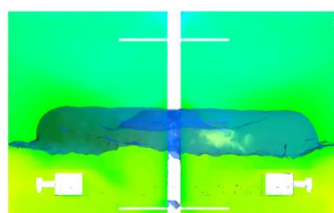
60 rpm,  $D/T=0.5$



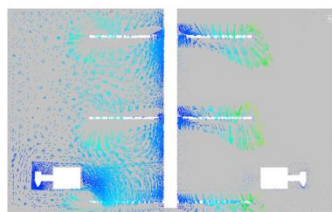
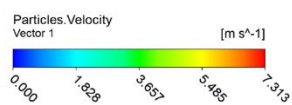
60 rpm,  $D/T=0.33$



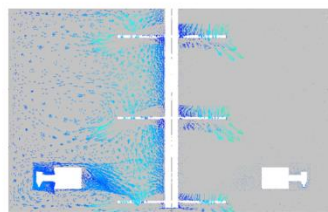
90 rpm,  $D/T=0.5$



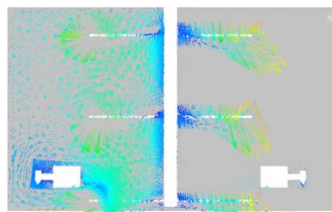
90 rpm,  $D/T=0.33$



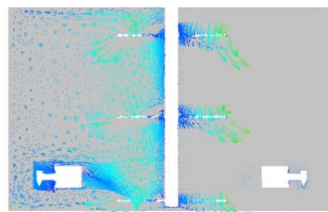
60 rpm,  $D/T=0.5$



60 rpm,  $D/T=0.33$



90 rpm,  $D/T=0.5$



90 rpm,  $D/T=0.33$

**Figure 4-9.** Particle volume fraction and velocity vector field of different  $D/T$  factor.

In the analysis of the change according to the impeller type (Figure 4-10), it was confirmed that the radial impeller (width = 100mm) has bad performance in terms of the solid suspension than the PBT. This basically supports the previous findings that axial velocity has a significant effect on the solid suspension. Also, our system shows that the rising edge of both side edges is important. However, at 60 rpm, it can be confirmed that the suspension is sufficiently performed even with the radial impeller.

Radial impellers, however, must be installed with sufficient width and length of the baffle to work properly. The baffle of the base case used in this model is very thin with a width of 100 mm and is not installed at the bottom of the reactor. Therefore, it seems necessary to separately analyze the effect of the radial impeller when supplementing the baffle.

Radial impellers do not form an axial velocity vector near the impeller, but rather push it radially. It is important to note that the spacing between the impellers is not sufficient and the intermediate circulation loops are not properly generated and interfere with each other. Therefore, baffle installation and clearance change are necessary.

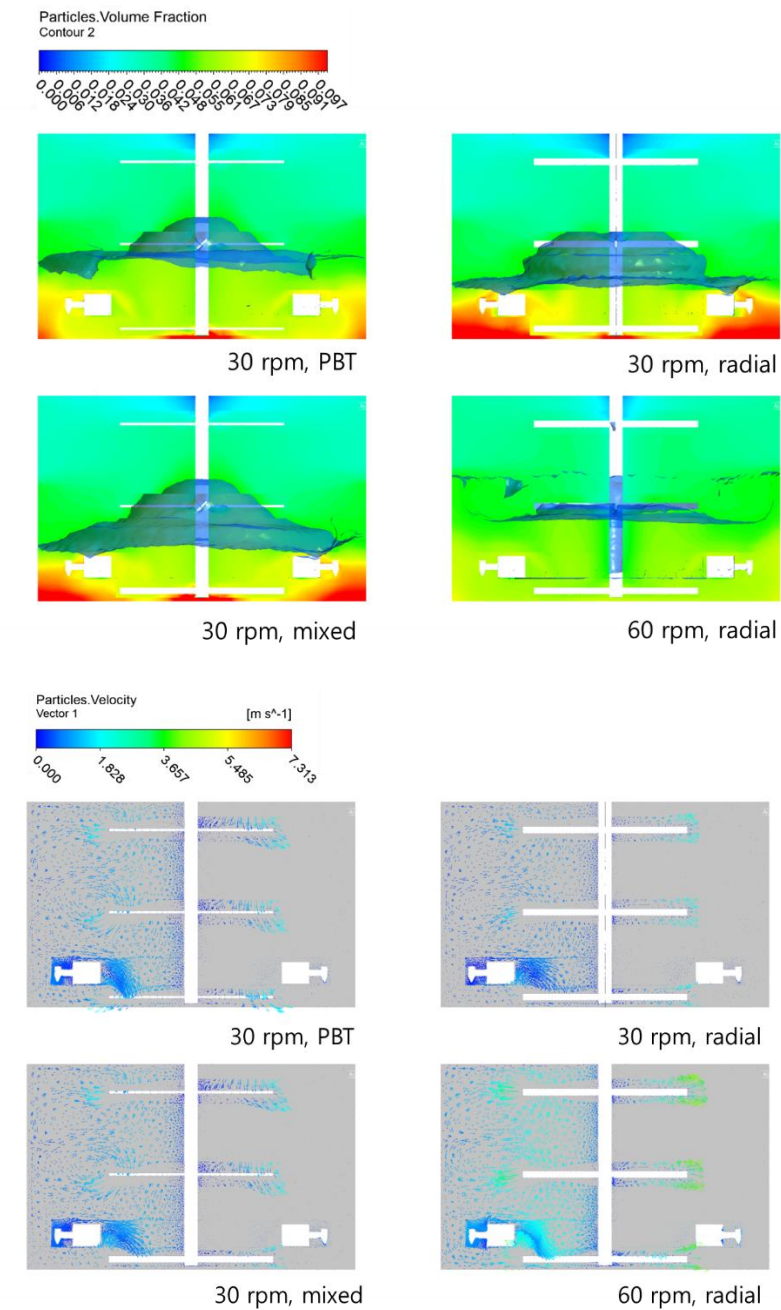
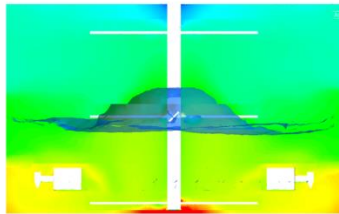
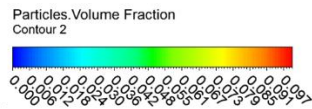


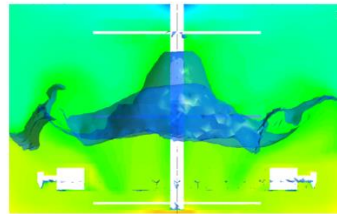
**Figure 4-10.** Particle volume fraction and velocity vector field of different Impeller type.

An analysis of the changes in the baffle (Figure 4-11) shows that when the baffle is simply lengthened (extending to the bottom of the reactor), it is better than without. And if the width increases to 250 mm, we can see that it gets better. In addition, even when the baffle is installed long and wide, it is still the same that the radial impeller is not as solid as the PBT. If the baffle is strengthened even at the same impeller rpm, the velocity vector in the ascending direction becomes stronger, and the circulating loop flow between the impellers becomes thicker. This is because the fluid moves out of the simple rotating motion and the baffle forces axial flow. This phenomenon is observed because the longer and wider the baffle makes the axial flow better.

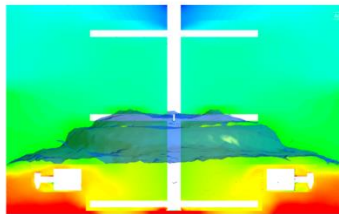




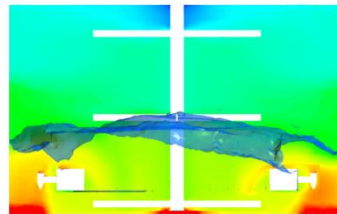
30 rpm, PBT, long, 100 mm



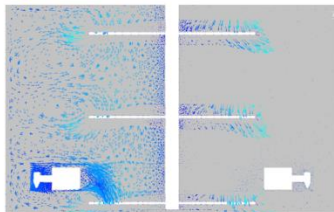
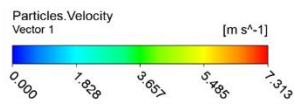
30 rpm, PBT, long, 250 mm



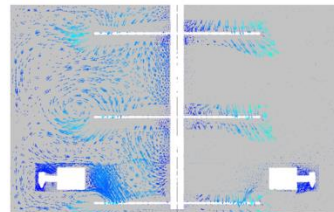
30 rpm, radial, long, 100 mm



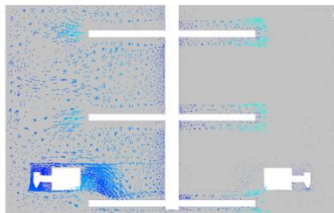
30 rpm, radial, long, 250 mm



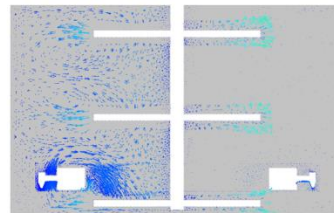
30 rpm, PBT, long, 100 mm



30 rpm, PBT, long, 250 mm



30 rpm, radial, long, 100 mm



30 rpm, radial, long, 250 mm

**Figure 4-11.** Particle volume fraction and velocity vector field of different baffle.

Clearance and dual impeller analysis are shown in Figure 4-12 and Figure 4-13. Overall, it is assumed that the position of the impeller is inefficiently positioned to produce an appropriate velocity field. Thus, two changes have been applied. First, we lowered the clearance of the middle and bottom impellers by about 350 mm to help the rise of the solid particles.

Also, the top impeller seemed to interfere with the flow of the middle impeller, thus eliminating the top impeller. As a result, the best suspension of all primary designs and the highest averaged cloud height. However, dual radial impeller showed poor results, so when using a two-layer impeller, both PBT types should be used.

When we checked the speed field, I could see why the dual impeller is the best for solid suspension. Usually, a solid flow is generated through a portion of the diffuser structure. In the case of a dual impeller, the top side of the diffuser is precisely struck to form a rising solid flow. Furthermore, it is sufficient for the flow to rise to the top without stopping by the top impeller. Thus, the design should be PBT dual impeller or mixed dual impeller (PBT+radial). However, if the median impeller is radial, the radial velocity created by the current rpm is too slow to allow the fluid to move to the wall quickly enough. It is not a good design because it does not show the collision effect (the baffle and the transformation into the axial flow from that part after the collision with the wall).

Finally, the height of the upper impeller of dual impeller increases 250 mm to simulate because the height is too low. From the result, installing the impeller in upper side gives the worse result. The velocity field shows why the impeller is not as good as when it is installed at a high altitude. It has been observed that the 2-stage impeller is too high to produce a circulating loop that reaches the bottom at a slower speed of 30 rpm. Therefore, it is considered that the structure that removes only the upper impeller from the clearance of the original design shows the best solid suspension.

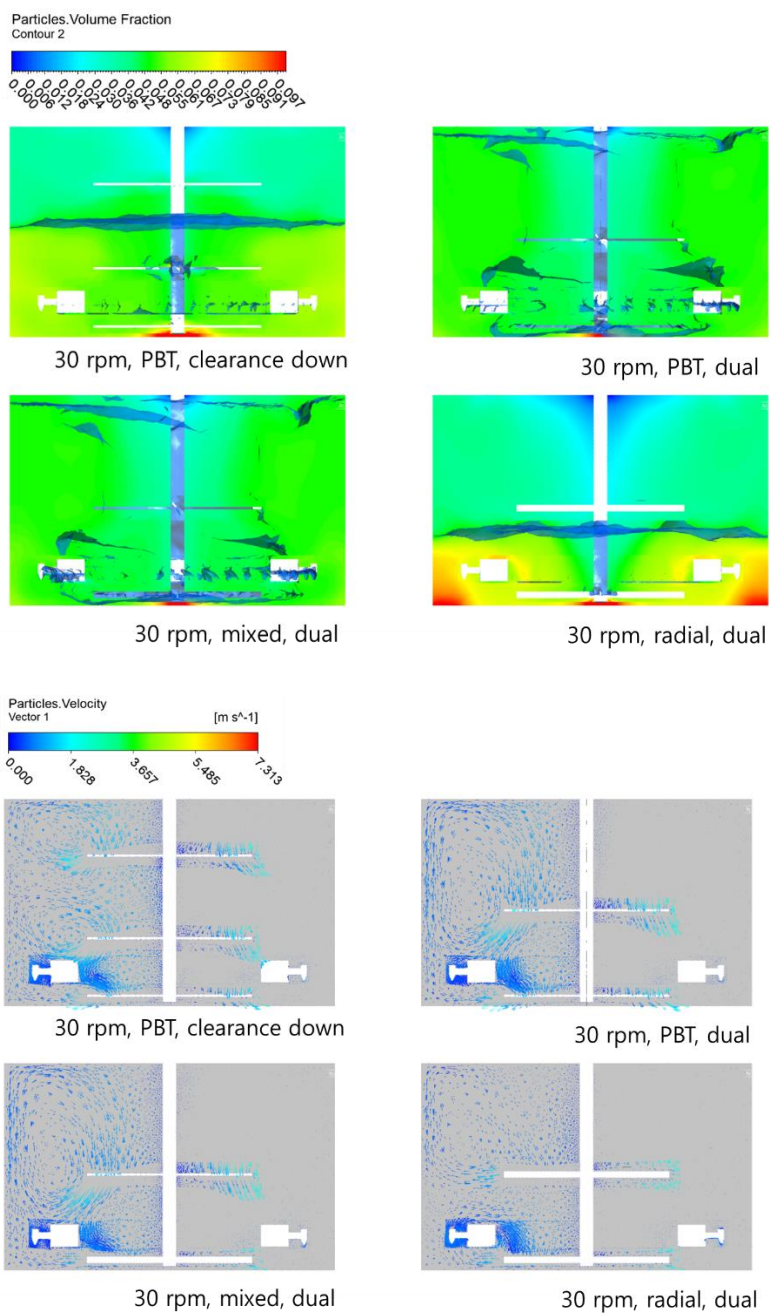


**Figure 4-12.** Particle volume fraction and velocity vector field of different clearance and dual impeller I.

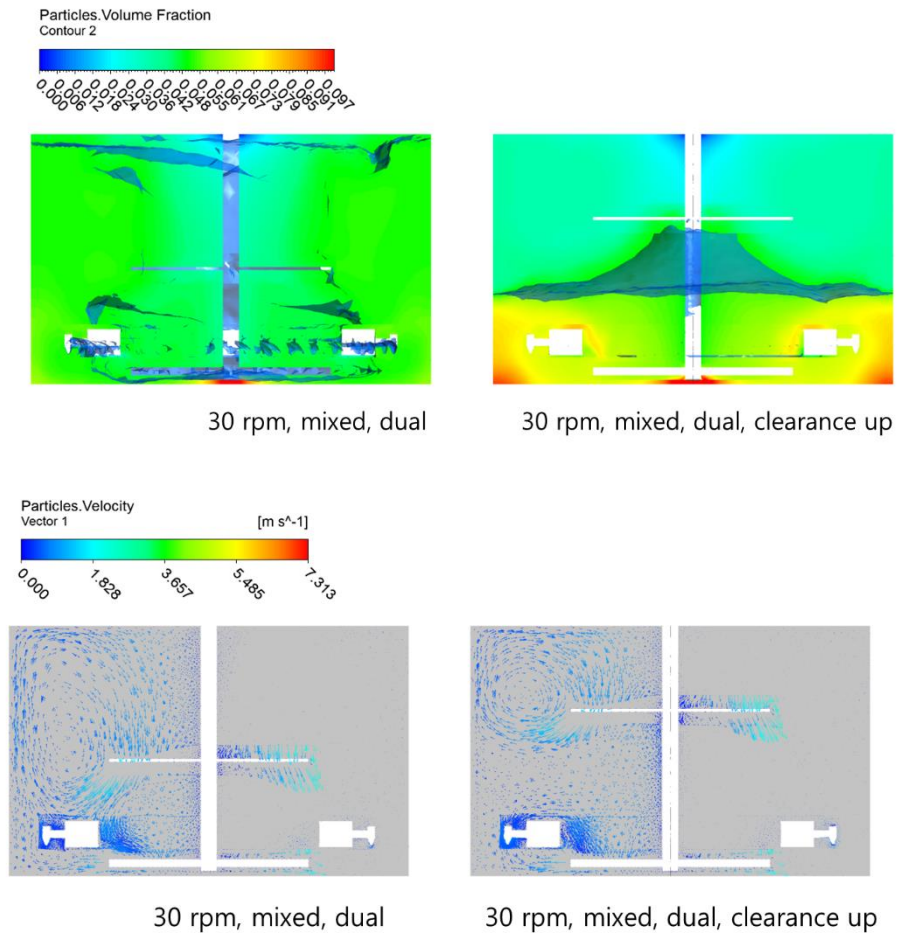


**Figure 4-13.** Particle volume fraction and velocity vector field of different clearance and dual impeller II.

Based on the 1<sup>st</sup> Design case, design variables are changed appropriately for performing the 2<sup>nd</sup> optimal design case study. Gas-liquid CFD simulation is not carried out because bubble characteristics are not that depended on the design variables. The result is organized in Table 4-3.

**Table 4-3.** 2<sup>nd</sup> Design result of each case.

	<b>Impeller</b>					<b>Diffuser</b>		<b>Baffle</b>		<b>Solid suspension</b>				
	rpm	D/T	type	#	clearance	position	length	width (mm)		top	mid	bot	STD	Cloud Height (m)
1	30	0.5	PBT	2	base	base	long	250		8%	8%	9%	0.001	1.133631
2	30	0.5	PBT	2	slope	base	long	250		8%	8%	9%	0.001	1.114928
3	30	0.33	PBT	2	slope	base	long	250		0%	5%	31%	0.134	0.728325
4	30	0.5	mix	2	base	base	long	250		8%	8%	9%	0.001	1.115463

First, when  $D/T = 0.33$ , it can be seen that even if another good design is introduced, the solid does not rise properly. It is confirmed that this is caused by the inability to make a good upflow by a small impeller. It is obvious with looking the vector field that follows. In the remaining 3 cases, we could see the almost similar flow, and it would be better to use anyone, but in practice, it is best to use 30 rpm, PBT,  $D/T = 0.5$ , dual, baffle (250 mm) and slope. Although cloud height can be lower than previous one, it does not have big meaning for overall solid suspension.

Finally, about the vector field, in the case of  $D/T=0.33$ , impeller is not sufficient to generate up flow of the solid particles where the others are sufficient. If reactor applies the slope structure in the bottom, rising flow is easily generated.

Therefore, it is recommended to change the triple impeller layer, which is a base case design, with a dual layer and use a long wide type baffle. Also, impeller velocity is best to drive at 30-60 rpm, and slope structure is good for rising flow, but not too bad even not exist so that it can be optional. With this change, the cloud height of 1.037 m would be 1.2 m, the suspension STD of 0.0141 would fall to 0.001, and the vortex and bypass possibilities would disappear.



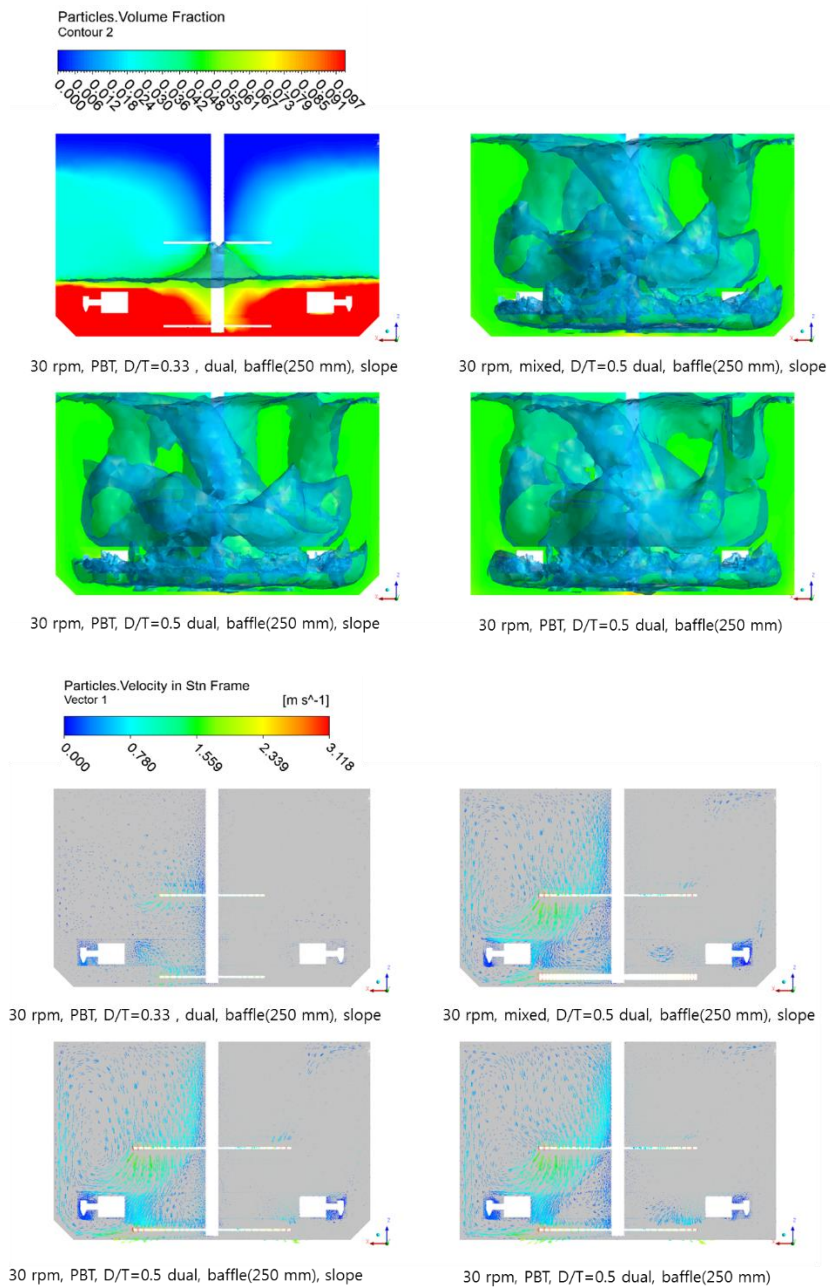


**Figure 4-14.** Particle volume fraction and velocity vector field of 2<sup>nd</sup> design result.

### 4.2.3. Conclusion

A tank agitator carbonation reactor in which the reaction between calcium oxide and carbon dioxide takes place is studied to understanding that how 6 design variables (the number of the impeller, impeller type, D/T, clearance, speed, baffle) affect to the solid dispersion using CFD simulation.

The number of the impeller has the greatest effect on solid suspension. 2 layer impeller has much better performance than 3 layer impeller because the first impeller acts as an obstacle to circular loop flow. Impeller types also have a big impact, with PBT much better than radial. Radial impellers are advantageous for gas dispersion, but they do not provide a uniform distribution of solids, even when the number of revolutions and baffle is increased.

In the case of impeller clearance, the solid suspension degree is not significantly influenced within the scope of this study, but the solid suspension degree is slightly improved when the clearance is slightly lower than the reference setting. The larger the diameter and the number of revolutions of the impeller are, the more the solid suspension is improved. Especially, if the number of revolution of the impeller increases, solid is well suspended even with the inefficient design because the effect of the other design variables decreases. However, since the number of revolutions and the diameter of the agitator is closely related to the power consumption of the impeller, the unnecessary excessive design should be avoided.

In the case of baffles, the longer and wider the shape, the higher the degree of solid dispersion, but the effect is not greater than the other variables. Among the length and width, the improvement is wider when the width is wider.

The analytical results obtained in this study show how the internal design parameters of the reactor affect the dispersion of the solid reactants. At the same time, an internal design combination was derived that evenly distributes the solid reactants. Equal distribution of solid reactants is critical to increasing the rate of dissolution of calcium oxide, which is the rate-determining step in a mineral carbonation reactor, and is a prerequisite for improving mass transfer rates and thus reaction rates. We will further examine the simulation results through further experiments and investigate the solid dispersion phenomenon that will vary when gas is introduced.

## CHAPTER 5. Concluding Remarks

### 5.1. Summary of Contributions

This thesis considered the application of computational science approach such as computational fluid dynamics (CFD), mathematical programming, derivative-free optimization, and machine learning technology to the process systems engineering topics. Especially, advanced modeling of reactor and process for Gas-to-Liquid (GTL) process and carbon capture, utilization, and storage (CCUS) process were performed. Moreover, optimization and analysis platform was developed for the unit, process, and plant-wide scale systems for various objectives. This chapter summarized the key contributions and conclusion of this thesis.

- Chapter 2.2 provided the 2D axisymmetric CFD model of FT microchannel reactor with porous media zone with lumped FT kinetics. In the same chapter, the 3D CFD based FT microchannel reactor block model with external heat source calculated by Aspen Plus was introduced.
- In Chapter 2.3, rigorous carbonation kinetics study with dynamics of the bubble and solid particle regarding DAE was performed. In the same chapter, Eulerian-granular multiphase carbonation reactor was modeled by CFD.

- Chapter 2.4 extended CFD reactor model to CFD-process simulator integrated platform for designing process and reactor simultaneously. The result of simulation shows CFD reactor modeling result, and process simulator (Aspen Plus) result perfectly exchange data and be designed automatically and simultaneously.

- Chapter 3.2 provided reactor scale systems optimization methodology. CFD reactor model function is perfectly connected to GA based multi-objective algorithm with the  $\epsilon$ -constraint method. Pareto optimal curve of  $C_{5+}$  productivity and  $\Delta T_{\max}$  is successfully solved.

- In Chapter 3.3, Lipschitz continuous function based derivative-free optimization algorithm was introduced for considering hidden constraint which is very important for optimizing process systems scale simulation. LNG liquefaction process is introduced to exemplify the performance of the algorithm, and 18.9% of operating cost is reduced than base case. In the same chapter, simultaneous synthesis of a heat exchanger network with multiple utilities using utility substages was explained. Thus, HEN of the sustainable process can be optimized with this systematic approach with various utilities.

- Chapter 3.4 provided a surrogate model for real-time analysis of toxic gas release in an overall plant system. Deep learning technology is used

for constructing the surrogate model and possibility of real-time calculation can help to apply this method to safety sustainable process.

- In Chapter 4.1, industrial application of proposed methodology presented in CHAPTER 2 and CHAPTER 3 for compact GTL process was provided. 1 BPD scale compact GTL pilot plant was constructed and tested with our FT microchannel reactor.

- Chapter 4.2 provided industrial application of computer-aided engineering reactor optimization procedure for 40 tonCO<sub>2</sub>/day CCUS carbonation reactor. Various designs of the reactor were analyzed, and optimal design will be applied by CCUS reactor of Daewoo E&C.

## 5.2. Future Work

It is believed that the recommended future work path is to explore the connection between the limitations of the various methodologies proposed in this study and other fields of computational science such as molecular dynamics and deep learning which are now rapidly developing. Considering multiphase and complicated reaction kinetics at the same time, reactor model with high convergence is very difficult to formulate, so it would be very valuable to study this part. Also, in the case of the integration framework in Section 2.4, it is necessary to consider a methodology that can be applied to more diverse reactors such as stirred tank reactors beyond simple packed bed reactors. Also, it is necessary to extend the various optimization algorithms presented to show high efficiency even under various conditions. In this thesis, only the autoencoder is included in the PSE field during deep learning, but it is expected that various deep learning techniques such as LSTM, GAN, and reinforcement learning can be applied to the PSE field.

**Reactor modeling.** CFD modeling has been carried out on packed bed reactors and stirred reactor type reactors, which are considered to be the most important in chemical reactions, but there are many other reactors used in chemical engineering. Therefore, it is necessary to study the CFD reactor modeling platform which can generally be used for various reactor modeling. In this study, lumped reaction kinetics or external kinetics calculation was used

because of the high computational cost of CFD. However, this would need to be addressed for more accurate modeling of the reactor, since this would show a much lower convergence and accuracy than simultaneous calculation in CFD at once.

**CFD-PSE integration framework.** The currently developed CFD-process simulation platform is simply a form in which the CFD model and the process simulator model exchange data at the same time. In practice, however, efficient data fabrication ideas are needed to apply this to more forms of sensitivity analysis. We also believe that this methodology, which is currently applied only to packed bed reactors, can be used in commercial parts as well as in combination with more diverse reactor types and process types.

**Improving the algorithms.** The modified DIRECT algorithm is designed to divide all hidden constraints. This may be good for solving a general non-convex searching space, but it has inefficiencies in normal process simulations. Therefore, additional research is needed to improve the algorithmic inefficiency.

**Deep learning.** We have seen through this thesis that data reduction through autoencoder can be used very effectively in the PSE field, but I have not thought about how other deep learning techniques could be able to graft the conventional PSE area. Therefore, CNN, which has strong ability to process image data, LSTM, which shows strong ability to voice processing or time series data, and GAN, which generates new data by appropriately processing



various data mixing, are very exciting to suggest ways to replace techniques used in existing PSE techniques. Also, we can expect a significant performance improvement using Bayesian optimization based method such as Gaussian process, which may be inefficient when using existing GA or deterministic algorithm in optimizing CFD.

**Applications.** Finally, we have applied GTL and CCUS to two commercial processes as industrial applications. In the future, however, we can see more diverse results by applying the computational science approach for design and optimization. It will be great future work.

# Nomenclature

## Acronyms & Abbreviations

AEGLs	acute exposure guideline levels
Adam	adaptive momentum estimation
AE	autoencoder
AIR	auto ignition reaction
ALAMO	algebraic models for optimization
BFW	Boiler feed water
BN	batch normalization
BPD	Barrel per day
BTL	Biomass to liquid
C3MR	propane precooled mixed refrigerant
CAE	computer-aided engineering
CCUS	carbon capture, utilization, and storage
CDR	carbon dioxide reforming of methane
CFD	computational fluid dynamics
CFL	courant-Friedrich-Levy
CNN	convolutional neural network
CTL	coal to liquid
DAE in 3.4	deep autoencoder
DAE	differential algebraic equation
DCAE	deep convolutional autoencoder
DIRECT	divide a hyper-rectangle
DME	dimethyl ether
DMR	dual mixed refrigerant
DNN	deep neural network
ERPGs	emergency response planning guidelines
FID	flame ionization detector
FPSO	floating production storage and offloading
FT	Fischer-Tropsch
GA	genetic algorithm
GC	gas chromatography
GHSV	gas hourly space velocity
GPS	generalized pattern search
GSS	generating set search
GTL	gas-to-liquid
HENS	heat exchanger network synthesis
HP	high pressure
IWI	incipient wetness impregnation
KOGAS	Korea gas corporation
LNG	liquefied natural gas
LP	low pressure
LPM	liter per minute
MADS	mesh adaptive direct search
MINLP	mixed integer non-linear programming
MP	middle pressure

MRF	multiple reference frame
MTA	minimum temperature approach
NAS	neighborhood assignment strategy
NG	natural gas
NN	neural network
Nu	Nusselt number
ORC	organic Rankine cycle
PBT	pitched blade turbine
PCA	principal component analysis
POM	partial oxidation of methane
Pr	Prandtl number
PSO	particle swarm optimization
RANS	Reynolds-averaged Navier-Stokes
Re	Reynolds number
RSMs	response surface methods
SA	simulated annealing
segPCT analysis	segmented principal component transform-principal component
SMR	single mixed refrigerant
SNOBFIT	stable noisy optimization by branch and fit
SNU	Seoul national university
SQP	sequential quadratic programming
SRM	steam reforming of methane
TCD	thermal conductivity detector
TEELs	temporary emergency exposure limits
TRM	tri-reforming process of methane
VAE	variational autoencoder
VAEDC	variational autoencoder with deep convolutional layers

## CHAPTER 2

### 2.2 Gas-to-Liquid (GTL) Fischer-Tropsch (FT) reactor model

$\vec{J}_j$	diffusion flux of species $j$ [mol/m <sup>2</sup> ·s]
$C_{S_{H_2}}$	hydrogen concentration on the surface of catalyst [mol/m <sup>3</sup> ]
$A$	area of Ca(OH) <sub>2</sub> [m <sup>2</sup> ]
$C_2$	inertial resistance factor [m <sup>-1</sup> ]
$C_H$	height of coolant channel [m]
$C_W$	width of coolant channel [m]
$CC_D$	distance between coolant channel and coolant channel [m]
$CP_D$	distance between coolant channel and process channel [m]
$D_p$	mean diameter of catalyst particle [m]
$D_p$	catalyst particle mean diameter (m)
$E$	energy (J)
$F$	force (N)
$\vec{g}$	gravitational acceleration [m/s <sup>2</sup> ]
$h$	heat transfer coefficient [W/m <sup>2</sup> ·K]
$J$	diffusive mass flux [mol/m <sup>2</sup> ·s]

$k_{\text{eff}}$	effective thermal conductivity [W/m·K]
$k_p$	thermal conductivity of catalyst particle [W/m·K]
$L$	reactor length [m]
$l$	zone length [m]
$m_{\text{cat}}$	catalyst mass in the reactor [kg]
$p$	static pressure [Pa]
$P$	penalty factor
$P_H$	height of process channel [m]
$P_L$	length of process channel [m]
$P_W$	width of process channel [m]
$Q$	heat flux [W/m <sup>2</sup> ]
$R$	reaction rate [kg/m <sup>3</sup> ·s]
$S_h$	heat source term [W/m <sup>3</sup> ]
$T$	temperature [°C]
$T_{\text{cmax}}$	maximum temperature of coolant channel [K]
$T_{\text{pmax}}$	maximum temperature of process channel [K]
$u_{\text{cin}}$	coolant inlet velocity [m/s]
$u_{\text{in}}$	reactant inlet velocity [m/s]
$v$	velocity [m/s]
$V_{\infty}$	superficial velocity [m/s]
$x$	zone dilution ratio
$Y$	mass fraction
$\alpha$	permeability [m <sup>2</sup> ]
$\varepsilon$	$\varepsilon$ -constraint
$\varepsilon_{\text{cat}}$	catalyst porosity
$\mu$	viscosity [kg/m·s]
$\rho$	density [kg/m <sup>3</sup> ]
$\vec{\tau}_{\text{eff}}$	viscous dissipation [m <sup>2</sup> /s <sup>3</sup> ]

#### Subscripts and superscripts

c	Chemical species
flu	Fluid
i	Zone position
o	Optimization
r	Radial direction
s	Simulation
sol	Solid
x	Direction of X

### 2.3 Carbon Capture, Utilization, and Storage (CCUS) multiphase carbonation reactor model

$A$	area of Ca(OH) <sub>2</sub> [m <sup>2</sup> ]
$a$	area of bubble [m <sup>2</sup> ]
$d$	diameter of bubble [m]
$E$	enhancement factor
$H_w$	Henry's coefficient [mol/m <sup>3</sup> ·Pa]
$n$	mole number of chemicals

$R$	gas constant [kJ/K·mol]
$V_g$	volume of gas [m <sup>3</sup> ]
$V_{\text{particle}}$	volume of solid particle [m <sup>3</sup> ]

## CHAPTER 3

### 3.2 Reactor systems scale optimization

*Same as 2.2*

### 3.3 Process systems scale optimization

$A_{cu_{i,k,n}}$	heat exchanger area of cold utility $n$ and hot stream $i$ at stage $k$
$A_{hu_{j,k,m}}$	heat exchanger area of hot utility $m$ and cold stream $j$ at stage $k$
$A_{i,j,k}$	heat exchanger area of hot stream $i$ and cold stream $j$ at stage $k$
$c$	center of hyper-rectangle
$CC_{i,n}$	area cost coefficient of cold utility
$CCU_n$	per unit cost of cold utility
$CFC_{i,n}$	fixed cost of cold utility heat exchanger
$CFH_{j,m}$	fixed cost of hot utility heat exchanger
$CF_{i,j}$	fixed cost of process stream heat exchanger
$CH_{j,m}$	area cost coefficient of hot utility
$CHU_m$	per unit cost of hot utility
$C_{i,j}$	area cost coefficient of heat exchanger
$CP$	set of cold process stream
$CU$	set of cold utilities
$d$	measure for hyper-rectangle
$D$	predefined constraints
$D_{\text{hidden}}$	hidden constraints
$d_{tcu_{i,k,n}}$	temperature approach for matching hot stream $i$ and cold utility at stage $k$
$d_{thu_{j,k,m}}$	temperature approach for matching hot utility and cold stream $j$ at stage $k$
$dtl_{i,j,k}$	left temperature approach for matching stream $i$ and $j$ at stage $k$
$dtr_{i,j,k}$	right temperature approach for matching stream $i$ and $j$ at stage $k$
$EMAT$	minimum approach temperature
$F_i$	heat capacity flow rate of hot stream
$F_j$	heat capacity flow rate of cold stream
$h_i$	heat transfer coefficient for hot stream $i$
$h_j$	heat transfer coefficient for cold stream $j$
$h_m$	heat transfer coefficient for hot utility $m$
$h_n$	heat transfer coefficient for cold utility $n$
$HP$	set of hot process stream
$HU$	set of hot utilities
$K$	potential optimal index
$LMTD_{i,j,k}$	Chen's log-mean temperature difference
$LMTDP_{i,j,k}$	Paterson's log-mean temperature difference
$m$ in 3.3.1	mole fraction in percentage
$M$	total heat contents of stream

NOK	number of stages
NOM	number of hot utilities
NON	number of cold utilities
$qcu_{i,k,n}$	heat exchanged between hot utility and cold stream j at stage k
$qhu_{j,k,m}$	heat exchanged between hot stream i and cold utility at stage k
$q_{i,j,k}$	heat exchanged between process stream i and j at stage k
ST	set of stages in the superstructure
ST'	expanded set of stages in the superstructure
$tc_{j,k,m}$	temperature of hot stream j at stage k and utility substage m
$th_{i,k,n}$	temperature of hot stream i at stage k and utility substage n
TINcu <sub>m</sub>	inlet temperature of cold utility
TINhu <sub>n</sub>	inlet temperature of hot utility
TIN <sub>i</sub>	inlet temperature of hot stream
TIN <sub>j</sub>	inlet temperature of cold stream
TOUTcu <sub>m</sub>	outlet temperature of cold utility
TOUThu <sub>n</sub>	outlet temperature of hot utility
TOUT <sub>i</sub>	outlet temperature of hot stream
TOUT <sub>j</sub>	outlet temperature of cold stream
$zcu_{i,j,n}$	binary variable denoting existence of heat exchanger between stream i and cold utility n
$zhu_{j,k,m}$	binary variable denoting existence of heat exchanger between stream j and hot utility m
$z_{i,j,k}$	binary variable denoting existence of heat exchanger between stream i and j
$\beta$	exponent for heat exchanger area cost
$\beta_{cu}$	exponent for heat exchanger area cost for cold utility
$\beta_{hu}$	exponent for heat exchanger area cost for hot utility
$\gamma$	penalty factor
$\gamma$	upper bound for temperature difference
$\delta$	positive constant for NAS
$\epsilon$	Jones factor
$\theta$	the maximum number of multiple utilities

### Subscripts and superscripts

i in 3.3.1	index of hyper-rectangle
i in 3.3.2	hot stream
j in 3.3.1	index of hyper-rectangle
j in 3.3.2	cold stream
k in 3.3.1	index of chemicals
k in 3.3.2	subscripts for the stages
m	hot utility
n	cold utility

### 3.4 Plant-wide systems scale modeling and optimization

$P_{\text{death}}$	Probability of death
$\beta_v$	volume porosity
$\rho$	density [kg/m <sup>3</sup> ]
$\beta_j$	area porosity in the $j$ th direction [m/s]
$u_j$	mean velocity ( $j$ th component, vector) [m/s]
$\dot{m}$	mass rate or release rate [kg/s]
$V$	volume [m <sup>3</sup> ]
$P$	gauge pressure, overpressure [Pa]
$\sigma_{ij}$	stress tensor [N/m <sup>2</sup> ]
$F_{o,i}$	flow resistance created by sub-grid obstacles [N]
$F_{w,i}$	flow resistance created by walls [N]
$\rho_0$	density of sub grid object [kg/m <sup>3</sup> ]
$g_i$	gravitational acceleration in the $i$ th direction [m/s <sup>2</sup> ]
$\delta_{ij}$	Kronecker delta function
$\mu_{\text{eff}}$	effective viscosity [Pa·s]
$\mu$	turbulent viscosity [Pa·s]
$C_\mu$	constant in the $k$ - $\epsilon$ equation; typically $C_\mu=0.09$
$\epsilon$	dissipation of turbulent kinetic energy [m <sup>2</sup> /s <sup>3</sup> ]
$k$	turbulent kinetic energy [m <sup>2</sup> /s <sup>2</sup> ]
$Pr$	probit
$c$	concentration in ppm by volume
$x$	$P_{\text{death}}$ contour data
$z$	latent space
$N_z$	the number of latent variables
$p_\theta(x z)$	probabilistic decoder as generator with parameter $\theta$
$q_\phi(z x)$	probabilistic encoder with parameter $\phi$
$v$	variable space
$f^*(v)$	surrogate model function
$f(v)$	CFD model function
$\mathcal{L}(\theta, \phi; x^{(i)})$	variational lower bound
$D_{\text{KL}}$	Kullback-Leibler divergence
$l(\theta, \phi; x^{(i)})$	loss function
$N_{\text{train}}$	the number of training data set
$N_v$	the number of variables

#### Subscripts and superscripts

gen	generated data
test	test set
train	training set
validation	validation set

### CHAPTER 4

Same as CHAPTER 2

## Reference

1. Joshi, J. and K. Nandakumar, *Computational modeling of multiphase reactors*. Annual review of chemical and biomolecular engineering, 2015. **6**: p. 347-378.
2. Na, J., et al., *Multi-objective optimization of microchannel reactor for Fischer-Tropsch synthesis using computational fluid dynamics and genetic algorithm*. Chemical Engineering Journal, 2017. **313**: p. 1521-1534.
3. Na, J., et al., *Computational Fluid Dynamics Study of Channel Geometric Effect for Fischer-Tropsch Microchannel Reactor*. Korean Chemical Engineering Research, 2014. **52**(6): p. 826-833.
4. Seongeon Park, et al., *CO<sub>2</sub> Mineral Carbonation Reactor Analysis using Computational Fluid Dynamics: Internal Reactor Design Study for the Efficient Mixing of Solid Reactants in the Solution*. Korean Chemical Engineering Research, 2016. **54**(5): p. 612-620.
5. Na, J., Y. Lim, and C. Han, *A modified DIRECT algorithm for hidden constraints in an LNG process optimization*. Energy, 2017. **126**: p. 488-500.
6. Na, J., et al., *Simultaneous synthesis of a heat exchanger network with multiple utilities using utility substages*. Computers & Chemical Engineering, 2015. **79**: p. 70-79.
7. Bao, B., M.M. El-Halwagi, and N.O. Elbashir, *Simulation, integration, and economic analysis of gas-to-liquid processes*. Fuel Processing Technology, 2010. **91**(7): p. 703-713.
8. Jun, K.W., *Trend of Fischer-Tropsch Synthesis technology*. News & Information for Chemical Engineers, 2007. **25**(1): p. 29-34.
9. EGINEERING, T., *Offshore GTL Process Development By Microchannel Reactor*. Automation Systems, 2012. **8**: p. 82-88.
10. Karim, A., et al., *Comparison of wall-coated and packed-bed reactors for steam reforming of methanol*. Catalysis Today, 2005. **110**(1-2): p. 86-91.
11. Myrstad, R., et al., *Fischer-Tropsch synthesis in a microstructured reactor*. Catalysis Today, 2009. **147**, **Supplement**: p. S301-S304.
12. Cao, C., et al., *Intensified Fischer-Tropsch synthesis process with microchannel catalytic reactors*. Catalysis Today, 2009. **140**(3-4): p. 149-156.
13. Holmen, A., et al., *Monolithic, microchannel and carbon nanofibers/carbon felt reactors for syngas conversion by Fischer-Tropsch synthesis*. Catalysis Today, 2013. **216**: p. 150-157.
14. Deshmukh, S.R., et al., *Scale-Up of Microchannel Reactors For Fischer-Tropsch Synthesis*. Industrial & Engineering Chemistry Research, 2010. **49**(21): p. 10883-10888.
15. Tonkovich, A.L., et al., *Laminated, leak-resistant chemical processors, methods of making, and methods of operating*. 2012, US patent 0132290.
16. Kshetrimayum, K.S., et al., *CFD Simulation of Microchannel Reactor Block for Fischer-Tropsch Synthesis: Effect of Coolant Type and Wall Boiling Condition on Reactor Temperature*. Industrial & Engineering Chemistry Research, 2016. **55**(3): p. 543-554.
17. Kshetrimayum, K.S., et al., *Simulation Study of Heat Transfer Enhancement due to Wall Boiling Condition in a Microchannel Reactor Block for Fischer-*



- Tropsch Synthesis*, in *Computer Aided Chemical Engineering*, J.K.H. Krist V. Gernaey and G. Rafiqul, Editors. 2015, Elsevier. p. 1355-1360.
18. Danziger, D., D. Popović, and G. Schulz-Ekloff, *Simulation of temperature peak attenuation by catalyst dilution in a tubular packed-bed reactor*. The Canadian Journal of Chemical Engineering, 1983. **61**(1): p. 126-128.
  19. Caldwell, A. and C. PH, *Catalyst Dilution-A Means of Temperature Control in Packed Tubular Reactors*. British Chemical Engineering, 1969. **14**(9): p. 470-&.
  20. Quina, M.M.J. and R.M. Quinta Ferreira, *Thermal Runaway Conditions of a Partially Diluted Catalytic Reactor*. Industrial & Engineering Chemistry Research, 1999. **38**(12): p. 4615-4623.
  21. Quina, M.M.J. and R.M.Q. Ferreira, *Start-up and wrong-way behavior in a tubular reactor: dilution effect of the catalytic bed*. Chemical Engineering Science, 2000. **55**(18): p. 3885-3897.
  22. Hwang, S. and R. Smith, *Heterogeneous catalytic reactor design with optimum temperature profile I: application of catalyst dilution and side-stream distribution*. Chemical Engineering Science, 2004. **59**(20): p. 4229-4243.
  23. Shin, D.-Y., et al., *CFD modeling of a modular reactor for the Fischer–Tropsch synthesis: Effectiveness of a micro-scale cross-current cooling channel*. Fuel, 2015. **158**: p. 826-834.
  24. Lee, Y., et al., *Analysis on Thermal Effects of Process Channel Geometry for Microchannel Fischer-Tropsch Reactor Using Computational Fluid Dynamics*. Korean Chemical Engineering Research, 2015. **53**(6): p. 818-823.
  25. Chabot, G., et al., *A mathematical modeling of catalytic milli-fixed bed reactor for Fischer–Tropsch synthesis: Influence of tube diameter on Fischer Tropsch selectivity and thermal behavior*. Chemical Engineering Science, 2015. **127**: p. 72-83.
  26. Shin, M.-S., et al., *Computational fluid dynamics model of a modular multichannel reactor for Fischer–Tropsch synthesis: Maximum utilization of catalytic bed by microchannel heat exchangers*. Chemical Engineering Journal, 2013. **234**: p. 23-32.
  27. Gumuslu, G. and A.K. Avci, *Parametric analysis of Fischer-tropsch synthesis in a catalytic microchannel reactor*. AIChE Journal, 2012. **58**(1): p. 227-235.
  28. Arzamendi, G., et al., *Computational fluid dynamics study of heat transfer in a microchannel reactor for low-temperature Fischer–Tropsch synthesis*. Chemical Engineering Journal, 2010. **160**(3): p. 915-922.
  29. Jung, I., et al., *Computational Fluid Dynamics Based Optimal Design of Guiding Channel Geometry in U-Type Coolant Layer Manifold of Large-Scale Microchannel Fischer-Tropsch Reactor*. Industrial and Engineering Chemistry Research, 2016. **55**(2): p. 505-515.
  30. Park, S., et al., *Design and modeling of large-scale cross-current multichannel Fischer–Tropsch reactor using channel decomposition and cell-coupling method*. Chemical Engineering Science, 2015. **134**: p. 448-456.
  31. Na, J., et al. *A Model of Mineral Carbonation Kinetics for Carbon Capture, Utilization and Storage (CCUS) Technology*. in *Korean Institute of Chemical Engineering Fall Conference*. 2016. Daejun, South Korea.

32. Van Der Laan, G.P. and A.A.C.M. Beenackers, *Kinetics and Selectivity of the Fischer–Tropsch Synthesis: A Literature Review*. Catalysis Reviews, 1999. **41**(3-4): p. 255-318.
33. Ergun, S., *Fluid flow through packed columns*. Chemical Engineering Progress, 1952. **48**: p. 89-94.
34. Merk, H.J., *The macroscopic equations for simultaneous heat and mass transfer in isotropic, continuous and closed systems*. Applied Scientific Research, Section A, 1959. **8**(1): p. 73-99.
35. Wakao, N. and S. Kaguei, *Heat transfer in packed beds*. Gordon and Breach Science, New York, 1982.
36. Philippe, R., et al., *Effect of structure and thermal properties of a Fischer–Tropsch catalyst in a fixed bed*. Catalysis Today, 2009. **147**, **Supplement**: p. S305-S312.
37. Knochen, J., et al., *Fischer–Tropsch synthesis in milli-structured fixed-bed reactors: Experimental study and scale-up considerations*. Chemical Engineering and Processing: Process Intensification, 2010. **49**(9): p. 958-964.
38. Post, M., et al., *Diffusion limitations in fischer-tropsch catalysts*. AIChE Journal, 1989. **35**(7): p. 1107-1114.
39. Menter, F.R., *Two-equation eddy-viscosity turbulence models for engineering applications*. AIAA journal, 1994. **32**(8): p. 1598-1605.
40. Derevich, I.V., V.S. Ermolaev, and V.Z. Mordkovich, *Liquid-vapor thermodynamic equilibrium in Fischer-Tropsch synthesis products*. Theoretical Foundations of Chemical Engineering, 2008. **42**(2): p. 216-219.
41. Derevich, I.V., et al., *Thermodynamics of wax formation in the fischer-tropsch synthesis products*. Theoretical Foundations of Chemical Engineering, 2013. **47**(3): p. 191-200.
42. Lee, C.-J., et al., *Optimal Gas-To-Liquid Product Selection from Natural Gas under Uncertain Price Scenarios*. Industrial & Engineering Chemistry Research, 2008. **48**(2): p. 794-800.
43. Cents, A.H.G., D.W.F. Brilman, and G.F. Versteeg, *absorption in carbonate/bicarbonate solutions: The Danckwerts-criterion revisited*. Chemical Engineering Science, 2005. **60**(21): p. 5830-5835.
44. Zhang, D., N. Deen, and J. Kuipers, *Numerical modeling of hydrodynamics, mass transfer and chemical reaction in bubble Columns*. 2007.
45. Weisenberger, S. and A. Schumpe, *Estimation of gas solubilities in salt solutions at temperatures from 273 K to 363 K*. AIChE Journal, 1996. **42**(1): p. 298-300.
46. Johannsen, K. and S. Rademacher, *Modelling the Kinetics of Calcium Hydroxide Dissolution in Water*. Acta hydrochimica et hydrobiologica, 1999. **27**(2): p. 72-78.
47. Velts, O., et al., *Waste oil shale ash as a novel source of calcium for precipitated calcium carbonate: Carbonation mechanism, modeling, and product characterization*. Journal of Hazardous Materials, 2011. **195**: p. 139-146.
48. Ogino, T., T. Suzuki, and K. Sawada, *The formation and transformation mechanism of calcium carbonate in water*. Geochimica et Cosmochimica Acta, 1987. **51**(10): p. 2757-2767.

49. Olajire, A.A., *A review of mineral carbonation technology in sequestration of CO<sub>2</sub>*. Journal of Petroleum Science and Engineering, 2013. **109**: p. 364-392.
50. Jin, B. and P. Lant, *Flow regime, hydrodynamics, floc size distribution and sludge properties in activated sludge bubble column, air-lift and aerated stirred reactors*. Chemical Engineering Science, 2004. **59**(12): p. 2379-2388.
51. Pangarkar, V.G., *Design of multiphase reactors*. 2014: John Wiley & Sons.
52. Zwietering, T.N., *Suspending of solid particles in liquid by agitators*. Chemical Engineering Science, 1958. **8**(3): p. 244-253.
53. Grenville, R.K., A.T. Mak, and D.A. Brown. *An improved correlation to predict "just suspension" speed for solid-liquid mixtures with axial flow impellers in stirred tanks*. in *North American Mixing Forum, Victoria, BC, Canada (June 20-June 25)*. 2010.
54. Smith, J., M. Warmoeskerken, and E. Zeef, *Flow conditions in vessels dispersing gases in liquids with multiple impellers*. AMERICAN INSTITUTE OF CHEMICAL ENGINEERS, NEW YORK, NY(USA). 1987., 1987.
55. Harris, C.K., et al., *Computational fluid dynamics for chemical reactor engineering*. Chemical Engineering Science, 1996. **51**(10): p. 1569-1594.
56. Kasat, G.R., et al., *CFD simulation of liquid-phase mixing in solid-liquid stirred reactor*. Chemical Engineering Science, 2008. **63**(15): p. 3877-3885.
57. Murthy, B.N., R.S. Ghadge, and J.B. Joshi, *CFD simulations of gas-liquid-solid stirred reactor: Prediction of critical impeller speed for solid suspension*. Chemical Engineering Science, 2007. **62**(24): p. 7184-7195.
58. Micale, G., et al., *CFD Simulation of Particle Distribution in Stirred Vessels*. Chemical Engineering Research and Design, 2000. **78**(3): p. 435-444.
59. Jafari, R., J. Chaouki, and P.A. Tanguy, *A comprehensive review of just suspended speed in liquid-solid and gas-liquid-solid stirred tank reactors*. International Journal of Chemical Reactor Engineering, 2012. **10**(1): p. 1-32.
60. Ljungqvist, M. and A. Rasmuson, *Numerical Simulation of the Two-Phase Flow in an Axially Stirred Vessel*. Chemical Engineering Research and Design, 2001. **79**(5): p. 533-546.
61. Khopkar, A.R., et al., *Gas-liquid flow generated by a Rushton turbine in stirred vessel: CARPT/CT measurements and CFD simulations*. Chemical Engineering Science, 2005. **60**(8-9): p. 2215-2229.
62. Gohel, S., et al., *CFD Modeling of Solid Suspension in a Stirred Tank: Effect of Drag Models and Turbulent Dispersion on Cloud Height*. International Journal of Chemical Engineering, 2012. **2012**: p. 9.
63. Kolda, T.G., R.M. Lewis, and V. Torczon, *Optimization by Direct Search: New Perspectives on Some Classical and Modern Methods*. SIAM Review, 2003. **45**(3): p. 385-482.
64. Leboreiro, J. and J. Acevedo, *Processes synthesis and design of distillation sequences using modular simulators: a genetic algorithm framework*. Computers & Chemical Engineering, 2004. **28**(8): p. 1223-1236.
65. Javaloyes-Antón, J., R. Ruiz-Femenia, and J.A. Caballero, *Rigorous Design of Complex Distillation Columns Using Process Simulators and the Particle Swarm Optimization Algorithm*. Industrial & Engineering Chemistry Research, 2013. **52**(44): p. 15621-15634.

66. Lee, U., A. Mitsos, and C. Han, *Optimal retrofit of a CO<sub>2</sub> capture pilot plant using superstructure and rate-based models*. International Journal of Greenhouse Gas Control, 2016. **50**: p. 57-69.
67. HAIMES, Y.Y., L.S. LASDON, and D.A. WISMER, *On a Bicriterion Formulation of the Problems of Integrated System Identification and System Optimization*. IEEE Transactions on Systems, Man, and Cybernetics, 1971. **SMC-1**(3): p. 296-297.
68. Miettinen, K., *Nonlinear multiobjective optimization*. Vol. 12. 2012: Springer Science & Business Media.
69. Caramia, M. and P. Dell'Olmo, *Multi-objective management in freight logistics: Increasing capacity, service level and safety with optimization algorithms*. 2008: Springer Science & Business Media.
70. Goldberg, D.E., *Genetic algorithm in search*. Optimization and Machine Learning, 1989.
71. Shokrian, M. and K.A. High, *Application of a multi objective multi-leader particle swarm optimization algorithm on NLP and MINLP problems*. Computers & Chemical Engineering, 2014. **60**: p. 57-75.
72. Yiqing, L., Y. Xigang, and L. Yongjian, *An improved PSO algorithm for solving non-convex NLP/MINLP problems with equality constraints*. Computers & chemical engineering, 2007. **31**(3): p. 153-162.
73. Cardoso, M.F., et al., *A simulated annealing approach to the solution of MINLP problems*. Computers & Chemical Engineering, 1997. **21**(12): p. 1349-1364.
74. Karunanithi, A.T., L.E.K. Achenie, and R. Gani, *A New Decomposition-Based Computer-Aided Molecular/Mixture Design Methodology for the Design of Optimal Solvents and Solvent Mixtures*. Industrial & Engineering Chemistry Research, 2005. **44**(13): p. 4785-4797.
75. Buxton, A., A.G. Livingston, and E.N. Pistikopoulos, *Optimal design of solvent blends for environmental impact minimization*. AIChE Journal, 1999. **45**(4): p. 817-843.
76. Papadopoulos, A.I., et al., *Toward Optimum Working Fluid Mixtures for Organic Rankine Cycles using Molecular Design and Sensitivity Analysis*. Industrial & Engineering Chemistry Research, 2013. **52**(34): p. 12116-12133.
77. Lee, U., A. Mitsos, and C. Han, *Optimal retrofit of a CO<sub>2</sub> capture pilot plant using superstructure and rate-based models*. International Journal of Greenhouse Gas Control, 2016. **50**: p. 57-69.
78. Egea, J.A., R. Martí, and J.R. Banga, *An evolutionary method for complex-process optimization*. Computers & Operations Research, 2010. **37**(2): p. 315-324.
79. Floudas, C.A., *Global optimization in design and control of chemical process systems*. Journal of Process Control, 2000. **10**(2-3): p. 125-134.
80. Kallrath, J., *Mixed Integer Optimization in the Chemical Process Industry: Experience, Potential and Future Perspectives*. Chemical Engineering Research and Design, 2000. **78**(6): p. 809-822.
81. Biegler, L.T., A.M. Cervantes, and A. Wächter, *Advances in simultaneous strategies for dynamic process optimization*. Chemical Engineering Science, 2002. **57**(4): p. 575-593.

82. Egea, J.A., et al., *Scatter search for chemical and bio-process optimization*. Journal of Global Optimization, 2007. **37**(3): p. 481-503.
83. Leineweber, D.B., et al., *An efficient multiple shooting based reduced SQP strategy for large-scale dynamic process optimization. Part 1: theoretical aspects*. Computers & Chemical Engineering, 2003. **27**(2): p. 157-166.
84. Lin, B. and D.C. Miller, *Tabu search algorithm for chemical process optimization*. Computers & Chemical Engineering, 2004. **28**(11): p. 2287-2306.
85. Lucia, A. and J. Xu, *Chemical process optimization using Newton-like methods*. Computers & Chemical Engineering, 1990. **14**(2): p. 119-138.
86. Rios, L.M. and N.V. Sahinidis, *Derivative-free optimization: a review of algorithms and comparison of software implementations*. Journal of Global Optimization, 2013. **56**(3): p. 1247-1293.
87. Deming, S.N., L.R. Parker, and M. Bonner Denton, *A Review of Simplex Optimization in Analytical Chemistry*. C R C Critical Reviews in Analytical Chemistry, 1978. **7**(3): p. 187-202.
88. Zhengji, Z., C.M. Juan, and M.V. Hove, *Using pattern search methods for surface structure determination of nanomaterials*. Journal of Physics: Condensed Matter, 2006. **18**(39): p. 8693.
89. Audet, C., V. Béchar, and J. Chaouki, *Spent potliner treatment process optimization using a MADS algorithm*. Optimization and Engineering, 2008. **9**(2): p. 143-160.
90. Han, J., M. Kokkolaras, and P.Y. Papalambros, *Optimal Design of Hybrid Fuel Cell Vehicles*. Journal of Fuel Cell Science and Technology, 2008. **5**(4): p. 041014-041014.
91. Hayes, R.E., et al., *Catalytic Combustion Kinetics: Using a Direct Search Algorithm to Evaluate Kinetic Parameters from Light-Off Curves*. The Canadian Journal of Chemical Engineering, 2003. **81**(6): p. 1192-1199.
92. Lee, U., K. Kim, and C. Han, *Design and optimization of multi-component organic rankine cycle using liquefied natural gas cryogenic exergy*. Energy, 2014. **77**: p. 520-532.
93. Lee, U., et al., *Techno-economic Optimization of a Green-Field Post-Combustion CO<sub>2</sub> Capture Process Using Superstructure and Rate-Based Models*. Industrial & Engineering Chemistry Research, 2016. **55**(46): p. 12014-12026.
94. Javaloyes-Antón, J., R. Ruiz-Femenia, and J. Caballero, *Rigorous design of complex distillation columns using process simulators and the particle swarm optimization algorithm*. Industrial & Engineering Chemistry Research, 2013. **52**(44): p. 15621-15634.
95. Cozad, A., N.V. Sahinidis, and D.C. Miller, *Learning surrogate models for simulation-based optimization*. AIChE Journal, 2014. **60**(6): p. 2211-2227.
96. Dixon, T., et al., *Framework for Optimization and Quantification of Uncertainty and Sensitivity for Developing Carbon Capture Systems*. Energy Procedia, 2014. **63**: p. 1055-1063.
97. Shi, H. and F. You, *A novel adaptive surrogate modeling-based algorithm for simultaneous optimization of sequential batch process scheduling and dynamic operations*. AIChE Journal, 2015. **61**(12): p. 4191-4209.

98. Quirante, N., J. Javaloyes, and J.A. Caballero, *Rigorous design of distillation columns using surrogate models based on Kriging interpolation*. AIChE Journal, 2015. **61**(7): p. 2169-2187.
99. Wahl, P.E., S.W. Løvseth, and M.J. Mølnvik, *Optimization of a simple LNG process using sequential quadratic programming*. Computers & Chemical Engineering, 2013. **56**: p. 27-36.
100. Van Duc Long, N. and M. Lee, *Design and optimization of a dividing wall column by factorial design*. Korean Journal of Chemical Engineering, 2012. **29**(5): p. 567-573.
101. Yi, Q., J. Feng, and W.Y. Li, *Optimization and efficiency analysis of polygeneration system with coke-oven gas and coal gasified gas by Aspen Plus*. Fuel, 2012. **96**: p. 131-140.
102. Alabdulkarem, A., et al., *Optimization of propane pre-cooled mixed refrigerant LNG plant*. Applied Thermal Engineering, 2011. **31**(6-7): p. 1091-1098.
103. Al-Lagtah, N.M.A., S. Al-Habsi, and S.A. Onaizi, *Optimization and performance improvement of Lekhwair natural gas sweetening plant using Aspen HYSYS*. Journal of Natural Gas Science and Engineering, 2015. **26**: p. 367-381.
104. Rodríguez, N., S. Mussati, and N. Scenna, *Optimization of post-combustion CO<sub>2</sub> process using DEA-MDEA mixtures*. Chemical Engineering Research and Design, 2011. **89**(9): p. 1763-1773.
105. Nuchitprasittichai, A. and S. Cremaschi, *Optimization of CO<sub>2</sub> capture process with aqueous amines using response surface methodology*. Computers & Chemical Engineering, 2011. **35**(8): p. 1521-1531.
106. Mokhatab, S., et al., *Handbook of liquefied natural gas*. 2013: Gulf Professional Publishing.
107. Mokhatab, S. and W.A. Poe, *Handbook of natural gas transmission and processing*. 2012: Gulf Professional Publishing.
108. Barron, R., *Cryogenic Systems*. 1985, Oxford, UK: Oxford University Press.
109. Timmerhaus, K.D. and T.M. Flynn, *Cryogenic process engineering*. 2013: Springer.
110. Venkatarathnam, G. and K.D. Timmerhaus, *Cryogenic mixed refrigerant processes*. 2008: Springer.
111. Bunnag, M., et al. *FLNG Development: Strategic Approaches to New Growth Challenges*. in *International Petroleum Technology Conference*. 2011.
112. Barclay, M.A. and C.C. Yang. *Offshore LNG: the perfect starting point for the 2-phase expander?* in *Offshore Technology Conference*. 2006. Houston, Texas.
113. Remeljei, C. and A. Hoadley, *An exergy analysis of small-scale liquefied natural gas (LNG) liquefaction processes*. Energy, 2006. **31**(12): p. 2005-2019.
114. Shirazi, M.M.H. and D. Mowla, *Energy optimization for liquefaction process of natural gas in peak shaving plant*. Energy, 2010. **35**(7): p. 2878-2885.
115. Xu, X., J. Liu, and L. Cao, *Optimization and analysis of mixed refrigerant composition for the PRICO natural gas liquefaction process*. Cryogenics, 2014. **59**: p. 60-69.

116. Khan, M.S., S. Lee, and M. Lee, *Optimization of single mixed refrigerant natural gas liquefaction plant with nonlinear programming*. Asia-Pacific Journal of Chemical Engineering, 2012. **7**(S1): p. S62-S70.
117. Khan, M.S. and M. Lee, *Design optimization of single mixed refrigerant natural gas liquefaction process using the particle swarm paradigm with nonlinear constraints*. Energy, 2013. **49**: p. 146-155.
118. Khan, M.S., et al., *Sequential coordinate random search for optimal operation of LNG (liquefied natural gas) plant*. Energy, 2015. **89**: p. 757-767.
119. Moein, P., et al., *APCI-LNG single mixed refrigerant process for natural gas liquefaction cycle: analysis and optimization*. Journal of Natural Gas Science and Engineering, 2015. **26**: p. 470-479.
120. Morosuk, T., et al., *Evaluation of the PRICO liquefaction process using exergy-based methods*. Journal of Natural Gas Science and Engineering, 2015. **27**: p. 23-31.
121. Mehrpooya, M. and H. Ansarinassab, *Exergoeconomic evaluation of single mixed refrigerant natural gas liquefaction processes*. Energy Conversion and Management, 2015. **99**: p. 400-413.
122. Park, K., W. Won, and D. Shin, *Effects of varying the ambient temperature on the performance of a single mixed refrigerant liquefaction process*. Journal of Natural Gas Science and Engineering, 2016. **34**: p. 958-968.
123. Zwe-Lee, G., *A particle swarm optimization approach for optimum design of PID controller in AVR system*. IEEE Transactions on Energy Conversion, 2004. **19**(2): p. 384-391.
124. Chow, T.T., et al., *Global optimization of absorption chiller system by genetic algorithm and neural network*. Energy and Buildings, 2002. **34**(1): p. 103-109.
125. Hakimi, S.M. and S.M. Moghaddas-Tafreshi, *Optimal sizing of a stand-alone hybrid power system via particle swarm optimization for Kahnouj area in south-east of Iran*. Renewable Energy, 2009. **34**(7): p. 1855-1862.
126. Ghorbani, B., et al., *Optimization of operation parameters of refrigeration cycle using particle swarm and NLP techniques*. Journal of Natural Gas Science and Engineering, 2014. **21**: p. 779-790.
127. Mokarizadeh Haghighi Shirazi, M. and D. Mowla, *Energy optimization for liquefaction process of natural gas in peak shaving plant*. Energy, 2010. **35**(7): p. 2878-2885.
128. He, T. and Y. Ju, *A novel conceptual design of parallel nitrogen expansion liquefaction process for small-scale LNG (liquefied natural gas) plant in skid-mount packages*. Energy, 2014. **75**: p. 349-359.
129. Bayat, M., M.R. Rahimpour, and B. Moghtaderi, *Genetic algorithm strategy (GA) for optimization of a novel dual-stage slurry bubble column membrane configuration for Fischer–Tropsch synthesis in gas to liquid (GTL) technology*. Journal of Natural Gas Science and Engineering, 2011. **3**(4): p. 555-570.
130. Rahimpour, M.R. and H. Elekaei, *Optimization of a novel combination of fixed and fluidized-bed hydrogen-permselective membrane reactors for Fischer–Tropsch synthesis in GTL technology*. Chemical Engineering Journal, 2009. **152**(2–3): p. 543-555.

131. Huyer, W. and A. Neumaier, *SNOBFIT--stable noisy optimization by branch and fit*. ACM Transactions on Mathematical Software (TOMS), 2008. **35**(2): p. 9.
132. Lee, G.C., R. Smith, and X.X. Zhu, *Optimal synthesis of mixed-refrigerant systems for low-temperature processes*. Industrial and Engineering Chemistry Research, 2002. **41**(20): p. 5016-5028.
133. Hwang, J.-H., M.-I. Roh, and K.-Y. Lee, *Determination of the optimal operating conditions of the dual mixed refrigerant cycle for the LNG FPSO topside liquefaction process*. Computers & Chemical Engineering, 2013. **49**: p. 25-36.
134. Hwang, J.-H., et al., *Optimal Design of Liquefaction Cycles of Liquefied Natural Gas Floating, Production, Storage, and Offloading Unit Considering Optimal Synthesis*. Industrial & Engineering Chemistry Research, 2013. **52**(15): p. 5341-5356.
135. Nogal, F.D., et al., *Optimal Design of Mixed Refrigerant Cycles*. Industrial & Engineering Chemistry Research, 2008. **47**(22): p. 8724-8740.
136. Baker, C.A., et al., *Parallel global aircraft configuration design space exploration*. 2000.
137. Belevičius, R., et al., *Optimal placement of piles in real grillages: experimental comparison of optimization algorithms*. Information Technology And Control, 2011. **40**(2): p. 123-132.
138. Carter, R.G., et al., *Algorithms for Noisy Problems in Gas Transmission Pipeline Optimization*. Optimization and Engineering, 2001. **2**(2): p. 139-157.
139. Cox, S.E., et al., *A Comparison of Global Optimization Methods for the Design of a High-speed Civil Transport*. Journal of Global Optimization, 2001. **21**(4): p. 415-432.
140. Gablonsky, J.M. and C.T. Kelley, *A Locally-Biased form of the DIRECT Algorithm*. Journal of Global Optimization, 2001. **21**(1): p. 27-37.
141. He, J., et al., *Dynamic Data Structures for a Direct Search Algorithm*. Computational Optimization and Applications, 2002. **23**(1): p. 5-25.
142. Liuzzi, G., S. Lucidi, and V. Piccialli, *A DIRECT-based approach exploiting local minimizations for the solution of large-scale global optimization problems*. Computational Optimization and Applications, 2010. **45**(2): p. 353-375.
143. di Serafino, D., et al., *A Modified DIviding RECTangles Algorithm for a Problem in Astrophysics*. Journal of Optimization Theory and Applications, 2011. **151**(1): p. 175-190.
144. Jones, D.R., C.D. Perttunen, and B.E. Stuckman, *Lipschitzian optimization without the Lipschitz constant*. Journal of Optimization Theory and Applications, 1993. **79**(1): p. 157-181.
145. Finkel, D.E. and C. Kelley, *Convergence analysis of the DIRECT algorithm*. Optimization On-line Digest, 2004.
146. Finkel, D.E., *Global optimization with the DIRECT algorithm*. Ph.D. thesis. North Carolina State University, 2005.
147. Fletcher, R., *Practical methods of optimization*. 2nd ed ed. 1987, New York: John Wiley & Sons.



148. Gablonsky, J.M., *Modifications of the DIRECT Algorithm*. Ph.D. thesis. North Carolina State University, 2001.
149. Paulavičius, R. and J. Žilinskas, *Simplicial global optimization*. 1st ed ed. 2014, New York: Springer.
150. Dixon, L.C.W. and G.P. Szegő, *Towards global optimisation 2*. 1st ed ed. 1978, New York: North-Holland\.
151. Coers, D.H. and J.W. Sudduth, *Refrigerant apparatus and process using multicomponent refrigerant*. 1976, United States patent. US 3932154.
152. Furman, K.C. and N.V. Sahinidis, *A critical review and annotated bibliography for heat exchanger network synthesis in the 20th century*. Industrial & Engineering Chemistry Research, 2002. **41**(10): p. 2335-2370.
153. Huang, K.F., E.M. Al-mutairi, and I.A. Karimi, *Heat exchanger network synthesis using a stagewise superstructure with non-isothermal mixing*. Chemical Engineering Science, 2012. **73**(0): p. 30-43.
154. Dipama, J., A. Teyssedou, and M. Sorin, *Synthesis of heat exchanger networks using genetic algorithms*. Applied Thermal Engineering, 2008. **28**(14–15): p. 1763-1773.
155. Yee, T.F. and I.E. Grossmann, *Simultaneous optimization models for heat integration—II. Heat exchanger network synthesis*. Computers & Chemical Engineering, 1990. **14**(10): p. 1165-1184.
156. Shenoy, U.V., A. Sinha, and S. Bandyopadhyay, *Multiple Utilities Targeting for Heat Exchanger Networks*. Chemical Engineering Research and Design, 1998. **76**(3): p. 259-272.
157. Sun, K.N., S.R. Wan Alwi, and Z.A. Manan, *Heat exchanger network cost optimization considering multiple utilities and different types of heat exchangers*. Computers & Chemical Engineering, 2013. **49**(0): p. 194-204.
158. Castier, M., *Rigorous multiple utility targeting in heat exchanger networks*. Energy Conversion and Management, 2012. **59**(0): p. 74-85.
159. Isafiade, A.J. and D.M. Fraser, *Interval-based MINLP superstructure synthesis of heat exchange networks*. Chemical Engineering Research and Design, 2008. **86**(3): p. 245-257.
160. Ponce-Ortega, J.M., M. Serna-González, and A. Jiménez-Gutiérrez, *Synthesis of Heat Exchanger Networks with Optimal Placement of Multiple Utilities*. Industrial & Engineering Chemistry Research, 2010. **49**(6): p. 2849-2856.
161. Huang, K.F. and I.A. Karimi, *Simultaneous synthesis approaches for cost-effective heat exchanger networks*. Chemical Engineering Science, 2013. **98**(0): p. 231-245.
162. Chen, J.J.J., *Comments on improvements on a replacement for the logarithmic mean*. Chemical Engineering Science, 1987. **42**(10): p. 2488-2489.
163. Huang, K. and I. Karimi, *Heat exchanger network synthesis with multiple utilities using a generalized stagewise superstructure with cross flows*. in *Proceedings of the 6th International Conference on Process Systems Engineering (PSE ASIA)*. 2013.
164. Huang, K.f. and I.A. Karimi, *Efficient algorithm for simultaneous synthesis of heat exchanger networks*. Chemical Engineering Science, 2014. **105**(0): p. 53-68.

165. Paterson, W., *A replacement for the logarithmic mean*. Chemical Engineering Science, 1984. **39**(11): p. 1635-1636.
166. Broughton, E., *The Bhopal disaster and its aftermath: a review*. Environmental Health, 2005. **4**(1): p. 6.
167. Barratt, R., *Atmospheric dispersion modelling: an introduction to practical applications*. 2013: Routledge.
168. Hanna, S. and D. Strimaitis, *Workbook of test cases for vapor cloud source emission and dispersion models*. CCPS/AIChE, New York, NY, 1988.
169. Delaunay, D., *Numerical simulation of atmospheric dispersion in an urban site: Comparison with field data*. Journal of Wind Engineering and Industrial Aerodynamics, 1996. **64**(2): p. 221-231.
170. Hanna, S.R., et al., *Detailed Simulations of Atmospheric Flow and Dispersion in Downtown Manhattan: An Application of Five Computational Fluid Dynamics Models*. Bulletin of the American Meteorological Society, 2006. **87**(12): p. 1713-1726.
171. Hanna, S.R., et al., *CFD model simulation of dispersion from chlorine railcar releases in industrial and urban areas*. Atmospheric Environment, 2009. **43**(2): p. 262-270.
172. Long, K.J., et al., *Modeling a Hypothetical Chlorine Release on a College Campus*. JCP, 2009. **4**(9): p. 881-890.
173. Xie, Z.-T., P. Hayden, and C.R. Wood, *Large-eddy simulation of approaching-flow stratification on dispersion over arrays of buildings*. Atmospheric Environment, 2013. **71**: p. 64-74.
174. Middha, P., et al., *CFD calculations of gas leak dispersion and subsequent gas explosions: Validation against ignited impinging hydrogen jet experiments*. Journal of Hazardous Materials, 2010. **179**(1): p. 84-94.
175. Yang, S., et al., *Accident analysis of the Gumi hydrogen fluoride gas leak using CFD and comparison with post-accidental environmental impacts*. Journal of Loss Prevention in the Process Industries, 2017. **48**: p. 207-215.
176. Palmer, K. and M. Realff, *Optimization and Validation of Steady-State Flowsheet Simulation Metamodels*. Chemical Engineering Research and Design, 2002. **80**(7): p. 773-782.
177. Caballero, J.A. and I.E. Grossmann, *Rigorous flowsheet optimization using process simulators and surrogate models*. Computer Aided Chemical Engineering, 2008. **25**: p. 551-556.
178. Caballero, J.A. and I.E. Grossmann, *An algorithm for the use of surrogate models in modular flowsheet optimization*. AIChE Journal, 2008. **54**(10): p. 2633-2650.
179. Gomes, M.V.C., et al., *Using kriging models for real-time process optimisation*. Computer Aided Chemical Engineering, 2008. **25**: p. 361-366.
180. Chen, T., et al., *Efficient meta-modelling of complex process simulations with time-space-dependent outputs*. Computers & Chemical Engineering, 2011. **35**(3): p. 502-509.
181. Wang, K., et al., *Meta-modelling for fast analysis of CFD-simulated vapour cloud dispersion processes*. Computers & Chemical Engineering, 2014. **69**: p. 89-97.

182. Loy, Y.Y., G.P. Rangaiah, and S. Lakshminarayanan, *Surrogate modelling for enhancing consequence analysis based on computational fluid dynamics*. Journal of Loss Prevention in the Process Industries, 2017. **48**: p. 173-185.
183. Kajero, O.T., et al., *Meta-modelling in chemical process system engineering*. Journal of the Taiwan Institute of Chemical Engineers, 2017. **73**: p. 135-145.
184. Masci, J., et al., *Stacked Convolutional Auto-Encoders for Hierarchical Feature Extraction*, in *Artificial Neural Networks and Machine Learning – ICANN 2011: 21st International Conference on Artificial Neural Networks, Espoo, Finland, June 14-17, 2011, Proceedings, Part I*, T. Honkela, et al., Editors. 2011, Springer Berlin Heidelberg: Berlin, Heidelberg. p. 52-59.
185. Kingma, D.P. and M. Welling *Auto-Encoding Variational Bayes*. ArXiv e-prints, 2013. **1312**.
186. Géron, A., *Hands on Machine Learning with scikit-learn and Tensorflow*. 2017, O'Reilly Media.
187. He, K., et al. *Delving Deep into Rectifiers: Surpassing Human-Level Performance on ImageNet Classification*. ArXiv e-prints, 2015. **1502**.
188. Glorot, X. and Y. Bengio, *Understanding the difficulty of training deep feedforward neural networks*, in *Proceedings of the Thirteenth International Conference on Artificial Intelligence and Statistics*, T. Yee Whye and T. Mike, Editors. 2010, PMLR: Proceedings of Machine Learning Research. p. 249--256.
189. Ioffe, S. and C. Szegedy *Batch Normalization: Accelerating Deep Network Training by Reducing Internal Covariate Shift*. ArXiv e-prints, 2015. **1502**.
190. Kingma, D.P. and J. Ba *Adam: A Method for Stochastic Optimization*. ArXiv e-prints, 2014. **1412**.
191. Hanna, S.R., O.R. Hansen, and S. Dharmavaram, *FLACS CFD air quality model performance evaluation with Kit Fox, MUST, Prairie Grass, and EMU observations*. Atmospheric Environment, 2004. **38**(28): p. 4675-4687.
192. Dharmavaram, S., S.R. Hanna, and O.R. Hansen, *Consequence analysis—Using a CFD model for industrial sites*. Process Safety Progress, 2005. **24**(4): p. 316-272.
193. Hansen, O.R., et al., *Validation of FLACS against experimental data sets from the model evaluation database for LNG vapor dispersion*. Journal of Loss Prevention in the Process Industries, 2010. **23**(6): p. 857-877.
194. Launder, B.E. and D.B. Spalding, *The numerical computation of turbulent flows*. Computer Methods in Applied Mechanics and Engineering, 1974. **3**(2): p. 269-289.
195. Hjertager, B., *Three-dimensional modeling of flow, heat transfer, and combustion*. Handbook of heat and mass transfer, 1986. **1**: p. 1303-1350.
196. Withers, R. and F. Lees, *The assessment of major hazards: The lethal toxicity of chlorine: Part 1, Review of information on toxicity*. Journal of hazardous materials, 1985. **12**(3): p. 231-282.
197. Withers, R. and F. Lees, *The assessment of major hazards: The lethal toxicity of chlorine: Part 2, Model of toxicity to man*. Journal of hazardous materials, 1985. **12**(3): p. 283-302.
198. Perry, W.W. and W.P. Articola, *Study to modify the vulnerability model of the risk management system*. 1980, ENVIRO CONTROL INC ROCKVILLE MD.

199. Ha, D., et al., *Improvement of principal component analysis modeling for plasma etch processes through discrete wavelet transform and automatic variable selection*. Computers & Chemical Engineering, 2016. **94**: p. 362-369.
200. Qin, S.J., *Survey on data-driven industrial process monitoring and diagnosis*. Annual Reviews in Control, 2012. **36**(2): p. 220-234.
201. Lee, J.-M., S.J. Qin, and I.-B. Lee, *Fault detection and diagnosis based on modified independent component analysis*. AIChE Journal, 2006. **52**(10): p. 3501-3514.
202. Jin, H.D., et al., *Robust Recursive Principal Component Analysis Modeling for Adaptive Monitoring*. Industrial & Engineering Chemistry Research, 2006. **45**(2): p. 696-703.
203. Misra, M., et al., *Multivariate process monitoring and fault diagnosis by multi-scale PCA*. Computers & Chemical Engineering, 2002. **26**(9): p. 1281-1293.
204. Kano, M., et al., *A new multivariate statistical process monitoring method using principal component analysis*. Computers & Chemical Engineering, 2001. **25**(7): p. 1103-1113.
205. Kresta, J.V., J.F. Macgregor, and T.E. Marlin, *Multivariate statistical monitoring of process operating performance*. The Canadian Journal of Chemical Engineering, 1991. **69**(1): p. 35-47.
206. Hinton, G.E. and R.R. Salakhutdinov, *Reducing the Dimensionality of Data with Neural Networks*. Science, 2006. **313**(5786): p. 504-507.
207. Goodfellow, I., Y. Bengio, and A. Courville, *Deep Learning*. 2016, MIT Press.
208. Radford, A., L. Metz, and S. Chintala *Unsupervised Representation Learning with Deep Convolutional Generative Adversarial Networks*. ArXiv e-prints, 2015. **1511**.
209. Gnanamani, M.K., et al., *Fischer–Tropsch synthesis: Effect of CO<sub>2</sub> containing syngas over Pt promoted Co/ $\gamma$ -Al<sub>2</sub>O<sub>3</sub> and K-promoted Fe catalysts*. Catalysis Communications, 2011. **12**(11): p. 936-939.
210. Song, C. and W. Pan, *Tri-reforming of methane: a novel concept for catalytic production of industrially useful synthesis gas with desired H<sub>2</sub>/CO ratios*. Catalysis Today, 2004. **98**(4): p. 463-484.
211. Cho, W., et al., *Optimal design and operation of a natural gas tri-reforming reactor for DME synthesis*. Catalysis Today, 2009. **139**(4): p. 261-267.
212. Halmann, M. and A. Steinfeld, *Thermoneutral tri-reforming of flue gases from coal- and gas-fired power stations*. Catalysis Today, 2006. **115**(1-4): p. 170-178.
213. Lee, S.-H., et al., *Tri-reforming of CH<sub>4</sub> using CO<sub>2</sub> for production of synthesis gas to dimethyl ether*. Catalysis Today, 2003. **87**(1-4): p. 133-137.
214. Tristantini, D., et al., *The effect of synthesis gas composition on the Fischer–Tropsch synthesis over Co/ $\gamma$ -Al<sub>2</sub>O<sub>3</sub> and Co–Re/ $\gamma$ -Al<sub>2</sub>O<sub>3</sub> catalysts*. Fuel Processing Technology, 2007. **88**(7): p. 643-649.
215. Jung, I., et al., *Optimal design of a large scale Fischer-Tropsch microchannel reactor module using a cell-coupling method*. Fuel Processing Technology, 2017. **159**: p. 448-459.
216. Iglesia, E., et al., *Selectivity Control and Catalyst Design in the Fischer-Tropsch*. Advances in Catalysis, 1993. **39**: p. 221.

- 217. Keim, W., *Catalysis in C1 chemistry*. Vol. 4. 2012: Springer Science & Business Media.
- 218. Bukur, D.B., et al., *Pretreatment effect studies with a precipitated iron Fischer-Tropsch catalyst*. Applied Catalysis A: General, 1995. **126**(1): p. 85-113.
- 219. Jalama, K., et al., *Co/TiO<sub>2</sub> Fischer-Tropsch catalyst activation by synthesis gas*. Catalysis Communications, 2012. **17**: p. 154-159.
- 220. N. Sharma, R. and A. A. Shaikh, *Solids suspension in stirred tanks with pitched blade turbines*. Chemical Engineering Science, 2003. **58**(10): p. 2123-2140.

## Abstract in Korean (국문초록)

최근 화학공학분야에서는 고성능 컴퓨터 연산능력과 알고리즘의 발전으로 컴퓨터 기반의 공정 프로세스 공학이 주목받고 있다. 이에 전통적으로는 응용수학분야에서 개발되고 있는 계산과학적 접근 방법들이 다양한 방식으로 공정 프로세스 공학에 이식되고 있다. 특히, 전산유체역학, 최적화 방법론, 기계학습 등의 기법들이 화학 반응기 모델링과 공정 최적화에 적용될 수 있는 방법에 대해서 연구되고 있다. 이런 계산과학적 접근법을 통해서 비전통연구 분야가 파생되고 있는데, 복잡한 3차원 반응기 구조의 유동현상이나, 기계학습을 통해 얻어진 대안모델을 활용한 최적화 방법 등이 그것이다. 이와 병행하게 지속가능한 공정에 대한 필요성이 대두되고 있다. 전통적인 화석연료를 기반으로 하는 화학공장은 원유가격에 매우 의존적이기 때문에 원료에 대한 다양한 포트폴리오를 준비하지 않으면 중동이나 미국등의 산유국의 원유가격 제한 등에 산업이 심각하게 타격 받을 수 있다. 추가적으로 이런 원유 기반 화학산업에서는 많은 양의 이산화탄소가 발생할 수 밖에 없다. 따라서, 이런 상황에서 지속가능한 화학공장을 유지하기 위해서는 이산화탄소 포집공정이 반드시 필요하며, 단순히 포집 후 저장하는 것으로는 경제성이 매우 떨어지기 때문에 이를 활용할 수 있는 방안이 간구 되고 있는 실정이다. 이런 일련의 공정의 필요성에 알맞는 공정은 Gas-to-Liquid (GTL) process 와 Carbon capture, utilization, and storage (CCUS)로 보여진다.

본 학위논문에서는 공정 및 반응기의 모델링, 최적화, 그리고 설계문제를 전산유체역학, 수리계획모델, 기계 학습, 그리고 다양한 최적화 알고리즘을 통해서 해결하고자 하였다. 먼저 지속가능한 공정에서 가장 중요하다고 볼 수 있는 GTL 공정의 FT 마이크로채널 반응기와 CCUS 공정의 삼상 탄산화 반응기를 전산유체역학을 통해서 모델링하였다. 추가로 전산유체역학을 통한 반응기모델과 공정 시뮬레이터를 연계한 플랫폼을 개발하여 기존의 공정 시스템 엔지니어링의 분야의 연구 범위 확장을 제안했다.

이렇게 개발된 반응기모델을 통해서, 확률적 최적화 알고리즘인 유전알고리즘과  $\epsilon$ -제약조건 방법을 이용하여 FT 마이크로채널 반응기에서  $C_{5+}$  생산성 최대화와 최대온도상승 폭의 최소화를 동시에 이루는 다중 목적함수 최적화를 수행하였다. 메인 정수혼합비선형 프로그래밍 (MINLP) 문제는 외부 CFD 반응기 모델 함수와 내부 최적화 제약조건으로 나누어진다. 다층 촉매충진 기법에 적용하여, 발열이 최대한 균등하게 나올 수 있게 하였다. 최적점은 다양한 크로스오버에 대해서 재생산이 가능하였으며, 다른 전통적인 비선형 최적화 알고리즘보다 효율적인 것으로 판단된다. 파레토 최적점을 보면,  $C_{5+}$  생산성은 기존 케이스에 대비해 22% 향상되었으며, 최대온도상승 폭은 63.2% 감소한 것으로 보인다.

공정수준에서의 최적화 플랫폼에서는 hidden constraints 를 처리하기 위해 sub-dividing step 을 적용한 modified DIRECT 알고리즘을 제안한다. 본 알고리즘의 성능은 극저온 단일 혼합 냉매를 이용한 천연가스 액화공정에 적용하여 검증하였다. 그리고

기존에 잘 알려져 있는 통계적 최적화 알고리즘인 (GA, PSO, SA), 모델 기반 최적화 알고리즘인 (SNOBFIT), 지역 최적화 기법인 (GPS, GSS, MADS, active-set, interior-point, SQP)과 비교하여 그 효과를 검증하였다. 기존 공정 대비 최적 공정의 경우 압축기 에너지를 18.9% 가량 줄일 수 있었다. 같은 장에서 열교환망 합성에 대한 연구도 함께 진행되었다. 다양한 유틸리티를 동시에 활용하여 CAPEX 와 OPEX 를 한번에 최적화하는 초구조를 제안하여 사용할 수 있는 유틸리티가 많은 경우 기존의 방법론으로는 찾기 힘들었던 획기적인 구조들을 찾아낼 수 있는 것으로 확인된다.

공장전체적인 수준에서의 분석방법에 대해서는 독성가스 누출 위험성을 줄이기 위한 CFD 대안모델을 개발하였다. 딥러닝 기법 중 convolutional layers 를 적용한 variational autoencoder 를 이용하여 대량의 CFD 데이터를 압축하고 이를 딥뉴럴네트워크 기반의 함수에 매핑하여 독성가스 확산계산 시간을 획기적으로 감소시켰다. 개발된 모델은 울산에 있는 미포 산업단지의 염소가스 누출 사고에 적용하여 검증하였다. 다른 대안모델보다 월등한 성능을 보였으며 변수공간 내 이미지 변화가 부드럽게 진행되어 이미지가 단순히 기억되는 것이 아니라 그 특징(feature)을 정확하게 훈련시켰음을 보였다.

최종적으로 개질기와 이산화탄소 분리장치, 그리고 FT 합성 반응기를 포함하는 1 BPD 급 GTL 파일럿 공정을 통해 산업적 적용가능성에 대해서 논의하였다. 체계적인 마이크로채널 반응기 설계 절차를 설명하고 실제 설계된 반응기의 형태와 구조가 어떤



논리를 통해서 도출되었는지에 대해서 설명한다. 평균 98.27%의 메탄전환률을 보이는 개질기와 2.08 의 CO/H<sub>2</sub> 비율로 합성가스를 공급해주는 이산화탄소 분리기를 거쳐 FT 마이크로채널 반응기로 합성가스가 주입된다. 반응기의 성능을 검증하기 위해서 FT 마이크로채널 반응기와 다중 채널 고정층반응기가 병렬 형태로 설치되었다. 전자의 경우 220°C-240°C 까지의 운전조건 범위 내에서 안전하게 온도제어가 된 반면, 후자의 경우에는 발열현상이 심각해지고 폭주반응이 일어나게 되어 마이크로채널 반응기의 제열성능이 훨씬 뛰어난 것으로 판단된다. 같은 장에서 CCUS 탱크교반 탄산화 반응기에 대한 컴퓨터 기반 설계방법론이 적용된 연구로 진행하였다. 6가지의 변수 (교반기 개수, 교반기 종류, 교반기 속도, D/T, 교반기 유격, 배플)에 대한 설계 검증을 통해서 40 tonCO<sub>2</sub>/day 급 탄산화 반응기의 최적 설계에 대해서 제안하였다.

주요어: 계산과학; 전산유체역학; 최적화; 디자인; Gas-to-Liquid (GTL); 피셔-트롭쉬; 마이크로채널 반응기; 탄소 포집, 전환, 저장; 기계학습; 딥러닝

학 번 : 2013-20968